ALGERIAN DEMOCRATIC AND POPULAR REPUBLIC
MINISTRY OF HIGHER EDUCATION AND SCIENTIFIC RESEARCH

ABDELHAMID IBN BADIS UNIVERSITY - MOSTAGANEM FACULTY
OF SCIENCE AND TECHNOLOGY
DEPARTMENT OF ELECTRICAL ENGINEERING

THESIS

PRESENTED TO OBTAIN

LMD DOCTORATE DEGREE

Specialty: Electronics

Option: Microelectronics and Embedded Microsystems

By

BENAHMEDI Lakhdar

COMPARATIVE STUDY OF THE STRUCTURAL, ELECTRONIC, OPTICAL, AND THERMOELECTRIC PROPERTIES OF A SERIES OF PEROVSKITE COMPOUNDS.

(APPLICATION TO EMBEDDED SYSTEMS)

Publicly defended on 05/05/2025 before the jury composed of:

Mr. BENSTAALI Wissam	Professor	Chair	UMAB - Mostaganem
Mrs. ABBAD Amel	Professor	Examiner	UMAB - Mostaganem
Mrs. CHERID Samira	Professor	Examiner	UMAB - Mostaganem
Mrs. BENTATA Rachida	Professor	Examiner	UMS - Mascara
Mr. DJELTI Radouane	Professor	Supervisor	UMAB - Mostaganem
Mrs. BESBES Anissa	Professor	Co-Supervisor	UMAB - Mostaganem

Academic Year: 2025-2026

Acknowledgement

All praise and gratitude are due to Almighty Allah, the Most Gracious, the Most Merciful, who granted me health, patience, and strength to complete this work. Without His divine guidance and blessings, none of this achievement would have been possible.

The completion of this thesis marks a significant milestone in my academic journey, one that would not have been possible without the support, encouragement, and guidance of many individuals and institutions. It is with deep appreciation that I acknowledge those who have contributed to this work, both directly and indirectly. First and foremost, I would like to express my sincere gratitude to my supervisors, **Prof. Djelti Radouane** and **Prof. Besbes Anissa**, for their invaluable guidance, constant encouragement, and professional expertise. Their patience, insightful advice, and unwavering support have been essential in shaping this work and enriching my academic and personal development.

My deep appreciation also goes to the **Technology and Solids Properties Laboratory, Faculty of Science and Technology, University of Mostaganem**, for providing the resources and a stimulating research environment. I am particularly grateful to its director, **Prof. Bouadjemi Bouabdellah**, for his leadership and support throughout the course of my doctoral studies.

My sincere thanks are also extended to the examiners and members of the thesis defense committee, whose careful review and insightful remarks have greatly contributed to the improvement of this work. I would like to express my special appreciation to: **Prof. BENSTAALI Wissam**, Chair of the committee; **Prof. ABBAD Amel**, Examiner; **Prof. CHERID Samira**, Examiner; and **Prof. BENTATA Rachida**, Examiner. Their valuable comments and constructive evaluations have greatly enhanced the quality of this thesis.

I would also like to extend my heartfelt gratitude to the **CFD**, **CSD**, and **CSF** committees for their efforts and dedication in processing and facilitating my thesis defense dossier. My sincere thanks are especially addressed to the Vice Dean, **Prof. Sardou Miloud**, and to **Mrs. Hezil Latifa** for their kind assistance, professionalism, and continuous support throughout the administrative procedures.

I am grateful to the **Ministry of Higher Education of Algeria** and the **Faculty of Science and Technology, University of Mostaganem**, for their support in facilitating my academic internships in Turkey.

During these internships at **Ondokuz Mayıs University in Samsun, Turkey**, I had the privilege of collaborating with esteemed scholars and colleagues. I would like to warmly thank **Prof. Nacemi Dege** and **Dr. Ibrahim Inanc** for their scientific guidance and generous support. I also extend my heartfelt gratitude to **Mr. Rakan Bashir, Mrs. Emine Berrin Poyraz, and Mr. Okan Simsek** for their assistance, kindness, and friendship, which enriched both my professional and personal experience during my stay.

Dedication

First and foremost, I bow in gratitude to Almighty Allah, the Most Gracious and the Most Merciful, whose blessings, guidance, and mercy have accompanied me at every stage of this journey. Without His will and support, none of this would have been possible. With this faith in my heart and with deepest respect, I dedicate this thesis to the people who have been my guiding light, my strength, and my constant source of motivation throughout this path.

At the very heart of this work, I dedicate it to my beloved **parents**, whose boundless love, sacrifices, and unwavering support have been the cornerstone of every achievement in my life. From my earliest days, they instilled in me the values of perseverance, integrity, and diligence. Their faith in me has provided the courage to confront challenges, while their encouragement has been a constant source of strength in moments of doubt. To my brother and sisters, I extend my deepest gratitude, for their affection and kindness have reminded me at every stage of this journey that I was never alone. This accomplishment belongs to them as much as it does to me.

To my dear **brother and sisters**, your love, encouragement, and unwavering belief in me have been a constant source of strength throughout my life. In moments of difficulty, your words reminded me to stay strong, and in times of achievement, your joy magnified my own. This work is as much a reflection of your support as it is of my effort. I dedicate this thesis to you, with gratitude, affection, and endless respect.

I also wish to dedicate this thesis to my esteemed supervisors, **Prof. Djelti Radouane** and **Prof. Anissa Besbes**. Their invaluable guidance, continuous encouragement, and generous support have shaped the course of this work and greatly enriched my academic path. They not only provided scientific advice but also inspired me with their dedication, patience, and trust. To have had the privilege of learning under their supervision is one of the greatest honors of my academic life.

My sincere dedication also goes to my former teacher and Master's degree supervisor, **Dr. Benzina Amina**, who played a pivotal role in my academic beginnings. Her mentorship, wisdom, and motivation during my early research years gave me the confidence and determination to pursue this doctoral journey.

This work is dedicated with special affection to my dear friends **Samia Moulebhar**, **Ali Aissani**, and **Sidahmed Bendehiba**, whose constant help, kindness, encouragement, and unwavering support have been invaluable throughout this journey. Their companionship, both academically and personally, especially during the most difficult moments, brought joy, balance, and strength to my academic life, and their friendship has been a true blessing. My heartfelt gratitude is equally extended to **Dr. Benosmane Sarra** and **Mrs. Hammou Kheira** for their kindness, support, and valued presence during this important stage of my life.

Lastly, but certainly not least, I dedicate this thesis to my PhD colleagues of the **2023 promotion, Hamdi Cherif Mohammed, Mechehoud Noureddine, Messaoudi Abdelkarim, Bentahar Heythem, Khatar Abdelhak, Hamiche Korichi, Sarra Merabet, Righi Aya, Mechehoud Khedidja, Khantar Sidahmed, and Bilel Achir**. Together, we shared not only academic discussions but also moments of solidarity, encouragement, and friendship. Their companionship created a spirit of unity and cooperation that turned this demanding academic experience into a journey filled with memorable moments. The bonds we forged through shared efforts and mutual support are among the most valuable outcomes of my doctoral studies.

This thesis, therefore, is not only the result of individual effort but also a collective achievement. It reflects the guidance of my teachers, the love of my family, the encouragement of my friends, and the solidarity of my colleagues. To all of you who have supported me, inspired me, and stood by my side in one way or another, I dedicate this work with endless gratitude, respect, and affection.

Table Of Contents

Table of Contents

Nomenclature

Nomenclature

Symbols	Meaning
ABX_3	General perovskite formula
$A_2BB'X_6$	Double perovskite formula
A_3BX	Anti-perovskite formula
A_3BX_3	New anti-perovskite derivative
Ψ	Wave function
$\hat{H}$	Hamiltonian operator
E	Energy eigenvalue
Te	Total kinetic energy of electrons
Tn	Total kinetic energy of nuclei
V_{ee}	Electron–electron interaction energy
V_{nn}	Nucleus–nucleus interaction energy
V_{en}	Electron–nucleus interaction energy
$\hbar$	Reduced Planck's constant
m_e	Electron mass
M_n	Mass of nucleus n
∇^2	Laplacian operator
e	Elementary charge
ε_0	Vacuum permittivity
$\rho(r)$	Electron density
Ne	Total number of electrons
E[ρ]	Total energy functional
F[ρ]	Universal functional (T+Vee)
Ts[ρ]	Kinetic energy of non-interacting system
Exc[ρ]	Exchange–correlation functional
EH[ρ]	Hartree energy (Coulomb)
Vext	External potential
φi(r)	Kohn–Sham orbital
εi	Kohn–Sham eigenvalue
Veff(r)	Effective potential
Ueff	Effective Hubbard parameter
nmmσ	Occupation number of localized orbital
BOA	Born–Oppenheimer Approximation
HF	Hartree–Fock approximation
SCF	Self-consistent field
DFT	Density Functional Theory
SDFT	Spin Density Functional Theory
HK theorem	Hohenberg–Kohn theorem
KS	Kohn–Sham formulation
XC	Exchange–Correlation
LDA	Local Density Approximation
LSDA	Local Spin Density Approximation
GGA	Generalized Gradient Approximation
PBE	Perdew–Burke–Ernzerhof functional

Symbols	Meaning
PBEsol	PBE for solids
WC	Wu–Cohen functional
BLYP	Becke–Lee–Yang–Parr functional
mBJ	Modified Becke–Johnson potential
BR	Becke–Roussel potential
DFT+U	DFT with Hubbard correction
APW	Augmented Plane Wave method
LAPW	Linearized Augmented Plane Wave method
FP-LAPW	Full-Potential Linearized Augmented Plane Wave
Ry	Rydberg unit of energy
C_{ij}	Elastic stiffness constants
σ_{ij}	Stress tensor
ε_{kl}	Strain tensor
U	Elastic strain energy per unit volume
B	Bulk modulus
G	Shear modulus
E	Young's modulus
ν	Poisson's ratio
A	Elastic anisotropy factor
B/G	Pugh ratio
C_P	Cauchy pressure
DFT	Density Functional Theory
S, SAB, SA, SB	Seebeck coefficient (thermoelectric power), difference between materials A and B
ΠAB	Peltier coefficient for junction of A and B
h	Thomson coefficient
E	Electric field
∇T	Temperature gradient
Q	Heat absorbed or released (Peltier effect)
I	Electric current
σ	Electrical conductivity
σ/τ	Electrical conductivity per relaxation time
κe	Electronic thermal conductivity
κL	Lattice thermal conductivity
κtot	Total thermal conductivity
τ	Relaxation time
J	Electrical current density
q	Heat current density
f(k,r,t)	Distribution function of carriers (probability at k, r, t)

Nomenclature

Symbols	Meaning
f_0	Equilibrium distribution function
Δf	Deviation from equilibrium
ε	Carrier energy
μ	Chemical potential
$v(k)$	Carrier velocity (from band structure)
k	Wavevector in Brillouin zone
Ω	Unit cell volume
N_k	Number of k-points in sampling
ZT	Dimensionless thermoelectric figure of merit
COP	Coefficient of performance (cooling efficiency)
R	Electrical resistance
Gth	Thermal conductance
W	Electrical work
SOC	Spin–Orbit Coupling
BTE	Boltzmann Transport Equation
RTA	Relaxation Time Approximation
DOS	Density of States
ω	Angular frequency of the incident light
$\varepsilon(\omega)$	Complex dielectric function
$\varepsilon_1(\omega)$	Real part of dielectric function
$\varepsilon_2(\omega)$	Imaginary part of dielectric function
IPA	Independent Particle Approximation
RPA	Random Phase Approximation
$n(\omega)$	Refractive index
$k(\omega)$	Extinction coefficient
c	Speed of light in vacuum
α	Absorption coefficient
$R(\omega)$	Reflectivity
$L(\omega)$	Energy loss function
JDOS	Joint Density of States
NIR	Near-Infrared region
VIS	Visible region
UV	Ultraviolet region
EELS	Electron Energy Loss Spectroscopy
ε_0 (static)	Static dielectric constant
PSC	Perovskite Solar Cell

Symbols	Meaning
SCAPS-1D	Solar Cell Capacitance Simulator (1D)
n-i-p	Cell architecture
p-i-n	Reverse cell architecture
ETL	Electron Transport Layer
HTL	Hole Transport Layer
FTO	Fluorine-doped Tin Oxide
Au	Gold, back contact
$\psi(x)$	Electrostatic potential
$\varepsilon(x)$	Position-dependent dielectric permittivity
q	Elementary charge
n(x), p(x)	Electron and hole concentration, respectively
ρdef(x)	Defect/trap-related charge density
Jn, Jp	Electron and hole current densities
G(x)	Photogeneration rate
R(x)	Recombination rate (SRH, radiative, Auger)
VOC	Open-circuit voltage
JSC	Short-circuit current density
FF	Fill Factor
PCE	Power Conversion Efficiency
EQE	External Quantum Efficiency
CBO	Conduction Band Offset
VBO	Valence Band Offset
Pin	Incident solar power (standard AM1.5G, 100 mW/cm²)
AM1.5G	Standard solar illumination spectrum
Li-Po 6S	Lithium-Polymer battery, 6 cells in series (22.2 V nominal)
MPPT	Maximum Power Point Tracking
INA169	Current sensor
B25	Voltage sensor
MOSFET (Q1)	Power transistor in DC-DC converter
L, C_0, C_1, D1	Inductor, capacitors, diode in DC–DC converter
LCD	Liquid Crystal Display (real-time monitoring)

List of Figures

CHAPTER I

CHAPTER III

List of Tables

General Introduction

General Introduction

Embedded systems have become an integral part of modern technological advancements, finding applications in a wide range of fields, including telecommunications, transportation, healthcare, and agriculture. These systems are designed to perform specific tasks with high efficiency, often in real-time environments, and are embedded within larger systems **[1]**. Their significance continues to grow as the world moves towards greater automation and sustainability. However, despite their rapid evolution, the development of embedded systems has faced several challenges **[2]**.

One of the primary obstacles is the increasing cost of raw materials, particularly those used in key components like solar cells and batteries. As the demand for renewable energy-powered embedded systems rises, materials such as silicon in solar cells, lithium in batteries, and III-V compounds in LEDs have become essential. Yet, the rising prices of these materials due to resource depletion and limited availability have made these systems more expensive. Additionally, embedded systems often require human interaction in fields such as agriculture, further increasing the cost-effectiveness of many projects **[2]**.

In response to the growing concerns about the scarcity of raw materials and the increasing costs of production, researchers have sought to develop embedded systems that are more self-sufficient. A key area of focus has been the integration of renewable energy sources, particularly solar energy, to reduce dependence on external power supplies. However, this transition is not without challenges. The high cost and weight of solar panels, particularly in agricultural applications, make it difficult to integrate renewable energy systems into embedded devices cost-effectively.

In recent years, a major trend in materials research has been the exploration of alternative materials to replace traditional ones used in solar cells, batteries, and LEDs. One of the most promising materials in this context is perovskite compounds. These materials have shown exceptional efficiency in solar cell applications, with perovskite-based cells achieving efficiencies up to 30%. They are also being explored for use in batteries and LEDs, with real-world examples such as perovskite solar cells showing great promise for large-scale deployment in renewable energy systems **[3]**.

This research seeks to explore and analyze the potential of perovskite materials in the context of embedded systems, focusing on their electronic, elastic, optical, and thermoelectric properties. Through a combination of theoretical and computational methods, this study aims to develop a comprehensive understanding of these materials' behavior and their potential for use in energy-efficient, low-cost embedded systems.

The primary objective of this research is to investigate new, clean, and non-toxic materials that can offer enhanced photovoltaic and energy performance at a lower cost than currently available materials. Specifically, this study focuses on perovskite compounds, including classic perovskites, double perovskites, and antiperovskites, and their application in embedded systems for industrial purposes. By examining the structural, electronic, elastic, optical, and thermoelectric properties of these materials, the research aims to:

- Examine the stability and feasibility of synthesizing perovskite compounds.
- Evaluate the photovoltaic efficiency and thermoelectric performance of these materials in embedded systems.
- Identify potential applications in renewable energy-powered embedded systems, particularly in off-grid and agricultural contexts.
- Propose novel materials that can replace traditional ones such as silicon, lithium, and III-V compounds, reducing reliance on rare and expensive raw materials.

The primary research questions are as follows:

- What are the structural, electronic, elastic, optical, and thermoelectric properties of perovskite materials, and how do they compare to traditional materials used in embedded systems?
- Can perovskite-based materials provide an effective alternative to silicon in solar cells, lithium in batteries, and III-V compounds in LEDs, in terms of both efficiency and cost?
- What are the potential challenges in integrating perovskite materials into renewable energy-powered embedded systems, and how can these challenges be addressed?

This research will focus on the theoretical and computational investigation of perovskite compounds for use in renewable energy-powered embedded systems. It will involve a comparative study of various perovskite materials, including classic perovskites, double

perovskites, and antiperovskites. Key properties such as structural stability, electronic band structure, elasticity, optical behavior, and thermoelectric performance will be analyzed using Density Functional Theory (DFT) and related computational techniques **[4]**.

The research employs a combination of computational methods to investigate the structural, electronic, elastic, optical, and thermoelectric properties of various perovskite materials. The primary computational tool is WIEN2k, which uses the Full-Potential Linearized Augmented Plane Wave (FP-LAPW) method to perform Density Functional Theory (DFT) calculations **[5,6]**. This method will be used to determine the materials' electronic structures, band gaps, and densities of states. Additionally, SCAPS-1D software will be used to simulate the performance of perovskite-based materials in solar cells, while MATLAB will be used to model the full performance of solar panels. Finally, Proteus will be utilized to simulate charging circuits for embedded systems powered by solar energy **[7]**.

This research is structured around seven chapters.

- ✓ **Chapter I:** Introduction to perovskite materials, including their historical development, structural characteristics, and synthesis techniques. This chapter will provide a background for the theoretical and computational work presented in later chapters.
- ✓ **Chapter II:** Overview of the theoretical and computational methods used to study perovskite materials, including Density Functional Theory (DFT), the WIEN2k code, and related techniques.
- ✓ **Chapter III:** Analysis of the structural and electronic properties of perovskite materials using DFT calculations, focusing on band structure, density of states, and other key structural parameters.
- ✓ **Chapter IV:** Investigation of the mechanical and vibrational properties of perovskite materials, including elastic constants and phonon dispersion relations, to assess their stability and suitability for embedded systems.
- ✓ **Chapter V:** Exploration of the thermoelectric properties of perovskite materials and their potential for use in energy harvesting applications.
- ✓ **Chapter VI:** Examination of the optical properties of perovskite materials and their relevance for applications in optoelectronics and energy harvesting technologies.
- ✓ **Chapter VII:** Discussion of the integration of perovskite solar cells into embedded systems, with a focus on agricultural applications and the challenges of using renewable energy in embedded systems.

Bibliography

[1] R. Camposano and J. Wilberg, Design Automation for Embedded Systems, 1996, 1, 5–50.
[2] T. Henzinger, J. S.-I. S. on F. Methods and undefined 2006, Springer, 2006, 4085 LNCS, 1–15.
[3] N. Tsvetkov, M. Lee, Y. Kim, D. Kim, J. S. Yun and H. Min, J Mater Chem A Mater, 2025, 13, 7656–7681.
[4] V. Butera, Physical Chemistry Chemical Physics, 2024, 26, 7950–7970.
[5] K. Schwarz and P. Blaha, Comput Mater Sci, 2003, 28, 259–273.
[6] M. Petersen, F. Wagner, L. Hufnagel, M. Scheffler, P. Blaha and K. Schwarz, Comput Phys Commun, 2000, 126, 294–309.
[7] E. A. Sobie, Sci Signal, 2011, 4, 7–8.

CHAPTER I

Research Background

I.1 Introduction

Perovskite materials, originally identified in the mineral $CaTiO_3$, have evolved into one of the most versatile classes of compounds in materials science. Defined by their adaptable ABX_3 crystal structure, perovskites accommodate a wide range of chemical elements, enabling the design of materials with tailored optical, electronic, magnetic, and thermal properties. This chapter outlines the historical evolution, structural characteristics, and compositional diversity of perovskites and their derivatives particularly double and anti-perovskites while also discussing key synthesis techniques and emerging applications. The aim is to establish a comprehensive background that contextualizes the theoretical and computational investigations presented in the following chapters.

I.2 Perovskites

The term perovskite refers both to a specific mineral and to a broad class of compounds that adopt the same crystal structure as that mineral. The perovskite structure was first identified in 1839, when the German mineralogist Gustav Rose discovered a naturally occurring compound with the chemical formula $CaTiO_3$ in the Ural Mountains **Figure (I.1)**. In honor of the Russian nobleman and mineralogist Lev Alekseevich Perovski, Rose named this new mineral perovskite **[1]**.

Figure I.1: A rare Perovskite in matrix cluster from Russia

Although the mineral was known in the 19th century, the structural and functional potential of perovskites began to attract significant scientific interest only in the mid-20th century, especially with the rise of crystallographic techniques and solid-state physics **[2]**. The 1980s and 1990s saw a surge in research due to ground-breaking findings like high-temperature superconductivity in perovskites based on copper oxide (e.g., $YBa_2Cu_3O_{7-\delta}$), which created new opportunities in materials science and condensed matter physics **[3]**. These advancements made the perovskite structure a very adaptable framework that can hold many anions and cations.

As scientific understanding progressed, the perovskite family expanded well beyond the original $CaTiO_3$ compound. Numerous derivative materials emerged, maintaining the characteristic three-dimensional framework but incorporating diverse chemical constituents. Among these, halide perovskites, particularly organic-inorganic hybrids such as $CH_3NH_3PbI_3$, gained rapid prominence in the early 2010s for their remarkable optoelectronic properties and potential in photovoltaic applications, eventually achieving power conversion efficiencies exceeding 25% in less than a decade **[4]**.

In parallel, other classes of perovskite-like materials were developed, including chalcogenide perovskites (e.g., $BaZrS_3$), oxide-based double perovskites ($A_2BB'O_6$), and halide double perovskites (such as $Cs_2AgBiBr_6$), each offering distinct advantages in terms of stability, toxicity, or band gap tunability. Structural diversification also led to the emergence of anti-perovskites, where the positions of cations and anions are effectively reversed compared to the classic perovskite structure. These materials typically adopt the general formula A_3BX, with a range of interesting electronic, magnetic, and thermoelectric behaviors **[5]**.

Moreover, complex perovskites and low-dimensional perovskites have been developed for targeted functionalities, including ferroelectricity, spintronics, and catalysis. These structural families are not only defined by the ABX_3 formula but also include layered, Ruddlesden-Popper, and Dion–Jacobson phases, further illustrating the adaptability of the perovskite framework **[6]**.

Recently, in 2023, anti-perovskite-inspired compounds with the generalized formula A_3BX_3 emerged as the subject of a novel theoretical framework within the broader field of perovskite derivatives. Guided predominantly by density functional theory (DFT) calculations,

recent studies have demonstrated that these materials exhibit strong optical absorption and suitable band gap values, positioning them as promising candidates for next-generation photovoltaic applications **[7]**. Theoretical investigations suggest that A_3BX_3 compounds offer a versatile platform for designing efficient solar absorbers by integrating the favorable electronic characteristics of conventional perovskites with the potential benefits of enhanced stability and reduced toxicity **[8]**.

The progression of perovskite research reflects a broader shift in materials science toward functional material design and structural tunability. What began as a mineralogical curiosity has evolved into one of modern materials research's most extensively explored and technologically significant structural frameworks **[9]**.

I.3 Chemical Diversity and Structural Flexibility

The perovskite crystal structure, first described in its ideal cubic form with the general formula ABX_3, is renowned for its remarkable tolerance to chemical substitution and structural deformation. This intrinsic flexibility underpins the vast compositional landscape of perovskites, making them a highly versatile platform for designing functional materials across diverse disciplines such as photovoltaics, catalysis, spintronics, and thermoelectrics **[10]**.

I.3.1 Ideal Structure and Symmetry Distortions

In the archetypal cubic perovskite (space group $Pm\bar{3}m$), the A cation is 12-fold coordinated in a cuboctahedral site, while the B cation resides in the center of an octahedron formed by six X anions **[11]**. This high-symmetry configuration is stable only for a narrow range of ionic radii ratios. When the size mismatch between A, B, and X ions increases, the lattice undergoes cooperative tilting of the BX_6 octahedra, leading to symmetry-lowered structures such as tetragonal, orthorhombic, monoclinic, or rhombohedral phases, as illustrated in **Figure (I.2) [12]**. These distortions, while preserving the overall perovskite framework, significantly alter the electronic bandwidth, orbital hybridization, and interatomic distances, thereby affecting the physical properties of the material.

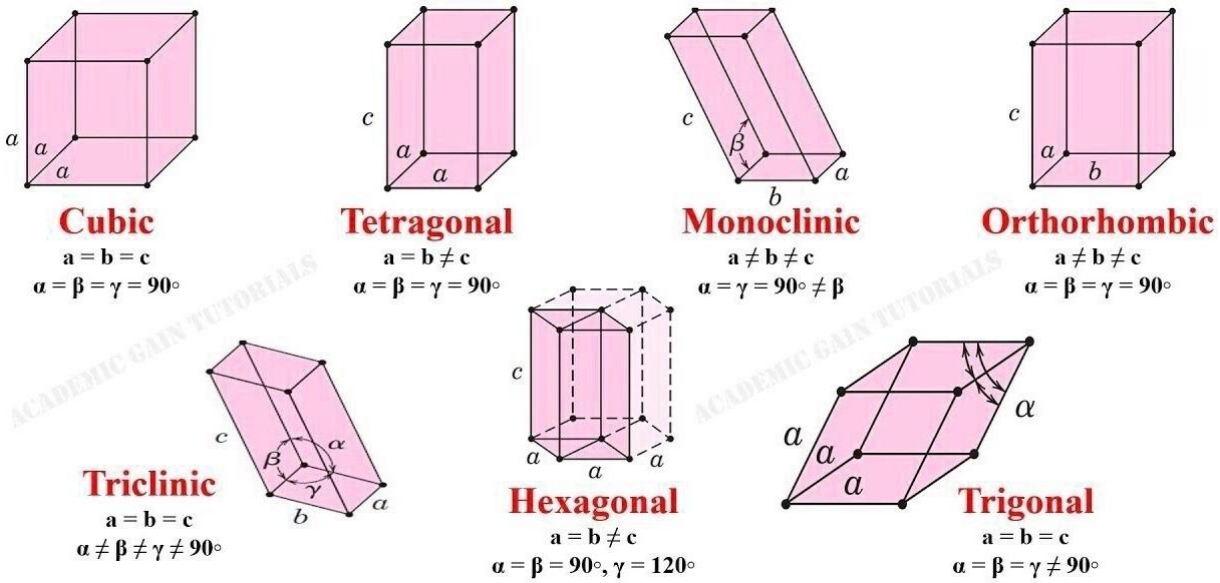

Figure I.2: The seven primitive crystal systems

I.3.2 Compositional Diversity at A, B, and X Sites

The inherent compositional flexibility of perovskite materials, with the formula ABX_3, is a defining characteristic that enables extensive tunability of their physical and chemical properties. Each of the crystallographic site's "A" typically a larger cation, "B" a smaller transition metal or main group element, and "X" an anion, often oxygen or a halogen, as shown in **Figure I.3(a)**, can be systematically varied to tailor the material for specific applications, such as photovoltaics, catalysis, ferroelectrics, magnetism, thermoelectrics, and superconductivity. The "A-site" is usually occupied by larger alkali, alkaline earth, or rare-earth cations such as Ca^{2+}, Sr^{2+}, Ba^{2+}, La^{3+}, or organic cations in hybrid perovskites (e.g., $CH_3NH_3^+$ (MA^+), $HC(NH_2)_2^+$, (FA^+)) see **Figure I.3(c)**. These cations primarily influence the structural stability and tolerance factor of the perovskite lattice **[13]**.

Historical studies, such as those by Müller and Roy in 1974 and Shannon in 1976, provided comprehensive ionic radius tables that were crucial for estimating the formability of perovskites based on this factor **[14]**. In oxide perovskites, "A-site" substitution has been used extensively to enhance ferroelectric and dielectric properties. For example, in $Ba_{1-x}Sr_xTiO_3$ solid solutions, gradual substitution of Ba^{2+} with the smaller Sr^{2+} tunes the ferroelectric Curie temperature and lattice constants, enabling precise control over dielectric behavior **[15]**.

The "B-site" hosts smaller cations, typically transition metals such as Ti^{4+}, Fe^{3+}, Mn^{3+}, Co^{3+}, Nb^{3+}, Mo^{3+}, or post-transition elements, which are often responsible for the electronic and magnetic functionalities of perovskites. The nature of the "B-site" atom critically determines the degree of hybridization with "X-site" anions, influencing band structures, magnetism, and conduction mechanisms **[13]**.

Pioneering studies on $LaBO_3$ (B = Mn, Co, Fe, Ni) perovskites by Nakamura and co-workers in the mid-20th century established the link between "B-site" electronic configurations and magnetic/electronic behavior, introducing concepts such as double exchange and super exchange interactions **[16]**. Moreover, in high-temperature superconducting perovskites like $YBa_2Cu_3O_{7-\delta}$, the Cu-O planes with Cu occupying the "B-site" are essential for superconductivity, demonstrating how delicate B-site chemistry controls emergent quantum phenomena **[17]**.

In recent years, the design of "B-site" ordered double perovskites such as Sr_2FeMoO_6, Ba_2FeReO_6, and La_2NiMnO_6 has opened new possibilities in spintronic applications due to the half-metallic nature and high spin polarization of these materials **[18]**. The "X-site", traditionally occupied by an anion such as O^{2-}, F^-, Cl^-, Br^-, or I^-, plays a pivotal role in mediating B-X-B connectivity and thereby impacts the dimensionality, band gap, and overall structural integrity. Anion substitution or mixing is a powerful strategy to control optical and electronic properties. In halide perovskites like $CH_3NH_3Pb(I_{1-x}Br_x)_3$, tuning the I^-/ Br^- ratio allows precise band gap engineering, which is vital for optimizing solar cell efficiency and stability **[13]**.

Furthermore, early studies on oxyfluoride and oxynitride perovskites such as $LaTiO_2N$ demonstrated how replacing oxygen with less electronegative anions like N^{3-} reduces the band gap, thereby enhancing visible-light photocatalytic activity **[19]**. Similarly, the introduction of chalcogenide anions (S^{2-}, Se^{2-}) in sulfide perovskites like $BaZrS_3$ has resulted in new materials with narrow band gaps and strong absorption coefficients, which are promising for photovoltaic and optoelectronic applications **[20]**. A major advantage of the perovskite framework lies in its capacity for multisite substitution, where combinations of "A, B, and X-site" doping produce synergistic effects. For example, in $(Ba,Sr)(Ti,Zr)O_3$, co-substitution at A- and B-sites is used to optimize piezoelectric and ferroelectric properties, while in $(La,Sr)MnO_3$, A-site doping with

Sr^{2+} introduces mixed valence Mn^{3+}/Mn^{4+} states at the B-site, enhancing colossal magnetoresistance **[21]**.

The compositional diversity of perovskites enables vast chemical design space and functional tailoring. Historical and contemporary studies consistently highlight that rational control over site-specific substitution leads to predictable and tunable properties, rendering perovskites a uniquely versatile class of materials for multifunctional applications **[22]**.

I.3.3 Derivative and Extended Perovskite Structures

While the canonical ABX_3 perovskite framework already allows considerable compositional and structural variation, numerous derivative and extended structures have been discovered or engineered that retain the essential features of the perovskite lattice namely, corner-sharing BX_6 octahedra but exhibit modified topologies, dimensionalities, or chemical ordering **[23]**. These variants arise due to the flexibility of the perovskite scaffold to accommodate larger unit cells, cationic ordering, and stacking faults. As a result, the term "perovskite" now encompasses a broader family of compounds, including double perovskites, layered perovskites, anti-perovskites, and molecular or hybrid variants, each of which is associated with unique physical properties and technological applications **[24]**.

I.3.3.1 Double Perovskites

Double perovskites represent one of the most well-studied extensions of the ABX_3 form, in which the B-site is occupied alternately by two different cations B and B′ in a rock-salt-type ordering. This structural modification typically leads to a doubling of the unit cell and can be formulated as $A_2BB'X_6$, as depicted in **Figure I.3(d)**. Double perovskites have attracted extensive interest due to their rich electronic and magnetic behavior, especially when B and B′ are transition metals with different oxidation states or spin configurations **[25]**.

A pioneering example is Sr_2FeMoO_6, reported in the mid-1990s **[26]**, which was found to exhibit half-metallic ferromagnetism and a high Curie temperature of ≈420 K, making it a promising material for spintronic applications. The origin of its magnetoresistance was attributed to strong hybridization between the Fe 3d and Mo 4d orbitals and spin polarized charge transport. Another historically significant compound is La_2MnNiO_6, first studied in the

1960s [27], which showed ferromagnetic behavior due to Mn^{3+}-O-Ni^{3+} super exchange interactions.

In more recent years, interest has shifted toward halide-based double perovskites, particularly in the context of lead-free alternatives for photovoltaics. $Cs_2AgBiBr_6$ has been intensively studied as a non-toxic, air-stable halide double perovskite [28], displaying an indirect band gap of ≈1.95 eV and high structural stability. While its photovoltaic efficiency remains modest compared to lead-based halide perovskites, compositional engineering (e.g., partial substitution of Bi^{3+} with Sb^{3+} or Ag^{+} with Cu^{+}) has been employed to tune the band structure toward direct transitions and higher absorption coefficients [29].

I.3.3.2 Anti-Perovskites

Anti-perovskites invert the typical perovskite stoichiometry and atomic arrangement. In these materials, the larger A-site cations occupy the positions normally taken by anions, while the central site is filled by a small electronegative atom such as nitrogen or oxygen **Figure I.3(b)** [30]. The most extensively studied examples include Li_3OX (X = Cl, Br), which are fast lithium-ion conductors with high ionic mobilities [31]. These materials have found applications in solid-state batteries and were first described in detail in the early 2000s [32].

In the realm of electronic structure, anti-perovskites such as Cu_3PdN and Mg_3Bi_2 have been shown to host topologically non-trivial phases, including Dirac semimetals and topological insulators, depending on the level of spin orbit coupling [33]. These findings have positioned anti-perovskites at the frontier of topological materials research.

More recently, anti-perovskite chalcogenides and pnictides for examples Ba_3SbP, Sr_3AsN have been proposed as potential semiconductors for thermoelectric and photovoltaic applications [34]. These compounds exhibit tunable band gaps, structural stability, and low effective masses, making them competitive with traditional perovskites in optoelectronic performance.

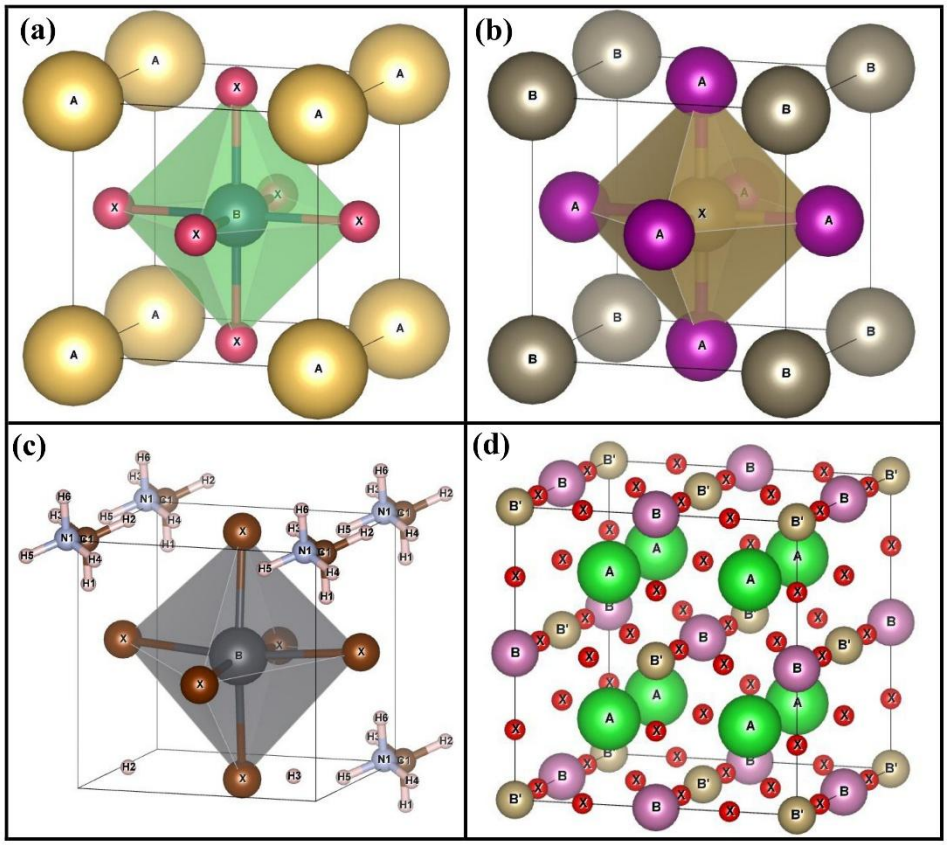

Figure I.3: Representative Crystal Structures of (a) Conventional Perovskite (ABX_3), (b) Anti-Perovskite, (c) Hybrid Organic–Inorganic Perovskite, and (d) Double Perovskite ($A_2BB'X_6$)

I.4 General Properties of Perovskites

The broad family of perovskite materials including simple perovskites, double perovskites, anti-perovskites, layered variants, and hybrid organic-inorganic analogues is renowned for its extraordinary range of functional properties, underpinned by a combination of chemical versatility and structural flexibility. Across its various subclasses, the perovskite framework supports a vast array of elemental compositions and bonding environments, giving rise to a rich palette of electrical, magnetic, optical, and thermal behaviors **[24]**.

One of the defining characteristics of the perovskite family is its capacity to host a wide variety of electronic ground states, ranging from insulating and semiconducting to metallic and even superconducting phases. This includes oxide-based perovskites with strong electron correlation effects, halide perovskites with exceptional optoelectronic performance, and anti-perovskites displaying unusual metallicity or topologically nontrivial band structures. Such

diversity renders perovskites highly adaptable to applications in electronics, spintronics, and quantum materials research **[35]**.

The optical properties of perovskite systems are equally diverse. Members of the family, including halide and chalcogenide perovskites, often exhibit high absorption coefficients, direct bandgaps, and tunable emission across the visible and near-infrared spectra. These features are of particular interest in solar photovoltaics, light-emitting diodes, and photodetectors. In layered and hybrid perovskites, quantum confinement and dielectric screening can further enhance excitonic effects, offering opportunities for low-dimensional optoelectronics **[36]**.

Perovskite materials are also known for a variety of ferroelectric, piezoelectric, and multiferroic behaviors, particularly in oxide and hybrid compositions. Structural distortions and cation displacements within the perovskite lattice can lead to spontaneous polarization, enabling applications in memory devices, sensors, and actuators **[37]**. In double and complex perovskites, ordered B-site cation arrangements can introduce magnetoelectric coupling and charge ordering phenomena, expanding the landscape of ferroic-functionalities **[38]**.

Moreover, magnetic ordering ranging from ferromagnetism and antiferromagnetism to spin glass and frustrated states is a recurrent feature in many transitions metal containing perovskites. Double perovskites, for instance, frequently host super exchange or double-exchange interactions, while certain anti-perovskites exhibit itinerant magnetism or topological magnetic textures **[39]**.

In addition, perovskite structures are notable for their ionic and protonic conductivity, which are especially relevant in energy conversion and storage technologies. Oxide perovskites have long been utilized as solid electrolytes and cathodes in solid oxide fuel cells (SOFCs), while hybrid and chalcogenide analogues are being explored for ion transport in batteries and sensors **[40]**.

Thermal and mechanical properties across the family vary considerably. While some members exhibit low thermal conductivity, beneficial for thermoelectric applications, others demonstrate excellent thermal stability, making them suitable for high-temperature environments **[41]**. The mechanical response elasticity, hardness, and resistance to deformation

also depends on the specific bonding character and structural topology of the variant in question **[42]**. The general properties of perovskites are not confined to a narrow set of characteristics but encompass a multifunctional and interdisciplinary landscape. Their ability to exhibit and combine diverse behaviors electronic, optical, magnetic, ferroic, and ionic within a single or closely related structural motif positions perovskites as central materials in modern and emerging technologies. Continued research into their derivative forms, including double and anti-perovskites, promises further discoveries and novel applications across energy, electronics, and quantum science **[42]**.

I.5 Synthesis Methods of Perovskite Compounds

The synthesis of perovskite compounds is a diverse and rapidly evolving field, reflecting the chemical and structural complexity of this family of materials. Various techniques have been developed to prepare perovskites with precise control over their composition, crystallinity, morphology, and phase purity. Among the most traditional approaches is the high-temperature solid state method, commonly employed for the synthesis of oxide and halide-based perovskites, as shown in **Figure I.4(a-i) [43]**. In this technique, stoichiometric amounts of precursor powders such as oxides, carbonates, or halides are intimately mixed and subjected to thermal treatment, typically above 1000 °C. This prolonged heating facilitates interdiffusion and enables crystallization into the perovskite phase. Although robust and scalable, this method often requires repeated grinding and calcination steps to achieve phase homogeneity and may lead to the formation of undesirable secondary phases if not carefully optimized **[44]**.

To circumvent some of these limitations, wet chemical techniques such as sol gel processing and combustion synthesis have gained prominence. These routes allow for precursor mixing at the molecular level, thus improving homogeneity and reducing synthesis temperatures. In sol-gel synthesis, metal alkoxides or salts undergo hydrolysis and condensation to form a gel, which upon thermal treatment converts to a crystalline perovskite. Similarly, combustion methods use redox reactions between metal nitrates and organic fuels to rapidly generate heat, driving the formation of the desired phase in a matter of minutes. These methods are particularly advantageous for synthesizing nanostructured or doped perovskites with controlled particle sizes **[43]**.

In recent years, hydrothermal and solvothermal methods have emerged as effective techniques for growing high-quality perovskite crystals under relatively mild conditions. By employing sealed autoclaves to heat aqueous or organic precursor solutions under high pressure, these approaches enable the crystallization of perovskites with well-defined morphologies at temperatures typically below 300 °C. This makes them suitable for synthesizing complex oxides, halides, and even chalcogenide perovskites, including metastable or low-symmetry structures that might be difficult to obtain through conventional solid-state reactions **[45]**.

For applications involving thin films such as photovoltaics, light-emitting diodes, or photodetectors solution-based methods such as spin-coating, dip-coating, and inkjet printing have become standard. These approaches, especially prevalent in the fabrication of hybrid organic-inorganic halide perovskites, rely on the deposition of precursor solutions onto substrates followed by thermal or solvent-assisted annealing to induce crystallization. These low-cost and scalable techniques have enabled rapid prototyping of perovskite devices and are increasingly being adapted for use with other types of perovskite compounds beyond the hybrid halides **[46]**.

In parallel, vapor-phase deposition methods have gained traction, particularly in high-performance electronic applications. Techniques such as chemical vapor deposition (CVD), physical vapor deposition (PVD), and thermal evaporation offer precise control over film thickness, interface quality, and composition. While more technologically demanding, vapor deposition ensures high reproducibility and is well-suited for the integration of perovskite materials into multi-layered device architectures. Such methods are being actively explored for the synthesis of double perovskites and other complex structures where stoichiometric precision is critical **[47]**.

Alternative routes such as mechanochemical synthesis and microwave-assisted methods have also emerged as attractive options. Mechanochemical processing involves the use of ball-milling to induce solid-state reactions at room temperature, offering a solvent-free, environmentally friendly approach to synthesizing perovskites with minimal energy input. This method has been successfully employed for the preparation of simple, double, and even anti-perovskite structures. On the other hand, microwave-assisted synthesis provides rapid and

uniform heating, leading to significantly reduced reaction times and enhanced crystallization kinetics, particularly beneficial for producing nanocrystalline or metastable phases **[48]**.

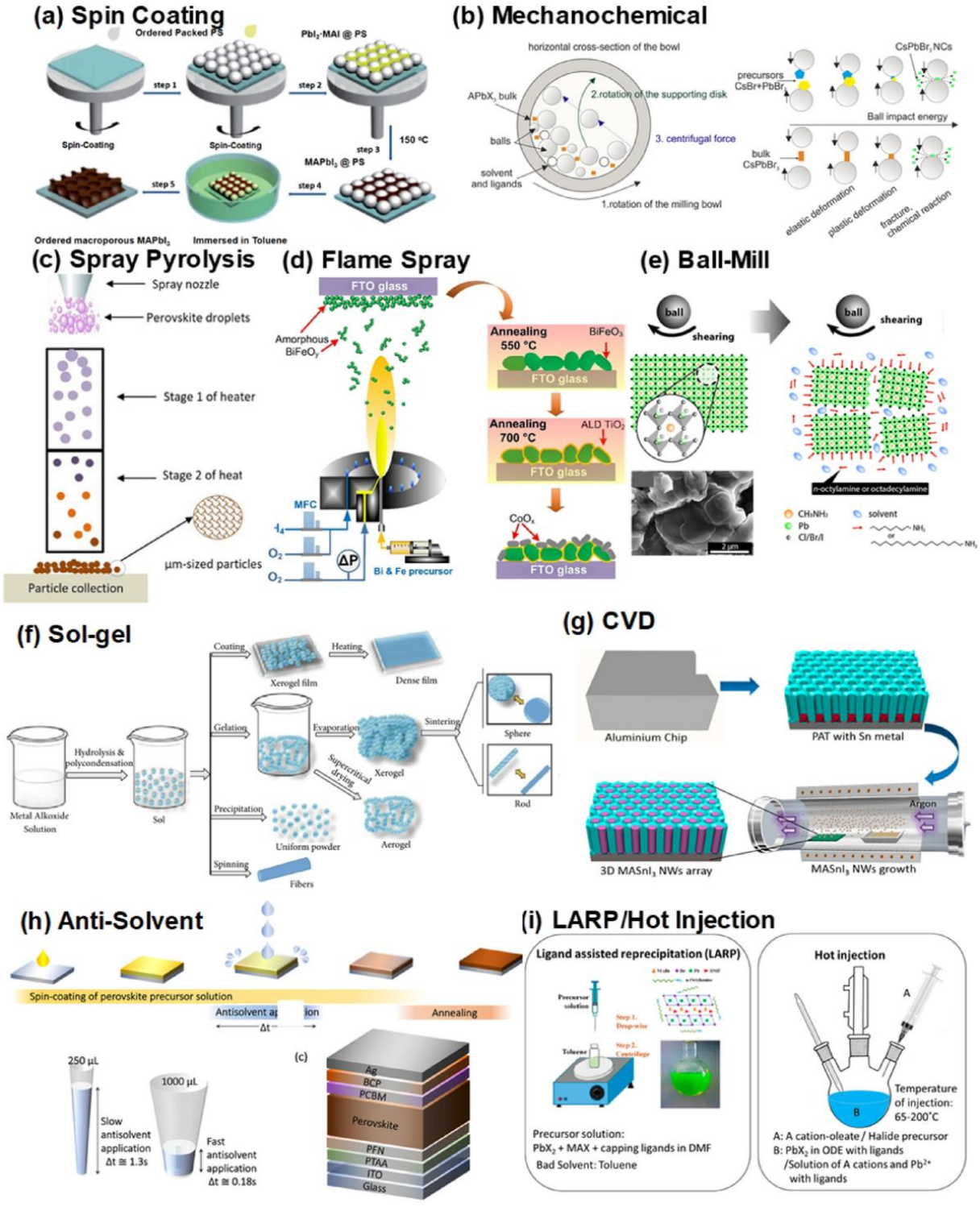

Figure I.4 Diverse Techniques for Synthesizing Perovskite and Nanocomposite Structures

The synthesis strategy chosen for a given perovskite system is dictated by the targeted structural complexity, desired morphology, functional application, and processing constraints. As the field expands to encompass novel architectures such as layered, anti, and complex perovskites, including theoretical A_3BX_3 type derivatives recently proposed as solar energy materials the development and refinement of advanced synthesis routes will be indispensable for transforming theoretical predictions into practical, experimentally realizable compounds.

I.6 Applications of Perovskites in Modern Technologies

Perovskite materials have garnered significant attention in recent years due to their versatile and impressive properties, which make them ideal candidates for a range of applications in modern technologies. The unique structural characteristics of perovskites, coupled with their tunable electronic, optical, and chemical properties, make them highly suitable for diverse fields such as solar energy conversion, optoelectronics, catalysis, and energy storage.

I.6.1 Perovskites in Solar Cells

The development of perovskite-based solar cells (PSCs) has been one of the most ground breaking advancements in renewable energy technology as shown in **Figure I.5**. Perovskite materials were first introduced to solar cell technology by Miyasaka et al. in 2009, who demonstrated that a lead halide perovskite $CH_3NH_3PbI_3$ could serve as the light-absorbing layer in a solar cell **[49]**. This discovery initiated a wave of research focused on improving the efficiency and stability of PSCs. Early efforts were led by researchers like Grätzel and co-workers, who developed the first solid state perovskite solar cells, achieving a power conversion efficiency (PCE) of around 3.8% **[50]**.

Since then, significant improvements have been made, with the PCE of perovskite solar cells exceeding 25% in recent years, making them competitive with traditional silicon solar cells **[51]**. The rapid advancement of this field can be attributed to the work of several researchers, including Kojima et al. in 2009 who developed high-efficiency devices using perovskite **[52]**, and Saliba et al. in 2016 who optimized the materials and processing techniques, pushing the PCE to 20% in laboratory settings **[53]**. The most recent work by Jeong et al. in 2020 has

demonstrated that perovskite solar cells can achieve a certified PCE of 25%, solidifying perovskites as a leading material for solar energy harvesting [54].

In addition to the improvements in efficiency, perovskite solar cells are attractive due to their low-cost processing techniques, such as spin coating and inkjet printing, pioneered by researchers like Parida et al. [55].These advances provide a pathway toward the large-scale production of PSCs with lower manufacturing costs compared to silicon-based cells.

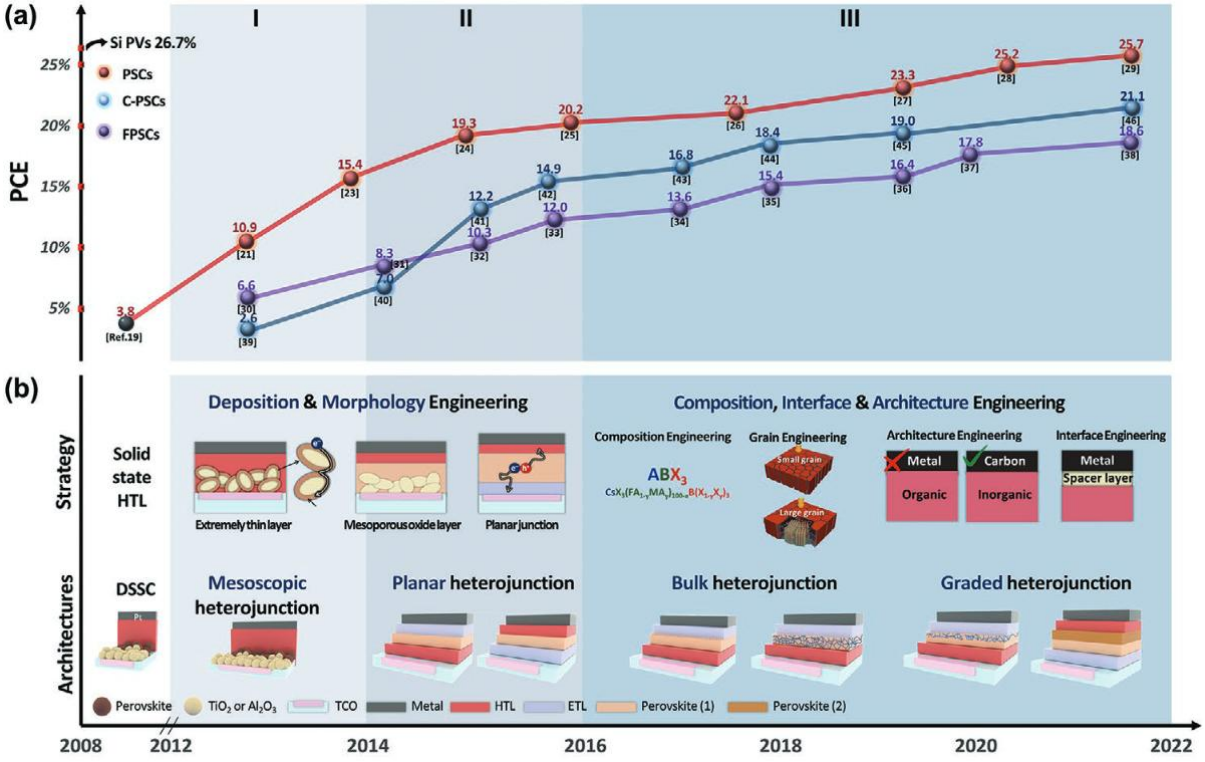

Figure I.5: Chronological Advancements in Perovskite Solar Cells: Efficiency Trends and Device Architectures

I.6.2 Perovskites in LEDs and Photodetectors

Perovskite materials have seen substantial progress in optoelectronics, particularly in photodetectors and light-emitting devices (LEDs). A significant milestone was achieved by Tan et al, who demonstrated the application of perovskites in light-emitting diodes, thereby highlighting their potential in LED technologies [56]. These materials enable the fabrication of bright and efficient LEDs due to their inherently high photoluminescence quantum efficiency. Subsequent advancements were reported by Xiao et al. and Lin et al, who developed perovskite

LEDs (PeLEDs) with outstanding brightness and color purity, positioning them as viable candidates for next-generation display technologies **[57]**.

In addition to light-emitting applications, perovskites have been actively investigated for photodetector technologies. Their broad optical absorption range, high carrier mobility, and elevated quantum efficiency make them excellent candidates for ultraviolet to visible light photodetection. Wang et al. demonstrated that perovskite-based photodetectors could deliver high sensitivity and rapid response times. Since then, ongoing improvements have enabled their application in diverse areas, such as safety monitoring, imaging, and optical communication **[58]**.

I.6.3 Perovskites in Catalysis and Batteries

In addition to their applications in solar energy and optoelectronics, perovskite materials are increasingly being investigated for their potential in catalysis and energy storage technologies, such as batteries. The versatility of perovskites in catalysis was first recognized by researchers like Liu et al, who explored the use of perovskite oxides in oxygen evolution reactions (OER) **[59]**. Since then, researchers such as Prašnikar et al. have demonstrated the use of perovskite catalysts in a wide range of reactions, including CO_2 reduction and hydrogen production **[60]**. The tunable electronic properties of perovskite materials allow for the optimization of catalytic activity, and their stability under harsh conditions further enhances their catalytic efficacy.

In the realm of energy storage, perovskite materials have shown promise in improving the performance of rechargeable batteries, particularly lithium-ion and sodium-ion batteries. The pioneering work by Paul et al. in 2021 on perovskite-based electrodes for lithium-ion batteries highlighted their ability to store and release energy efficiently. Since then, perovskite-based materials have been explored for their use in next-generation battery technologies, such as all-solid-state batteries **[61]**. Researchers like Liu et al. have demonstrated that perovskite materials can form stable interfaces with electrolyte materials, improving battery safety and performance **[62]**.

I.7 Challenges and Opportunities

Despite the remarkable progress in the development and application of perovskite materials, several critical challenges remain. These challenges, if overcome, can open the door to widespread commercial adoption and novel technological breakthroughs. Here, we discuss four main areas of concern and opportunity: stability and degradation, toxicity, compatibility and integration, and efficiency optimization **[63]**.

I.7.1 Stability and Degradation

One of the foremost challenges facing perovskite-based devices is their environmental instability. Since the pioneering work of Miyasaka et al, who introduced organic-inorganic lead halide perovskites for solar cells, it has been observed that perovskite materials are highly sensitive to moisture, oxygen, heat, and light. These environmental factors contribute to phase transitions, ion migration, and decomposition, which in turn lead to rapid performance degradation over time **[64]**.

To address this, researchers have explored various strategies such as the incorporation of 2D perovskite layers such as of Grancini et al. in 2017 **[65]**, encapsulation methods Wang et al. in 2016 **[66]**, and the use of all-inorganic compositions for example $CsPbI_3$ to enhance thermal and moisture resistance **[67]**. Additionally, the substitution of volatile organic cations like methylammonium with formamidinium or cesium has shown to improve structural stability **[68]**. Nevertheless, achieving long-term operational stability (over 20 years) under real-world conditions remains an open research frontier. Innovations in compositional engineering, interfacial passivation, and scalable encapsulation technologies continue to be critical.

I.7.2 Toxicity

The presence of lead in many high-performing perovskite compounds raises significant environmental and health concerns. Lead is a well-known toxic heavy metal, and its potential leaching from broken or discarded solar panels or devices could pose ecological risks **[69]**. Consequently, regulatory and public acceptance barriers hinder the commercial deployment of lead-based perovskite technologies.

Researchers have investigated lead-free alternatives, including tin (Sn), bismuth (Bi), and antimony (Sb) based perovskites **[70]**. While these materials mitigate toxicity concerns, they often suffer from reduced performance or stability due to issues like tin oxidation ($Sn^{2+} \rightarrow Sn^{4+}$). Despite these drawbacks, Bi-based perovskite derivatives for example $(CH_3NH_3)_3Bi_2I_9$ and double perovskites such as $Cs_2AgBiBr_6$ have shown promise for low-toxicity optoelectronic applications **[66]**. Therefore, the tradeoff between environmental safety and device efficiency continues to drive intensive research in the design of sustainable perovskite materials.

I.7.3 Compatibility and Integration

For perovskites to transition from laboratory scale studies to commercial technologies, they must be compatible with existing device architectures and scalable manufacturing techniques. This includes integration with silicon in tandem solar cells, incorporation into flexible substrates for wearable electronics, and compatibility with low-cost printing methods for large-area coatings **[71]**.

Notable progress in this domain includes the development of perovskite-silicon tandem solar cells with record efficiencies over 30%, as well as advances in roll-to-roll printing techniques. However, interfacial instability, lattice mismatch, and thermal expansion differences remain technical barriers. Additionally, the use of perovskites in light-emitting devices, sensors, and photodetectors requires interface engineering to ensure optimal charge transport and minimal recombination losses. Researchers are actively investigating hybrid architectures and novel buffer layers to address these challenges **[72]**.

I.7.4 High Efficiency and Performance Limits

The exceptional optoelectronic properties of perovskites such as long carrier diffusion lengths, high absorption coefficients, and low exciton binding energies have facilitated rapid improvements in device performance. From initial power conversion efficiencies of ≈3.8% in 2009 to over 26% in 2023, perovskite solar cells have become a major focus in next-generation photovoltaics **[53]**. However, the path to surpassing the Shockley Queisser limit approximately 33.7% for single-junction solar cells requires novel approaches such as multi-junction architectures, photon recycling, hot carrier extraction, and the mitigation of non-radiative recombination losses **[53]**. Furthermore, balancing efficiency with scalability and

reproducibility under ambient conditions is a major concern. Batch to batch variation, defect control, and hysteresis effects during operation continue to affect reproducibility and device performance. Despite these challenges, the high tunability and facile processing of perovskite materials present extraordinary opportunities. With continued interdisciplinary efforts, perovskites are poised to revolutionize multiple sectors of materials science, energy, and electronics **[73]**.

I.8 Perovskites in Embedded Systems

Embedded systems, defined as specialized computing units designed to perform dedicated functions within larger mechanical or electrical systems, are now omnipresent in modern technology. These systems are integral to a wide range of applications from household appliances and automotive controls to medical devices, smart agriculture, and wearable technologies. As the demand for autonomy, miniaturization, and real-time performance increases, the need for self-sufficient and energy efficient embedded systems has become more critical than ever **[74]**.

One of the central challenges in embedded system design today is power management. Traditional energy sources such as lithium-ion batteries often limit the operational lifetime, mobility, or environmental adaptability of these devices. In response, research and development have increasingly turned toward integrating renewable energy harvesting technologies most notably, solar energy to enable autonomous operation. This strategic shift has opened the door for advanced materials capable of efficient, lightweight, and low-cost solar energy conversion.

In recent years, several companies have begun exploring the integration of photovoltaic systems into their embedded products. For example, Lenovo has developed concept laptops powered by integrated solar panels, as depicted in **Figure I.6**, aiming to reduce dependency on electrical outlets and enhance mobility in outdoor or remote areas. Similarly, solar-powered smartphones have been proposed and prototyped, especially for use in off grid or emergency scenarios. In the agricultural domain, research-driven companies and academic institutions are investigating smart, solar-powered systems for precision farming, irrigation automation, and environmental monitoring seeking to reduce labor costs and ensure sustainable resource use.

Figure I.6: Lenovo's solar-powered laptop

The convergence of embedded systems and energy-harvesting technologies has led to increased attention toward novel photovoltaic materials. Perovskites and its structural derivatives such as double perovskites, anti-perovskites, and hybrid organic-inorganic variants, have emerged as highly promising candidates. The development of perovskite-based solar cells particularly their potential to outperform traditional silicon technologies in terms of power to weight ratio and ease of integration has opened new possibilities for embedding them into small-scale or portable devices. Moreover, their compatibility with flexible substrates makes them ideal for curved surfaces or non-traditional form factors found in embedded designs. However, the full exploitation of perovskites in embedded systems is still constrained by issues as discussed earlier.

I.9 Conclusion

In conclusion, perovskite materials owing to their structural flexibility and chemical tunability have become central to the development of advanced functional materials. Their ability to accommodate a wide range of compositions has enabled the design of systems with tailored optical, electronic, and magnetic properties, suitable for diverse applications including photovoltaics, optoelectronics, and energy storage. Derivative structures such as double and anti-perovskites further expand this versatility, offering new

opportunities for lead-free and stable alternatives. Despite existing challenges related to stability, toxicity, and integration, continuous advances in synthesis and theoretical modeling are rapidly driving innovation in this field. This chapter lays the groundwork for the computational investigation of novel perovskite compounds, which forms the core of the present thesis.

Bibliography

[1] Mahajan, Padha, Verma, Gupta, Datt, Tsoi, Satapathi & Arya, Journal of Energy Chemistry, 2022, 68, 330–386.

[2] Trifiletti, Asker, Tseberlidis, Riva, Zhao, Tang, Binetti & Fenwick, Frontiers in Electronics, 2021, 2, 758603.

[3] Soderholm, Zhang, Hinks, Beno, Jorgensen, Segre & Schuller, Nature, 1988, 328, 604–605.

[4] Sahare, Pham, Angmo, Ghoderao, MacLeod, Khan, Lee, Singh & Sonar, Adv Energy Mater, 2021, 11, 2101085.

[5] Kim, Lee, Im, Lee, Moehl, Marchioro, Moon, Humphry-Baker, Yum, Moser, Grätzel & Park, Scientific Reports 2012 2:1, 2012, 2, 1–7.

[6] Soultati, Tountas, Armadorou, Yusoff, Vasilopoulou & Nazeeruddin, Energy Advances, 2023, 2, 1075–1115.

[7] Feng & Zhang, Appl Phys Lett, DOI:10.1063/5.0039936/39516.

[8] Hossain, Almohamadi, Islam, Hasan, Haque, Akhtaruzzaman & Uddin, DOI:10.2139/SSRN.5212789.

[9] Mao, Stoumpos & Kanatzidis, J Am Chem Soc, 2019, 141, 1171–1190.

[10] Irvine, Rupp, Liu, Xu, Haile, Qian, Snyder, Freer, Ekren, Skinner, Celikbilek, Chen, Tao, Shin, O'Hayre, Huang, Duan, Papac, Li, Celorrio, Russell, Hayden, Nolan, Huang, Wang, Metcalfe, Neagu & Martín, Journal of Physics: Energy, 2021, 3, 031502.

[11] Emly, Kioupakis & Van Der Ven, Chemistry of Materials, 2013, 25, 4663–4670.

[12] Kishida, Goto & Inui, Acta Crystallogr B, 2009, 65, 405–415.

[13] Li, Zhao, Liang, Luo, Chen, Shi, Lu, Gao, Hu, Liu & Sun, J Mater Chem A Mater, 2021, 9, 6650–6670.

[14] Shannon, urn:issn:0567-7394, 1976, 32, 751–767.

[15] Patil, Lokare, Devan, Chougule, Kanamadi, Kolekar & Chougule, Mater Chem Phys, 2007, 104, 254–257.

[16] Nakamura, Petzow & Gauckler, Mater Res Bull, 1979, 14, 649–659.

[17] Soderholm, Zhang, Hinks, Beno, Jorgensen, Segre & Schuller, Nature, 1988, 328, 604–605.

[18] Kerrai, Zaim & Kerouad, Vacuum, 2024, 222, 113090.

[19] Chen, Habu, Masubuchi, Torii, Kamiyama & Kikkawa, Solid State Sci, 2016, 54, 2–6.

[20] Thakur, Aly, Mohery, Ebrahium, Kumar & Sharma, J Alloys Compd, 2023, 957, 170457.

[21] Joseph, Vimala, Raju & Murthy, J Phys D Appl Phys, 1999, 32, 1049.

[22] Saparov & Mitzi, Chem Rev, 2016, 116, 4558–4596.

[23] Wang, Wang, Doherty, Stranks, Gao & Yang, Nature Reviews Chemistry 2025 9:4, 2025, 9, 261–277.

[24] Phung, Bracesco, Creatore, Kalita, Sahu & Manju, J Phys D Appl Phys, 2024, 57, 343002.

[25] Ji & Xiao, Chemistry of Materials, 2022, 34, 8207–8212.

[26] Sarma, Sampathkumaran, Ray, Nagarajan, Majumdar, Kumar, Nalini & Guru Row, Solid State Commun, 2000, 114, 465–468.

[27] Lan, Zhao, Xu, Ma, Hayase & Ma, J Alloys Compd, 2016, 655, 208–214.

[28] Lei, Hardy & Gao, Adv Funct Mater, 2021, 31, 2105898.
[29] Macdonald, Lanzetta, Liang, Ding & Haque, Advanced Materials, 2023, 35, 2206684.
[30] Krivovichev, Zeitschrift fur Kristallographie, 2008, 223, 109–113.
[31] Li, Zhu, Wang, Howard, Lü, Li, Kumar, Wang, Daemen & Zhao, Solid State Ion, 2016, 284, 14–19.
[32] Lin, Zhang & Dong, J Energy Storage, 2024, 101, 113795.
[33] Mao, Zhu, Ding, Liu, Gamage, Chen & Ren, Science (1979), 2019, 365, 495–498.
[34] Liang, Hu, Zhao, Tang, Gao, Wu & Tang, Chem Phys Lett, 2022, 808, 140127.
[35] Huang, Yuan, Shao & Yan, Nature Reviews Materials 2017 2:7, 2017, 2, 1–19.
[36] Ju, Dai, Ma & Zeng, Adv Energy Mater, 2017, 7, 1700216.
[37] Banerjee & Tyagi, .
[38] Kumar, Sharma, Kumari, Kaur, Saha, Thakur & Shandilya, Ionics 2024 30:9, 2024, 30, 5159–5188.
[39] Laha, .
[40] Hayashi, Inaba, Matsuyama, Lan, Dokiya & Tagawa, Solid State Ion, 1999, 122, 1–15.
[41] Ding, Li, Li, Li, Yao, Liu, Tian, Su, Chen & Shi, J Mater Chem A Mater, 2019, 7, 540–548.
[42] Song, Zheng, Feng, Liu, Ye, Li, Wang, Liu & Yang, Advanced Materials, 2024, 36, 2312041.
[43] Ecija, Vidal, Larrañaga, Ortega-San-Martín, Isabel Arriortua & Químicas, .
[44] Athayde, Souza, Silva, Vasconcelos, Nunes, Da Costa & Vasconcelos, Ceram Int, 2016, 42, 6555–6571.
[45] Walton, Chemistry - A European Journal, 2020, 26, 9041–9069.
[46] Kim, Park, Kim, Pak, Lee & Jung, Electrochim Acta, 2017, 245, 734–741.
[47] Abzieher, Moore, Roß, Albrecht, Silvia, Tan, Jeangros, Ballif, Hoerantner, Kim, Bolink, Pistor, Goldschmidt, Chiang, Stranks, Borchert, McGehee, Morales-Masis, Patel, Bruno & Paetzold, Energy Environ Sci, 2024, 17, 1645–1663.
[48] López, Abia, Alvarez-Galván, Hong, Martínez-Huerta, Serrano-Sánchez, Carrascoso, Castellanos-Gómez, Fernández-DÍaz & Alonso, ACS Omega, 2020, 5, 5931–5938.
[49] Miyasaka & Jena, Perovskite Photovoltaics and Optoelectronics: From Fundamentals to Advanced Applications, 2021, 1–60.
[50] Grätzel, Acc Chem Res, 2017, 50, 487–491.
[51] Chang, Fang, Fan, Luo, Su, Zhang, Lu, Tsetseris, Anthopoulos, Liu & Zhao, Advanced Materials, 2020, 32, 2001243.
[52] Kojima, Teshima, Shirai & Miyasaka, J Am Chem Soc, 2009, 131, 6050–6051.
[53] Saliba, Stolterfoht, Wolff, Neher & Abate, Joule, 2018, 2, 1019–1024.
[54] Jeong, Choi, Go, Cho, Kim, Lee, Jeong, Jo, Choi, Lee, Bae, Kwak, Kim & Yang, Science (1979), DOI:10.1126/SCIENCE.ABB7167/SUPPL_FILE/ABB7167_JEONG_SM.PDF.
[55] Parida, Singh, Kalathil Soopy, Sangaraju, Sundaray, Mishra, Liu & Najar, Advanced Science, 2022, 9, 2200308.
[56] Tan, Moghaddam, Lai, Docampo, Higler, Deschler, Price, Sadhanala, Pazos, Credgington, Hanusch, Bein, Snaith & Friend, Nature Nanotechnology 2014 9:9, 2014, 9, 687–692.
[57] Lin, Xing, Quan, de Arquer, Gong, Lu, Xie, Zhao, Zhang, Yan, Li, Liu, Lu, Kirman, Sargent, Xiong & Wei, Nature, 2018, 562, 245–248.
[58] Wang & Kim, Chem Soc Rev, 2017, 46, 5204–5236.
[59] Liu, Zhou, Bai, Ai, Du, Chen, Liu, Ip, Lo, Kwok, Chen, Wang, Xing, Wang & Pan, Small, 2021, 17, 2101605.
[60] Prašnikar, D. B. C. Dasireddy & Likozar, Chem Eng Sci, 2022, 250, 117423.
[61] Paul, Maiti, Chatterjee, Bairi, Das, Thakur & Chattopadhyay, Journal of Physical Chemistry C, 2021, 125, 16892–16902.
[62] Liu, Yuan, Masse, Jia, Bi, Neale, Shen, Xu, Tian, Zheng, Tian & Cao, Advanced Materials, 2021, 33, 1905245.

[63] Körber, Storm, Seton, -, Tupkar, Kumar, Sakhale, Nishijima, Eckroad, Marian & Urbina, Journal of Physics: Energy, 2020, 2, 022001.
[64] Li, Niu, Chen & Zhou, Chem Soc Rev, 2020, 49, 8235–8286.
[65] Grancini, Roldán-Carmona, Zimmermann, Mosconi, Lee, Martineau, Narbey, Oswald, De Angelis, Graetzel & Nazeeruddin, Nature Communications 2017 8:1, 2017, 8, 1–8.
[66] Wang, Ahmad, Leung, Lin, Chen, Liu, Ng, Zhang & Djurišić, ACS Materials Au, 2022, 2, 215–236.
[67] Swarnkar, Marshall, Sanehira, Chernomordik, Moore, Christians, Chakrabarti & Luther, Science (1979), 2016, 354, 92–95.
[68] Huang, Lei, He, Jiang & Yuan, Adv Energy Mater, 2022, 12, 2100690.
[69] Schileo & Grancini, J Mater Chem C Mater, 2021, 9, 67–76.
[70] Román-Vázquez, Vidyasagar, Muñoz-Flores & Jiménez-Pérez, J Alloys Compd, 2020, 835, 155112.
[71] Goje, Ludin, Fahsyar, Syafiq, Chelvanathan, Syakirin, Teridi, Ibrahim, Su'ait, Sepeai & Yasir, Materials for Renewable and Sustainable Energy 2024 13:1, 2024, 13, 155–179.
[72] Williams, Rajagopal, Chueh & Jen, Journal of Physical Chemistry Letters, 2016, 7, 811–819.
[73] Ehrler, Alarcón-Lladó, Tabernig, Veeken, Garnett & Polman, ACS Energy Lett, 2020, 5, 3029–3033.
[74] Raghunathan & Chou, Proceedings of the International Symposium on Low Power Electronics and Design, 2006, 2006, 369–374.

CHAPTER II

Methods And Computational Approaches

II.1 Introduction

This chapter outlines the theoretical and computational methods used to investigate the physical properties of materials. It begins with the fundamental principles of quantum mechanics, particularly the time-independent Schrödinger equation and the Born-Oppenheimer approximation, which allow for the decoupling of electronic and nuclear motions in complex systems. The discussion then transitions to mean-field approximations, including the Hartree and Hartree-Fock methods, which simplify many-electron systems by treating electron interactions in an average sense. These form the basis for the development of Density Functional Theory (DFT), the primary framework employed in this work. The Kohn-Sham formulation of DFT is introduced, emphasizing the role of the exchange-correlation functional and common approximations such as the Local Density Approximation (LDA), Generalized Gradient Approximation (GGA), and the modified Becke-Johnson (mBJ) potential. Extensions including spin-polarization and Hubbard "U" corrections are also presented. Finally, the chapter describes the Full-Potential Linearized Augmented Plane Wave (FP-LAPW) method and its implementation in the WIEN2k code, which provides an accurate all-electron approach for solving the Kohn-Sham equations and computing electronic, magnetic, and optical properties of materials.

II.2 Schrödinger Equation

The Schrödinger equation, denoted as **eq. (II.1)** in this thesis, is pivotal in solid-state physics, providing profound insights into electron behavior within materials. Introduced by Erwin Schrödinger in 1926, this equation revolutionized our understanding of atomic and subatomic processes by describing particles using wave functions **[1]**.

$$\hat{\mathbf{H}}\boldsymbol{\psi}(\mathbf{r}) = \mathbf{E}\boldsymbol{\psi}(\mathbf{r}) \qquad \textbf{(II.1)}$$

Where $\hat{H}\psi(r)$ represents the Hamiltonian operator, which accounts for the total energy of the system. It includes kinetic energy of electrons and potential energy due to interactions with atomic nuclei and other electrons. E denotes the energy eigenvalue associated with the quantum state $\psi(r)$. $\psi(r)$ is the wave function describing the quantum state of electrons in the material. It provides a probability amplitude for finding an electron at position r. Ψ is its wave

function, which depends on the coordinates of the electrons $\vec{r}_i, i = 1, \dots, N_e$ (where N_e is the number of electrons) and the nuclei $\vec{R}_\alpha, \alpha = 1, \dots, N_\alpha$ (where N_α is the number of atoms in the system).

For a given system, the total Hamiltonian is an operator **eq. (II.2)** that can be written to encompass all energy contributions within the system. It incorporates terms representing the kinetic energy of electrons, potential energies arising from interactions between electrons and atomic nuclei, as well as interactions among electrons themselves. This comprehensive description allows the Hamiltonian to capture the complex interactions and dynamics of particles within solids, providing a foundational framework for understanding their electronic properties and behaviors. the Hamiltonian $\hat{\mathrm{H}}$ of a system can be expressed as the sum of the kinetic energy operator $\hat{\mathrm{T}}$ and the potential energy operator $\hat{\mathrm{V}}$ **[2,3]**.

$$\hat{\mathbf{H}} = \hat{\mathbf{T}} + \hat{\mathbf{V}} \tag{II.2}$$

Here, $\hat{\mathrm{T}}$ and $\hat{\mathrm{V}}$ are operators associated with the kinetic and potential energies, respectively. For a system comprising electrons and nuclei, this can be further broken down into:

$$\hat{\boldsymbol{T}} = \hat{\boldsymbol{T}}_{\boldsymbol{e}} + \hat{\boldsymbol{T}}_{\boldsymbol{N}} \tag{II.3}$$

$$\hat{\boldsymbol{V}} = \hat{\boldsymbol{V}}_{\mathbf{ee}} + \hat{\boldsymbol{V}}_{\mathbf{Ne}} + \hat{\mathbf{V}}_{\mathbf{NN}} \tag{II.4}$$

Where, $\hat{T}_e$ represents the total kinetic energy of electrons in the system. It is given by.

$$\hat{\boldsymbol{T}}_{\boldsymbol{e}} = \sum_{\boldsymbol{i=1}}^{\boldsymbol{N_e}} \left(-\frac{\hbar^2}{2\boldsymbol{m_e}} \boldsymbol{\nabla_i^2} \right) \tag{II.5}$$

where N_e is the number of electrons, $\hbar$ is the reduced Planck's constant, m_e is the mass of an electron, and ∇_i^2 denotes the Laplacian operator acting on the i-th electron's position. $\hat{T}_N$ represents the total kinetic energy of nuclei in the system. It is given by.

$$\hat{\boldsymbol{T}}_{\boldsymbol{N}} = \sum_{\boldsymbol{\alpha=1}}^{\boldsymbol{N_\alpha}} \left(-\frac{\hbar^2}{2\boldsymbol{M_\alpha}} \boldsymbol{\nabla_\alpha^2} \right) \tag{II.6}$$

where N_α is the number of nuclei, M_α is the mass of a nucleus, and ∇_α^2 denotes the Laplacian operator acting on the α-th nucleus's position. $\hat{V}_{ee}$ denotes the potential energy of interaction between electrons. It is given by.

$$\hat{\boldsymbol{V}}_{\boldsymbol{ee}} = \frac{\mathbf{1}}{\mathbf{4\pi\epsilon_0}} \sum_{\boldsymbol{i=1}}^{\boldsymbol{N_e}} \sum_{\boldsymbol{j\neq i}}^{\boldsymbol{N_e}} \hat{\boldsymbol{e}}^{\mathbf{2}} \boldsymbol{Z_i} \tag{II.7}$$

where e is the elementary charge, Z_i is the charge of the i-th electron, and ϵ_0 is the permittivity of free space. $\hat{V}_{NN}$ represents the potential energy of interaction between nuclei. It is given by.

$$\hat{\boldsymbol{V}}_{\boldsymbol{NN}} = \frac{\mathbf{1}}{\mathbf{4\pi\varepsilon_0}} \sum_{\boldsymbol{\alpha=1}}^{\boldsymbol{N_\alpha}} \sum_{\boldsymbol{\beta=\alpha}}^{\boldsymbol{N_\alpha}} \frac{\boldsymbol{Z_\alpha Z_\beta e^2}}{\boldsymbol{|R_\alpha - R_\beta|}} \tag{II.8}$$

where Z_α and Z_β are the charges of nuclei α and β, respectively, and $\vec{R}_\alpha$ and $\vec{R}_\beta$ are their positions. $\hat{V}_{Ne}$ represents the potential energy of interaction between electrons and nuclei. It is given by.

$$\hat{\boldsymbol{V}}_{\boldsymbol{Ne}} = -\frac{\mathbf{1}}{\mathbf{4\pi\epsilon_0}} \sum_{\boldsymbol{i=1}}^{\boldsymbol{N_e}} \sum_{\boldsymbol{\alpha=1}}^{\boldsymbol{N_\alpha}} \frac{\boldsymbol{Z_s e^2}}{\boldsymbol{|\vec{R}_\alpha - \vec{r}_i|}} \tag{II.9}$$

where Z_s is the charge of nucleus α and $\vec{r}_i$ are the positions of nucleus α and electron i, respectively. The Schrödinger equation for such a system can be represented as.

$$\left(\hat{\mathbf{T}}_\mathbf{e} + \hat{\mathbf{T}}_\mathbf{N} + \hat{\mathbf{V}}_\mathbf{ee} + \hat{\mathbf{V}}_\mathbf{NN} + \hat{\mathbf{V}}_\mathbf{Ne}\right)\boldsymbol{\Psi}\left(\vec{\mathbf{r}}_\mathbf{1}, \vec{\mathbf{r}}_\mathbf{2}, \ldots, \vec{\mathbf{R}}_\mathbf{1}, \vec{\mathbf{R}}_\mathbf{2}, \ldots\right) = \mathbf{E}\boldsymbol{\Psi}\left(\vec{\mathbf{r}}_\mathbf{1}, \vec{\mathbf{r}}_\mathbf{2}, \ldots, \vec{\mathbf{R}}_\mathbf{1}, \vec{\mathbf{R}}_\mathbf{2}, \ldots\right) \tag{II.10}$$

Here, $\Psi\left(\vec{r}_1, \vec{r}_2, \ldots, \vec{R}_1, \vec{R}_2, \ldots\right)$ represents the wave function of the system, which encapsulates all observable properties. Solving this Schrödinger equation with the Hamiltonian $\hat{H}$ is computationally challenging for systems involving approximately 10^{23} electrons, necessitating the use of approximate methods.

II.3 Solving the Schrödinger Equation in Solid-State Physics

II.3.1 Approximation de Born-Oppenheimer

The Born-Oppenheimer approximation is a fundamental principle in quantum mechanics that has been pivotal for understanding the behavior of molecules and condensed matter systems **[4,5]**. It recognizes the vast difference in mass between electrons and atomic

nuclei, and leverages this to simplify the quantum mechanical calculations required. The core idea is to treat the atomic nuclei as essentially stationary, while focusing on solving the electronic Schrödinger equation. This is possible because the electrons move much faster than the nuclei, allowing us to first determine the electronic states in the fixed potential created by the nuclei.

$$\boldsymbol{\Psi(\vec{\mathbf{R}},\vec{\mathbf{r}}) = \Psi_N(\vec{\mathbf{R}})\Psi_e(\vec{\mathbf{r}},\vec{\mathbf{R}})} \quad \textbf{(II.11)}$$

The wave function $\Psi(\vec{R},\vec{r})$ is expressed as a product of nuclear ($\Psi_N(\vec{R})$) and electronic ($\Psi_e(\vec{r},\vec{R})$ wave functions, where $\vec{R}$ and $\vec{r}$ denote the coordinates of nuclei and electrons, respectively. The electronic wave function $\Psi_e(\vec{r},\vec{R})$ explicitly depends on electron coordinates $\vec{r}$ and parametrically on nuclear coordinates $\vec{R}$. This separation of variables is computationally extremely useful, as it allows us to efficiently calculate the electronic properties of molecules and solids without having to fully solve the complete quantum mechanical problem. By decoupling the nuclear and electronic degrees of freedom, the Born-Oppenheimer approximation makes many problems tractable that would otherwise be intractable. The approximation is not perfect, as there are situations where the coupling between nuclear and electronic motion cannot be neglected. But in the vast majority of cases, it provides an excellent description that agrees very well with experimental observations. The Schrödinger equation in this framework is given by.

$$\boldsymbol{(T_e + T_N + V_{ee} + V_{NN} + V_{Ne})\Psi_N\Psi_e = E\Psi_N\Psi_e} \quad \textbf{(II.12)}$$

Here, T_e, T_N, V_{ee}, V_{NN}, and V_{Ne} represent the kinetic energies and potential energy operators for electrons and nuclei eq **(II.5)** to eq **(II.9)**. The Born-Oppenheimer approximation (adiabatic approximation) holds when the electronic wave function Ψ_e adjusts instantaneously to changes in nuclear positions. This allows us to separate the Hamiltonian into electronic and nuclear parts:

$$\boldsymbol{\hat{H}(\Psi_N\Psi_e) = \Psi_e(T_N + V_{NN})\Psi_N + \Psi_N(T_e + V_{Ne} + V_{ee})\Psi_e = E\Psi_N\Psi_e} \quad \textbf{(II.13)}$$

This approximation is solved in two steps. Firstly, the electronic equation is solved assuming fixed nuclei:

$$(\boldsymbol{T_e} + \boldsymbol{V_{Ne}} + \boldsymbol{V_{ee}})\boldsymbol{\Psi_e} = \boldsymbol{E_e}(\vec{\boldsymbol{R}}_{\boldsymbol{\alpha}})\boldsymbol{\Psi_e} \quad \textbf{(II.14)}$$

Here, E_e is the energy of the electrons in the fixed potential field of the nuclei. The nuclear coordinates $\vec{R}_\alpha$ act as parameters in this equation. Next, the nuclear Schrödinger equation is solved in the potential created by the electrons:

$$(\boldsymbol{T_N} + \boldsymbol{V_{NN}})\boldsymbol{\Psi_N} = \left(\boldsymbol{E} - \boldsymbol{E_e}(\vec{\boldsymbol{R}}_{\boldsymbol{\alpha}})\right)\boldsymbol{\Psi_N} \quad \textbf{(II.15)}$$

This process effectively decouples the motion of electrons and nuclei, simplifying the complex interactions in the system. The approximation neglects the effects of electronic transitions on nuclear movement, allowing us to solve for electronic properties with fixed nuclear positions. Despite this simplification, directly solving the electronic Schrödinger equation for systems with many electrons remains challenging, often requiring further approximations to make the computations feasible.

II.3.2 Hartree Approximation

The Hartree approximation, named after Douglas Hartree who introduced it in the 1920s, is a method essential for describing the electronic structure of multi-electron atoms and molecules. It simplifies the intricate interactions between electrons by treating each electron as moving in an average field created by all others. This mean-field approximation is crucial in the development of quantum mechanical methods for understanding the behavior of electrons in atoms and molecules. The direct solution of the Schrödinger equation for systems with many electrons (Equation II.14) is impractical due to the large number of particles involved. This approach approximates the total wave function of the system **[6,7]**.

$$\boldsymbol{\Psi_e}(\dot{\boldsymbol{r}}_1, \dot{\boldsymbol{r}}_2, \ldots\ldots \dot{\boldsymbol{r}}_{\mathbf{Ne}}) = \boldsymbol{\varphi_1}(\dot{\boldsymbol{r}}_1)\boldsymbol{\varphi_2}(\dot{\boldsymbol{r}}_2)\ldots\ldots\boldsymbol{\varphi_{Ne}}(\dot{\boldsymbol{r}}_{\boldsymbol{Ne}}) \quad \textbf{(II.16)}$$

as a product of individual wave functions for each electron, $\varphi_i(\dot{r}_i)$, effectively treating each electron independently within the averaged influence of all others. However, in reality, electrons interact with each other and with atomic nuclei, complicating the direct solution of the Schrödinger equation **Eq. (II.9)** for multi-electron systems. To address this complexity, the Hartree approximation transforms **Eq. (II.9)** into a set of single electron equations.

$$\left[-\frac{\hbar^2}{2m_e}\nabla_i^2 + V_{\text{ext}}\left(\vec{r},\vec{R}\right) + V_{ee}(\vec{r})\right]\phi_i(\vec{r},\vec{R}) = \epsilon_i(\vec{R})\phi_i(\vec{r},\vec{R}) \quad \textbf{(II.17)}$$

Here, $\phi_i(\vec{r},\vec{R})$ represents the wave function of the i-th electron, depending on both the electronic coordinates $\vec{r}$ and the nuclear coordinates $\vec{R}$. The term V_{ext} $(\vec{r},\vec{R})$ combines potentials arising from nucleus-nucleus interactions and electron-nucleus interactions. The term $V_{ee}(\vec{r})$, also known as the Hartree potential $V_H(\vec{r})$, describes the Coulomb interaction among electrons, which is approximated as the integral of the electron density

$$\rho_i(\vec{r}') = \sum_{\substack{j=1 \\ j\neq i}}^{N_e} |\phi_i(\vec{r})|^2 \quad \textbf{(II.18)}$$

This approach simplifies the complex problem of interacting electrons by treating each electron as moving in an average field created by all other electrons, neglecting quantum mechanical effects such as electron-electron correlations beyond the mean-field level. However, it introduces an approximation that violates the Pauli exclusion principle by not properly accounting for the fact that no two electrons can occupy the same quantum state simultaneously. In summary, while the Hartree approximation provides a practical method for tackling the electronic structure problem in multi-electron systems, it does so by making simplifying assumptions that limit its accuracy for strongly interacting systems where electron correlations play a crucial role.

II.3.3 Hartree-Fock Approximation

The Hartree-Fock approximation stands as a significant improvement over the Hartree method, which overlooks the Pauli exclusion principle. Developed by Hartree and expanded by Fock, this approach ensures that the wave function adheres to the Pauli principle by utilizing a determinant known as the Slater determinant. This method provides a more accurate description of electron interactions in atoms and molecules, capturing essential quantum mechanical effects such as electron exchange and correlation, crucial for understanding chemical bonding and molecular properties. In the Hartree-Fock approximation, the wave function for a system of Ne electrons is expressed as a single determinant known as the Slater determinant **[8]**.

$$\Psi_{HF}(\vec{r}_1, \vec{r}_2, \ldots, \vec{r}_{N_e}) = \frac{1}{\sqrt{N_e!}} \begin{vmatrix} \psi_1(\vec{r}_1) & \psi_2(\vec{r}_1) & \cdots & \psi_{N_e}(\vec{r}_1) \\ \psi_1(\vec{r}_2) & \psi_2(\vec{r}_2) & \cdots & \psi_{N_e}(\vec{r}_2) \\ \vdots & \vdots & \ddots & \vdots \\ \psi_1(\vec{r}_{N_e}) & \psi_2(\vec{r}_{N_e}) & \cdots & \psi_{N_e}(\vec{r}_{N_e}) \end{vmatrix} \quad \textbf{(II.19)}$$

$\frac{1}{\sqrt{N_e!}}$ is the normalization factor, and σ represents the spin. $\psi_i(\vec{r}_i, \vec{\sigma}_i)$ is the single-electron wave function depending on the spatial coordinates $\vec{r}_i$ and spin $\vec{\sigma}_i$. The function ψ_e given by Equation **(II.19)** leads to the Hartree-Fock equations for a single-particle system. While the Hartree method fails to account for the impossibility of two electrons with the same spin occupying the same quantum state, the Hartree-Fock method addresses this issue by introducing quantum effects known as 'exchange interactions' (as represented by the last term in Equation **(II.20)**. In the Hartree-Fock framework, each electron creates a region of reduced electron density, termed an 'exchange hole,' around itself. This exchange interaction lowers the system's energy. The difference between the ground state energy calculated using Equation **(II.17)** and that determined from Equation **(II.20)** is referred to as the exchange energy **[9,10]**.

$$\left[-\frac{\hbar^2}{2m_e}\nabla_i^2 + V_{ext}(\vec{r}) + \sum_{j=1}^{N_e}\int \frac{|\phi_j(\vec{r}')|^2}{|\vec{r}-\vec{r}^7|} d^3r'\right]\phi_i(\vec{r}) - \sum_{j=1, j\neq i}^{N_e} \delta_{\sigma i \sigma_j} \int \frac{\phi_j(\vec{r}')\phi_i(\vec{r})}{|\vec{r}-\vec{r}'|} d^3r' \phi_j(\vec{r}) \quad \textbf{(II.20)}$$

In this model, electron-electron interactions are described as each electron interacting with an average field created by the other electrons. This model does not include the strong correlation that exists between two electrons with opposite spins, which keeps them at a certain distance from each other. The difference between the true ground state energy and the energy determined from **(II.20)** is the correlation energy. Slater's approach helps to address the lack of correlation by introducing an expression for the exchange potential.

$$V_x(\vec{r}) = -6\alpha\left(\frac{3\rho(\vec{r})}{4\pi}\right)^{1/3} \quad \textbf{(II.21)}$$

where α is a dimensionless parameter, and $\rho(\vec{r})$ is the charge density. Slater sets $\alpha = 1$, corresponding to a homogeneous non-interacting electron gas. Slater's method highlights two essential points: the simplicity of this potential compared to the Hartree-Fock approximation, and it provides a straightforward form for the exchange correlation term. As the number of

electrons increases, the Hartree-Fock-Slater approximation becomes computationally demanding. This method incorporates several key components necessary for solving the Schrödinger equation: the kinetic energy of a non-interacting electron system, the Hartree potential, as well as exchange and correlation terms. These elements form the basis for Density Functional Theory (DFT), a more computationally efficient approach, which will be discussed in the next section.

II.4 Density Functional Theory (DFT)

Density Functional Theory (DFT) has become a cornerstone in the analysis and understanding of the physical and chemical properties of complex systems with many electrons. Its significance lies in its ability to offer a practical approach to the many-body quantum problem, which is central to fields like computational chemistry and condensed matter physics **[11-13]**. Unlike traditional methods such as Hartree and Hartree-Fock, which rely on the wave function, DFT uses the electronic density as the fundamental variable. This shift simplifies the problem, making calculations more feasible and efficient for large systems. The conceptual foundation of DFT dates back to the late 1920s, with the pioneering work of Llewellyn Thomas and Enrico Fermi. They proposed an approach that utilized electronic density instead of the wave function to describe a system **[14]**. Their early model treated the electron system as a homogeneous gas and considered the kinetic energy as a functional of the local density. However, this initial approximation did not adequately account for electron-electron interactions, leading to limitations in accuracy. A significant advancement in DFT came in 1930, when Paul Dirac introduced the local exchange approximation, which incorporated exchange-correlation effects critical interactions resulting from the antisymmetric of the wave function and electron correlation **[15]**. This refinement addressed the shortcomings of the Thomas-Fermi model and made the functional approach more applicable to real-world systems where electron interactions are crucial. The goal of DFT is to determine the ground state properties of a system of electrons interacting with point-like nuclei, based solely on the electronic density. This focus on density simplifies the computational process while providing comprehensive insights into the system's properties.

II.4.1 Electron density

In earlier sections, we described electrons as indefinite particles, an electron can be considered as a material point localized by its probability of presence within a volume element devoid of potential, near the electronic density $\rho(\vec{r})$. The electronic density $\rho(\vec{r})$ should be viewed collectively, as part of the electron cloud, which provides a means to define the total number of electrons exceeding a given potential. The electronic density $\rho(\vec{r})$ depends solely on the three spatial coordinates (x, y, z). In fact, in a classical approach, this expression represents Ne, the total number of electrons **[16,17]**.

$$\begin{cases} \boldsymbol{\rho(\vec{r} \to \infty) = 0} \\ \boldsymbol{\rho(\vec{r}) = N_e} \end{cases} \quad \textbf{(II.22)}$$

$\rho(\vec{r})$ represents the probability of finding an electron within a unit volume $d\tau$ defined by the position vector r. Unlike the wave function, electron density is an observable quantity that can be measured experimentally, such as through X-ray diffraction. Moreover, electron density $\rho(\vec{r})$ appears to carry enough information to describe a system, whereas the wave function Ψ contains more details, some of which are unnecessary for explaining chemical bonding. These considerations suggest that electron density alone may be sufficient to fully determine the properties of an atomic system. This idea led to several efforts to develop a quantum formalism based on electron density. However, it was Hohenberg and Kohn who introduced an exact formalism (free from approximations), presented as two fundamental theorems.

II.4.2 Hohenberg-Kohn Theorem

The two theorems proposed by Hohenberg and Kohn provide a theoretical framework that allows solving the Schrödinger equation using electron density as the primary variable **[18]**.

II.4.2.1 First theorem of the Hohenberg-Kohn Theorem

The first theorem of the Hohenberg-Kohn (HK) theorem is a cornerstone of Density Functional Theory (DFT), establishing that the ground-state properties of a many-body system of interacting particles are uniquely determined by its electron density $\rho(\vec{r})$. This theorem asserts that there exists a one-to-one correspondence between the ground-state density $\rho(\vec{r})$ and

the external potential $V_{\text{ext}}(\vec{r})$ in a quantum mechanical system. Mathematically, the total energy $E[\rho(\vec{r})]$ of a system can be expressed as a functional of the electron density **[19]**.

$$\boldsymbol{E[\rho(\vec{r})] = F_{HK}[\rho(\vec{r})] + \int \rho(\vec{r}) V_{\text{ext}}(\vec{r})\, dr} \quad \textbf{(II.23)}$$

where $F_{HK}[\rho(\vec{r})]$ is the universal functional of the density that encompasses the kinetic energy and the electron-electron interaction energy. Furthermore, the functional $F_{HK}[\rho(\vec{r})]$ can be decomposed into contributions from the electronic kinetic energy $T_e[\rho(\vec{r})]$ and the electron-electron interaction potential $V_{ee}[\rho(\vec{r})]$.

$$\boldsymbol{F_{HK}[\rho(\vec{r})] = T_e[\rho(\vec{r})] + V_{ee}[\rho(\vec{r})]} \quad \textbf{(II.24)}$$

Thus, the total energy can also be reformulated as:

$$\boldsymbol{E[\rho(\vec{r})] = T_e[\rho(\vec{r})] + V_{ee}[\rho(\vec{r})] + V_{N-e}[\rho(\vec{r})]} \quad \textbf{(II.25)}$$

where $V_{N-e}[\rho(\vec{r})]$ represents the interaction between the nuclei and the electrons. The significance of the first theorem lies in its implication that the ground-state density can be used to compute all ground-state properties of the system, enabling a reformulation of quantum mechanics in terms of density rather than wave functions. This forms the foundation for the development of practical computational methods in DFT, making it a powerful tool for studying electronic systems in various fields of physics and materials science. The classical form of the electron-electron interaction energy, which can be extracted from the Hartree functional, is expressed as:

$$\boldsymbol{V_{ee}[\rho] = \frac{1}{2} \int \int \frac{\rho(\vec{r})\rho(\vec{r'})}{|\vec{r} - \vec{r'}|}\, dr\, dr'} \quad \textbf{(II.26)}$$

where $|\vec{r} - \vec{r'}|$ is the distance between two points in space.

II.4.2.2 Second theorem of the Hohenberg-Kohn Theorem

The second theorem of the Hohenberg-Kohn (HK) theorem provides a vital criterion for confirming that a given electronic density corresponds to the ground state of a many-body system. However, a pertinent question arises: how can we be certain that a given density is indeed the sought ground state density **[20]**. Hohenberg and Kohn address this concern through

a second postulate, which can be stated as follows: the energy $E[\rho]$, associated with any trial electronic density ρ, corresponds to the ground state energy (the minimum of the functional $E[\rho]$ is achieved at the equilibrium density $\rho_0(\vec{r})$). This second postulate guarantees the uniqueness of the electronic density for any ground state system. The Hohenberg-Kohn theorem represents a substantial conceptual simplification of the quantum mechanical problem of determining the physical properties of the ground state of an interacting electron system. It replaces the traditional wave function description (which depends on $3N_e$ variables, where N_e is the total number of electrons) with a more manageable description in terms of electronic density, which depends solely on the three spatial coordinates. The primary drawback of this theorem for practical applications is that the form of the functional $E[\rho]$ is unknown. This issue can be circumvented through approximations, the most widespread of which is the Kohn-Sham approach. Satisfying the necessary boundary conditions, the second theorem states that for any trial density ρ, associated with an external potential $V_{\text{ext}}(\vec{r})$, the energy $E[\rho]$ is greater than or equal to the energy associated with the ground state electronic density $\rho_0(\vec{r})$ **[21]**.

$$\boldsymbol{E[\rho] \geq E[\rho_0]} \qquad \textbf{(II.27)}$$

This theorem can be seen as the variational principle expressed for energy functionals of a density ρ rather than a wave function ψ. From this, we can establish a correspondence between the variational principle in its wave function version and its density functional version

$$\boldsymbol{E[\rho] \geq \min_{\rho}\left[\langle\psi|\hat{H}|\psi\rangle\right]} \qquad \textbf{(II.28)}$$

The energy of the system $E[\rho]$ reaches its minimum value if and only if the density ρ corresponds to the true ground state density $\rho_0(\vec{r})$.

II.4.3 Kohn-Sham Equations

In their groundbreaking reformulation of Density Functional Theory (DFT), Kohn and Sham introduced a pivotal idea that significantly advanced the practical calculation of ground-state properties of many-electron systems. Their approach centers on the transformation of the complex many-body problem into a more tractable one by introducing a fictitious system of non-interacting electrons. This reference system is constructed such that it yields the same

ground-state electron density ρ(r) as the true, interacting system **[22]**. This conceptual shift offers an elegant resolution to one of the principal challenges of many-body quantum mechanics: the exact treatment of electron–electron interactions and the corresponding kinetic energy. While the classical Coulomb energy (Hartree energy) can be expressed exactly in terms of the electron density, the true kinetic energy of an interacting system remains inaccessible in closed form. Kohn and Sham circumvented this issue by asserting that the kinetic energy of a system of non-interacting particles with the same density as the interacting system could serve as a reference. This allows one to write an exact expression for the kinetic energy $T_s[\rho]$ of non-interacting electrons as a functional of the density. Mathematically, the total energy functional of the system is expressed as.

$$\boldsymbol{E[\rho] = T_s[\rho] + \int V_{ext}(\mathbf{r})\rho(\mathbf{r})\, d\mathbf{r} + \frac{1}{2}\int \frac{\rho(\mathbf{r})\rho(\mathbf{r}')}{|\mathbf{r}-\mathbf{r}'|}\, d\mathbf{r}\, d\mathbf{r}' + E_{xc}[\rho]} \qquad \textbf{(II.29)}$$

Were, $T_s[\rho]$ denotes the kinetic energy of a fictitious system of non-interacting electrons, $V_{ext}(\mathbf{r})$ is the external potential due to the nuclei or applied fields, The double integral represents the classical electrostatic (Hartree) energy $E_H[\rho]$, $E_{xc}[\rho]$ is the exchange-correlation energy functional, which encapsulates all remaining quantum mechanical effects, including electron exchange, correlation, and the difference between the true and reference kinetic energies. This decomposition has far-reaching implications. The many-body wavefunction $\Psi(r_1, \ldots, r_N)$, which depends on all spatial and spin coordinates of N electrons, is replaced by a set of N single-particle wavefunctions $\psi_i(r)$, and the electron density is recovered via.

$$\boldsymbol{\rho(\mathbf{r}) = \sum_{i=1}^{N} |\psi_i(\mathbf{r})|^2} \qquad \textbf{(II.30)}$$

The central result of the Kohn–Sham formalism is a set of self-consistent equations derived from the variational principle applied to the total energy functional under the orthonormality constraint of the single-particle orbitals. These equations resemble the Schrödinger equation.

$$\boldsymbol{\left[-\frac{\hbar^2}{2m}\nabla^2 + V_{eff}(\mathbf{r})\right]\psi_i(\mathbf{r}) = \varepsilon_i \psi_i(\mathbf{r})} \qquad \textbf{(II.31)}$$

where the effective potential $V_{eff}(\mathbf{r})$ is composed of three contributions.

$$\boldsymbol{V_{\text{eff}}(\mathbf{r}) = V_{\text{ext}}(\mathbf{r}) + V_H(\mathbf{r}) + V_{\text{xc}}(\mathbf{r})} \quad \textbf{(II.32)}$$

The individual terms are defined as follows.

$$\boldsymbol{V_{\text{ext}}(\mathbf{r}) = \sum_{\alpha} \frac{-Z_\alpha e^2}{|\mathbf{r}-\mathbf{R}_\alpha|}} \quad \textbf{(II.33)}$$

$$\boldsymbol{V_H(\mathbf{r}) = \int \frac{\rho(\mathbf{r}')}{|\mathbf{r}-\mathbf{r}'|}\, d\mathbf{r}'} \quad \textbf{(II.34)}$$

$$\boldsymbol{V_{\text{xc}}(\mathbf{r}) = \frac{\delta E_{\text{xc}}[\rho]}{\delta \rho(\mathbf{r})}} \quad \textbf{(II.35)}$$

These three equations must be solved iteratively to achieve self-consistency. The process is typically carried out through the following steps, initialize a trial electron density $\rho^{(0)}(\mathbf{r})$, Compute $V_{\text{eff}}^{(0)}(\mathbf{r})$ using **Eq. (II.31)**, Solve the Kohn–Sham equations to obtain the orbitals $\psi_i(\mathbf{r})$, Reconstruct the density.

$$\boldsymbol{\rho^{(1)}(\mathbf{r}) = \sum_{i=1}^{N} \left|\psi_i^{(0)}(\mathbf{r})\right|^2} \quad \textbf{(II.36)}$$

Repeat until $\rho^{(n+1)}(\mathbf{r}) \approx \rho^{(n)}(\mathbf{r})$. The success of the Kohn–Sham method hinges on the treatment of the exchange-correlation energy $E_{\text{xc}}[\rho]$. This term is defined to contain everything not known exactly **[22,23]**.

$$\boldsymbol{E_{\text{xc}}[\rho] = (T[\rho] - T_s[\rho]) + (V_{\text{ee}}[\rho] - E_H[\rho])} \quad \textbf{(II.37)}$$

Since $E_{\text{xc}}[\rho]$ is not known exactly, it is subject to approximations, such as, Local Density Approximation (LDA) assumes that E_{xc} depends only on the local density, Generalized Gradient Approximation (GGA) includes gradients of the density, Hybrid Functionals mix exact exchange from Hartree–Fock theory with GGA terms. By isolating the complexity into a single term, Kohn and Sham minimized the error introduced by approximations. Since $E_{\text{xc}}[\rho]$ typically represents only a small fraction of the total energy, the overall error remains modest even for relatively simple forms of the functional.

II.5 Exchange-Correlation Treatment

An essential component of Density Functional Theory (DFT) is the exchange-correlation (XC) functional, which captures many-body interactions among electrons beyond the classical Coulomb terms [24]. Since the exact form of the exchange-correlation energy functional $E_{xc}[\rho]$ is unknown, several approximations have been developed. This section presents the three principal forms used in this work Local Density Approximation (LDA), Generalized Gradient Approximation (GGA), and the modified Becke-Johnson (mBJ) potential as well as their extensions to include spin-polarization and Hubbard U corrections.

II.5.1 Local Density Approximation (LDA)

The LDA is the simplest and historically earliest approximation in DFT. It assumes that the exchange-correlation energy at a point in space depends only on the local electron density, as in a homogeneous electron gas. The functional form is given by [25,26].

$$\boldsymbol{E_{xc}^{LDA}[\rho] = \int \rho(\mathbf{r})\, \varepsilon_{xc}^{unif}\big(\rho(\mathbf{r})\big)\, d\mathbf{r}} \qquad \textbf{(II.38)}$$

where $\varepsilon_{xc}^{unif}(\rho)$ is the exchange-correlation energy per particle of a uniform electron gas with density ρ. LDA typically overbinds atoms and underestimates band gaps in semiconductors and insulators.

II.5.2 Generalized Gradient Approximation (GGA)

The GGA improves upon the LDA by including the gradient of the electron density. It incorporates non-uniformity effects by expanding the exchange–correlation functional to depend on both $\rho(\mathbf{r})$ and its gradient $\nabla\rho(\mathbf{r})$[27], [28].

$$\boldsymbol{E_{xc}^{GGA}[\rho] = \int f\big(\rho(\mathbf{r}), \nabla\rho(\mathbf{r})\big)\, d\mathbf{r}} \qquad \textbf{(II.39)}$$

One of the most widely used GGA functionals is that of Perdew-Burke-Ernzerhof (PBE) [27], which offers a balanced description of exchange and correlation energies while preserving the exact properties of the uniform electron gas in the slowly varying density limit Beyond PBE, several other GGA functionals have been developed to address specific limitations or to improve predictive accuracy for particular classes of materials. For example, the revised PBE

for solids (PBEsol) [29], modifies the gradient dependence to yield better lattice constants and bulk moduli, making it more suitable for solid-state systems. The Wu-Cohen (WC) GGA [30], is another variant designed to further improve structural predictions for dense solids. Additionally, functionals such as BLYP (Becke-Lee-Yang-Parr) [31], are commonly employed in molecular and chemical simulations due to their accurate treatment of exchange-correlation effects in molecular systems, although they are less commonly used in solid-state physics. GGA functionals provide significantly improved total energies, equilibrium volumes, and atomic positions over LDA, while maintaining a relatively modest computational cost. However, they still tend to underestimate electronic band gaps due to their inability to capture the derivative discontinuity of the exchange-correlation potential. This shortcoming has motivated the development of more advanced approaches such as meta-GGA and hybrid functionals.

II.5.3 Modified Becke-Johnson Potential (mBJ)

The mBJ potential is a semi-local exchange potential developed to improve band gap predictions while retaining computational efficiency. It modifies the Becke–Roussel (BR) exchange potential by introducing a term involving the kinetic energy density [32].

$$v_x^{mBJ}(\mathbf{r}) = c\, v_x^{BR}(\mathbf{r}) + (3c-2)\frac{1}{\pi}\sqrt{\frac{5}{12}}\sqrt{\frac{2t(\mathbf{r})}{\rho(\mathbf{r})}} \qquad \textbf{(II.40)}$$

Where, $t(\mathbf{r})$ is the kinetic energy density, $\rho(\mathbf{r})$ is the electron density, and c is a semi-empirical parameter dependent on the system. The mBJ potential often gives band gaps close to experimental values, making it a preferred choice for studying electronic and optical properties.

II.5.4 Spin-Polarized LDA, GGA, and mBJ Approximations

In magnetic systems, electron spin must be explicitly considered. This leads to the spin-density functional theory (SDFT), where the total electron density $\rho(\mathbf{r})$ is decomposed into spin-up ($\rho_\uparrow$) and spin-down ($\rho_\downarrow$) components [33].

$$\rho(\mathbf{r}) = \rho_\uparrow(\mathbf{r}) + \rho_\downarrow(\mathbf{r}), \quad \zeta(\mathbf{r}) = \frac{\rho_\uparrow(\mathbf{r}) - \rho_\downarrow(\mathbf{r})}{\rho(\mathbf{r})} \qquad \textbf{(II.41)}$$

The spin-polarized LDA (LSDA) exchange–correlation energy becomes.

$$E_{xc}^{LSDA}[\rho_{\uparrow},\rho_{\downarrow}] = \int \rho(\mathbf{r})\,\varepsilon_{xc}^{unif}\big(\rho_{\uparrow}(\mathbf{r}),\rho_{\downarrow}(\mathbf{r})\big)\,d\mathbf{r} \quad \textbf{(II.42)}$$

Similarly, the GGA and mBJ functionals can be spin-polarized. The spin-polarized mBJ potential is expressed as.

$$v_{xc,\sigma}^{mBJ}(\mathbf{r}) = c_{\sigma}\,v_{x,\sigma}^{BR}(\mathbf{r}) + (3c_{\sigma}-2)\frac{1}{\pi}\sqrt{\frac{5}{12}}\sqrt{\frac{2t_{\sigma}(\mathbf{r})}{\rho_{\sigma}(\mathbf{r})}}, \quad \sigma = \uparrow,\downarrow \quad \textbf{(II.43)}$$

These spin-polarized versions are crucial for accurate modeling of ferromagnetic and antiferromagnetic materials, as they allow for the calculation of spin-resolved electronic structures and magnetic moments.

II.5.5 LDA, GGA, and mBJ with Hubbard U Correction

For materials with localized electrons (e.g., $3d$ or $4f$ orbitals), standard DFT functionals often fail due to the self-interaction error and inadequate treatment of strong on-site Coulomb repulsion. To correct this, the DFT+U method adds an explicit Hubbard-like term to the total energy **[34,35]**.

$$E^{DFT+U} = E^{DFT} + E_U - E_{dc} \quad \textbf{(II.44)}$$

where E^{DFT} is the total energy from LDA, GGA, or mBJ, E_U is the Hubbard correction, and E_{dc} is the double-counting term. In the rotationally invariant form by Dudarev *et al.*, the correction simplifies to **[34]**.

$$E_U = \frac{U_{eff}}{2}\sum_{m,\sigma}(n_{m\sigma} - n_{m\sigma}^2) \quad \textbf{(II.45)}$$

where $U_{eff} = U - J$ is the effective on-site interaction, and $n_{m\sigma}$ is the occupation number of the localized orbital with magnetic quantum number m and spin σ.

This correction improves predictions for systems with electron correlation effects, such as Mott insulators, transition metal oxides, and rare-earth compounds. It is particularly effective when combined with the mBJ potential (mBJ+U), allowing for accurate determination of electronic band gaps and magnetic properties.

II.6 Full-Potential Linearized Augmented Plane Wave Method (FP-LAPW)

The Full-Potential Linearized Augmented Plane Wave (FP-LAPW) method is one of the most accurate and widely used approaches for electronic structure calculations within the framework of Density Functional Theory (DFT) **[36]**. It is particularly effective for treating systems with localized d or f electrons, complex crystal structures, and anisotropic charge densities.

II.6.1 Augmented Plane Wave Method (APW)

The original Augmented Plane Wave (APW) method was introduced by Slater in 1937 to solve the Kohn–Sham equations more accurately than traditional plane wave methods by taking into account the atomic nature of the potential. The method divides the unit cell into two distinct regions **[37,38]**.

- **Muffin-tin spheres**: Non-overlapping spheres centered at atomic nuclei, within which the potential is assumed to be spherically symmetric.
- **Interstitial region**: The space outside the muffin-tin spheres, where the potential is constant or slowly varying.

In the APW method, the basis functions are constructed as follows.

$$\boldsymbol{\phi}_{\mathbf{k+G}}(\mathbf{r}) = \begin{cases} \sum_{\ell,m} \boldsymbol{A}_{\ell m}^{\mathbf{k+G}}\, \boldsymbol{u}_{\ell}(\boldsymbol{r}, \boldsymbol{E}_{\ell}) \boldsymbol{Y}_{\ell m}(\hat{\mathbf{r}}), & \textbf{inside muffin-tin spheres} \\ \boldsymbol{e}^{\boldsymbol{i}(\mathbf{k+G})\cdot\mathbf{r}}, & \textbf{in the interstitial region} \end{cases} \qquad \textbf{(II.47)}$$

where $u_\ell(r, E_\ell)$ are radial solutions of the Schrödinger equation at fixed energy E_ℓ, and $Y_{\ell m}$ are spherical harmonics. The coefficients $A_{\ell m}^{\mathbf{k+G}}$ ensure the continuity of the basis functions at the sphere boundaries.

A major limitation of APW is that the basis functions depend on the eigenvalues through $u_\ell(r, E_\ell)$, making the secular equation nonlinear and computationally expensive.

II.6.2 Principle of the Linearized Augmented Plane Wave Method (LAPW)

To overcome the nonlinearity in the APW method, Andersen introduced the Linearized APW (LAPW) method, where the energy dependence of the radial wavefunctions is removed

via a linear expansion around a fixed energy E_ℓ. Inside the muffin-tin spheres, the basis functions are expanded as [39,40].

$$\boldsymbol{u_\ell(r,E) \approx u_\ell(r,E_\ell) + (E - E_\ell)\dot{u}_\ell(r,E_\ell)} \quad \textbf{(II.48)}$$

where $\dot{u}_\ell(r,E_\ell) = \frac{\partial u_\ell(r,E)}{\partial E}\Big|_{E=E_\ell}$ is the energy derivative of the radial function. Thus, the LAPW basis set takes the form.

$$\boldsymbol{\phi_{\mathbf{k+G}}(\mathbf{r}) = \begin{cases} \sum_{\ell,m}\left[A_{\ell m}^{\mathbf{k+G}} u_\ell(r,E_\ell) + B_{\ell m}^{\mathbf{k+G}} \dot{u}_\ell(r,E_\ell)\right] Y_{\ell m}(\hat{\mathbf{r}}), & r \le R_{\mathrm{MT}} \\ e^{i(\mathbf{k+G})\cdot\mathbf{r}}, & r > R_{\mathrm{MT}} \end{cases}} \quad \textbf{(II.48)}$$

This linearization allows for a generalized eigenvalue problem and significantly improves computational efficiency while maintaining accuracy.

II.6.3 Concept of the Full-Potential LAPW Method (FP-LAPW)

In standard LAPW, the potential and charge density are approximated using the muffin-tin approximation, assuming a spherical potential inside the spheres and a constant potential in the interstitial. However, this approximation becomes inadequate for materials with strong anisotropies or non-spherical charge distributions [36]. The Full-Potential LAPW (FP-LAPW) method removes these shape approximations. The total potential $V(\mathbf{r})$ and the electron density $\rho(\mathbf{r})$ are expanded without spherical constraints:

$$\boldsymbol{V(\mathbf{r}) = \begin{cases} \sum_{\ell,m} V_{\ell m}(r) Y_{\ell m}(\hat{\mathbf{r}}), & r \le R_{\mathrm{MT}} \\ \sum_{\mathbf{G}} V_{\mathbf{G}}\, e^{i\mathbf{G}\cdot\mathbf{r}}, & r > R_{\mathrm{MT}} \end{cases}} \quad \textbf{(II.49)}$$

The FP-LAPW method thus uses.

- A full-potential expansion no shape approximation for either the potential or the charge density.
- Augmented plane wave basis with linearization.
- Local orbitals (LOs) to treat semicore states and enhance flexibility.

The addition of local orbitals is especially useful for describing states with energies close to core levels or for improving the variational flexibility [41].

$$\boldsymbol{\phi}_{\ell m}^{\mathrm{LO}}(\mathbf{r}) = \begin{cases} \left[\boldsymbol{u}_{\ell}(\boldsymbol{r}, \boldsymbol{E}_{\ell}) + \boldsymbol{a}_{\ell}\, \dot{\boldsymbol{u}}_{\ell}(\boldsymbol{r}, \boldsymbol{E}_{\ell}) + \boldsymbol{b}_{\ell}\, \boldsymbol{u}_{\ell}\left(\boldsymbol{r}, \boldsymbol{E}_{\ell}^{\mathrm{LO}}\right)\right] \boldsymbol{Y}_{\ell m}(\hat{\mathbf{r}}), & \boldsymbol{r} \leq \boldsymbol{R}_{\mathrm{MT}} \\ \mathbf{0}, & \boldsymbol{r} > \boldsymbol{R}_{\mathrm{MT}} \end{cases} \quad \textbf{(II.50)}$$

where a_ℓ and b_ℓ are coefficients chosen to ensure normalization and orthogonality. the FP-LAPW method offers the highest precision among all DFT-based methods for solving the Kohn-Sham equations, particularly when dealing with systems that exhibit complex structural, electronic, or magnetic characteristics.

II.7 The WIEN2k Code and Its Auxiliary Programs

WIEN2k is a powerful and extensively validated computational software package designed for the calculation of the electronic structure of periodic solids using density functional theory (DFT). It is based on the full-potential (linearized) augmented plane wave plus local orbitals method, one of the most accurate all-electron approaches available for crystalline materials. Unlike pseudopotential-based methods, WIEN2k treats all electrons explicitly and does not approximate the potential or electron density within the so-called muffin-tin spheres or in the interstitial region. This results in highly precise total energies, electronic structures, and derived properties, especially for systems containing transition metals, heavy elements, or materials with low symmetry. Developed and maintained by Peter Blaha and collaborators, WIEN2k is the successor to the original WIEN code and is written predominantly in Fortran. It has evolved to support a wide variety of physical calculations, including structural optimization, electronic and magnetic properties, density of states (DOS), band structure, optical spectra, electric field gradients (EFG), hyperfine interactions, and thermoelectric transport coefficients **[42,43]**.

II.7.1 Core Theoretical Framework

The FP-LAPW method employed in WIEN2k expands the Kohn-Sham wave functions differently in two distinct regions of the unit cell: inside the muffin-tin spheres (around atomic nuclei) and in the interstitial space. Within the spheres, radial solutions of the Schrödinger equation multiplied by spherical harmonics are used, while plane waves are used in the interstitial. The “+lo” extension allows the inclusion of additional local orbitals that improve the variational flexibility of the basis set, particularly for semicore and high-lying unoccupied states. This is essential for accurate band gap calculations and for materials with complex

valence electronic configurations. Relativistic effects are included in a scalar-relativistic fashion for valence electrons and fully relativistically for core states. For heavy elements, spin-orbit coupling (SOC) is included using a second-variational scheme, which is computationally efficient and accurate.

II.7.2 Input Structure and Initialization

WIEN2k uses a modular architecture wherein each module is responsible for a specific part of the calculation. The workflow typically begins with the init_lapw script, which generates all necessary input files. This step involves specifying the crystal structure (lattice type, space group, and atomic positions), the muffin-tin radii (RMT) for each atom, the basis set cutoff parameter $R_{MT} \times K_{max}$, and the exchange-correlation functional to be used. The symmetry module is invoked to detect the space group symmetries and reduce the number of k-points needed for Brillouin zone integration. The choice of $R_{MT} \times K_{max}$, which is the product of the smallest muffin-tin radius and the maximum reciprocal lattice vector of the plane wave expansion, governs the basis set size. A typical value ranges from 6 to 9, but convergence tests are essential for accurate total energies and electronic properties.

II.7.3 SCF Cycle and Main Executables

Once initialized, the self-consistent field (SCF) cycle is run using run_lapw, which orchestrates several key modules:

- **lapw0** computes the Coulomb and exchange-correlation potential on a mesh, including potential contributions from core and valence charge densities.
- **lapw1** solves the Kohn–Sham equations and determines the energy eigenvalues and eigenfunctions by diagonalizing the Hamiltonian in the APW basis.
- **lapw2** computes the total electron density from the eigenfunctions, including both muffin-tin and interstitial contributions.
- **mixer** compares the input and output charge densities to assess convergence, applying mixing algorithms (e.g., Broyden mixing) to accelerate convergence.

- **lapwso** (optional) adds spin-orbit interaction using the second-variational procedure.

The SCF loop continues until the energy and charge convergence criteria are met. The convergence threshold for energy is typically set to 0.0001 Ry or lower, while the charge density is required to change by less than 0.001 e or smaller between cycles.

II.7.4 Advanced Functionalities and Post-processing Modules

WIEN2k includes a wide range of auxiliary programs that extend its capabilities beyond the basic electronic structure:

- **spaghetti**: Generates the electronic band structure by calculating eigenvalues along high-symmetry directions in the Brillouin zone. It allows visual inspection of band dispersion, energy gaps, and critical points.

- **tetra**: Implements the tetrahedron method for accurate Brillouin zone integration, particularly for the DOS and optical spectra. It subdivides the Brillouin zone into small tetrahedra and integrates over them analytically.

- **dos** and **tetra**: Used in combination to compute the total and partial density of states.

- **optic** and **joint**: These programs calculate frequency-dependent optical properties, including the complex dielectric function ($\varepsilon_1(\omega)$, $\varepsilon_2(\omega)$), refractive index, reflectivity, and absorption coefficient. optic uses the momentum matrix elements from lapw1, while joint calculates the joint DOS.

- **lapw2 -qtl**: Generates the orbital character of the electronic bands, which is useful for plotting fat bands or analyzing the contribution of atomic orbitals to each band.

- **qtl**: Produces the orbital-projected DOS (also called partial DOS or PDOS) by projecting the wave functions onto atomic-like orbitals.

- **irrep**: Computes the irreducible representations of eigenstates at symmetry points, aiding in symmetry analysis and characterization of degeneracies.

- **efg**: Computes the electric field gradient tensor at the nuclei, which is relevant for interpreting Mössbauer spectroscopy, NMR, and nuclear quadrupole resonance (NQR) experiments.
- **nmr**: Calculates NMR chemical shielding and spin densities.
- **lapwdm**: Computes the spin and orbital magnetic moments inside the muffin-tin spheres.
- **xcrysden** and **VESTA** (external programs): WIEN2k provides compatible output formats for visualization of crystal structures, charge densities, and potential maps using these widely used visualization tools.

II.7.5 Parallel Execution and Scalability

To handle the high computational demands of all-electron calculations, WIEN2k is parallelized at multiple levels. Parallelism can be applied over k-points, symmetry operations, and bands. For distributed memory systems, MPI (Message Passing Interface) is used, while OpenMP is employed for shared-memory parallelism within nodes. This scalability allows efficient use of high-performance computing resources, enabling the study of large unit cells and complex magnetic configurations. In addition, hybrid parallelization combining MPI and OpenMP is supported for modules such as lapw1, lapw2, and lapwso. The parallelization is particularly advantageous when dealing with large k-point meshes or when using computationally demanding hybrid functionals or spin–orbit coupling.

II.7.6 Support for Advanced Exchange-Correlation Functionals

WIEN2k supports a wide range of exchange-correlation (XC) functionals through the LibXC library. Among the most widely used are:

- **GGA (Generalized Gradient Approximation – PBE functional):** Utilized as the baseline exchange–correlation functional, the PBE (Perdew-Burke-Ernzerhof) version of GGA improves upon the Local Density Approximation (LDA) by incorporating both the electron density and its spatial gradient. This results in enhanced accuracy for structural properties such as lattice constants, bond lengths, and bulk moduli, making it widely applicable for crystalline solids.

- **DFT+U method (implemented via the orb module)**: To correct for the self-interaction errors and better treat strong on-site Coulomb interactions, particularly in systems with localized d and f electrons (e.g., transition metal oxides and rare-earth compounds), the DFT+U approach was employed. The orb module in WIEN2k facilitates the inclusion of the Hubbard U parameter, which improves the description of electron correlation, magnetic ordering, and possible Mott-insulating behavior in correlated materials.
- **mBJ (modified Becke-Johnson potential)**: An empirical meta-GGA exchange potential introduced by Tran and Blaha, the mBJ potential is specifically designed to improve the prediction of electronic band gaps. It mimics the behavior of the exact exchange potential from Hartree–Fock theory while maintaining computational efficiency. It is particularly effective for semiconductors and insulators, often yielding band gaps that are much closer to experimental values than GGA or LDA.
- **Hybrid functionals (using the hf module):** These functionals incorporate a portion of exact Hartree-Fock exchange with DFT exchange–correlation terms, leading to significantly improved accuracy for electronic structure calculations of systems with strong electronic localization and correlation. The hf module in WIEN2k enables the implementation of screened hybrid functionals in an all-electron full-potential framework. Such methods are especially beneficial for capturing the correct band gaps, magnetic properties, and localization effects in complex oxides and strongly correlated systems.

These features make WIEN2k highly versatile for investigating a wide range of material classes, including metals, insulators, semiconductors, strongly correlated materials, magnetic compounds, and topological phases.

II.7.7 Magnetism, Spin-Orbit Coupling, and Spin Polarization

Magnetic calculations are straightforward in WIEN2k. Initial magnetic moments can be specified for each atom, and spin-polarized SCF calculations are then carried out using the runsp_lapw script. Non-collinear magnetism is also supported, although more complex input preparation is required. The lapwso module adds spin-orbit coupling in a second-variational approach that requires eigenvectors from lapw1 as input. WIEN2k allows the user to explore different magnetic configurations, including ferromagnetic (FM), antiferromagnetic (AFM),

and nonmagnetic (NM) phases. By comparing total energies of these configurations, one can determine the ground-state magnetic ordering and estimate exchange interactions, particularly when combined with supercell approaches or the Heisenberg model.

II.8 Conclusion

This chapter has provided a detailed exposition of the theoretical models and computational frameworks employed in this work. Starting from the foundational Schrödinger equation and the Born-Oppenheimer approximation, we explored successive approximations Hartree, Hartree-Fock, and Density Functional Theory that render the many-body problem tractable for realistic systems. The formal structure of DFT, as articulated through the Hohenberg-Kohn theorems and the Kohn-Sham approach, was presented with emphasis on the role and approximation of the exchange-correlation functional. We reviewed the commonly used LDA, GGA (including PBE, PBEsol, WC, and BLYP variants), and the mBJ potential, along with spin-polarized and Hubbard-corrected extensions tailored for magnetic and correlated materials. We then turned to the Full-Potential Linearized Augmented Plane Wave (FP-LAPW) method, a high-precision approach for solving the Kohn-Sham equations without shape approximations. Its implementation within the WIEN2k software was outlined, emphasizing the code's modular design, SCF workflow, and capabilities for analyzing a wide range of physical properties. Altogether, the methodologies described in this chapter constitute the theoretical and computational backbone of the subsequent analyses presented in this thesis. They enable the predictive modeling of structural, electronic, magnetic, and optical properties of complex materials, facilitating insights that guide experimental validation and technological application.

Bibliography

[**1**] E. Schrödinger, Physical Review, 1926, 28, 1049.
[**2**] C. G. Weaver, "Hamilton, Hamiltonian Mechanics, and Causation," Nov. 2020.
[**3**] P. Kireev, la physique des semiconducteurs, 2ème...,
[**4**] M. Born, Born-oppenheimer approximation, Ann. Phys, 1927, vol. 84.
[**5**] H. Essén, Int J Quantum Chem, 1977, 12, 721–735.
[**6**] D. R. Hartree, Mathematical Proceedings of the Cambridge Philosophical Society, 1928, 24, 89–110.
[**7**] H. J. Schnitzer, Physical Review D, 1974, 10, 2042.
[**8**] P. Lykos and G. W. Pratt, Rev Mod Phys, 1963, 35, 496.

[**9**] The quantum theory of molecular electronic structure: a lecture-note and reprint volume | CiNii Research, https://cir.nii.ac.jp/crid/1130282270708886656, (accessed 2 May 2025).
[**10**] R. G. Parr, The quantum theory of molecular electronic structure: a lecture-note and reprint volume.
[**11**] E. Engel and R. M. Dreizler, Theoretical and Mathematical Physics(United States), 2011, E3–E4.
[**12**] E. Engel and R. M. Dreizler, 2011, 307–349.
[**13**] E. Engel and R. M. Dreizler, 2011, 401–402.
[**14**] L. H. Thomas, Mathematical Proceedings of the Cambridge Philosophical Society, 1930, 26, 123–126.
[**15**] P. A. M. Dirac, Mathematical Proceedings of the Cambridge Philosophical Society, 1934, 30, 150–163.
[**16**] R. G. Parr, Horizons of Quantum Chemistry, 1980, 5–15.
[**17**] W. Kohn, A. D. Becke and R. G. Parr, Journal of Physical Chemistry, 1996, 100, 12974–12980.
[**18**] A. Görling, Phys Rev A (Coll Park), 1999, 59, 3359.
[**19**] J. C. Slater, Advances in Quantum Chemistry, 1964, 1, 35–58.
[**20**] T. L. Gilbert, Phys Rev B, 1975, 12, 2111.
[**21**] W. Kohn and L. J. Sham, Physical Review, 1965, 137, A1697.
[**22**] W. Kohn and L. J. Sham, Physical Review, 1965, 140, A1133.
[**23**] J. Harris and R. O. Jones, Journal of Physics F: Metal Physics, 1974, 4, 1170.
[**24**] M. A. L. Marques, M. J. T. Oliveira and T. Burnus, Comput Phys Commun, 2012, 183, 2272–2281.
[**25**] Pure and Applied Analysis Vol. 2, No. 1, 2020, https://msp.org/paa/2020/2-1/p03.xhtml, (accessed 2 May 2025).
[**26**] F. Herman, J. P. Van Dyke and I. B. Ortenburger, Phys Rev Lett, 1969, 22, 807.
[**27**] J. P. Perdew, K. Burke and M. Ernzerhof, Phys Rev Lett, 1996, 77, 3865.
[**28**] W. Kohn, Rev Mod Phys, 1999, 71, 1253.
[**29**] Z. Wu and R. E. Cohen, Phys Rev B Condens Matter Mater Phys, 2006, 73, 235116.
[**30**] A. D. Becke, Phys Rev A (Coll Park), 1988, 38, 3098.
[**31**] C. Lee, W. Yang and R. G. Parr, Phys Rev B, 1988, 37, 785.
[**32**] J. A. Camargo-Martínez and R. Baquero, Phys Rev B Condens Matter Mater Phys, 2012, 86, 195106.
[**33**] R. Zeller, NIC Series, 2006, 31, 419–445.
[**34**] E. B. Linscott, D. J. Cole, M. C. Payne and D. D. O'Regan, Phys Rev B, 2018, 98, 235157.
[**35**] B. Himmetoglu, A. Floris, S. De Gironcoli and M. Cococcioni, Int J Quantum Chem, 2014, 114, 14–49.
[**36**] M. Petersen, F. Wagner, L. Hufnagel, M. Scheffler, P. Blaha and K. Schwarz, Comput Phys Commun, 2000, 126, 294–309.
[**37**] L. Nordström, G. K. H. Madsen, P. Blaha, K. Schwarz and E. Sjöstedt, Phys Rev B, 2001, 64, 195134.
[**38**] E. Krasovskii, Phys Rev B, 1997, 56, 12866.
[**39**] Planewaves, Pseudopotentials and the LAPW Method, 2006, 43–52.
[**40**] Planewaves, Pseudopotentials, and the LAPW Method - David J. Singh, Lars Nordstrom - Google Books.

[**41**] J. P. Lewis, K. R. Glaesemann, G. A. Voth, J. Fritsch, A. A. Demkov, J. Ortega and O. F. Sankey, Phys Rev B, 2001, 64, 195103.

[**42**] P. K. Blaha Karlheinz Schwarz Georg H Madsen Dieter Kvasnicka Joachim Luitz Robert Laskowski Fabien Tran Laurence D Marks, P. Blaha, K. Schwarz, G. K. H Madsen, D. Kvasnicka, J. Luitz, R. Laskowski, F. Tran and L. D. Marks, .

[**43**] K. Schwarz and P. Blaha, Comput Mater Sci, 2003, 28, 259–273.

CHAPTER III

Electro-Structural Properties

III.1 Introduction

In this chapter, we present a comprehensive analysis of the electronic properties of several structurally diverse materials using first-principles density functional theory (DFT) calculations. The materials under investigation include a range of perovskite, double perovskite, and antiperovskite compounds. These systems were selected based on their chemical diversity, structural stability, and potential applicability in modern electronic and optoelectronic technologies. The study employs a multi-step theoretical framework to evaluate the electronic band structure and density of states (DOS) of each compound. Exchange-correlation interactions were treated within the generalized gradient approximation (GGA) using the Perdew Burke Ernzerhof (PBE) functional, supplemented by the Hubbard U correction for materials with localized d or f electrons, and the modified Becke-Johnson (TB-mBJ) potential to improve band gap predictions. These computational techniques allow for a more accurate description of the electronic structure, particularly in capturing the magnitude and character (direct or indirect) of band gaps, which are often underestimated in standard DFT.

III.2 Structural Properties

III.2.1 Crystal Symmetry and Lattice Systems

Crystallography provides the formal framework to describe the long-range periodicity of atomic arrangements in solids **[1]**. A crystal lattice can be represented as a set of discrete points in space, generated by translations of a unit cell along three non-coplanar vectors. Depending on the relationships between the lattice parameters (lengths and angles), crystal structures are classified into seven lattice systems and 14 Bravais lattices. Among them, the cubic, tetragonal, and hexagonal systems are particularly relevant due to their prevalence in inorganic compounds and their influence on physical properties **[2]**.

- **Cubic systems** exhibit high symmetry with equal lattice constants (a=b=c) and angles (α=β=γ=90°), often leading to isotropic behavior in mechanical, optical, and electronic responses.
- **Tetragonal systems** maintain right angles but have one distinct lattice constant (a=b≠c), resulting in anisotropic behavior along the c-axis.
- **Hexagonal systems** are characterized by two equal lattice constants (a = b ≠ c) and angles of α=β=90°, γ=120°, introducing additional anisotropy and complexity in bonding and coordination environments.

The space group of a crystal, combining translational symmetry with point group operations such as rotation, reflection, and inversion, plays a crucial role in determining the allowed electronic states and selection rules for optical transitions.

III.2.2 Lattice Parameters, Unit Cell Volume, and Atomic Positions

Quantitative description of a crystal structure includes the lattice constants (a, b, c), interaxial angles (α, β, γ), and the atomic coordinates expressed in fractional units relative to the unit cell axes. The unit cell volume (V), derived from these parameters, serves as a measure of atomic packing and is often related to material density and bulk modulus. Atomic positions are typically described using Wyckoff notations, which reflect the symmetry and multiplicity of atomic sites. In computational structural optimization, these positions are relaxed to minimize the total energy, allowing the system to adopt its most energetically favorable configuration. This process involves solving the Kohn-Sham equations iteratively until the forces acting on atoms fall below a chosen convergence threshold **[1,2]**.

III.2.3 The Goldschmidt tolerance factor

The Goldschmidt tolerance factor (t) is a key parameter used to predict the stability of crystal structures, particularly in perovskite-like materials. It is calculated using the equation **[3]**.

$$\mathbf{t = \frac{r_A + r_X}{\sqrt{2}(r_B + r_X)}} \qquad \mathbf{(III.1)}$$

where r_A is the ionic radius of the A cation, r_B is the ionic radius of the B cation, and r_X represents the ionic radius of the anion. The tolerance factor helps to assess whether the ionic sizes of the cations are compatible with forming a stable crystal structure. When the tolerance factor is close to 1, the ionic radii are well-matched, leading to minimal strain and a stable lattice. A tolerance factor greater than 1 suggests that the A cation is too large, which causes strain in the lattice, while a value less than 1 indicates that the A cation is too small, potentially leading to instability. This factor is widely used in materials science to predict the structural stability of various materials and their suitability for different applications **[4]**.

III.2.4 Formation Energy and Cohesive Energy

To evaluate thermodynamic stability, two fundamental energetic descriptors are commonly employed. The formation energy (Δ_{Hf}) is defined as the difference between the total energy of the compound and the sum of the energies of its constituent elements in their standard states. Mathematically **[5]**.

$$\mathbf{\Delta H_f = E_{compound} - \sum E_{elements}} \qquad \mathbf{(III.2)}$$

Where E_{compound} is the total energy of the compound, and E_{elements} is the sum of the energies of the constituent elements in their most stable forms. A negative formation energy implies that the compound is thermodynamically stable with respect to decomposition into its elemental constituents. The cohesive energy (E_{coh}), on the other hand, is calculated as the energy released when isolated free atoms bond together to form the crystal **[6]**.

$$\mathbf{E_{coh} = E_{ISO_{compound}} - \sum E_{ISO_{elements}}} \quad \textbf{(III.3)}$$

Where $\mathbf{E_{ISO_{compound}}}$ is the sum of the total energies of all isolated atoms in their ground state, and $\sum \mathbf{E_{ISO_{elements}}}$ is the total energy of the compound per formula unit. It provides a measure of bonding strength and internal stability of the structure. Higher cohesive energy generally correlates with enhanced mechanical strength and resistance to thermal decomposition. Both quantities are crucial in predicting the synthesizability and long-term structural stability of novel materials.

III.2.5 Structural Characterization and X-ray Diffraction

X-ray diffraction (XRD) is a fundamental experimental technique for determining crystal structures as shown in **Figure III.1**. In computational work, theoretical XRD patterns can be simulated based on optimized atomic positions and lattice parameters. These simulations are instrumental in validating the predicted structures by comparing them with experimental data. Rietveld refinement techniques may also be employed to refine structural models and reduce the discrepancy between observed and simulated diffraction profiles **[7]**.

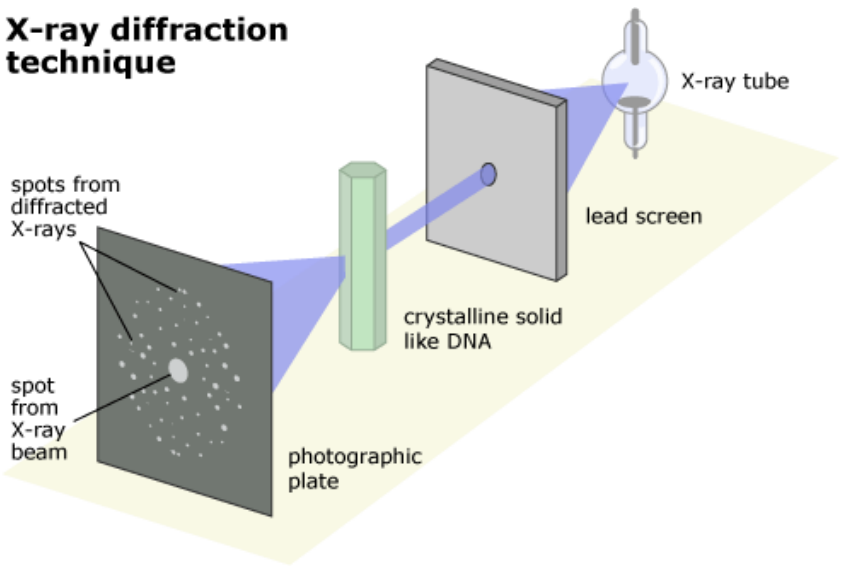

Figure III.1. X-ray diffraction (XRD) techniques for materials characterization

III.3 Electronic Properties

III.3.1 Band Theory and Electronic States

The electronic properties of solids arise from the quantum mechanical treatment of electrons in a periodic potential. According to band theory, the discrete energy levels of isolated atoms broaden into continuous bands when atoms are brought together in a solid. The two most significant bands near the Fermi energy are the valence band (VB) and conduction band (CB), separated by a band gap (E_g). The position of the Fermi level (E_F), defined as the highest occupied energy level at 0 K, determines the carrier concentration and electrical behavior as depicted in **Figure III.2 [8]**.

- In metals, "E_F" lies within an overlapping band, allowing free movement of electrons.
- In semiconductors, "E_F" lies within the band gap, with thermal excitation enabling electrons to transition from the VB to CB.
- In insulators, the band gap is too large for significant electronic conduction under normal conditions.

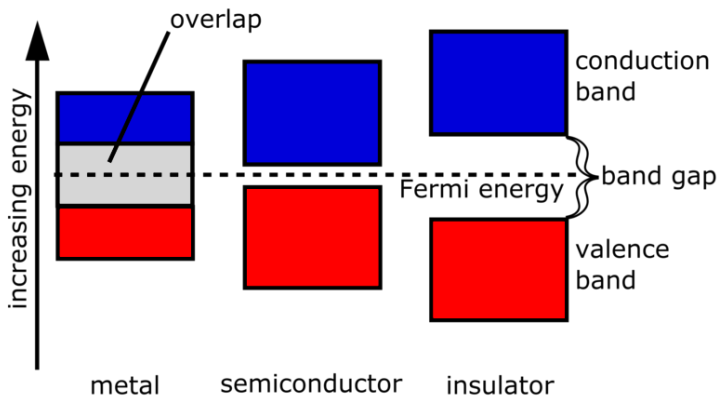

Figure III 2. Difference between Conductor, Semiconductor and Insulator

III.3.2 Direct and Indirect Band Gaps

The nature of the band gap whether direct or indirect is of paramount importance for optoelectronic applications. In a direct band gap material, the minimum of the CB and the maximum of the VB occur at the same k-point in reciprocal space, allowing vertical electronic transitions ($\Delta k = 0$), as shown in **Figure III.3**. This is favorable for light emission and absorption processes. Conversely, an indirect band gap material exhibits a mismatch in k-space between VB maximum and CB minimum ($\Delta k \neq 0$), necessitating phonon assistance for optical

transitions, which typically reduces the material's optical efficiency. The band gap and its character are determined from the computed electronic band structure, obtained by solving the Kohn-Sham equations across high-symmetry paths in the Brillouin zone **[9]**.

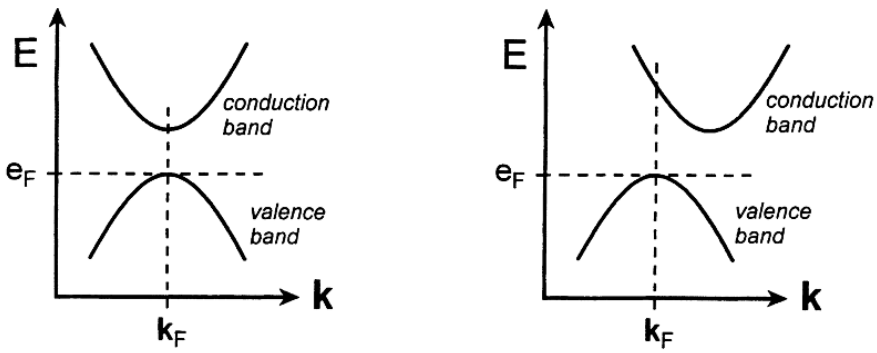

Figure III.3. Difference between direct and indirect band gap semiconductor material

III.3.3 Density of States (DOS): Total, Partial, and Spin-Resolved

The Density of States (DOS) represents the number of electronic states available per unit energy. The Total DOS (TDOS) integrates over all atomic and orbital contributions, while the Partial DOS (PDOS) decomposes the contributions by element and orbital type (s, p, d, f). The Spin-resolved DOS distinguishes the up and down spin channels, essential for magnetic and spintronic materials. The DOS near the Fermi level offers insight into electronic conductivity, bonding nature, and reactivity, a high DOS at "E_F" may indicate metallic behavior or magnetic instabilities, whereas a clean gap indicates insulating or semiconducting characteristics as shown in **Figure III.4 [10]**.

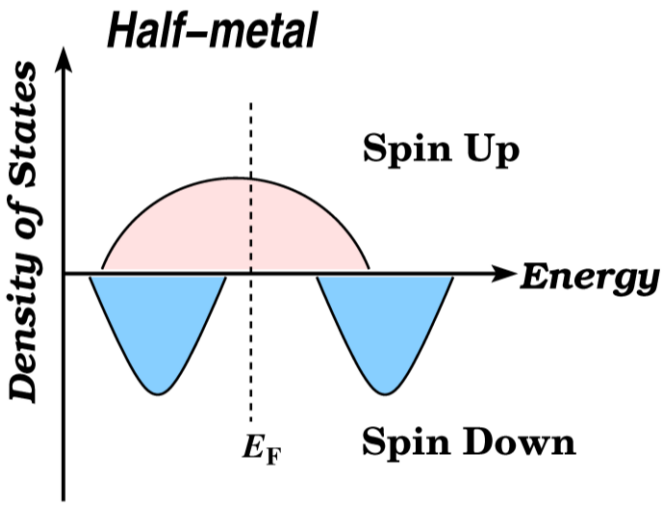

Figure III.4. Density of States (DOS) of a Half-Metallic Material: Spin-Up Metallic and Spin-Down Semiconducting Behavior

III.3.4 Orbital Contributions to Band Structure

In multi-element systems, the hybridization of atomic orbitals significantly influences the shape and character of the electronic bands. The interaction between transition metal d-orbitals and p-orbitals from chalcogens or pnictogens often determines the position of band edges and the magnitude of the band gap. Furthermore, crystal field effects arising from different symmetries (e.g., octahedral, tetrahedral) cause energy-level splitting of degenerate orbitals, which directly modulates the band dispersion and DOS features. These effects are critical in tailoring the electronic structure through compositional or structural modifications **[11]**.

III.4 Results and Discussion

III.4.1 Structural properties

III.4.1.1 Perovskite ABX_3

For our selection of materials within the ABX_3 perovskite family, we conducted a comprehensive structural analysis focusing on two distinct groups: halide perovskites $ASiCl_3$, where A = Li, Rb, Cs and chalcogenide perovskites $CsTaX_3$, where X = S, Se. The calculated Goldschmidt tolerance factors, derived from precise bond length measurements, are summarized in **Table III.1**. These values provide critical insights into the structural stability and symmetry of the compounds under investigation.In the halide perovskite series, the A-Cl bond lengths range from 3.57 Å in $LiSiCl_3$ to 3.70 Å in $CsSiCl_3$, while the Si-Cl bond lengths vary between 2.53 Å and 2.62 Å. These measurements correspond to tolerance factors approximately between 0.99 and 1.00. Such values are indicative of a stable cubic perovskite structure, as they fall within the optimal range for maintaining cubic symmetry. This structural arrangement is characterized by the A-site cations (Li^+, Rb^+, Cs^+) occupying the corners of the cube, the Si^{4+} cation at the center, and Cl^- anions at the face centers, forming a three-dimensional network of corner-sharing $[SiCl_6]^{4-}$ octahedra **[12]**. The unit cell of these compounds adopts the cubic space group Pm-3m (No. 221), as depicted in **Figure III.5(a)**.

Conversely, the chalcogenide perovskites exhibit different structural characteristics. The Cs-X bond lengths are measured at 4.21 Å for $CsTaS_3$ and 4.24 Å for $CsTaSe_3$, with corresponding Ta-X bond lengths of 2.66 Å and 2.84 Å, respectively. These bond lengths result in higher tolerance factors of 1.10 for $CsTaS_3$ and 1.05 for $CsTaSe_3$. Values exceeding unity suggest a deviation from the ideal cubic structure, leading to the adoption of a hexagonal symmetry. This is consistent with the observed crystallization of these compounds in the

hexagonal space group $P6_3mc$ (No. 186). In this configuration, Cs^+ ions occupy the 2d Wyckoff positions at (1/3, 2/3, 3/4), Ta^{5+} ions are located at 4e positions with coordinates (0, 0, u), where u = 0.045195 for $CsTaS_3$ and u = 0.455105 for $CsTaSe_3$, and the chalcogen atoms (S^{2-}, Se^{2-}) reside at 6h positions with specific fractional coordinates for each compound. The resulting structure comprises TaX_6 octahedra that share corners and faces, forming a three-dimensional network distinct from the cubic arrangement of the halide counterparts **[12]**. These structural configurations are illustrated in Figures III.5(b-e).

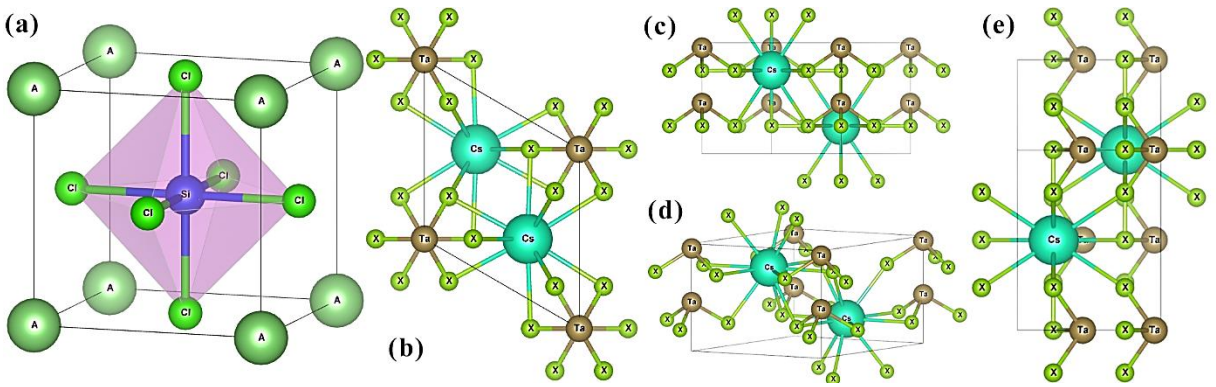

Figure III.5. Crystal structures of (a) Cubic $ASiCl_3$ (A = Li, Rb, Cs); (b–e) Hexagonal $CsTaX_3$ (X = S, Se)

Table III.1: Optimized lattice parameters and total energies for $ASiCl_3$ (A = Li, Rb, Cs) in non-magnetic (NM), ferromagnetic (FM), and antiferromagnetic (AFM) configurations, and for $CsTaX_3$ (X = S, Se) in the NM state.

Materials	State	Lattice Parameter (Å)			B′	E_{min} (Ry)	E_{coh} (Ry)	Δ_{Hf} (Ry)	T_G
		a	c	c/a					
Cubic Symmetry									
$LiSiCl_3$	**NM**	**5.06**	//	//	**3.83**	**-3364.417541**	-1.11	-0.56	0.99
	FM	5.08	//	//	4.01	-3364.417539			
	AFM	5.08	//	//	3.95	-3364.417538			
$RbSiCl_3$	**NM**	**5.17**	//	//	**4.53**	**-9312.466785**	-1.15	-0.89	1.00
	FM	5.18	//	//	4.87	-9312.466712			
	AFM	5.17	//	//	3.97	-9312.466696			
$CsSiCl_3$	**NM**	**5.24**	//	//	**3.84**	**-18930.082444**	-1.12	-0.78	0.99
	FM	5.24	//	//	4.36	-18930.082441			
	AFM	5.22	//	//	3.75	-18930.082427			
Hexagonal Symmetry									
$CsTaS_3$	NM	7.44	6.01	0.81	4.32	-98456.817991	-2.23	-0.55	1.10
$CsTaSe_3$	NM	7.71	6.14	0.80	4.39	-112829.065766	-1.95	-1.19	1.05
Other Works									
$CsTaS_3$	NM	7.26^{e1}	5.96^{e1}	//	//	//	//	//	//
$CsTaSe_3$	NM	7.50^{e1}	6.18^{e1}	//	//	//	//	//	//
$CsTaS_3$	NM	7.25^{t1}	5.94^{t1}	//	//	//	//	//	//

Experimental: ^{e1} Ref **[13]** Theoritical: ^{t1} Ref **[14]**

To further elucidate the structural characteristics of our selected ABX_3 perovskite materials, we performed a comprehensive optimization of their structural properties. Given the novelty of the $ASiCl_3$ compounds, we investigated three magnetic configurations non-magnetic (NM), ferromagnetic (FM), and antiferromagnetic (AFM) to determine the most stable phase. The results, summarized in **Table III.1**, indicate that the NM state exhibits the lowest total energy across all halide perovskite compounds studied, suggesting it as the most stable configuration. Analyzing the lattice parameters, we observed a systematic increase in the lattice constant 'a' with the substitution of larger A-site cations: 5.06 Å for $LiSiCl_3$, 5.17 Å for $RbSiCl_3$, and 5.24 Å for $CsSiCl_3$. This trend reflects the influence of the ionic radius of the alkali metal cations on the unit cell dimensions. Such behavior has been reported in other alkali-based perovskite materials, including $ASnCl_3$, $AGeCl_3$, and $ASnBr_3$ (A = Li, K, Rb, Cs), where the lattice parameters expand with increasing cation size due to the accommodation of larger ions within the crystal structure **[15-17]**.

For the chalcogenide perovskites, our study focused on the NM state, aligning with previous experimental and theoretical findings that classify these compounds as non-magnetic. Notably, studies such as those by Pell et al. have demonstrated that $CsTaS_3$ and $CsTaSe_3$ exhibit non-magnetic behavior, corroborating our computational results **[13]**. Our calculated lattice parameters for $CsTaS_3$ and $CsTaSe_3$ are 7.44 Å and 7.71 Å for the 'a' axis, and 6.01 Å and 6.14 Å for the 'c' axis, respectively. These values show a slight increase when substituting sulfur with the larger selenium anion, consistent with the expected expansion of the lattice due to the larger ionic radius of Se^{2-} compared to S^{2-}. This phenomenon has also been observed in related compounds such as $BaZrX_3$ (X = S, Se), where the lattice parameters increase with the incorporation of heavier chalcogen elements **[18]**. Our calculated lattice parameters are in reasonable agreement with previously reported experimental and theoretical values, supporting the validity of our computational approach, Pell et al. and Bie et al. **[13,14]**, reported lattice constants of approximately 7.26 Å for 'a' and 5.96 Å for 'c' in $CsTaS_3$, and 7.50 Å for 'a' and 6.18 Å for 'c' in $CsTaSe_3$, which closely match our findings.

III.4.1.2 Double Perovskite $A_2BB'X_6$

In this section, we investigate the structural characteristics and magnetic phase stability of two double perovskites, Ba_2InOsO_6 and Sr_2MnSbO_6, both belonging to the $A_2BB'X_6$ family. The structural stability was initially assessed using the Goldschmidt tolerance factor (t), calculated based on Shannon's effective ionic radii. For Ba_2InOsO_6, the ionic radii used were,

Ba^{2+}: 1.61 Å, In^{3+}: 0.80 Å, Os^{5+}: 0.63 Å, O^{2-}: 1.40 Å. Using these values, the tolerance factor was found to be T_G=1.00, indicating an ideal cubic symmetry. This is in excellent agreement with prior experimental results reported by Feng et al. **[19]**, which confirmed that Ba_2InOsO_6 crystallizes in a cubic structure (space group Fm-3m, No. 225). In this phase, Ba atoms occupy the 8c Wyckoff positions at (0.25, 0.25, 0.25), In at 4a (0, 0, 0), Os at 4b (0.5, 0.5, 0.5), and O at 24e (0.239219, 0, 0), as illustrated in **Figure III.6(a)**.

The optimized lattice parameters and corresponding energies for different magnetic configurations are summarized in **Table III.2**. Among the considered magnetic phases (NM, FM, FiM, and AFM), the ferromagnetic (FM) configuration yielded the lowest total energy, signifying its thermodynamic favorability. The optimized lattice parameter for the FM phase is a=8.31 Å, which closely matches the experimental value of 8.22 Å **[19]**, further validating the robustness of our computational approach. For Sr_2MnSbO_6, the tolerance factor was similarly calculated using, Sr^{2+}: 1.44 Å, Mn^{3+}: 0.645 Å, Sb^{5+}: 0.60 Å, O^{2-}: 1.40 Å, which gave a value of T_G=1.05. This deviation from unity suggests the stabilization of a lower-symmetry structure, likely tetragonal or hexagonal. Our theoretical predictions were corroborated by a detailed study conducted by Sosa-Correa et al. **[20]**, who compared three space groups, No. 225 (cubic), No. 87 (tetragonal I4/m), and No. 128 (orthorhombic). Their results identified space group No. 87 as the most energetically stable, which aligns with our findings. In the I4/m tetragonal phase, Sr atoms reside at 4d (0.25, 0.75, 0.5), Mn at 2b (0.5, 0, 0), and Sb at 2a (0, 0, 0). Oxygen atoms split between two Wyckoff positions: O1 at 4e (0, 0, 0.233504) and O2 at 8h (0.303572, 0.204493, 0), as shown in Figures III.6(b). The occupancy of distinct oxygen sites ensures appropriate local coordination environments for Mn and Sb cations, optimizing bond lengths and angles to enhance structural stability. Optimization under four magnetic configurations revealed that the FM phase is again the ground state, with the lowest total energy. The corresponding lattice parameters were determined to be a=5.52 Å and c=8.52 Å, yielding a c/a ratio of 1.53. These values are consistent with prior theoretical and experimental reports by Ivanov et al. **[21]**, Cheah et al. **[22]**, Mandal et al. **[23]**, and Sosa-Correa et al. **[20]**, as summarized in **Table III.2**.

Table III.2: Optimized Structural Parameters, Ground-State Energies, and Formation Energies for Ba_2InOsO_6 and Sr_2MnSbO_6 in Various Magnetic Phases

Material	State	Lattice parameter (Å)			B′	E_{min} (Ry)	T_G	E_{coh} (Ry)	Δ_{Hf} (Ry)
		a=b	c	c/a					
Cubic Symmetry									
Ba_2InOsO_6	NM	8.30	//	//	4.91	-79791.651946	1.01	-3.48	-2.32
	FM	**8.31**	//	//	**4.86**	**-79791.689683**			
	FiM	8.30	//	//	4.86	-79791.668953			
	AFM	8.30	//	//	4.91	-79791.685998			
Other Works									
Ba_2InOsO_6	FM	8.22[e1]	//	//	//	//	//	//	//
Tetragonal Symmetry									
Sr_2MnSbO_6	NM	5.55	8.41	1.53	4.57	-28907.508863	1.05	-4.22	-2.52
	FM	**5.52**	**8.52**	**1.53**	**4.73**	**-28907.780769**			
	FiM	5.51	8.53	1.53	4.79	-28907.590846			
	AFM	5.51	8.54	1.53	4.77	-28907.670735			
Other Works									
Sr_2MnSbO_6	FM	5.63[t1]	8.05	1.43	//	//	//	//	//
	FM	5.52[e2]	8.04	1.45	//	//	//	//	//
	FM	5.53[e3]	8.08	1.46	//	//	//	//	//
	FM	5.54[e4]	8.09	1.46	//	//	//	//	//

Experimental: [e1] Ref **[19]**, [e2] Ref **[21]**,[e3] Ref **[22]**,[e4] Ref **[23]**
Theoritical: [t1] Ref **[20]**

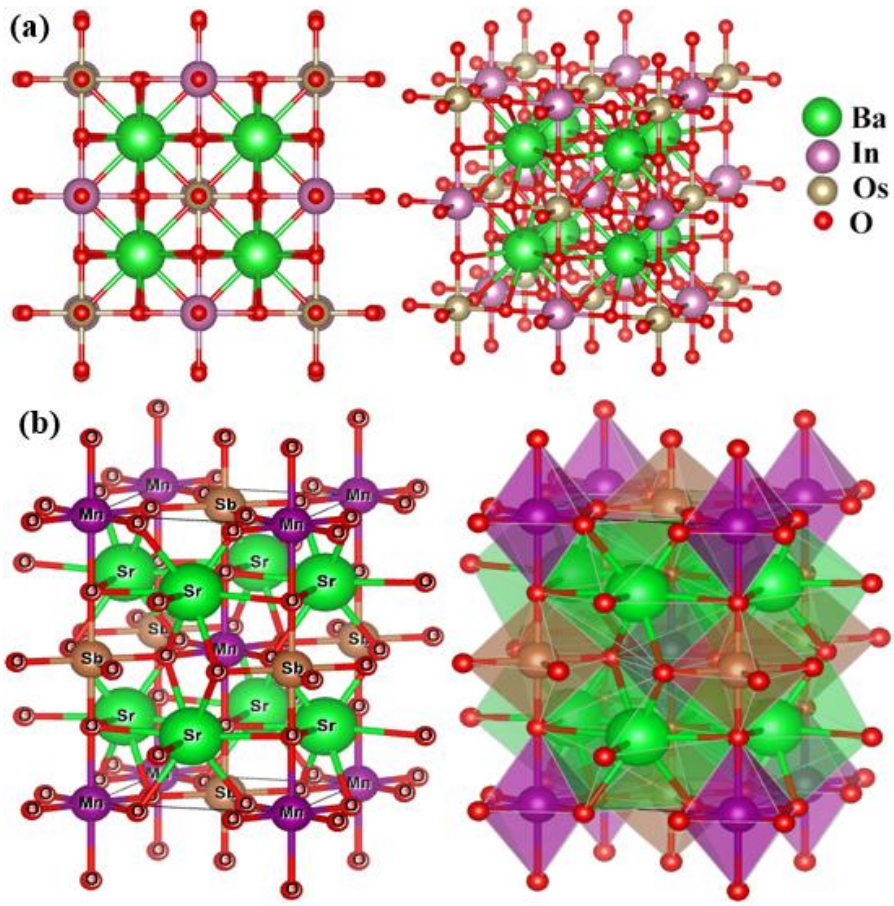

Figure III.6. Crystal structures of (a) Cubic Ba_2InOsO_6; (b) Tetragonal Sr_2MnSbO_6

III.4.1.3 Double Perovskite (A_2BX_6)

In this section, we present a comprehensive analysis of the structural evolution of the cubic double perovskite compound Rb_2PtBr_6 under partial substitution of the B-site cation Pt^{4+} by Pd^{4+}. The Pd concentration was varied systematically from x = 0.0 to x = 1.0 in steps of 0.25, leading to five distinct compositions: Rb_2PtBr_6, $Rb_2Pt_{0.75}Pd_{0.25}Br_6$, $Rb_2Pt_{0.5}Pd_{0.5}Br_6$, $Rb_2Pt_{0.25}Pd_{0.75}Br_6$, and Rb_2PdBr_6. To initially assess the geometric stability of the resulting compositions, we calculated the Goldschmidt tolerance factor (T_G), the values employed in our calculations were adopted from Shannon's effective ionic radii, R_{Rb} = 1.52 Å, R_{Pt} = 0.625 Å, R_{Pd} = 0.615 Å, and R_{Br} = 1.96 Å. The computed tolerance factors for all compositions are listed in **Table III.3**. The values range narrowly from 0.951 to 0.955 across the alloying series, remaining within the accepted stability window for cubic perovskites ($0.9 \leq T_G \leq 1.0$). This strongly suggests that all $Rb_2Pt_{1-x}Pd_xBr_6$ compounds are structurally stable and are likely to retain cubic symmetry. All five compositions were modeled in the ideal cubic double perovskite structure, characterized by the space group $Fm\bar{3}m$ (No. 225). The atomic arrangement follows standard Wyckoff positions: the B-site cation (Pt^{4+}/Pd^{4+}) resides at 4a (0, 0, 0), Rb^+ occupies the 8c (¼, ¼, ¼) site, and Br^- anions are positioned at 24e (½, 0, u), where u is the internal anion coordinate refined during structural relaxation. In the DFT study of alloying Rb_2PtBr_6 with Pd at concentrations of 0.25, 0.5, 0.75, and 1, it was observed that although the structure did not naturally maintain its cubic form, the cubic structure was retained for computational consistency. This decision was based on the close similarity in the ionic radii of Pt (0.137 nm) and Pd (0.137 nm), which would typically suggest that a cubic lattice could remain stable. Additionally, the Goldschmidt tolerance factor was calculated, remaining close to unity across the alloying concentrations. This factor indicates that the cubic structure should be energetically favorable, as the lattice would experience minimal distortion due to the similar ionic radii of Pt and Pd. Although the system did not naturally stabilize in a cubic phase in the DFT calculations, retaining the cubic structure was considered reasonable, given that the Goldschmidt factor and the close ionic radii indicated minimal disruption to the crystal lattice. This behavior is consistent with the structural stability observed in other compounds, such as $MAPbI_{3-x}Br_x$ and $CsPbI_{3-x}Br_x$, where the cubic structure remains stable at lower concentrations due to the ionic compatibility between the elements involved. For example, in the case of $MAPbI_{3-x}Br_x$ ($x < 0.5$), the cubic structure remains stable, and the same trend is observed in $CsPbI_{3-x}Br_x$, where $x < 0.5$ also results in the retention of the cubic phase **[24-26]**.

In this section, we present a comprehensive analysis of the structural evolution of the cubic double perovskite compound Rb_2PtBr_6 under partial substitution of the B-site cation Pt^{4+} by Pd^{4+}. The Pd concentration was varied systematically from x = 0.0 to x = 1.0 in steps of 0.25, leading to five distinct compositions: Rb_2PtBr_6, $Rb_2Pt_{0.75}Pd_{0.25}Br_6$, $Rb_2Pt_{0.5}Pd_{0.5}Br_6$, $Rb_2Pt_{0.25}Pd_{0.75}Br_6$, and Rb_2PdBr_6. To initially assess the geometric stability of the resulting compositions, we calculated the Goldschmidt tolerance factor (T_G), the values employed in our calculations were adopted from Shannon's effective ionic radii, R_{Rb}=1.52 Å, R_{Pt}=0.625 Å, R_{Pd}=0.615 Å, and R_{Br}=1.96 Å. The computed tolerance factors for all compositions are listed in **Table III.3**. The values range narrowly from 0.951 to 0.955 across the doping series, remaining within the accepted stability window for cubic perovskites ($0.9 \leq T_G \leq 1.0$). This strongly suggests that all $Rb_2Pt_{1-x}Pd_xBr_6$ compounds are structurally stable and are likely to retain the cubic symmetry. All five compositions were modeled in the ideal cubic double perovskite structure, characterized by the space group $Fm\bar{3}m$ (No. 225). The atomic arrangement follows standard Wyckoff positions: the B-site cation (Pt^{4+}/Pd^{4+}) resides at 4a (0, 0, 0), Rb^+ occupies the 8c (¼, ¼, ¼) site, and Br^- anions are positioned at 24e (½, 0, u), where u is the internal anion coordinate refined during structural relaxation. To accurately represent partial Pd substitution at the B-site, 2×2×2 supercells were constructed for the mixed compositions (x = 0.25, 0.5, 0.75), allowing for statistical modeling of alloy disorder. The structural models for each composition are depicted in Figures III.7(a-e). Based on prior experimental and theoretical studies, both Pt^{4+}- and Pd^{4+}-based halide perovskites are known to favor non-magnetic (NM) ground states. Hence, all structural optimizations in our study were conducted within the NM configuration. The optimized parameters are summarized in **Table III.3**. A clear monotonic trend is observed in the lattice parameter as a function of Pd concentration. The lattice constant decreases progressively from 10.86 Å for pristine Rb_2PtBr_6 (x = 0.0) to 10.62 Å for fully substituted Rb_2PdBr_6 (x = 1.0). This contraction of the lattice is attributed to the slightly smaller ionic radius of Pd^{4+} (0.615 Å) compared to Pt^{4+} (0.625 Å), which leads to reduced B-Br bond lengths and thus overall lattice shrinkage. This phenomenon of lattice compression upon isovalent substitution has been previously observed in similar alloying studies, such as $Cs_2Ag_{1-x}Na_xInCl_6$ **[27]**, $Cs_2Bi_{1-x}In_xO_6$ **[28]**. Importantly, our computed lattice parameters at the end compositions (x = 0.0 and x = 1.0) show strong agreement with previous theoretical and experimental reports. For Rb_2PtBr_6, our calculated value of 10.86 Å closely matches both the theoretical value of 10.72 Å **[29]** and the experimental result of 10.86 Å **[30]**. Similarly, for Rb_2PdBr_6, we obtained a lattice constant of 10.62 Å. This value agrees well with the theoretical prediction of 10.70 Å

[29] and is reasonably close to the experimental measurement of 10.02 Å [30], considering possible deviations due to synthesis conditions. These comparisons confirm the reliability and accuracy of our structural modeling and computational framework.

Table III.3: Optimized Structural Parameters, Ground-State Energies, Formation Energies, and Goldschmidt Tolerance Factor for $Rb_2Pt_{1-x}Pd_xBr_6$

Materials	a (Å)			B′	E_{min} (Ry)	E_{coh} (Ry)	Δ_{Hf} (Ry)	T_G
	This work	Other Works	Exp					
Rb_2PtBr_6	10.86	10.72[t1]	10.86[e1]	4.96	-80099.762807	-3.88	-1.37	0.951
$Rb_2Pt_{0.75}Pd_{0.25}Br_6$	10.80	//	//	5.14	-73386.171707	-4.02	-1.33	0.952
$Rb_2Pt_{0.5}Pd_{0.5}Br_6$	10.72	//	//	5.33	-66700.077582	-4.55	-1.28	0.953
$Rb_2Pt_{0.25}Pd_{0.75}Br_6$	10.67	//	//	5.10	-60091.235481	-4.16	-1.25	0.954
Rb_2PdBr_6	10.62	10.7[t1]	10.02[e1]	4.69	-53300.388914	-3.56	-1.22	0.955

Experimental: [e1] Ref [30]
Theoritical: [t1] Ref [29]

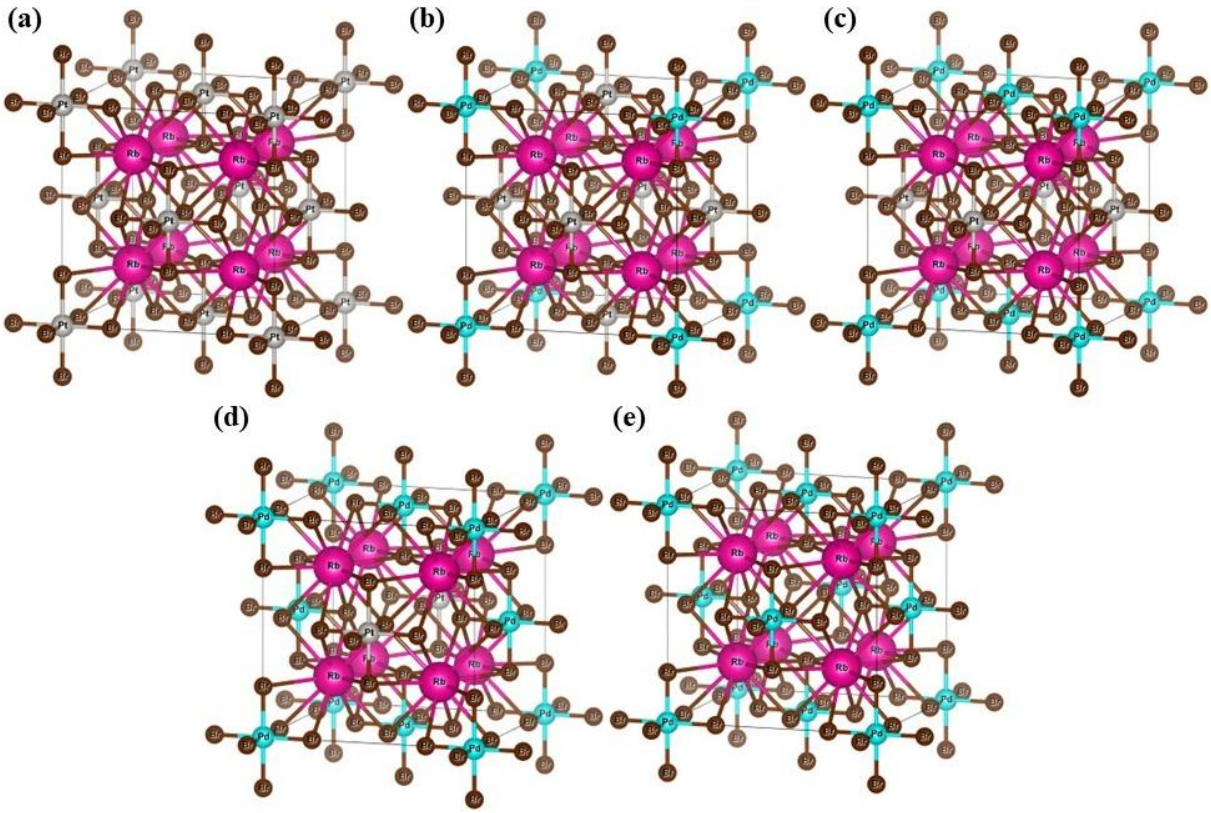

Figure III.7. Crystal structures of $Rb_2Pt_{1-x}Pd_xbr6$ (a) x = 0.0, (b) x = 0.25, (c) x = 0.5, (d) x = 0.75, and (e) x = 1.0.

III.4.1.4 Antiperovskite A_3BX

We began our investigation of the A_3SbAs (A = Ba, Sr, and Ca) antiperovskite compounds by calculating the Goldschmidt tolerance factor based on the optimized bond lengths. All the calculated values were found to be close to 1, specifically between 0.99 and 1.00. This result suggests that the compounds are structurally stable and likely to adopt a cubic crystal structure, as tolerance factors in this range are generally indicative of a stable cubic phase. These compounds crystallize in the cubic symmetry with space group $Pm\bar{3}m$ (221). A detailed analysis of their crystallographic structure shows that the A-site cations (Ba, Sr, and Ca) occupy the 3c Wyckoff positions at coordinates (0, 1/2, 1/2), while the Sb atoms are located at 1a (0, 0, 0), and the As atoms occupy the 1b (1/2, 1/2, 1/2) sites.

The ideal cubic structure formed by this arrangement is shown in **Figure III.8**. To determine the ground-state magnetic configuration, we performed structural optimization for each compound in three magnetic states, nonmagnetic (NM), ferromagnetic (FM), and antiferromagnetic (AFM). According to the total energy results summarized in **Table III.4**, the NM configuration exhibited the lowest ground-state energy in all cases, indicating that this is the most stable magnetic state for these materials. Analyzing the optimized lattice constants, we observed a clear trend: Ba_3SbAs has the largest lattice parameter at 6.18 Å, Sr_3SbAs follows with 5.84 Å, and Ca_3SbAs has the smallest value at 5.49 Å. This decrease in lattice constant from Ba to Ca is consistent with the decreasing ionic radii of the A-site cations. As the size of the alkaline-earth metal decreases, the overall unit cell volume contracts. This behavior is not unique to this system; similar trends have been reported in other antiperovskite materials such as Mg_3XN and Ca_3XN, where X is As, Sb, or Bi **[31,32]**.

Table III.4: Lattice Parameters, Bulk Moduli, and Energetic Properties of A_3SbAs Antiperovskite in Different Magnetic States

Materials	State	a (Å)	B′	E_{min} (Ry)	E_{coh} (Ry)	Δ_{Hf} (Ry)
Ba_3SbAs	**NM**	**6.18**	**4.21**	**-66326.024893**	-1.361	-0.457
	FM	6.18	4.25	-66326.022889		
	AFM	6.18	4.09	-66326.019766		
Sr_3SbAs	**NM**	**5.84**	**4.36**	**-36568.875233**	-1.376	-0.924
	FM	5.84	4.79	-36568.874251		
	AFM	5.84	3.91	-36568.873792		
Ca_3SbAs	**NM**	**5.49**	**4.28**	**-21572.183863**	-1.517	-0.951
	FM	5.49	4.34	-21572.182358		
	AFM	5.49	3.97	-21572.181851		

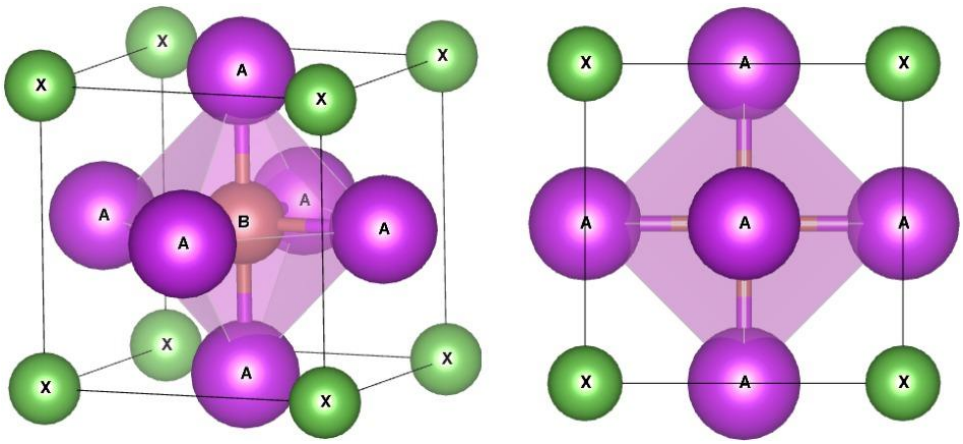

Figure III.8. Crystal structures of A_3BX Antiperovskite

III.4.1.5 Derivative Antiperovskite A_3BX_3

In this study, we focus on a new class of materials structurally derived from the antiperovskite lattice, which are increasingly being categorized as perovskite-inspired compounds due to targeted structural modifications that enhance their dynamic stability. These modifications, particularly the redistribution of atomic positions within the crystal, result in stable configurations that preserve essential features of the traditional antiperovskite framework. To assess the structural stability of these materials, we first applied the Goldschmidt tolerance factor. For our A_3BiI_3 compounds (A = Ba, Sr, Ca), the calculated tolerance factor values lie within the range of 0.9 to 1.0, indicating a high likelihood of forming stable cubic structures. This is consistent with the structural integrity typically observed in ideal perovskite and antiperovskite systems **[33]**. **Figure III.9** schematically illustrates the atomic rearrangement strategy employed to derive these new compounds from the parent antiperovskite structure. Starting from the conventional cubic antiperovskite configuration with the general formula A_3BX_3 (space group N°221), the B-site cation occupies the center of the cube Wyckoff position 1b, while the X-site anions and A-site cations occupy the 1a and 3c positions, respectively. To engineer derivative structures, the X-site anion is shifted from the 1a site to the 3d positions. This redistribution splits the original atomic site into three symmetry-related positions: (0.5, 0, 0), (0, 0.5, 0), and (0, 0, 0.5), which are now occupied by X atoms (such as halides). To maintain charge neutrality, the valence state of the A-site cations is adjusted accordingly. This leads to a new family of antiperovskite derivatives of the form A_3BX_3, where X represents halide ions (e.g., F, Cl, Br, I), B is a pnictogen such as Bi or Sb, and A is a divalent alkaline-earth metal. Following this structural design, we performed a full optimization of three magnetic configurations, nonmagnetic (NM), ferromagnetic (FM), and antiferromagnetic (AFM) for each

compound. The results, summarized in **Table III.5**, clearly based on the fact that the total energy in the NM configuration is consistently lower than in either the FM or AFM states indicate that all three compounds are energetically most stable in the nonmagnetic phase. A closer examination of the optimized lattice parameters reveals a systematic trend correlated with the size of the A-site cation. Ba_3BiI_3 exhibits the largest lattice constant of approximately 7.09 Å, followed by Sr_3BiI_3 at 6.69 Å, and Ca_3BiI_3 with the smallest value at 6.38 Å. This trend reflects the expected contraction in lattice volume as the ionic radius of the A-site cation decreases from Ba to Ca. The corresponding bulk modulus values further confirm this behavior, as the lattice becomes more compact, the material's resistance to uniform compression increases slightly, particularly evident when comparing the values across the series. These structural trends are consistent with previous reports on related compounds such as A_3SbAs and halide-based analogs like Sr3PnCl3 (Pn= P, As, Sb), further validating the observed lattice contraction and mechanical stiffening upon substitution of smaller A-site cations **[34]**.

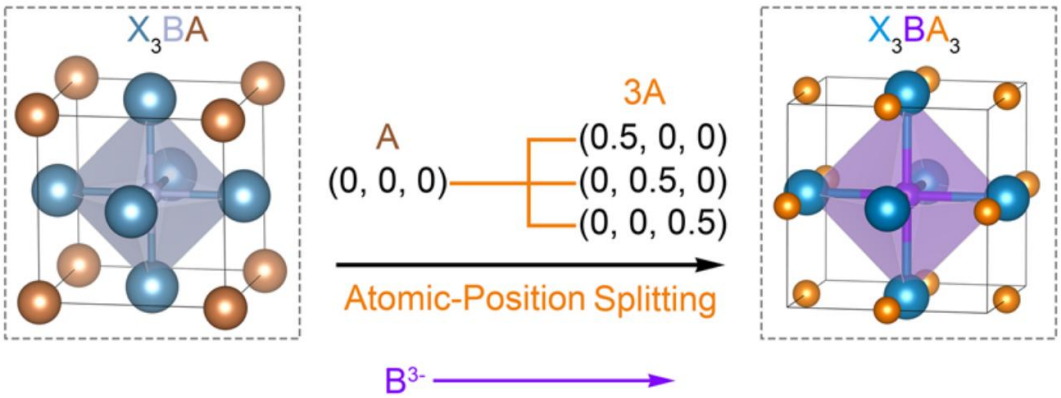

Figure III.9. Crystal structures of X_3BA Antiperovskite compared to Derivative Antiperovskite X_3BA_3 structure

Table III.5: Lattice Parameters, Bulk Moduli, and Energetic Properties of A_3BiI_3 Antiperovskite in Different Magnetic States

Materials	State	a (Å)	B'	Emin (Ry)	E_{coh} (Ry)	ΔH_f (Ry)
Ba_3BiI_3	**NM**	**7.09**	**4.90**	**-134714.507290**	-1.68	-2.48
	FM	7.09	4.77	-134714.506883		
	AFM	7.10	4.65	-134714.506297		
Sr_3BiI_3	**NM**	**6.69**	**4.82**	**-89960.389980**	-1.7	-2.45
	FM	6.69	4.88	-89960.383553		
	AFM	6.69	4.92	-89960.378658		
Ca_3BiI_3	**NM**	**6.38**	**3.88**	**-104957.232253**	-1.6	-2.25
	FM	6.38	3.79	-104957.230277		
	AFM	6.38	3.75	-104957.229988		

III.4.2 Dynamical stability

The formation energy and cohesive energy for the various compounds have been calculated using the equations outlined in Equations III.1 and III.2, respectively. The results for each compound are presented in their respective structural tables, spanning from **Table III.1** to **Table III.5**. Upon reviewing the data, it is observed that all compounds exhibit negative formation and cohesive energies. A negative formation energy indicates that the formation of these compounds from their constituent elements is thermodynamically favorable, meaning that the reaction is exothermic and will proceed spontaneously under standard conditions. This suggests that the compounds are stable relative to their individual components **[5]**. Similarly, a negative cohesive energy indicates a strong binding between the atoms or molecules within the compound, implying that the material is tightly bound and stable. This further confirms the robustness and stability of the compounds under normal conditions **[6]**.

III.4.3 Electronic properties
III.4.3.1 Perovskite ABX3

In this section, we analyze the electronic characteristics of the cubic halide perovskites $ASiCl_3$ (A = Li, Rb, Cs), focusing on their band structure and density of states (DOS). The electronic band diagrams, displayed along the high-symmetry path R-Γ-X-M-Γ, are shown in **Figure III.10(a-c)**. From these plots, it is evident that all three compounds exhibit semiconducting behavior, as indicated by the presence of an energy band gap. The valence band maximum (VBM) and the conduction band minimum (CBM) are both located at the R-point, confirming that the materials possess a direct band gap. Using the GGA-PBE approximation, the calculated band gap energies for $LiSiCl_3$, $RbSiCl_3$, and $CsSiCl_3$ are approximately 0.243 eV, 0.205 eV, and 0.358 eV, respectively. further refinements were carried out using the TB-mBJ potential. This approach yielded corrected band gaps of 0.287 eV, 0.378 eV, and 0.546 eV for $LiSiCl_3$, $RbSiCl_3$, and $CsSiCl_3$, respectively, marking a significant enhancement over the GGA values. The variation in band gap across the three compounds is primarily influenced by the ionic radius of the A-site cations, which follows the order: $Li^+ < Rb^+ < Cs^+$. The increase in ionic radius alters the position of the CBM, leading to a narrowing of the band gap. Consequently, this trend shifts the optical absorption edge from the visible to the infrared region, potentially improving electron transport and enhancing the compounds performance in optoelectronic applications.

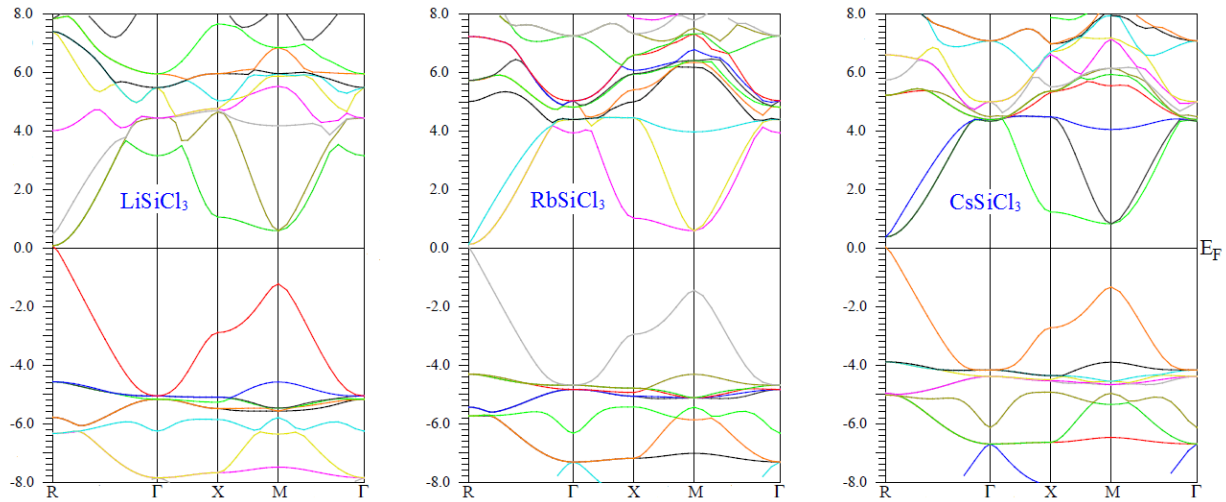

Figure III.10. Band structure diagrams for $ASiCl_3$ perovskite using the TB-mBJ approximation

The total and partial density of states (TDOS and PDOS), computed using the TB-mBJ functional, are presented in **Figure III.11(a-c)** over an energy range spanning from –8 eV to +8 eV. The valence band region lies below (E_F), while the conduction band extends above it. The clear gap observed around (E_F) in all three compounds reaffirms their semiconducting nature. The PDOS analysis reveals that in the valence band, the dominant contributions originate from the Cl-p orbitals, while in the conduction band, the leading contributions differ among the compounds: Si-p states for $LiSiCl_3$, Rb-d states for $RbSiCl_3$, and Cs-d states for $CsSiCl_3$. Near the Fermi level, the Cl atoms continue to contribute most significantly, whereas the Si atoms play a lesser role, and the A-site cations (Li, Rb, Cs) contribute minimally. Between approximately 0.5 eV and 4.5 eV in the conduction band, there is a noticeable hybridization between Cl-p and Si-p orbitals, which suggests the presence of covalent character in the chemical bonding. Additionally, since the Fermi levels for all three compounds are positioned closer to the VBM than the CBM, these materials exhibit a likely p-type semiconducting behavior.

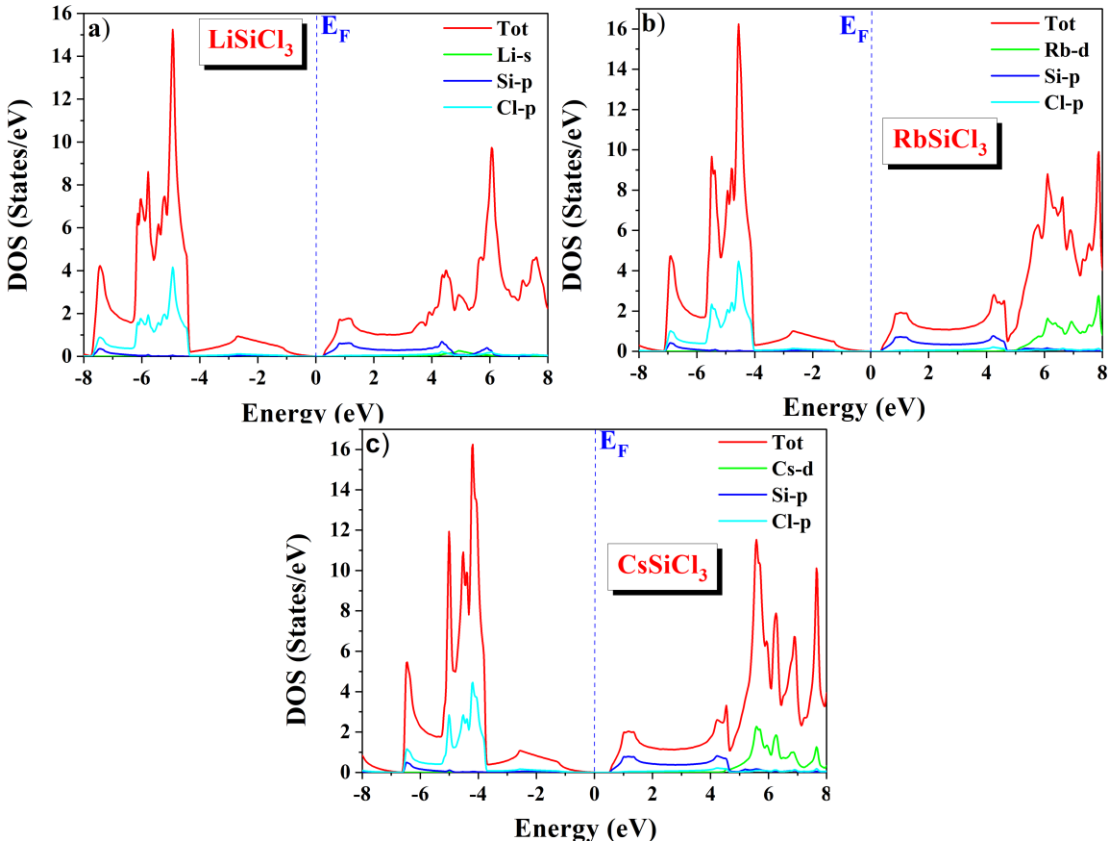

Figure III.11. DOS & PDOS diagrams for $ASiCl_3$ perovskite using the TB-mBJ approximation

The electronic band structures of $CsTaS_3$ and $CsTaSe_3$, shown in **Figure III.12(d-e)**, provide a clear depiction of their semiconducting character. Both compounds exhibit indirect band gaps, with the valence band maximum (VBM) located at the Γ point and the conduction band minimum (CBM) positioned along the Δ path, confirming the Γ–Δ transition typical of indirect semiconductors. For $CsTaS_3$, the band gap is found to be moderately wide, with the corrected value reaching 0.90 eV, indicating that this material could be suitable for certain electronic or optoelectronic applications, albeit with limited efficiency in direct optical transitions due to its indirect nature. In contrast, $CsTaSe_3$ exhibits a noticeably narrower band gap of 0.41 eV, which suggests a relatively higher intrinsic carrier concentration and enhanced electrical conductivity **[35]**. However, the small gap also implies increased sensitivity to thermal excitations and potentially reduced performance in optoelectronic applications where higher excitation thresholds are desirable. The reduction in the band gap from $CsTaS_3$ to $CsTaSe_3$ reflects the substitution of sulfur with the heavier and more polarizable selenium atom, which generally leads to a downshift in the conduction band and thus a narrowing of the gap. This trend is consistent with general chemical behavior in chalcogenide perovskites.

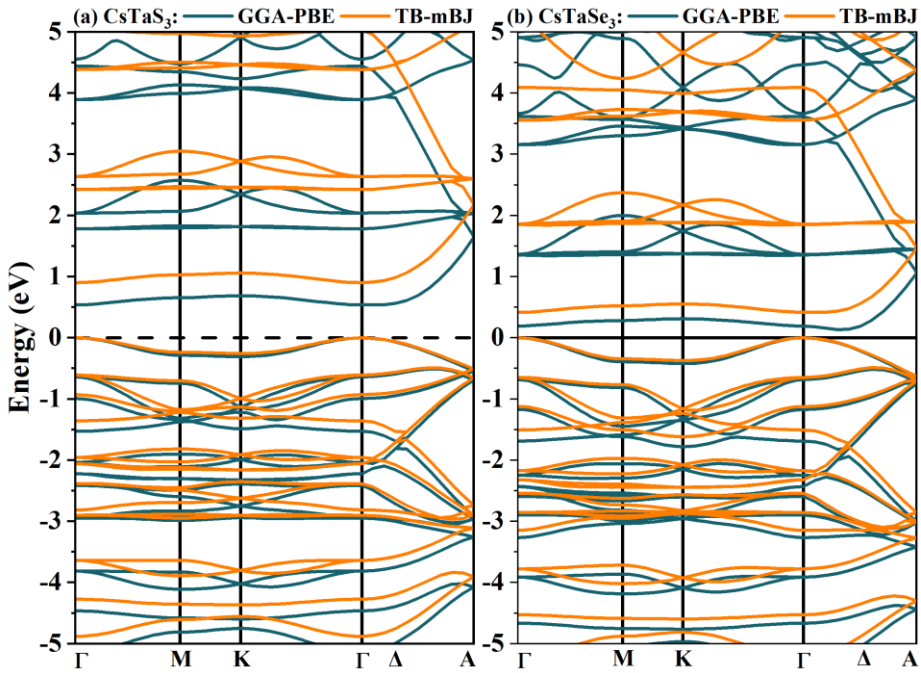

Figure III.12. Band structure diagrams for $CsTaX_3$ perovskite using the GGA-PBE and TB-mBJ approximations

The density of states (DOS) profiles of $CsTaS_3$ and $CsTaSe_3$, is presented in Figures III.13(a-b). The total and partial DOS highlight the dominant role of Ta 5d orbitals in both the valence and conduction bands, particularly near the Fermi level. In the valence band region, especially from approximately -3 eV to 0 eV, the Ta 5d states are prominent, indicating their significant involvement in the electronic states just below the Fermi level. Deeper in the valence band, between -6 eV and -3 eV, a strong hybridization between Ta 5d and chalcogen p orbitals (S 3p or Se 4p) is observed. This hybridization suggests the formation of covalent bonds between the Ta and X atoms, which is essential for structural stability and influences the material's electronic transport properties. The Cs 5s states, in contrast, exhibit minimal interaction with the valence or conduction bands, reflecting their core-like, electrostatic role rather than a direct contribution to the electronic conduction mechanism. Above the Fermi level, the conduction band is once again dominated by Ta 5d states, with contributions from chalcogen p states extending into this region as well. Notably, in $CsTaSe_3$, the Se 4p orbitals show a broader overlap with the Ta 5d states in the conduction band compared to the S 3p orbitals in $CsTaS_3$. This broader distribution reflects a stronger Ta-Se interaction, which correlates with the smaller band gap observed in $CsTaSe_3$ and supports a higher density of available states for conduction near the Fermi level.

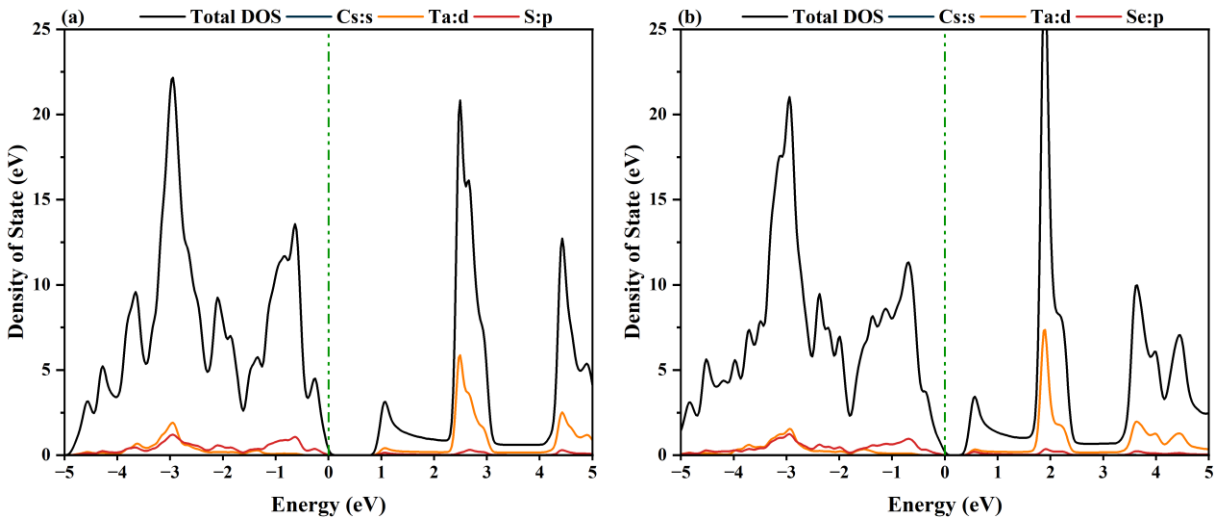

Figure III.13. DOS & PDOS diagrams for $CsTaX_3$ perovskite using the TB-mBJ approximation

III.4.3.2 Double perovskite $A_2BB'X_6$

Moving to the double perovskite family, we investigated the electronic structure of Ba_2InOsO_6 by performing spin-polarized band structure calculations using various exchange-correlation approximations. The results, illustrated in **Figure 14(a-f)**. Under the standard GGA-PBE approximation, the spin-up channel exhibits semiconducting behavior with a direct band gap of 0.61 eV at the X-point. In contrast, the spin-down channel shows an indirect band gap of 1.95 eV along the Γ-W direction, reflecting a semiconducting nature in both spin channels. These results represent the system without corrections for strong electron-electron interactions or relativistic effects. Upon incorporating the Hubbard U correction through the GGA+U method, Ba_2InOsO_6 transitions to a half-metallic state. In this case, the spin-up channel becomes metallic, while the spin-down channel remains semiconducting, with an enhanced indirect band gap of 2.28 eV. This enhancement arises from the improved treatment of on-site Coulomb interactions, particularly affecting the 5d orbitals of the Os atoms, which are inadequately described by GGA alone. Application of the TB-mBJ potential combined with Hubbard U (mBJ+U) further amplifies the band gap in the spin-down channel to 3.62 eV, representing a 58.8% increase compared to GGA+U. The spin-up channel remains metallic. While the spin-orbit coupling (SOC) effect was also considered in our calculations. SOC plays a crucial role in systems containing heavy atoms like Os, where relativistic effects significantly influence the electronic structure. In Ba_2InOsO_6, the inclusion of SOC leads to the equalization of band gaps in both spin channels, with the spin-down band gap reduced to 2.27 eV. This reduction is attributed to the mixing of spin states, which weakens the localization effects introduced by the U term and the TB-mBJ potential.

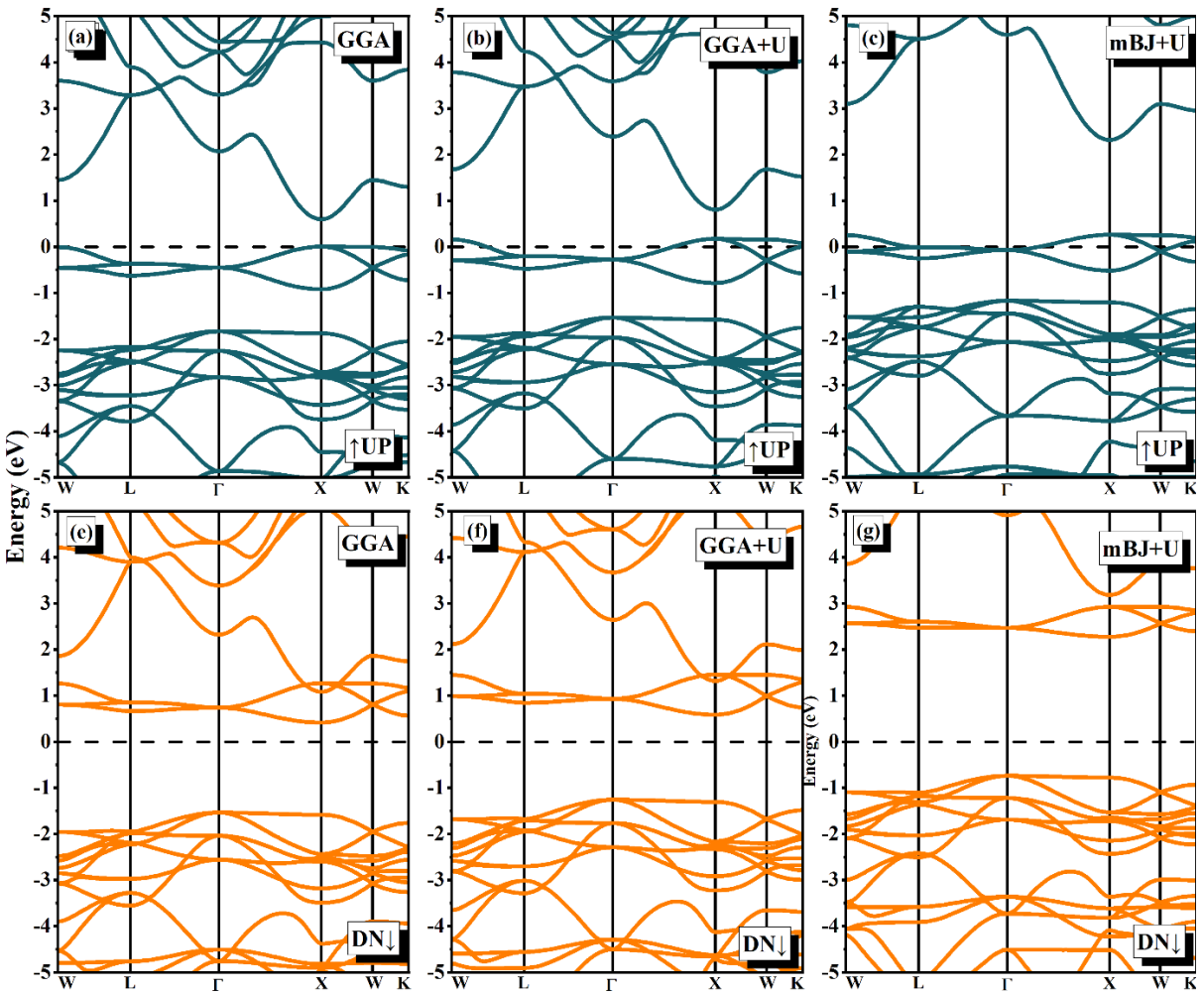

Figure III.14. Band structure diagrams for Ba2InOsO6 double perovskite using the GGA, GGA+U and TB-mBJ+U approximations

The TDOS and PDOS for Ba_2InOsO_6 are presented in **Figure III.15(a-b)** and **Figure III.16**, calculated using three exchange-correlation approximations: GGA, GGA+U, and mBJ+U. Within the energy range of -6 eV to +6 eV relative to the Fermi level (E_F), the PDOS reveals a series of distinct peaks that clarify the nature of the electronic states. The valence band, primarily localized between -6 eV and -2 eV, is dominated by oxygen 2p states, with minor hybridization from Os 5d states. This hybridization reflects covalent interactions between Os and O atoms, which are essential for the material's structural stability. The conduction band, beginning just above the Fermi level, features significant contributions from Os 5d orbitals, along with moderate participation from Ba 4d and In 5p states. Under the GGA approximation, Ba_2InOsO_6 displays semiconducting behavior in both spin channels, with noticeable asymmetry between them. However, upon introducing the Hubbard U correction (GGA+U), the spin-up channel becomes metallic while the spin-down channel retains a clear band gap, confirming the emergence of half-metallicity. This behavior intensifies under the mBJ+U approximation, where

the spin-up metallicity is preserved and the spin-down band gap is further widened. In all cases, the dominant states at the Fermi level in the spin-up channel arise from Os 5d orbitals, indicating that these orbitals govern the half-metallic nature of the compound. The strong spin polarization observed in the DOS, driven by exchange splitting of the Os 5d orbitals, aligns well with the band structure findings and explains the calculated magnetic moment of the material. This half-metallicity, along with full spin polarization at the Fermi level, suggests that Ba_2InOsO_6 is a promising candidate for spintronic applications.

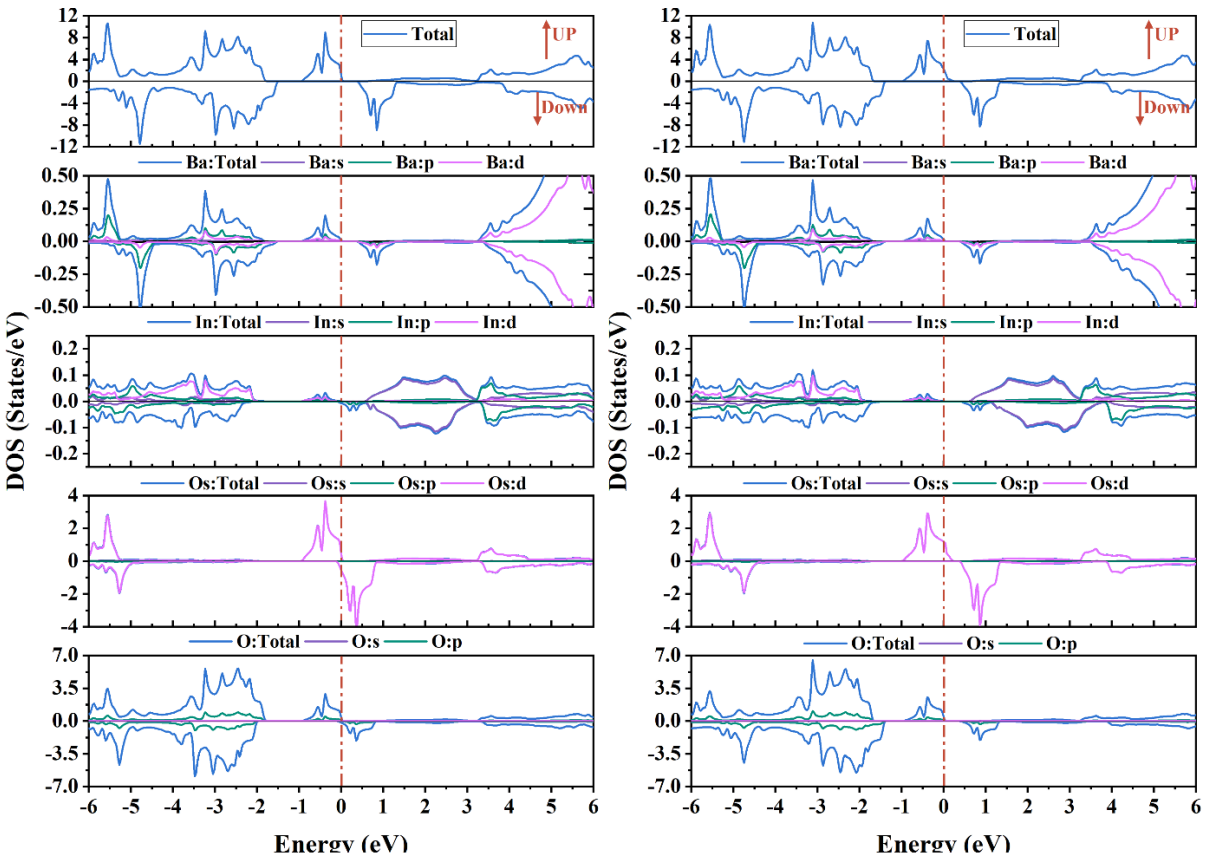

Figure III. 15. DOS & PDOS diagrams for Ba_2InOsO_6 perovskite using GGA and GGA+U approximations

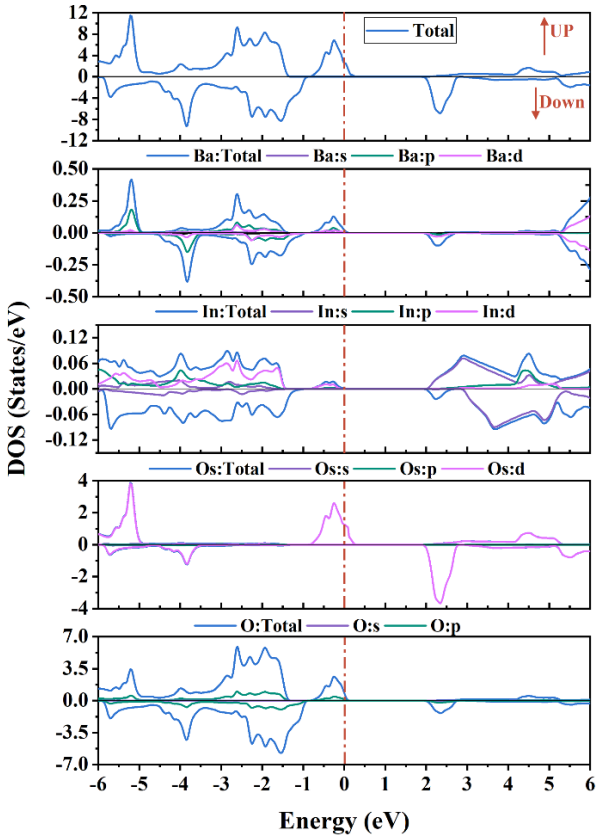

Figure III. 16. DOS & PDOS diagrams for Ba_2InOsO_6 perovskite using mBJ+U approximation

Now that we have discussed the cubic Ba_2InOsO_6 in earlier sections, we shift our focus to the tetragonal Sr_2MnSbO_6, which reveals distinct yet complementary electronic and magnetic characteristics under the same theoretical framework. After confirming the stability of Sr_2MnSbO_6 in the ferromagnetic (FM) state, we proceeded to investigate the influence of the Hubbard parameter U on both the magnetic moment and the band gap. Due to the lack of experimental data for this specific compound, we systematically varied the U value to identify the most physically meaningful results. Based on the data shown in **Figure III.17**, a value of U = 4 eV yields the most favorable outcomes, especially in terms of magnetic moment enhancement. The band gap in the spin-down channel increases with increasing U, reflecting stronger electron correlation effects. Our choice of U = 4 eV is consistent with values used in other Mn-based double perovskites such as A_2FeReO_6 (A =Ba, Sr, Ca) and Sr_2MMoO_6 (M =Cr, Mn, Fe, Co) **[36]**, where U = 4 eV has been shown to reproduce essential magnetic and electronic features. Furthermore, Sosa-Correa et al. have also adopted this value in related studies, reinforcing the credibility of our selection **[20]**.

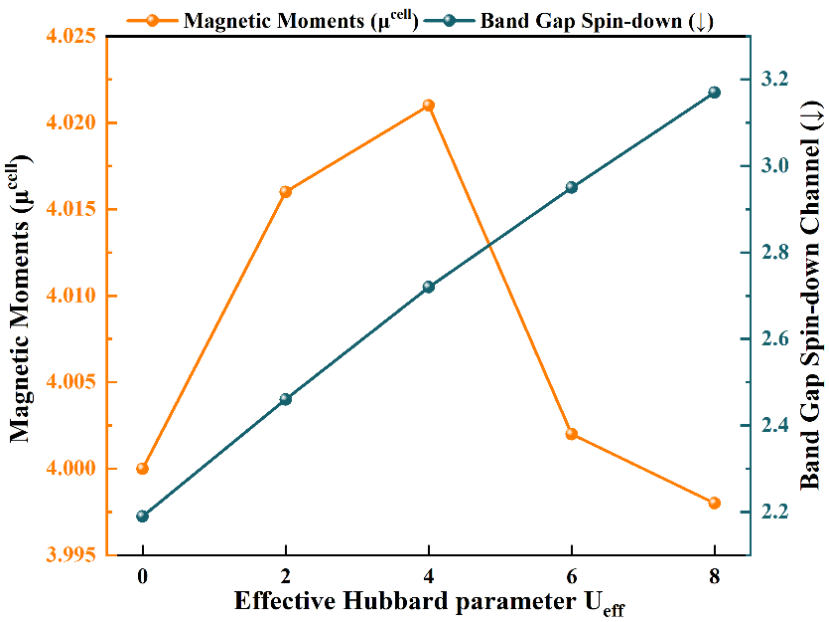

Figure III.17. Variation of Total Magnetic Moment and Band Gap with Respect to the U Value

We then examined the electronic structure of Sr_2MnSbO_6 in its tetragonal configuration using three exchange-correlation schemes: GGA, GGA+U, and mBJ+U. The band structure results are presented in **Figure III.18(a-f)**. For the spin-up channel, the compound behaves as a semiconductor with an indirect band gap of approximately 0.20 eV along the Γ-N direction under GGA. However, when the U correction is applied, this gap closes, and the system transitions to a metallic state. Notably, this metallic nature persists even with the use of the mBJ functional, suggesting that the spin-up channel is intrinsically metallic when electron correlation is considered. This shift highlights the crucial role of electronic correlations in shaping the band structure. In contrast, the spin-down channel retains an indirect semiconducting nature throughout all computational schemes. The band gap increases with the inclusion of U, rising from 2.19 eV (GGA) to 2.72 eV (GGA+U) and reaching 3.79 eV with mBJ+U. This trend confirms that the unoccupied Mn-3d states are pushed further into the conduction band due to stronger on-site Coulomb repulsion. Consequently, Sr_2MnSbO_6 demonstrates half-metallic behavior, with a metallic spin-up channel and a semiconducting spin-down channel. This half-metallicity leads to 100% spin polarization at the Fermi level, a highly desirable characteristic for spintronic applications.

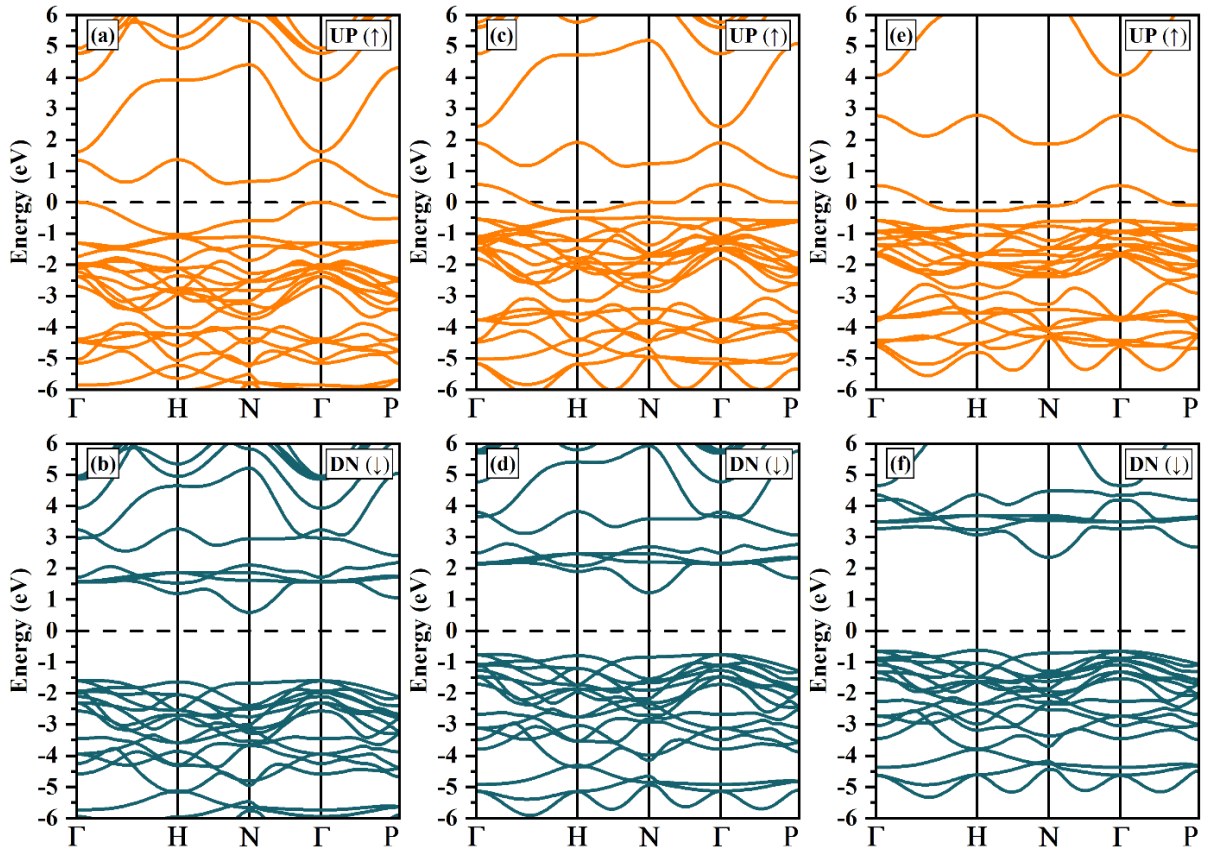

Figure III.18. Band structure diagrams for Sr_2MnSbO_6 double perovskite using the GGA, GGA+U and TB-mBJ+U approximations

The DOS and PDOS of Sr_2MnSbO_6 have been plotted in **Figure III.19(a-c)** under three different approximations: GGA, GGA+U, and mBJ+U, all these approximations show consistent contributions from similar atomic orbitals. In the valence band (VB), the oxygen atoms O1 and O2 play a crucial role through their 2p orbitals, which hybridize extensively with Mn 3d orbitals, especially the t_2g states. This strong Mn–O hybridization stabilizes the lower-energy region of the VB. Near the valence band maximum (VBM), the Mn 3d orbitals dominate the electronic states, while the Sb 5p orbitals contribute only weakly at deeper energies, and Sr orbitals have minimal influence near the Fermi level. In the conduction band (CB), Mn 3d eg orbitals are the main contributors at the conduction band minimum (CBM). Sb 5p orbitals become more prominent at higher energies, particularly under the mBJ+U approximation, indicating increasing hybridization with Mn states. Oxygen orbitals have a reduced role in the CB, mostly appearing at higher energies. When examining the spin channels, GGA results show that Sr_2MnSbO_6 behaves as a semiconductor in both spin-up and spin-down states, with a clear band gap. However, introducing the Hubbard U correction (GGA+U) causes the spin-up channel to become metallic as the Mn 3d states shift and cross the Fermi level, closing the band

gap. The spin-down channel remains semiconducting, maintaining its band gap. This metallic behavior in the spin-up channel is confirmed and refined in the mBJ+U approach, which better accounts for electron localization and band energies.

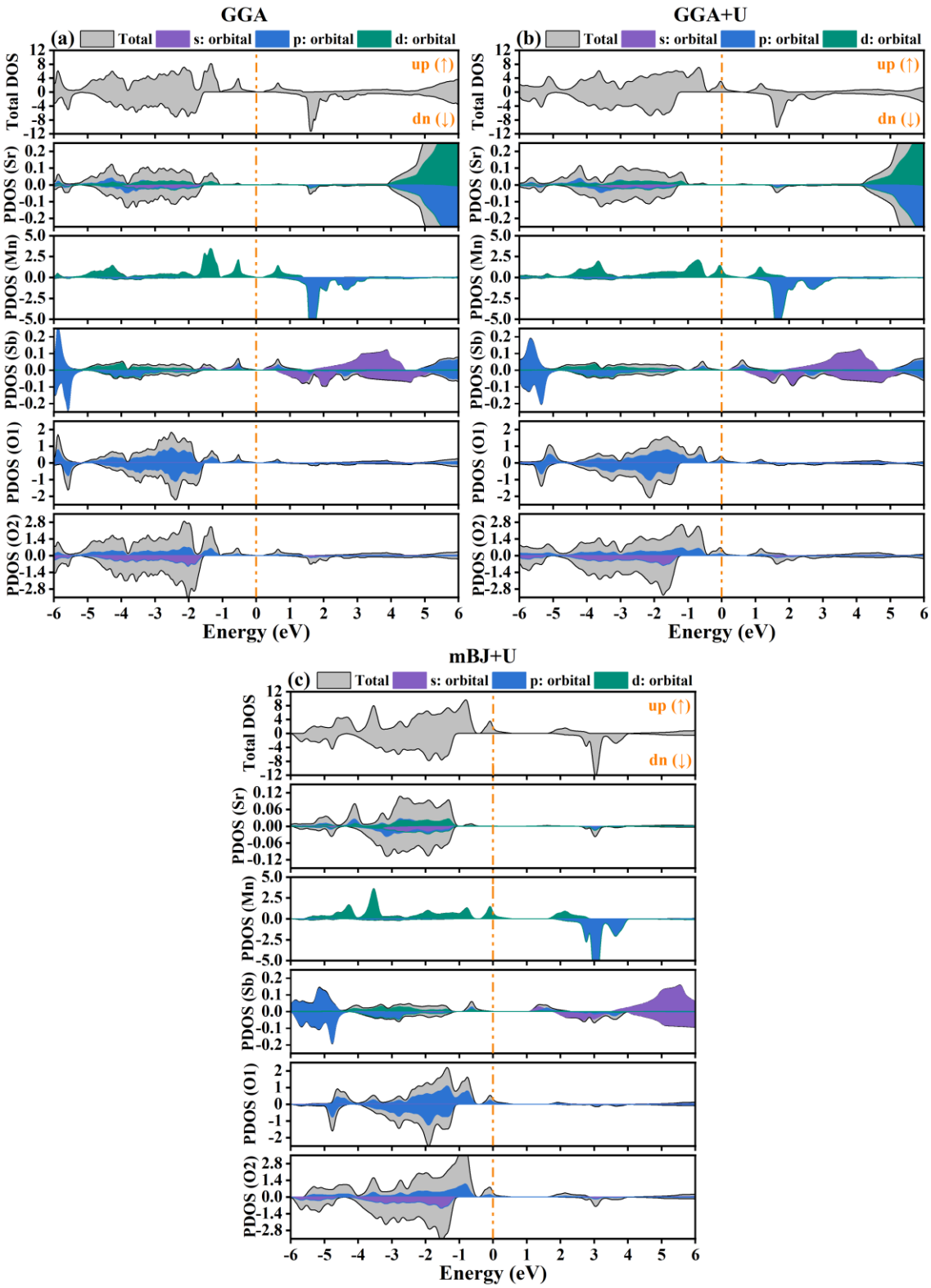

Figure III.19. DOS & PDOS diagrams for Sr_2MnSbO_6 perovskite using the different approximations

III.4.3.3 Double perovskite A_2BX_6

The band gap analysis of the $Rb_2Pt_{1-x}Pd_xBr_6$ (x = 0.0, 0.25, 0.5, 0.75, and 1.0) double perovskites reveals interesting insights into the evolution of electronic properties as a function of Pd substitution as plotted in **Figure III.20(a-e)** and **Figure III.21(a-e)**. For the parent compound Rb_2PtBr_6, the calculated band gap shows an indirect character with values of 1.34 eV (GGA-PBE) and 2.18 eV (TB-mBJ). These results are in good agreement with previous studies, confirming the reliability of the computational methods used. The indirect nature of the band gap, where the valence band maximum (VBM) is located at the R point and the conduction band minimum (CBM) is at the Γ point, suggests that the material may have relatively slower charge carrier dynamics compared to direct band gap materials. As Pd is progressively incorporated into the lattice, the band gap shows a marked reduction. At x = 0.25 ($Rb_2Pt_{0.75}Pd_{0.25}Br_6$), the band gap decreases to 0.99 eV (GGA-PBE) and 1.69 eV (TB-mBJ), with a notable shift from an indirect to a direct band gap. This transition is particularly significant for optoelectronic applications, as direct band gaps enable more efficient optical absorption and emission, making this composition of interest for devices such as light-emitting diodes and photovoltaic absorbers. Further substitution at x = 0.50 ($Rb_2Pt_{0.5}Pd_{0.5}Br_6$) leads to a further narrowing of the band gap, down to 0.80 eV (GGA-PBE) and 1.52 eV (TB-mBJ), with a return to an indirect band gap. This reversion highlights the complex interplay between Pd and Pt in tuning the electronic properties, particularly with respect to the spatial separation between the VBM and CBM. For compositions with higher Pd content, such as x = 0.75 ($Rb_2Pt_{0.25}Pd_{0.75}Br_6$), the band gap continues to narrow, showing values of 0.72 eV (GGA-PBE) and 1.44 eV (TB-mBJ), while maintaining a direct band gap at the Γ point. This indicates a non-monotonic behavior in the band gap as a function of Pd concentration, with the system displaying alternating direct and indirect band gap characteristics. Finally, for the fully Pd-substituted compound Rb_2PdBr_6, the band gap is reduced to 0.50 eV (GGA-PBE) and 1.20 eV (TB-mBJ), maintaining an indirect nature, consistent with previous theoretical studies.

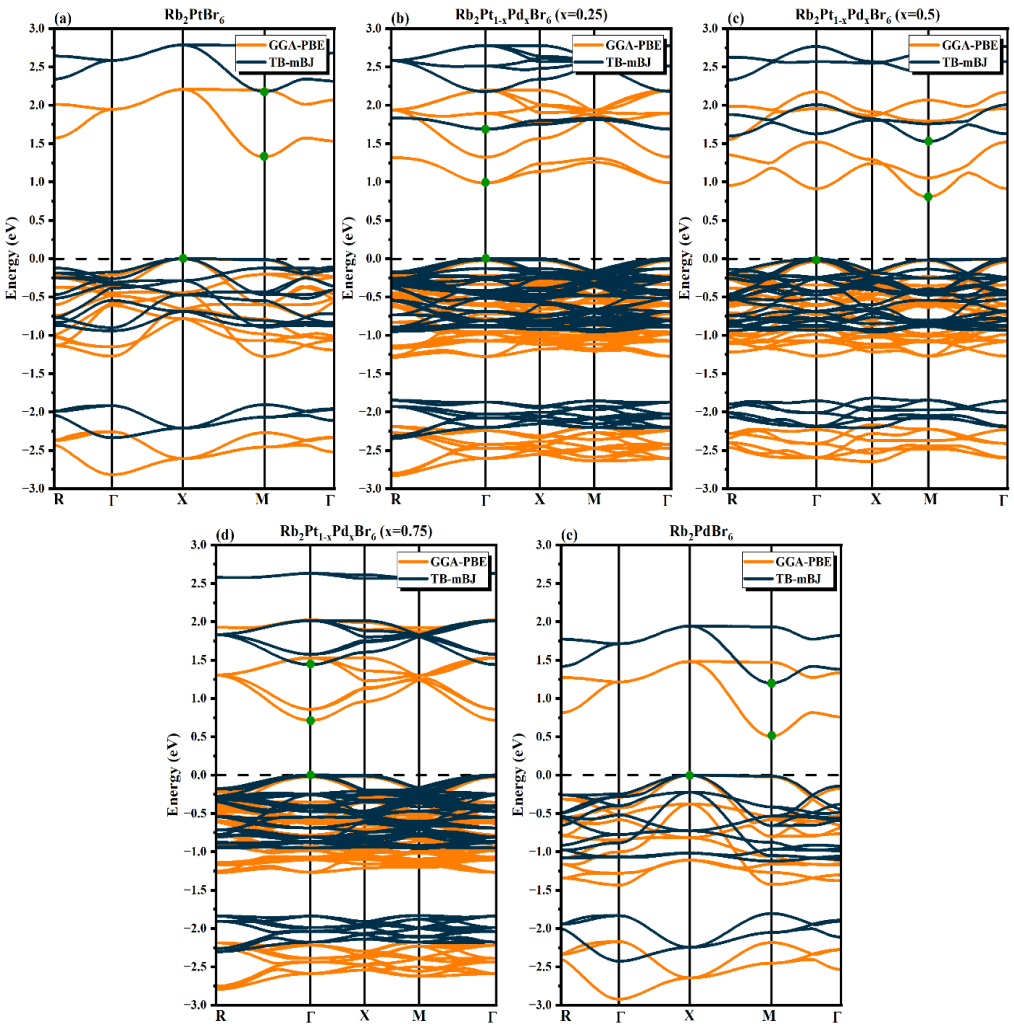

Figure III.20. Band structure diagrams for $Rb_2Pt_{1-x}PdBr_6$ double perovskite using the GGA-PBE and TB-mBJ approximations

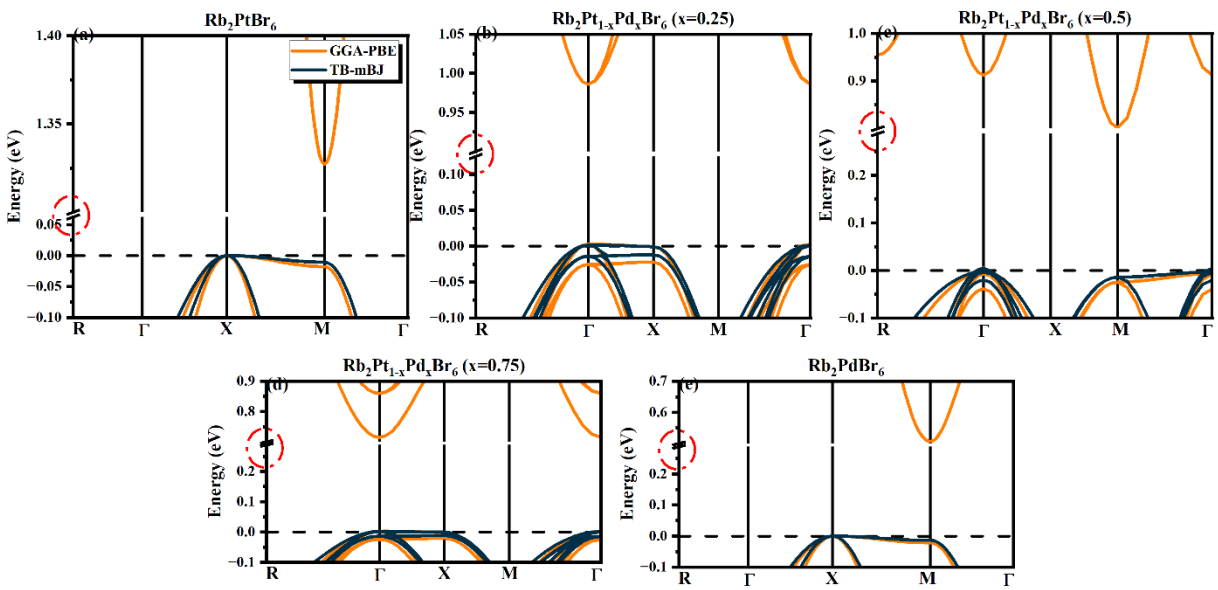

Figure III.21. Band structure diagrams (zoomed) for $Rb_2Pt_{1-x}PdBr_6$ double perovskite using the GGA-PBE and TB-mBJ approximations

The electronic structure of the $Rb_2Pt_{1-x}Pd_xBr_6$ series has been analyzed through total and partial density of states (TDOS and PDOS), as presented in Figures III.22, III.23 and III24. These plots illustrate the evolution of orbital contributions across the valence and conduction bands as Pd is progressively substituted for Pt. Key features include the dominant role of Br-4p and transition metal (Pt-5d or Pd-4d) orbitals near the Fermi level, with minimal contribution from Rb atoms due to their closed-shell configuration. The increasing presence of Pd enhances hybridization with Br, leading to notable changes in the band edge characteristics. For clarity and to avoid redundancy, the detailed orbital contributions in different energy intervals across the series are comprehensively summarized in **Table III.6**. This table outlines the specific roles of atomic orbitals in the lower valence band, upper valence band, and conduction band for each composition.

Table III.6: The analysis of the partial densities of states across different regions of the band structure of the $Rb_2Pt_{1-x}Pd_xBr6$ double perovskite

Materials		**The energy intervals in the Band structure**					
		Lower Valence Band		**Upper Valence Band**		**Conduction Band**	
$Rb_2Pt_{1-x}PdBr_6$		-5.00 to -3.00 eV		-3.00 to 0.00 eV		0.00 to 5.00 eV	
Concentrations	**Atoms**	**Orbitals**	**Contributions**	**Orbitals**	**Contributions**	**Orbitals**	**Contributions**
X=0	**Rb**	(s, p)	Low	(s, p, d)	Low	(s, p, d)	Low
	Pt	d	Dominant	d	Moderate	d	Dominant
	Br	p	Moderate	p	Dominant	p	Moderate
X=0.25	**Rb**	p	low	(s, p, d)	Low	(s, p, d)	Low
	Pt	d	Dominant	d	Moderate	d	Dominant
	Pd	d	Moderate	d	Low	d	Dominant
	Br	p	Moderate	p	Dominant	p	Moderate
X=0.5	**Rb**	p	Low	(s, p, d)	Low	(s, p, d)	Low
	Pt	d	Dominant	d	Moderate	d	Dominant
	Pd	d	Dominant	d	Moderate	d	Dominant
	Br	p	Moderate	p	Dominant	p	Moderate
X=0.75	**Rb**	p	Low	(s, p, d)	Low	(s, p, d)	Low
	Pt	d	Moderate	d	Low	d	Dominant
	Pd	d	Dominant	d	Moderate	d	Dominant
	Br	p	Moderate	p	Dominant	p	Moderate
X=1	**Rb**	(s, p)	Low	(s, p, d)	Low	(s, p, d)	Low
	Pd	d	Dominant	d	Moderate	d	Dominant
	Br	p	Moderate	p	Dominant	p	Moderate

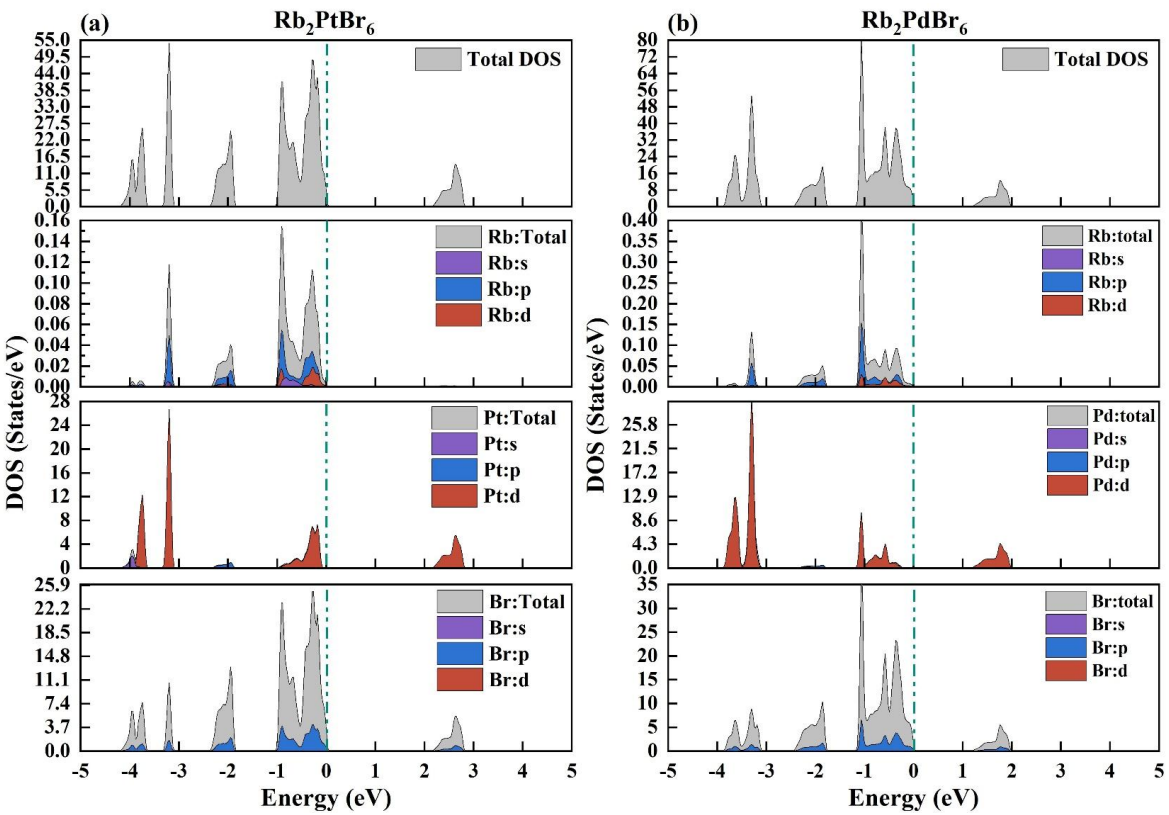

Figure III.22. DOS & PDOS diagrams for Rb_2XBr_6 (X=Pt and Pd) perovskite using the TB-mBJ approximation

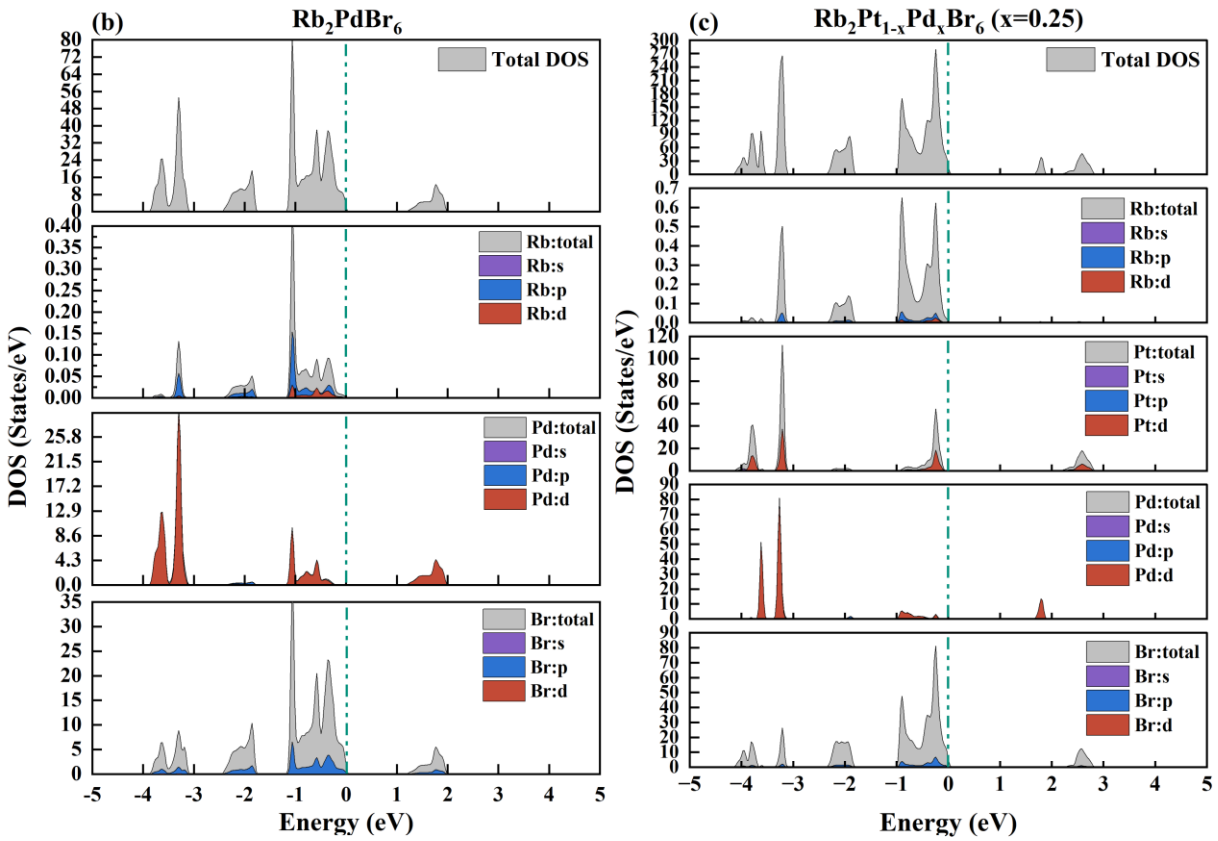

Figure III.23. DOS & PDOS diagrams for $Rb_2Pt_{1-x}PdBr_6$ (x=0.25 and 0.5) perovskite using the TB-mBJ approximation

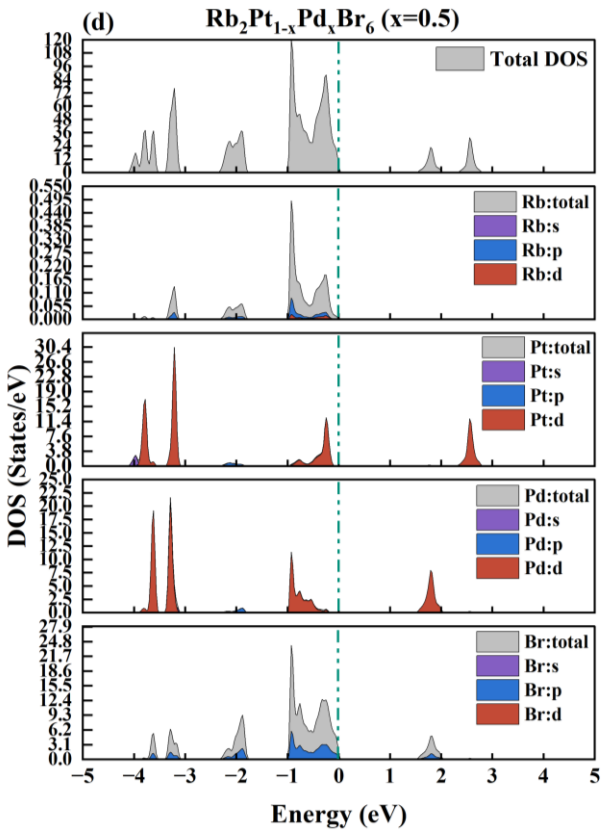

Figure III. 24. DOS & PDOS diagrams for $Rb_2Pt_{1-x}PdBr_6$ (x=0.75) perovskite using the TB-mBJ approximation

III.4.3.4 Antiperovskite A_3BX

The calculated band structures, presented in **Figure III.25(a-c)**, clearly indicate that the A_3SbAs (A = Ba, Sr, and Ca) antiperovskites exhibit direct band gap semiconducting behavior, with both the VBM and CBM located at the Γ point in the Brillouin zone. A comparative analysis of the three compounds reveals that Ca_3SbAs possesses the widest band gap, followed by Sr_3SbAs, and then Ba_3SbAs, within the TB-mBJ approximation. This trend is consistent with the decrease in the ionic radius and increase in electronegativity from Ba to Ca, which modifies the crystal field environment and the degree of orbital hybridization. In Ca_3SbAs, the smaller Ca^{2+} cations exert a stronger electrostatic potential, pulling the anionic orbitals closer and thereby widening the energy gap between the valence and conduction bands. The band dispersion around the VBM and CBM is moderate, indicating relatively low effective masses for both electrons and holes, which is advantageous for carrier mobility **[37]**. The curvature is more pronounced in Ca_3SbAs, suggesting slightly enhanced transport properties in this compound compared to its Ba and Sr analogues. However, all three maintain relatively dispersive bands near the Fermi level, pointing to their potential for electronic transport and

photovoltaic performance. The subsequent use of the TB-mBJ potential provides a substantial correction, yielding band gaps of 0.978 eV for Ba_3SbAs, 1.003 eV for Sr_3SbAs, and 1.195 eV for Ca_3SbAs. These corrected values place all compounds within the optimal range for solar energy harvesting, particularly under the Shockley-Queisser limit (≈1.34 eV), suggesting strong potential for single-junction solar cell applications.

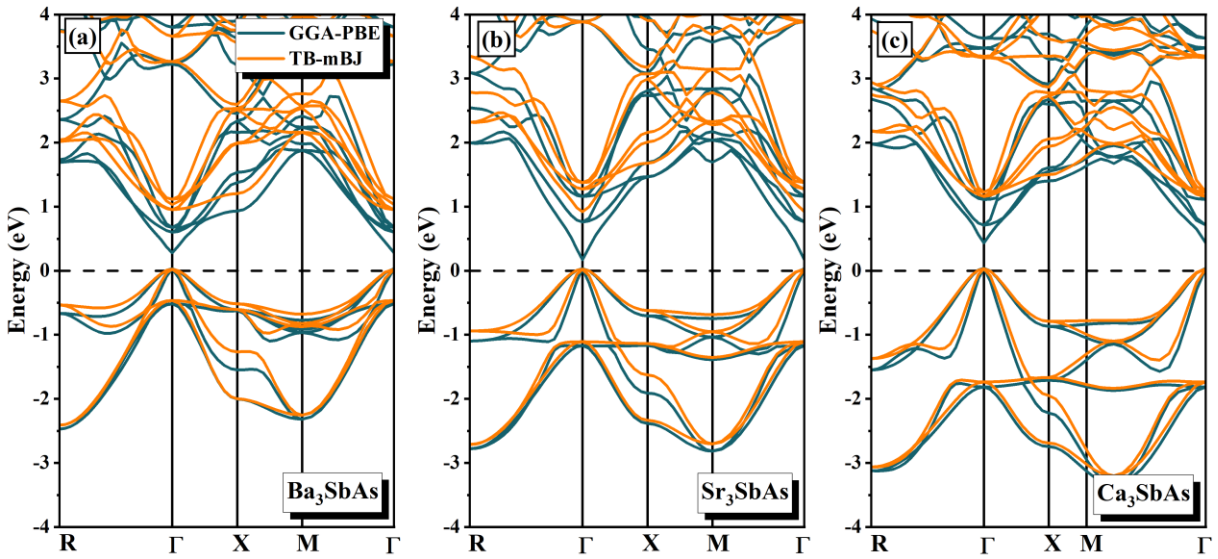

Figure III.25. Band structure diagrams for A_3SbAs antiperovskite using the GGA-PBE and TB-mBJ approximations

The total and partial density of states (DOS and PDOS) for A_3SbAs (A = Ba, Sr, Ca), shown in **Figure III.26(a-c)**, provide valuable insight into the orbital interactions and electronic structure near the Fermi level (E_F). In the valence band region (-6 to -2 eV), As-4p orbitals dominate and strongly overlap with Sb-5p orbitals, indicating significant p-p hybridization between arsenic and antimony atoms. This covalent-like interaction stabilizes the valence band and the crystal structure. Closer to E_F, the DOS is mainly shaped by Sb-5p states, with smaller contributions from As-4p, showing that Sb atoms are the primary contributors to electronic activity near E_F. The d-orbitals of the A-site cations (Ba-5d, Sr-4d, Ca-3d) partially overlap with Sb-5p orbitals at the valence band edge and conduction band onset, indicating d-p hybridization that enhances charge carrier delocalization and electronic transitions. The s-states of the alkaline earth metals lie well below -6 eV and do not significantly contribute near E_F, confirming that A-site cations primarily play an electrostatic role in stabilizing the octahedral Sb-As sublattice without directly influencing the frontier electronic states. In the conduction band, the DOS increase beyond the band gap consists mainly of hybridized As-4p, Sb-5p, and A-site d-states, with Ba-5d states contributing more prominently in Ba_3SbAs. This affects electron effective

mass and transport properties. Similar DOS features observed for Ba_3SbAs, Sr_3SbAs, and Ca_3SbAs suggest that electronic structure variations are mainly driven by the A-site cation size and electronic configuration, subtly modifying hybridization and band widths. These trends align with previous reports on related antiperovskite materials such as X_3ZN (X = Ca, Sr, Ba; Z = As, Sb, Bi) **[38]**.

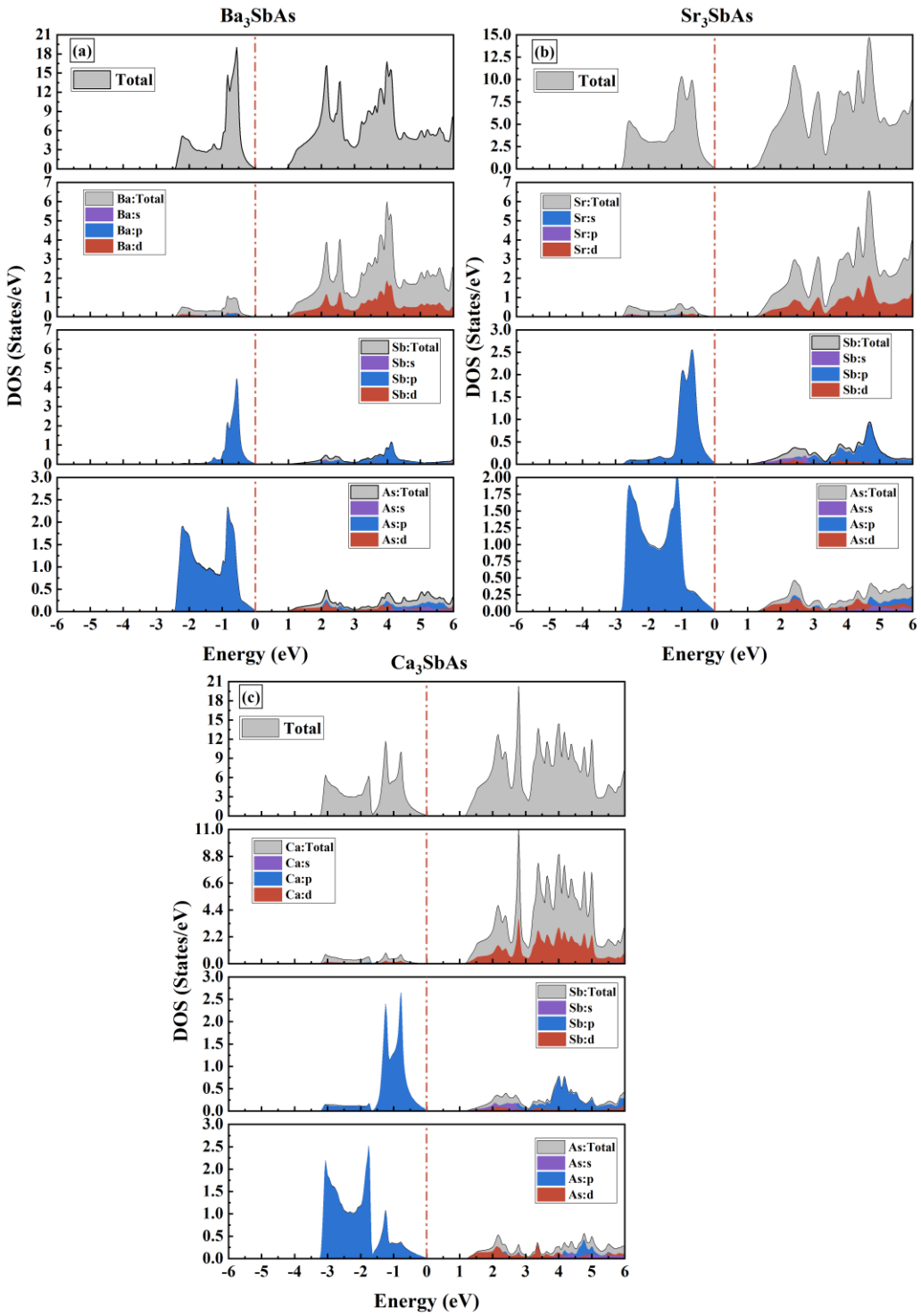

Figure III.26. DOS & PDOS diagrams for A_3SbAs perovskite using the TB-mBJ approximation

III.4.3.5 Derivative Antiperovskite A_3BX_3

The electronic band structures of the antiperovskite compounds Ca_3BiI_3, Sr_3BiI_3, and Ba_3BiI_3 plotted in **Figure III.27(a-c)**, computed using the GGA-PBE and TB-mBJ exchange-correlation functionals, reveal semiconducting characteristics with direct band gap nature in all three cases. These results provide important insights into their potential performance in optoelectronic applications. For Ca_3BiI_3 and Sr_3BiI_3, the GGA-PBE calculations yield band gaps of 1.36 eV and 1.30 eV, respectively, while Ba_3BiI_3 shows a smaller band gap of 0.85 eV. These moderate values are typical of materials with visible to near-infrared photon absorption capabilities. When the TB-mBJ potential is applied, a notable enhancement in the band gap is observed: Ca_3BiI_3 increases to 1.61 eV (a rise of 18.38%), Sr_3BiI_3 to 1.79 eV (a 37.69% increase), and Ba_3BiI_3 to 1.43 eV (a substantial 68.24% increase). The improved accuracy of the TB-mBJ functional for estimating band gaps brings these values closer to the ideal range (1.1–1.6 eV) for single-junction photovoltaic devices, as prescribed by the Shockley-Queisser limit.

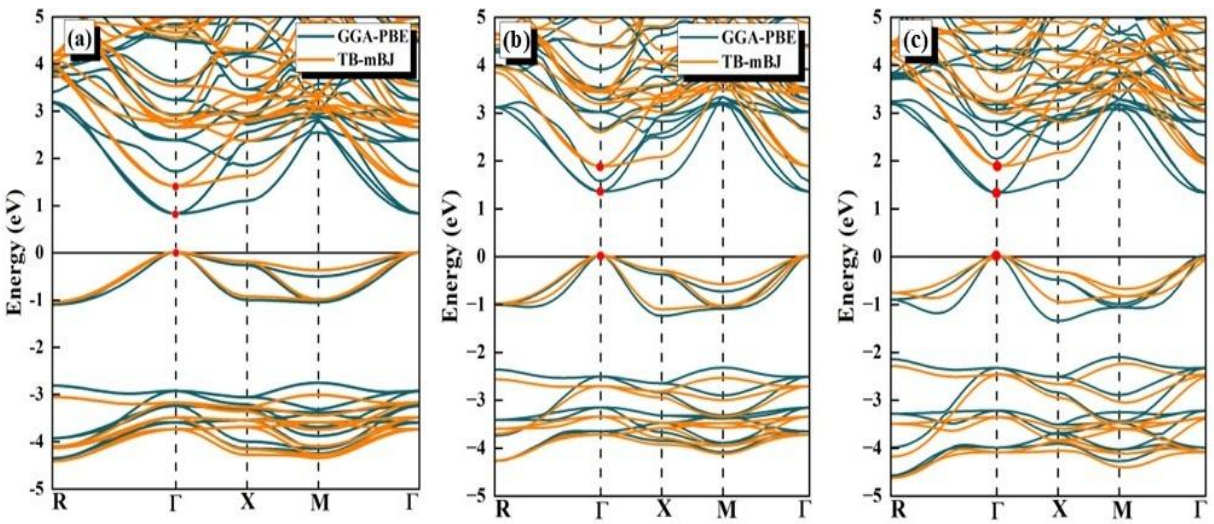

Figure III.27. Band structure diagrams for A_3BiI_3 Derivative Antiperovskite using the GGA-PBE and TB-mBJ approximations

The total and partial density of states (DOS and PDOS), presented collectively in **Figure III.28(a-c)**, offer essential insights into the electronic structure of the inorganic perovskite compounds A_3BiI_3 (A = Ca, Sr, Ba). By resolving the contributions from individual atomic orbitals, this analysis reveals the nature of chemical bonding, the character of the valence and conduction bands, and the potential of these materials for optoelectronic and thermoelectric applications. Across all A_3BiI_3 compounds, the DOS is examined over the energy range from -5 eV to +5 eV, encompassing both the valence and conduction band regions. The valence band

region (-5 eV to 0 eV) is predominantly composed of iodine (I) 5p and bismuth (Bi) 6p states. The lower energy segment, particularly from -5 eV up to approximately -2.5 eV, shows strong contributions from I-5p orbitals. As the energy increases toward the valence band maximum (VBM), the Bi-6p orbitals become increasingly significant, leading to clear evidence of hybridization between I-5p and Bi-6p states. This hybridization plays a crucial role in defining the chemical bonding and electronic properties of the compounds, particularly by enhancing charge delocalization. The presence of a sharp peak near the VB indicates a high density of available electronic states, which is essential for efficient hole conduction, especially under thermal or optical excitation. This is indicative of p-type semiconducting behavior, consistent across the A_3BiI_3 family.

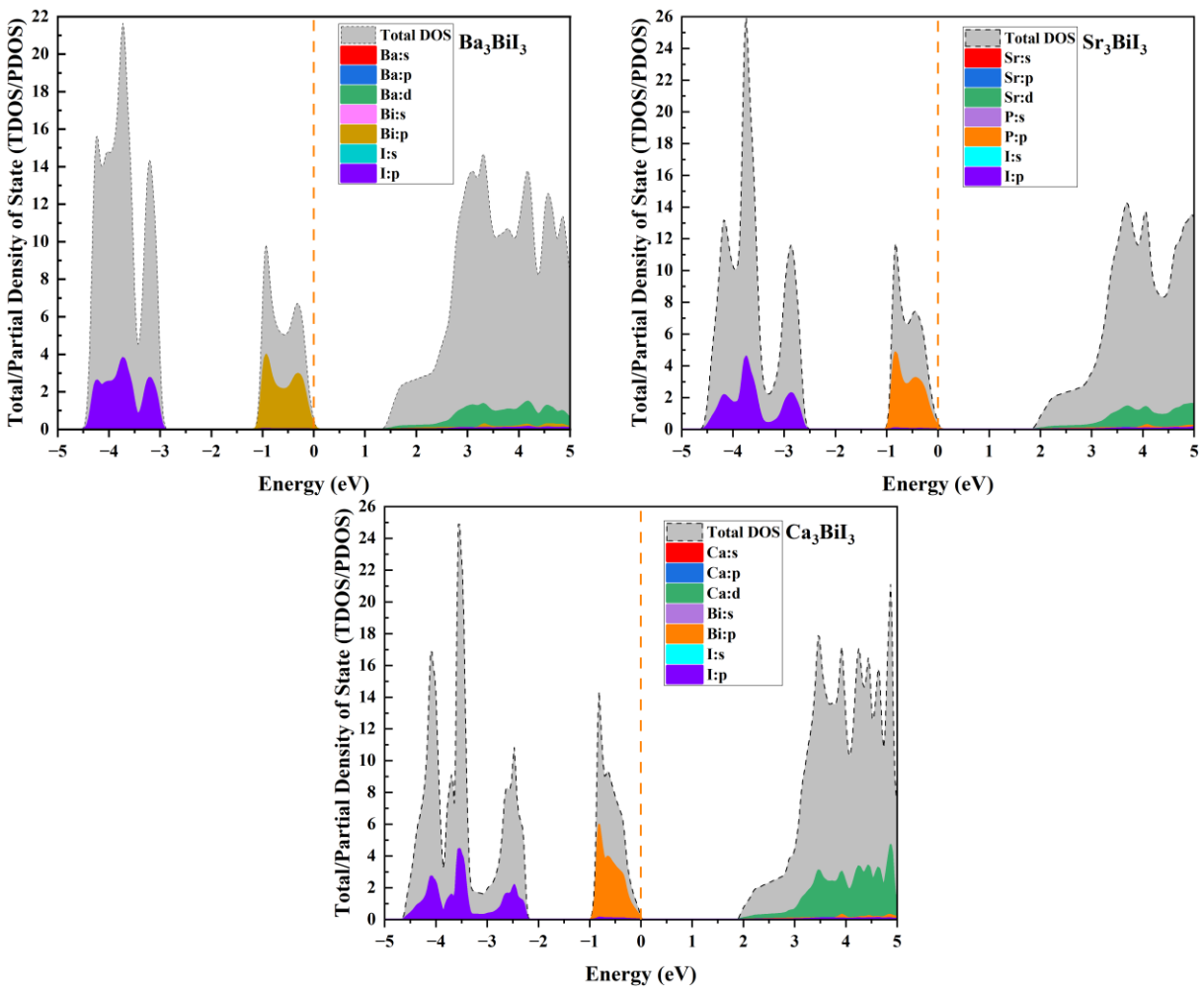

Figure III.28. DOS & PDOS diagrams for A_3BiI_3 perovskite using the TB-mBJ approximation

The conduction band region (0 eV to +5 eV) reveals an initial increase in the total DOS just above the Fermi level, indicating the onset of unoccupied states. These states are primarily derived from Bi-6p orbitals, confirming their role in the electronic transition from the valence

to conduction band. As the energy increases further, contributions from the A-site cations (Ca, Sr, Ba) become evident through their respective d-orbitals. For Ca_3BiI_3 and Sr_3BiI_3, the Ca-3d and Sr-4d states begin to influence the upper conduction band, while for Ba_3BiI_3, the Ba-5d orbitals contribute more significantly beyond ≈1.5 eV. These differences reflect the impact of the A-site ionic radius and electronic configuration on the conduction characteristics and potentially on the effective mass of charge carriers.

III.5 Conclusion

This chapter provided a comprehensive investigation into the structural and electronic properties of various classes of materials, including perovskites, double perovskites, and antiperovskites, using advanced first-principles density functional theory (DFT) calculations. By employing methodologies such as GGA-PBE, Hubbard U corrections, and the modified Becke-Johnson potential (TB-mBJ), the study achieved improved accuracy in predicting key electronic features, particularly band gaps. The analysis demonstrated that crystal structure and symmetry critically influence the materials' stability and electronic behavior. The calculated negative formation and cohesive energies confirmed the thermodynamic stability and feasibility of synthesizing these compounds. Electronic band structures revealed a range of behaviors from semiconducting (direct and indirect band gaps) to half-metallicity, highlighting potential applications in optoelectronics and spintronics. Furthermore, trends in lattice parameters and electronic properties were consistently linked to ionic sizes and chemical composition, confirming known physical principles and aligning well with available experimental data.

Bibliography

[**1**] W. F. Kuhs, urn:issn:0108-7673, 1992, 48, 80–98.
[**2**] Fundamentals of Crystals: Symmetry, and Methods of Structural Crystallography - Boris K. Vainshtein - Google Books.
[**3**] V. M. Goldschmidt, Naturwissenschaften, 1930, 18, 999–1013.
[**4**] R. Sarmiento-Pérez, T. F. T. Cerqueira, S. Körbel, S. Botti and M. A. L. Marques, Chemistry of Materials, 2015, 27, 5957–5963.
[**5**] S. J. Mole, X. Zhou and R. Liu, Journal of Physical Chemistry, 1996, 100, 14665–14671.
[**6**] P. Philipsen and E. Baerends, Phys Rev B, 1996, 54, 5326.
[**7**] H. Khan, A. S. Yerramilli, A. D'Oliveira, T. L. Alford, D. C. Boffito and G. S. Patience, Can J Chem Eng, 2020, 98, 1255–1266.
[**8**] Band Theory and Electronic Properties of Solids – John.
[**9**] L. Gu, V. Srot, W. Sigle, C. Koch, P. Van Aken, F. Scholz, S. B. Thapa, C. Kirchner, M. Jetter and M. Rühle, Phys Rev B Condens Matter Mater Phys, 2007, 75, 195214.
[**10**] P. Blaha and K. Schwarz, Int J Quantum Chem, 1983, 23, 1535–1552.

[**11**] H. Zhu, W. Sun, R. Armiento, P. Lazic and G. Ceder, Appl Phys Lett, DOI:10.1063/1.4866861/132689.
[**12**] C. R. Kagan, D. B. Mitzi and C. D. Dimitrakopoulos, Science (1979), 1999, 286, 945–947.
[**13**] M. A. Pell, G. V. M. Vajenine and J. A. Ibers, J Am Chem Soc, 1997, 119, 5186–5192.
[**14**] J. Bie, J. Zhou and W. Fa, Adv Theory Simul, 2022, 5, 2200022.
[**15**] M. Houari, B. Bouadjemi, S. Haid, M. Matougui, T. Lantri, Z. Aziz, S. Bentata and B. Bouhafs, Indian Journal of Physics, 2020, 94, 455–467.
[**16**] B. S. D. Ramlina Vamhindi, S. J. Koyambo-Konzapa and E. K. K. Abavare, Computational Condensed Matter, 2025, 43, e01018.
[**17**] M. Ullah, R. Neffati, G. Murtaza, S. Khan, M. Haneef and M. W. Ashraf, Mater Sci Semicond Process, 2022, 150, 106977.
[**18**] N. Thakur, P. Kumar, R. Neffati and P. Sharma, Phys Scr, 2023, 98, 065921.
[**19**] H. L. Feng, K. Yamaura, L. H. Tjeng and M. Jansen, J Solid State Chem, 2016, 243, 119–123.
[**20**] W. O. Sosa-Correa, L. F. Muñoz-Martínez, J. Otálora-Acevedo, J. Roa-Rojas and J. A. Rodríguez, Rev Acad Colomb Cienc Exactas Fis Nat, 2023, 47, 72–80.
[**21**] S. A. Ivanov, P. Nordblad, R. Tellgren and A. Hewat, Mater Res Bull, 2009, 44, 822–830.
[**22**] M. Cheah, P. J. Saines and B. J. Kennedy, osti.govM Cheah, PJ Saines, BJ KennedyJ. Solid State Chem., 2008•osti.gov, 2006, 179, 1775–1781.
[**23**] T. K. Mandal, V. V. Poltavets, M. Croft and M. Greenblatt, J Solid State Chem, 2008, 181, 2325–2331.
[**24**] I. Ornelas-Cruz, A. Trejo, R. Oviedo-Roa, F. Salazar, E. Carvajal, A. Miranda and M. Cruz-Irisson, Comput Mater Sci, 2020, 178, 109619.
[**25**] E. Vega, M. Mollar and B. Mari, Proceedings of 2015 IEEE International Renewable and Sustainable Energy Conference, IRSEC 2015, DOI:10.1109/IRSEC.2015.7455117.
[**26**] A. Ghorai, S. Mahato, S. K. Srivastava and S. K. Ray, Adv Funct Mater, 2022, 32, 2202087.
[**27**] Q. Wu, J. Zhang, C. Sun, X. Zhang, M. Liu, R. Zeng, M. Liu, G. Wei, P. Wang, Z. Qiao and Z. Lin, J Solid State Chem, 2023, 322, 123913.
[**28**] K. Z. Du, W. Meng, X. Wang, Y. Yan and D. B. Mitzi, Angewandte Chemie - International Edition, 2017, 56, 8158–8162.
[**29**] Q. Mahmood, M. Hassan, T. H. Flemban, B. Ul Haq, S. AlFaify, N. A. Kattan and A. Laref, Journal of Physics and Chemistry of Solids, 2021, 148, 109665.
[**30**] M. Faizan, K. C. Bhamu, G. Murtaza, X. He, N. Kulhari, M. M. AL-Anazy and S. H. Khan, Scientific Reports 2021 11:1, 2021, 11, 1–9.
[**31**] S. Lin, J. Yue, W. Ren, C. Shen and H. Zhang, J Mater Chem A Mater, 2024, 12, 19567–19579.
[**32**] Z. yue Gao, W. Wang, B. chen Li, L. Sun and F. Wang, J Supercond Nov Magn, 2022, 35, 3277–3290.
[**33**] H. J. Feng and Q. Zhang, Appl Phys Lett, DOI:10.1063/5.0039936/39516.
[**34**] K. K. Mishra, S. Chahar and R. Sharma, Phys Lett A, 2024, 523, 129817.
[**35**] H. Huang and P. G. Pickup, Chemistry of Materials, 1998, 10, 2212–2216.
[**36**] H. Wu, Phys Rev B, 2001, 64, 125126.
[**37**] S. Yu, H. D. Xiong, K. Eshun, H. Yuan and Q. Li, Appl Surf Sci, 2015, 325, 27–32.
[**38**] I. Ullah, G. Murtaza, R. Khenata, A. Mahmood, M. Muzzamil, N. Amin and M. Saleh, J Electron Mater, 2016, 45, 3059–3068.

CHAPTER IV

Mechanical And Dynamical

IV.1 Introduction

This chapter addresses the mechanical and dynamical stability of a range of perovskite and antiperovskite materials, focusing on their elastic, mechanical, and vibrational properties as determined through first-principles calculations. Building upon the framework of elasticity theory, we begin by presenting the fundamental role of elastic constants, derived from the stress-strain relationships encoded in the stiffness tensor, and the Born-Huang mechanical stability criteria that ensure thermodynamic stability under infinitesimal deformations. Using Density Functional Theory (DFT) and the stress-strain method, we compute the complete elastic tensor for each compound, considering their respective crystallographic symmetries (cubic, tetragonal, or hexagonal). From these, we derive key mechanical parameters such as bulk modulus, shear modulus, Young's modulus, Poisson's ratio, anisotropy factors, and the Pugh ratio, all critical for characterizing macroscopic mechanical behavior, including ductility and brittleness. Furthermore, to assess dynamic stability, phonon dispersion relations are calculated using DFT-based lattice dynamics, identifying the presence or absence of imaginary phonon modes as an indicator of the system's resilience to lattice vibrations and potential phase transitions. This chapter integrates detailed computational results with theoretical models, providing a rigorous assessment of the mechanical integrity and vibrational stability of these advanced materials, thereby laying the groundwork for their potential applications in functional devices.

IV.2 Elastic Constants and Mechanical Stability Criteria

Elastic constants are fundamental parameters that characterize the response of a crystalline solid to small mechanical deformations. They provide quantitative insight into the stiffness of a material and are essential for evaluating mechanical stability, anisotropy, and elastic behavior under stress. These constants originate from the second-order derivatives of the total energy with respect to strain and are represented by a fourth-rank tensor C_{ijkl}, which links the stress tensor σ_{ij} to the strain tensor ε_{kl} via the generalized Hooke's law **[1]**.

$$\boldsymbol{\sigma_{ij} = C_{ijkl}\,\varepsilon_{kl}} \qquad \textbf{(IV.1)}$$

Due to the symmetries of stress and strain tensors and the intrinsic symmetry of the crystal, the number of independent elastic constants is significantly reduced. In practice, the

elastic stiffness tensor is commonly represented in Voigt notation as a 6×6 matrix C_{ij}. The number of independent elastic constants varies with the crystal system, cubic systems have 3, hexagonal have 5, tetragonal have 6 or 7 (depending on subtype), orthorhombic have 9, monoclinic have 13, and triclinic systems require 21 independent constants **[2]**.

Each constant within the matrix C_{ij} reflects a specific mechanical response:

- Diagonal terms such as C_{11}, C_{22}, and C_{33}, correspond to axial stiffness along principal directions.
- Off-diagonal terms like C_{12}, C_{13}, and C_{23}, represent coupling between axial stresses and orthogonal strains.
- Shear constants, including C_{44}, C_{55}, and C_{66}, quantify resistance to shape deformation under shear stress.

The elastic constants must satisfy the Born-Huang mechanical stability criteria, which depend on the crystal symmetry. These criteria ensure that the elastic strain energy density remains positive for any small, arbitrary deformation a necessary condition for mechanical and thermodynamic stability. Violation of these conditions indicates mechanical instability and may lead to structural phase transitions under stress or pressure **[3,4]**. Mathematically, the elastic strain energy per unit volume U can be expressed as **[5]**.

$$\mathbf{U = \frac{1}{2}\sum_{i,j=1}^{6} C_{ij}\ \varepsilon_i\ \varepsilon_j > 0 \quad \text{for all non-zero strains } \varepsilon_i} \qquad (\mathbf{IV.2})$$

This condition implies that the stiffness matrix C_{ij} must be positive definite, meaning that all of its eigenvalues are positive and its leading principal minors are greater than zero. Physically, this requirement guarantees that any infinitesimal distortion increases the system's total energy, thus ensuring stability at the equilibrium configuration. Although the general condition of positive definiteness is universally applicable, explicit analytical expressions for the mechanical stability criteria vary depending on the symmetry of the crystal structure. These symmetry-dependent conditions ensure that the elastic energy remains positive for any infinitesimal strain. For commonly studied systems, the criteria are as follows **[6,7]**.

Cubic systems: 3 independent constants (C_{11}, C_{12}, C_{44})

$$\mathbf{C_{44} > 0;\quad C_{11} - C_{12} > 0;\quad C_{11} + 2C_{12} > 0;\quad C_{44} > 0} \qquad (\mathbf{IV.3})$$

Tetragonal systems: 6 or 7 independent constants, depending on the subtype

$$\mathbf{C_{66} > 0;\quad C_{11} > |\, C_{12}\, |;\quad 2C_{13}^2 < C_{33}(C_{11} + C_{12});\quad C_{44} > 0;\quad C_{66} > 0} \qquad (\mathbf{IV.4})$$

Hexagonal systems: 5 independent constants (C_{11}, C_{12}, C_{13}, C_{33}, C_{44})

$$\mathbf{C_{44} > 0;\quad C_{11} > |\, C_{12}\, |;\quad 2C_{13}^2 < C_{33}(C_{11} + C_{12});\quad C_{44} > 0} \qquad (\mathbf{IV.5})$$

These inequalities ensure that the crystal maintains mechanical integrity under all infinitesimal deformations. Violations of any of these conditions suggest that the structure may be mechanically unstable and could undergo spontaneous symmetry breaking or phase transitions.

IV.3 Calculation of Elastic Constants Using Density Functional Theory (DFT)

In this study, the elastic constants were determined using first-principles calculations based on Density Functional Theory (DFT), which provides a reliable and parameter-free approach to predicting mechanical properties of solids. Specifically, the stress-strain method was employed, which involves computing the stress response of the system to small, symmetry-adapted deformations.

The procedure consists of the following steps:

1. **Structural Optimization**: The equilibrium geometry of the unit cell is obtained by minimizing the total energy and atomic forces.
2. **Application of Strain**: A set of small deformations (typically ±4.5%) are applied individually to the optimized structure. These deformations are designed to extract specific components of the elastic tensor.
3. **Stress Tensor Calculation**: For each strained configuration, the resulting stress tensor is computed self-consistently within the DFT framework.

4. **Elastic Tensor Extraction**: By fitting the stress-strain data using a linear regression model consistent with Hooke's law, the independent components of the stiffness tensor C_{ij} are determined.

These calculations were conducted using the WIEN2k software package, and strict convergence criteria were maintained to ensure the reliability of the obtained results.

IV.4 Mechanical Moduli and Derived Elastic Parameters

To evaluate the macroscopic mechanical behavior of crystalline materials, it is essential to derive a set of scalar moduli from the elastic constants. These include the bulk modulus (B), shear modulus (G), Young's modulus (E), Poisson's ratio (ν), anisotropy factor (A), and the Pugh's ratio (B/G). These parameters offer critical insights into the resistance of a material to deformation, its stiffness, ductility, and elastic anisotropy. The following subsections present the theoretical background and mathematical formulations of these quantities.

IV.4.1 The bulk modulus (B)

The bulk modulus B, also called the incompressibility modulus, quantifies a material's resistance to uniform volumetric compression and is defined as **[8]**.

$$\mathbf{B} = -\mathbf{V}\left(\frac{\partial \mathbf{P}}{\partial \mathbf{V}}\right)_{\mathbf{T}} \qquad (\mathbf{IV.6})$$

For anisotropic crystals, B can be derived from elastic constants C_{ij}, with expressions depending on symmetry. In tetragonal crystals, where $a = b \neq c$, the bulk modulus is given by.

$$\mathbf{B} = \frac{\mathbf{2(C_{11} + C_{12}) + 4C_{13} + C_{33}}}{\mathbf{9}} \qquad (\mathbf{IV.7})$$

This expression accounts for the stiffness along both in-plane and out-of-plane directions. Notably, the same formula applies to hexagonal systems because they share the same relevant elastic constants $C_{11}, C_{12}, C_{13}, C_{33}$, and their response to hydrostatic pressure is analogous despite structural differences. In contrast, cubic crystals, having higher symmetry with only three independent elastic constants, use a simplified form **[9]**.

$$\mathbf{B} = \frac{\mathbf{1}}{\mathbf{3}}(\mathbf{C_{11}} + \mathbf{2C_{12}}) \qquad (\mathbf{IV.8})$$

Here, the symmetry leads to identical mechanical behavior in all directions, and constants like C_{13} and C_{33} are not independently defined. Thus, while cubic systems exhibit isotropic compression, tetragonal and hexagonal systems require more directional elastic information to compute B.

IV.4.2 The shear modulus (G)

The shear modulus G, also known as the modulus of rigidity, measures a material's resistance to shape deformation under applied shear stress. It is defined as the ratio of shear stress to the corresponding shear strain and is expressed in terms of the elastic constants. For anisotropic crystals, G depends on crystal symmetry and is often calculated using the Voigt, Reuss, or Hill approximations for polycrystalline materials **[10]**. In the Voigt approximation, which assumes uniform strain throughout the material, the shear modulus for a tetragonal crystal is given by **[11]**.

$$\mathbf{G_V} = \frac{\mathbf{1}}{\mathbf{15}}(\mathbf{2C_{11}} + \mathbf{C_{33}} - \mathbf{C_{12}} - \mathbf{2C_{13}} + \mathbf{6C_{44}} + \mathbf{3C_{66}}) \qquad (\mathbf{IV.9})$$

In the Reuss approximation, which assumes uniform stress, it is expressed as.

$$\mathbf{G_R} = \left[\frac{\mathbf{15}}{\mathbf{4(S_{11}} + \mathbf{S_{33}} - \mathbf{2S_{13}} - \mathbf{S_{12}}) + \mathbf{6S_{44}} + \mathbf{3S_{66}}}\right]^{\mathbf{-1}} \qquad (\mathbf{IV.10})$$

where S_{ij} are the elastic compliance constants, i.e., the elements of the inverse of the stiffness tensor C_{ij}. The Hill average, G_H, considered the most realistic estimate for polycrystalline aggregates, is the arithmetic mean of the Voigt and Reuss bounds.

$$\mathbf{G} = \frac{\mathbf{G_V} + \mathbf{G_R}}{\mathbf{2}} \qquad (\mathbf{IV.11})$$

The same expressions apply to hexagonal crystals, as the symmetry constraints in both tetragonal and hexagonal systems lead to similar forms of elastic behavior under shear. For cubic crystals, the shear modulus is often approximated by **[10-12]**.

$$\mathbf{G} = \frac{\mathbf{1}}{\mathbf{5}}(\mathbf{C_{11}} - \mathbf{C_{12}} + \mathbf{3C_{44}}) \qquad (\mathbf{IV.12})$$

due to the higher symmetry and fewer independent elastic constants. The shear modulus is a key parameter in assessing the rigidity and mechanical stability of materials, and in conjunction with the bulk modulus B, it helps determine other important mechanical properties such as Young's modulus and Poisson's ratio.

IV.4.3 Young's modulus (E)

Young's modulus E, also referred to as the modulus of elasticity, characterizes a material's resistance to uniaxial deformation. It is defined as the ratio of tensile (or compressive) stress to the corresponding strain along a specific direction. In anisotropic crystals, E varies with crystallographic orientation and can be derived from the bulk modulus B and shear modulus G using isotropic approximations, particularly suitable for polycrystalline materials **[13]**. For polycrystalline aggregates, assuming quasi-isotropy, E is expressed by the well-known relation**[13,14]**.

$$\mathbf{E} = \frac{\mathbf{9BG}}{\mathbf{3B} + \mathbf{G}} \qquad (\mathbf{IV.12})$$

where B is the bulk modulus and G is the shear modulus, typically obtained through the Hill averaging scheme. This equation provides a good estimate of elastic stiffness for materials lacking strong anisotropy. Since both tetragonal and hexagonal crystals require directional stiffness data (due to lower symmetry than cubic), E is usually evaluated using the same isotropic approximation when discussing polycrystalline behavior. For cubic crystals, the approximation also holds, though more precise orientation-dependent expressions may be derived using elastic compliance constants.

IV.4.4 Poisson's ratio (ν)

Poisson's ratio ν quantifies the transverse strain response of a material to uniaxial stress. It is defined as the negative ratio of transverse strain to axial strain in the elastic deformation regime. For polycrystalline and quasi-isotropic materials, ν can be estimated using the bulk modulus B and shear modulus G through the following relation**[12,14]**.

$$\boldsymbol{\nu = \frac{3B - 2G}{2(3B + G)}} \qquad (\mathbf{IV.13})$$

This expression arises from the assumption of isotropy and is widely used to evaluate the elastic behavior of polycrystalline materials, regardless of crystal symmetry. In practice, the values of B and G are typically calculated using the Hill averaging method to account for both the Voigt and Reuss bounds. For tetragonal and hexagonal systems, although anisotropy may exist, the same isotropic relation is frequently adopted for approximate evaluation of the macroscopic Poisson's ratio in polycrystalline aggregates. In the case of cubic crystals, this expression also applies due to their higher symmetry and isotropic mechanical behavior in the polycrystalline state. Poisson's ratio provides insight into the ductility and interatomic bonding characteristics of materials. Values of $\nu > 0.26$ generally indicate ductile behavior, whereas lower values suggest brittleness.

IV.4.5 The anisotropy factor (A)

The anisotropy factor A quantifies the degree of directional dependence in the elastic properties of a material. It is a measure of the extent to which the material's mechanical properties, such as the bulk modulus, shear modulus, or Young's modulus, differ along different crystallographic directions. A high anisotropy factor indicates significant directional dependence, whereas a low value suggests near-isotropic behavior. For a material with orthorhombic symmetry, the anisotropy factor for Young's modulus A_E can be expressed as **[15]**.

$$\boldsymbol{A_E = \frac{E_{max}}{E_{min}}} \qquad (\mathbf{IV.14})$$

where E_{max} and E_{min} are the maximum and minimum values of Young's modulus, respectively, observed along different crystallographic directions. A similar definition holds for other mechanical moduli, such as the shear modulus G and the bulk modulus B, where the maximum and minimum values are taken along the principal directions. For cubic crystals, the material's isotropy leads to an anisotropy factor $A = 1$, meaning that all mechanical properties are identical in every direction. In contrast, for hexagonal and tetragonal crystals, the anisotropy

factor is typically greater than 1, reflecting the inherent directional dependence in these systems due to their lower symmetry. The anisotropy factor is important for understanding the material's performance in various applications, such as the design of structural components or for optimizing materials in devices that experience directional stresses **[15]**.

IV.4.6 The Pugh ratio (B/G)

The Pugh ratio $\frac{B}{G}$, also known as the ratio of bulk modulus to shear modulus **[16]**, is an important indicator used to predict the mechanical behavior of a material. It is particularly useful in evaluating the ductility or brittleness of materials **[16]**.

$$\frac{\mathbf{B}}{\mathbf{G}} = \frac{\textbf{Bulk Modulus}}{\textbf{Shear Modulus}} \qquad (\mathbf{IV.15})$$

According to Pugh's criterion, materials with a Pugh ratio $\frac{B}{G} > 1.75$ are generally considered ductile, whereas materials with a ratio $\frac{B}{G} < 1.75$ tend to be brittle. This empirical relationship arises from the fact that a high bulk modulus B relative to the shear modulus G indicates a material that can better accommodate elastic deformation under pressure without undergoing shear failure. For polycrystalline materials, such as those with cubic, tetragonal, or hexagonal symmetries, the Pugh ratio provides a rough approximation of the material's ability to withstand mechanical stress. In general, materials with higher values of $\frac{B}{G}$ exhibit greater resistance to brittle fracture and are more likely to deform plastically, while those with lower values are more prone to fracture under stress.

IV.5 Phonons and Dynamic Stability

Phonons are quantized vibrations of atoms within a crystal lattice and are essential for understanding the thermal, mechanical, and electrical properties of solids. In the context of dynamic stability, phonons provide insight into the behavior of materials under small perturbations. The phonon dispersion curves, which map the energy of phonons as a function of their wavevector, are crucial for assessing stability. The absence of imaginary frequencies in these curves indicates dynamic stability, meaning the atoms in the material will return to

equilibrium after a disturbance. Imaginary frequencies, on the other hand, signal instability, where atoms would move away from equilibrium **[17]**.

Phonons also play a central role in phase transitions, especially in systems exhibiting soft modes. Soft modes are phonon modes with low frequencies that become increasingly unstable as a material approaches a phase transition, leading to structural changes, in ferroelectric materials, the appearance of soft modes is a precursor to symmetry-breaking transitions from a high-temperature paraelectric phase to a ferroelectric phase **[18]**.

Thermally, phonons are the primary carriers of heat through lattice vibrations. The thermal conductivity of materials is largely governed by phonons, with higher-frequency phonons contributing more at higher temperatures and lower-frequency phonons dominating at lower temperatures. Phonon-phonon interactions, or scattering, can reduce thermal conductivity, which is particularly important in nanomaterials and thermoelectric devices, where managing heat flow is essential for efficiency. Similarly, phonons contribute to the specific heat of a material, with low-temperature specific heat being primarily phonon-driven, as described by the Debye model. At higher temperatures, the specific heat reaches a constant value as more phonon modes are excited **[19]**. Phonon scattering, driven by defects, grain boundaries, and interfaces, plays a significant role in thermal management. In thermoelectric materials, reducing phonon scattering improves efficiency by insulating heat while maintaining good electrical conductivity. In nanostructured materials, where surface-to-volume ratios are high, phonon scattering is particularly pronounced, allowing for tailored control of thermal properties **[20,21]**.

IV.5.1 Phonon Dispersion Calculation Using Density Functional Theory (DFT)

To calculate the phonon dispersion curve using Density Functional Theory (DFT), we employed the Phonopy software in combination with a 2x2x2 supercell to model the material's lattice vibrations. The supercell was chosen to ensure that the interactions between atoms are accurately represented without excessive computational cost. A k-point mesh of 10x10x10 was used for sampling the Brillouin zone, providing a sufficient level of precision for the phonon calculations. The Phonopy package was used to generate the necessary force constants by calculating the forces on the atoms in the supercell after small displacements. These force

constants were then used to compute the phonon frequencies at each k-point in the Brillouin zone, resulting in the phonon dispersion curve. This approach allows for the detailed study of the material's vibrational properties and dynamic stability **[22]**.

IV.6 Results and discussion

IV.6.1 Elastic Constants

The elastic constants of various perovskite and antiperovskite materials spanning classical, double, and derivative structures have been computed using Density Functional Theory (DFT) as described in Section IV.3. These materials exhibit different crystallographic symmetries, including cubic, tetragonal, and hexagonal phases. For all compounds under investigation, the independent elastic constants C_{11}, C_{12}, and C_{44} have been evaluated. Additionally, for tetragonal Sr_2MnSbO_6 and hexagonal $CsTaX_3$ (X = S, Se), the symmetry-specific constants C_{13}, C_{33} and C_{66} were also determined to account for their anisotropic mechanical responses. Notably, several of the cubic double perovskite compounds such as Rb_2PtBr_6 and its Pd-substituted derivatives exhibit low values of C_{11} and C_{44}, indicating moderate stiffness and suggesting that they are relatively soft materials, a feature that may benefit applications requiring mechanical flexibility. The Ba_2InOsO_6 compound, by contrast, exhibits significantly higher values, reflecting a higher mechanical rigidity, consistent with its high atomic weight and denser crystal packing.

The calculated elastic constants are summarized in **Table IV.1**. These constants provide critical insights into the material's resistance to various types of mechanical deformation, such as uniaxial stress and shear. To assess the mechanical stability of the compounds, the computed constants were examined using the Born mechanical stability criteria **[4]**, with the appropriate equations (IV.3, IV.4, and IV.5) applied based on the symmetry of each compound cubic, tetragonal, or hexagonal, respectively. In all cases, the criteria were satisfied, confirming that the structures are mechanically stable under small deformations. **Table IV.1** not only includes the complete elastic tensor components but also indicates ductility for selected materials based on the Pugh's ratio and related criteria. These elastic constants form the foundation for further mechanical and thermodynamic property evaluations, including bulk modulus, shear modulus, Young's modulus, and Poisson's ratio.

Table IV.1: Calculated Elastic Constants (in GPa) for Various Perovskite Compounds with Cubic, Tetragonal, and Hexagonal Symmetries

Elastic Constant	C_{11}	C_{12}	C_{13}	C_{33}	C_{44}	C_{66}	Classification
Cubic symmetry							
$LiSiCl_3$	47.96	11.09	//	//	6.44	//	Ductile
$RbSiCl_3$	46.48	10.10	//	//	11.86	//	Brittle
$CsSiCl_3$	32.91	10.68	//	//	9.31	//	Ductile
Ba_2InOsO_6	261.497	85.844	//	//	84.107	//	Ductile
Ba_3SbAs	56.256	2.374	//	//	16.51	//	Brittle
Sr_3SbAs	73.771	2.491	//	//	16.381	//	Brittle
Ca_3SbAs	94.668	6.681	//	//	15.666	//	Brittle
Ba_3BiI_3	58.170	5.736	//	//	10.284	//	Brittle
Sr_3BiI_3	64.361	7.939	//	//	13.670	//	Ductile
Ca_3BiI_3	70.542	12.531	//	//	10.365	//	Ductile
Rb_2PtBr_6	21.523	10.847	//	//	8.736	//	Ductile
$Rb_2Pt_{0.75}Pd_{0.25}Br_6$	21.320	10.750	//	//	8.750	//	Ductile
$Rb_2Pt_{0.5}Pd_{0.5}Br_6$	20.911	10.608	//	//	8.810	//	Ductile
$Rb_2Pt_{0.25}Pd_{0.75}Br_6$	20.450	10.422	//	//	8.857	//	Ductile
Rb_2PdBr_6	20.351	11.254	//	//	8.805	//	Ductile
Hexagonal symmetry							
$CsTaS_3$	100.228	30.762	20.112	130.246	15.716	16.593	Ductile
$CsTaSe_3$	90.025	25.106	18.515	110.398	12.732	14.177	Ductile
Tetragonal symmetry							
Sr_2MnSbO_6	262.042	84.524	121.847	140.389	64.158	97.422	Ductile

IV.6.2 Mechanical Moduli and Derived Elastic Parameters

Based on the obtained elastic constants, various mechanical moduli and derived elastic parameters have been calculated using the relations defined in Eqs. (IV.6) to (IV.15). These include the bulk modulus, shear modulus, Young's modulus, Poisson's ratio, Cauchy pressure, anisotropic factor, and Pugh's ratio. The computed results for all studied compounds are comprehensively presented in **Table IV.2**.

IV.6.2.1 The bulk modulus (B)

The bulk moduli of the compounds show clear trends based on their ionic radii and bonding characteristics. $LiSiCl_3$, $RbSiCl_3$, and $CsSiCl_3$ exhibit decreasing bulk moduli, with the trend reflecting the increasing ionic radius of the A-site cation ($Li^+ < Rb^+ < Cs^+$). The smaller Li^+ cation results in stronger electrostatic interactions and a stiffer lattice, making $LiSiCl_3$ the least compressible. In contrast, the larger Cs^+ ion leads to weaker bonding and greater

compressibility, making $CsSiCl_3$ the most compressible. $CsTaS_3$ and $CsTaSe_3$ have bulk moduli of 52.52 GPa and 46.08 GPa, respectively. The substitution of sulfur (S) by selenium (Se) reduces lattice stiffness due to the larger atomic size of Se, leading to lower compressibility resistance. Despite this, both compounds possess relatively high bulk moduli, reflecting their robust mechanical structures. In the A_3SbAs series, bulk moduli increase from Ba_3SbAs (20.13 GPa) to Sr_3SbAs (24.25 GPa), and then to Ca_3SbAs (35.34 GPa). This trend is attributed to the decreasing ionic radius of the A-site cation, which strengthens the lattice and enhances structural rigidity. Ca_3SbAs shows the highest bulk modulus, indicating superior resistance to volume deformation and mechanical durability. Similarly, in the A_3BiI_3 series, bulk moduli increase from Ba_3BiI_3 (23.05 GPa) to Sr_3BiI_3 (31.22 GPa) and then to Ca_3BiI_3 (38.20 GPa), following the trend of decreasing A-site ionic radius and stronger lattice cohesion. Ca_3BiI_3 demonstrates the highest bulk modulus, reflecting enhanced structural integrity. Ba_2InOsO_6 exhibits a significantly higher bulk modulus of 144.40 GPa, which is much higher than the other cubic compounds. This is due to the presence of heavy transition metals (In and Os) and strong metal oxygen bonding, contributing to its exceptional resistance to volume changes. Sr_2MnSbO_6 has the highest bulk modulus of all compounds studied, at 146.77 GPa. Its tetragonal structure, combined with strong Mn-O and Sb-O bonds, contributes to its remarkable mechanical rigidity, making it highly resistant to compression. The bulk moduli of the $Rb_2Pt_{1-x}Pd_xBr_6$ compounds range narrowly between 14.27 GPa and 14.41 GPa, indicating relatively soft lattices **[23]**. The minimal variation in bulk modulus with changing Pt/Pd ratios suggests that substitution between Pt and Pd does not significantly affect the material's compressibility.

IV.6.2.2 The shear modulus (G)

The shear modulus for the $ASiCl_3$ (A = Li, Rb, Cs) cubic perovskites demonstrates a trend where $RbSiCl_3$ exhibits the highest resistance to shear deformation (14.68 GPa), while $CsSiCl_3$ shows the lowest (10.03 GPa). $LiSiCl_3$, with a shear modulus of 11.45 GPa, falls in between. The variation is due to a combination of ionic size and bonding strength. The smaller Li^+ cation, while contributing to a stronger electrostatic interaction, has relatively weaker bonding compared to Rb^+, leading to a lower modulus despite the small ionic size. In contrast, the larger Cs^+ cation induces lattice expansion and reduces interatomic forces, weakening the shear modulus. In the hexagonal $CsTaX_3$ series (X = S, Se), the shear modulus values are 26.64

GPa for $CsTaS_3$ and 23.46 GPa for $CsTaSe_3$. The stronger shear resistance in $CsTaS_3$ is attributed to the higher electronegativity and smaller atomic radius of sulfur compared to selenium. These characteristics result in stronger Ta–S bonds, contributing to the higher shear modulus. The shift from sulfur to selenium reduces bond strength and lattice rigidity, which is reflected in the lower shear modulus of $CsTaSe_3$. In the A_3SbAs (A = Ba, Sr, Ca) antiperovskites, the shear modulus increases with the decreasing ionic radius of the A-site cation: 26.94 GPa for Ba_3SbAs, 35.64 GPa for Sr_3SbAs, and 43.99 GPa for Ca_3SbAs. This trend suggests that smaller cations allow for denser atomic packing and stronger covalent interactions, leading to higher shear resistance. The high shear modulus of Ca_3SbAs (43.99 GPa) indicates enhanced angular stiffness and structural integrity, likely resulting from its more tightly packed lattice and stronger A-X bond lengths. Similarly, the A_3BiI_3 series (A = Ba, Sr, Ca) shows a gradual increase in shear modulus: 26.21 GPa for Ba_3BiI_3, 28.21 GPa for Sr_3BiI_3, and 29.51 GPa for Ca_3BiI_3. The trend mirrors that seen in the A_3SbAs series, with the increase in shear modulus attributed to the smaller ionic radii of the A-site cations. The smaller cations lead to stronger bonding and increased rigidity of the lattice, which results in a higher shear modulus. For the $Rb_2Pt_{1-x}Pd_xBr_6$ compounds with cubic symmetry, the shear modulus values remain relatively constant, ranging from 10.51 GPa for Rb_2PtBr_6 to approximately 10.5-10.66 GPa for the doped variants. The minimal variation in the shear modulus with Pt/Pd substitution indicates that partial replacement of Pt with Pd does not significantly affect the shear resistance. This is likely due to the similar bonding characteristics of the Pt–Br and Pd–Br interactions, which do not drastically alter the shear behavior of the lattice. The double perovskite Ba_2InOsO_6 stands out with a high shear modulus of 85.60 GPa. This value reflects the strong resistance to angular deformation, largely due to the robust In-O and Os-O bonds in the perovskite structure. The presence of heavy transition metal elements (In and Os) enhances the material's rigidity, making it less susceptible to shear deformation compared to other compounds in the dataset. Lastly, the tetragonal Sr_2MnSbO_6 exhibits an even higher shear modulus of 90.72 GPa, indicating exceptional shear rigidity. The strong shear resistance in Sr_2MnSbO_6 is attributed to its mixed-valence B-site configuration and the robust oxygen framework, which are reinforced by 3d–5p interactions. These interactions strengthen the lattice and make it highly resistant to angular deformation under shear stress. This exceptional shear modulus suggests that Sr_2MnSbO_6 may

be particularly suitable for applications where high mechanical strength under shear stress is required.

IV.6.2.3 The Young's modulus (E)

The Young's modulus values for the $ASiCl_3$ (A = Li, Rb, Cs) cubic perovskites are 29.52 GPa for $LiSiCl_3$, 36.09 GPa for $RbSiCl_3$, and 25.39 GPa for $CsSiCl_3$. $RbSiCl_3$ exhibits the highest stiffness, suggesting greater resistance to axial deformation, while $CsSiCl_3$ shows the lowest due to its expanded lattice and weaker interatomic forces. In the hexagonal $CsTaX_3$ compounds, $CsTaS_3$ has a higher Young's modulus (68.36 GPa) than $CsTaSe_3$ (60.17 GPa), attributed to the stronger Ta–S bonds resulting from sulfur's smaller size and higher electronegativity. The A_3SbAs (A = Ba, Sr, Ca) series shows an increasing Young's modulus with decreasing ionic radius: 17.42 GPa for Ba_3SbAs, 29.97 GPa for Sr_3SbAs, and 56.78 GPa for Ca_3SbAs. Smaller cations enhance atomic packing, leading to stronger interatomic bonding and improved resistance to strain. The A_3BiI_3 (A = Ba, Sr, Ca) series displays a similar trend, with the Young's modulus increasing from 29.71 GPa for Ba_3BiI_3 to 53.67 GPa for Ca_3BiI_3, reflecting stronger bonding interactions and a more compact structure in the smaller cation variants. For the $Rb_2Pt_{1-x}Pd_xBr_6$ cubic halide double perovskites, the Young's modulus remains nearly constant, ranging from 17.5 GPa in Rb_2PtBr_6 to 18.4 GPa in $Rb_2Pt_{0.25}Pd_{0.75}Br_6$. This minimal variation indicates that partial Pd substitution does not significantly alter axial stiffness. Ba_2InOsO_6, a cubic double perovskite, exhibits a high Young's modulus of 214.42 GPa, reflecting strong In-O and Os-O bonds and a tightly packed perovskite structure, contributing to its excellent resistance to deformation. Sr_2MnSbO_6, a tetragonal double perovskite, has the highest Young's modulus at 225.80 GPa. This exceptional stiffness results from strong Mn–O and Sb–O bonds and the anisotropic lattice structure, making it highly resistant to elastic deformation.

IV.6.2.4 The Poisson’s ratio (v)

In the $ASiCl_3$ (A = Li, Rb, Cs) cubic compounds, the Poisson's ratios are 0.29 for $LiSiCl_3$, 0.23 for $RbSiCl_3$, and 0.27 for $CsSiCl_3$. $LiSiCl_3$ and $CsSiCl_3$ are ductile, while $RbSiCl_3$, with a lower ratio, is more brittle due to stronger directional bonding. In the hexagonal $CsTaX_3$ series, Poisson's ratios are 0.283 for $CsTaS_3$ and 0.282 for $CsTaSe_3$, both indicating ductile

behavior, reflecting their strong metallic-covalent bonding and ability to withstand plastic deformation. The A_3SbAs (A = Ba, Sr, Ca) compounds show very low Poisson's ratios: 0.02 for Ba_3SbAs, 0.033 for Sr_3SbAs, and 0.066 for Ca_3SbAs. These low values suggest brittle fracture due to strong directional bonding, with a slight increase in ductility in Ca_3SbAs. For the A_3BiI_3 (A = Ba, Sr, Ca) series, Poisson's ratios range from 0.186 for Ba_3BiI_3 to 0.291 for Ca_3BiI_3. Ba_3BiI_3 is more brittle, while Sr_3BiI_3 and Ca_3BiI_3 show more ductile behavior, with Sr_3BiI_3 approaching the critical ductile threshold. In the $Rb_2Pt_{1-x}Pd_xBr_6$ halide double perovskites, Poisson's ratios remain near 0.235-0.239 across compositions, suggesting moderate ductility and minimal impact of Pt ↔ Pd substitution on elasticity. Ba_2InOsO_6 has a Poisson's ratio of 0.253, indicating a mixed bonding character and moderate ductility, suggesting it can withstand some plastic deformation without fracture Sr_2MnSbO_6, with a Poisson's ratio of 0.2438, is slightly on the brittle side, showing high stiffness but limited plastic deformation due to its directional bonding in the tetragonal lattice.

IV.6.2.5 Cauchy pressure

In the cubic $ASiCl_3$ (A = Li, Rb, Cs) family, the Cauchy pressures are 4.65 for $LiSiCl_3$, -1.76 for $RbSiCl_3$, and 1.37 for $CsSiCl_3$. The positive values for $LiSiCl_3$ and $CsSiCl_3$ suggest ductile behavior with ionic or metallic bonding, while the negative value for $RbSiCl_3$ indicates stronger covalent bonding and brittleness, consistent with its Poisson ratio. In the hexagonal $CsTaX_3$ series, the Cauchy pressures are 15.05 for $CsTaS_3$ and 12.37 for $CsTaSe_3$, indicating ductility and metallic bonding. The large positive values reflect strong d-electron bonding interactions in the Ta-centered octahedra. The A_3SbAs (A = Ba, Sr, Ca) compounds show highly negative Cauchy pressures: -14.136 for Ba_3SbAs, -13.89 for Sr_3SbAs, and -8.985 for Ca_3SbAs, suggesting directional covalent bonding and brittleness. The less negative value for Ca_3SbAs indicates reduced brittleness, likely due to increased structural compactness and bond symmetry. In the A_3BiI_3 (A = Ba, Sr, Ca) series, Cauchy pressures range from -4.548 for Ba_3BiI_3 to 2.166 for Ca_3BiI_3. The positive value for Ca_3BiI_3 suggests improved ductility with more isotropic bonding, while the negative values for Ba_3BiI_3 and Sr_3BiI_3 reflect brittleness due to higher covalent bonding. In the halide double perovskites $Rb_2Pt_{1-x}Pd_xBr_6$, Cauchy pressures range from 1.224 to 1.032, consistently positive, indicating ductile behavior across compositions. Substitution of Pt by Pd does not significantly alter the mechanical properties.

Ba_2InOsO_6 has a Cauchy pressure of 1.737, indicating a mixed ionic-covalent bonding character with moderate ductility, suggesting mechanical robustness. Finally, Sr_2MnSbO_6 has the highest Cauchy pressure of 20.366, indicating strong ductility and metallic bonding tendencies due to Mn-O and Sb-O orbital hybridization.

IV.6.2.6 The anisotropic factor

In the cubic $ASiCl_3$ (A = Li, Rb, Cs) compounds, the anisotropic factors range from 0.34 for $LiSiCl_3$ to 0.83 for $CsSiCl_3$. $LiSiCl_3$ shows the least anisotropy, indicating more isotropic mechanical properties, while $RbSiCl_3$ and $CsSiCl_3$ exhibit higher anisotropic factors, reflecting a greater directional dependence due to variations in ionic radii and crystal structure. For the hexagonal $CsTaX_3$ series, the anisotropic factors are low: 0.452 for $CsTaS_3$ and 0.392 for $CsTaSe_3$, suggesting moderately isotropic mechanical properties, consistent with the lower anisotropy expected in hexagonal symmetry. The A_3SbAs (A = Ba, Sr, Ca) compounds show a range of anisotropic factors. Ba_3SbAs has an anisotropic factor of 0.32, while Sr_3SbAs and Ca_3SbAs have even lower values (0.243 and 0.169, respectively), indicating more isotropic mechanical properties due to smaller cations and more compact structures. In the A_3BiI_3 (A = Ba, Sr, Ca) series, the anisotropic factors are higher: 0.714 for Ba_3BiI_3, 0.654 for Sr_3BiI_3, and 0.530 for Ca_3BiI_3, suggesting greater anisotropy due to variations in ionic sizes and bonding in the Bi-centered perovskite structure. For the $Rb_2Pt_{1-x}Pd_xBr_6$ series, anisotropic factors decrease slightly as Pd content increases, ranging from 0.607 for Rb_2PtBr_6 to 0.514 for Rb_2PdBr_6, indicating a small increase in isotropy. Ba_2InOsO_6, with a cubic structure, has an anisotropic factor of 0.958, indicating nearly isotropic mechanical properties due to strong metallic bonding and uniform crystal structure. Finally, Sr_2MnSbO_6, a tetragonal compound, has an anisotropic factor of 0.723, indicating moderately anisotropic mechanical properties, consistent with its tetragonal symmetry.

IV.6.2.7 The Pugh ratio

In the cubic $ASiCl_3$ (A = Li, Rb, Cs) series, the Pugh ratios vary from 2.04 for $LiSiCl_3$ (ductile) to 1.51 for $RbSiCl_3$ (borderline ductile and brittle), and 1.80 for $CsSiCl_3$ (relatively ductile). The differences in Pugh ratios reflect the varying ionic radii of the cations, influencing bond strength and mechanical response. For the hexagonal $CsTaX_3$ series, the Pugh ratios of

1.97 for $CsTaS_3$ and 1.96 for $CsTaSe_3$ indicate ductile behavior, exceeding the critical value of 1.75. The slight differences between the materials can be attributed to variations in ionic sizes and bonding interactions. In the A_3SbAs (A = Ba, Sr, Ca) compounds, Pugh ratios range from 0.32 for Ba_3SbAs (highly brittle) to 0.803 for Ca_3SbAs, with Sr_3SbAs having 0.679. These low ratios suggest these compounds are brittle, likely due to their specific bonding and crystal structures. In the A_3BiI_3 (A = Ba, Sr, Ca) series, the Pugh ratios are higher, with Ba_3BiI_3 at 0.878, Sr_3BiI_3 at 1.107, and Ca_3BiI_3 at 1.295, indicating more ductility than the A_3SbAs series. The increase in Pugh ratio correlates with increasing ionic radii, suggesting more ductile behavior due to altered bonding and structural interactions. For the $Rb_2Pt_{1-x}Pd_xBr_6$ series, the Pugh ratios range from 2.17 to 2.26, indicating ductility, with a slight reduction in ductility as Pd content increases. All values suggest the materials are suitable for flexible applications. Ba_2InOsO_6 has a Pugh ratio of 1.687, indicating it is ductile but closer to the brittle threshold. Sr_2MnSbO_6, with a Pugh ratio of 1.618, is also ductile but exhibits more brittleness compared to other materials with higher ratios.

Table IV.2: Calculated Mechanical Properties of Different Perovskite Compounds

Property	Bulk Modulus	Shear Modulus	Young Modulus	Poisson Ratio	Cauchy Pressure	Anisotropic Factor	Pugh Ratio
Cubic symmetry							
$LiSiCl_3$	23.38	11.45	29.52	0.29	4.65	0.34	2.04
$RbSiCl_3$	22.23	14.68	36.09	0.23	-1.76	0.63	1.51
$CsSiCl_3$	18.09	10.03	25.39	0.27	1.37	0.83	1.80
Ba_2InOsO_6	144.395	85.595	214.42	0.253	1.737	0.958	1.687
Ba_3SbAs	20.126	26.941	17.423	0.02	-14.136	0.32	0.32
Sr_3SbAs	24.246	35.64	29.973	0.033	-13.89	0.243	0.679
Ca_3SbAs	35.344	43.993	56.783	0.066	-8.985	0.169	0.803
Ba_3BiI_3	23.047	26.217	29.708	0.186	-4.548	0.714	0.878
Sr_3BiI_3	31.220	28.211	40.262	0.297	-5.731	0.654	1.107
Ca_3BiI_3	38.201	29.506	53.670	0.291	2.166	0.530	1.295
Rb_2PtBr_6	14.406	10.514	18.449	0.235	1.224	0.607	2.26
$Rb_2Pt_{0.75}Pd_{0.25}Br_6$	14.273	10.535	18.376	0.236	1.213	0.607	2.24
$Rb_2Pt_{0.5}Pd_{0.5}Br_6$	14.375	10.601	18.236	0.237	1.173	0.585	2.21
$Rb_2Pt_{0.25}Pd_{0.75}Br_6$	14.265	10.664	18.064	0.239	1.136	0.566	2.17
Rb_2PdBr_6	14.286	10.599	17.505	0.236	1.032	0.514	2.19
Hexagonal symmetry							
$CsTaS_3$	52.52	26.64	68.36	0.283	15.05	0.452	1.97
$CsTaSe_3$	46.08	23.46	60.17	0.282	12.37	0.392	1.96
Tetragonal symmetry							
Sr_2MnSbO_6	146.768	90.716	225.8	0.2438	20.366	0.723	1.618

IV.6.3 Phonon Dispersion

The phonon dispersion curves for the studied compounds, namely A_3SbAs, A_3BiI_3, $Rb_2Pt_{1-x}Pd_xBr_6$ (with x = 0.25, 0.5, and 0.75), and the double perovskite Ba_2InOsO_6 and Sr_2MnSbO_6, were calculated and are depicted in **Figures IV.1** to **IV.4**. The absence of any imaginary phonon frequencies (negative values) across the entire Brillouin zone in all these compounds indicates their dynamic stability at 0 K. This confirms that these materials are thermodynamically stable and free from soft phonon modes that typically signal structural instability. It is worth noting that while Rb_2PtBr_6, Rb_2PdBr_6, and $CsTaX_3$ (X = S, Se) were not included in the present phonon calculations, prior theoretical studies have verified their dynamic stability, providing supporting evidence for their stable crystal structures under standard conditions. In contrast, the $ASiCl_3$ (A = Li, Rb, Cs) perovskite series exhibited imaginary phonon frequencies, indicating dynamic instability in their cubic phase. Such instabilities are typically manifested through soft modes near high-symmetry points in the Brillouin zone and suggest a tendency of the crystal to undergo a structural distortion or phase transition. However, it is important to emphasize that the presence of imaginary phonon modes does not necessarily imply that a compound is entirely unstable. Several materials, including many perovskites, exhibit phonon instabilities in their high-symmetry phases but become dynamically stable at finite temperatures due to anharmonic lattice effects or through structural distortions that lower the symmetry. For example, $CsSnI_3$, a well-known halide perovskite, shows imaginary frequencies in its high-temperature cubic phase but becomes dynamically stable in its low-symmetry tetragonal or orthorhombic phases at lower temperatures. This phenomenon reflects the role of temperature-dependent lattice dynamics and entropy in stabilizing perovskite phases that would otherwise appear unstable at 0 K within the harmonic approximation.

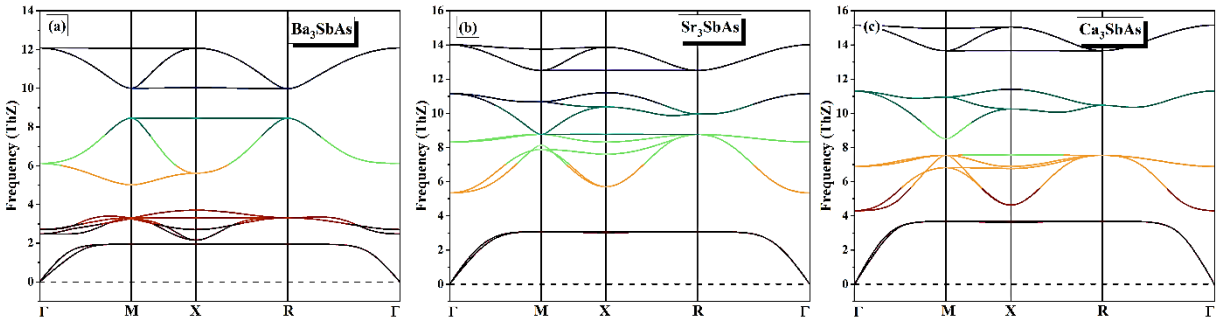

Figure IV.1. Phonon dispersion curves of A_3SbAs

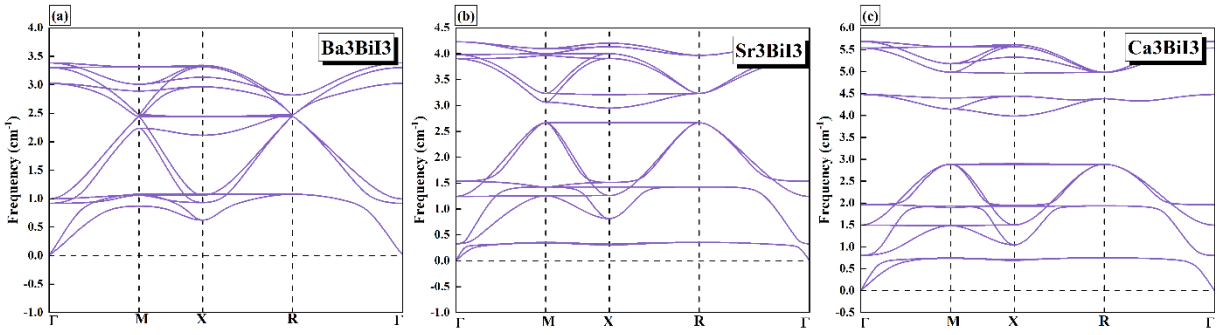

Figure IV.2. Phonon dispersion curves of A_3BiI_3

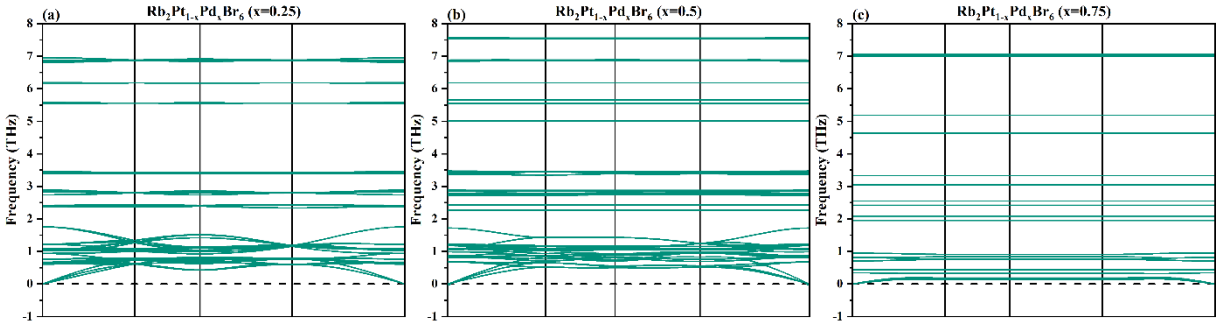

Figure IV.3. Phonon dispersion curves of $Rb_2Pt_{1-x}Pd_xBr_6$ (with x = 0.25, 0.5, and 0.75)

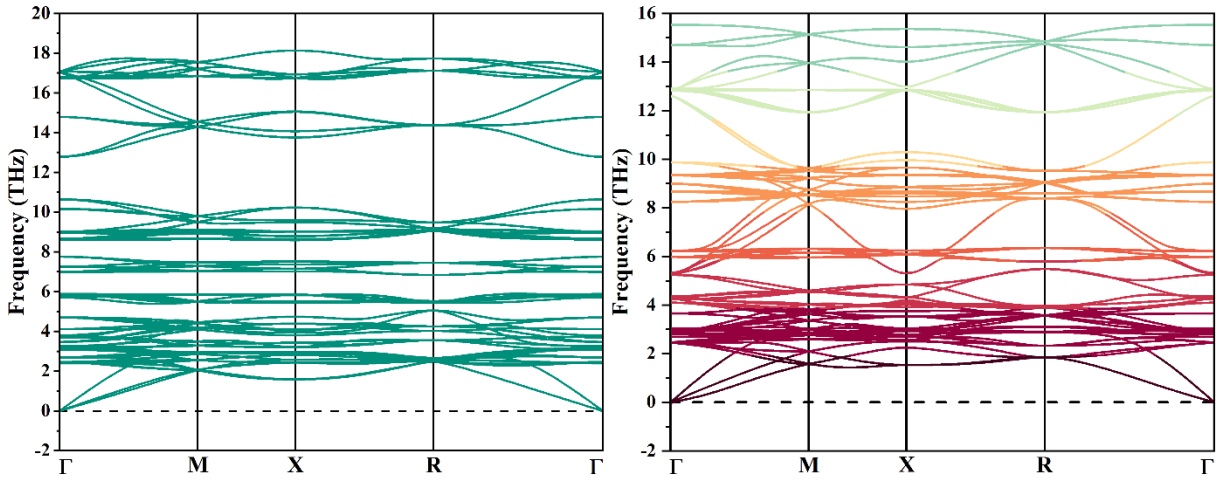

Figure IV.4. Phonon dispersion curves of Ba_2InOsO_6 and Sr_2SbMnO_6

IV.7 Conclusion

In this chapter, we have conducted a comprehensive analysis of the mechanical and dynamical stability of selected perovskite and antiperovskite compounds through an integration of first-principles calculations and elasticity theory. The evaluation of elastic constants and derived mechanical parameters confirms that most studied materials satisfy the symmetry-adapted Born-Huang criteria, indicating mechanical robustness under small deformations. The derived moduli and Pugh ratios reveal detailed insights into the ductility, stiffness, and anisotropic mechanical behavior of these materials, with trends systematically linked to cation size, bonding characteristics, and crystal symmetry. Phonon dispersion calculations further validate the dynamical stability of several compounds, while highlighting instabilities in others, particularly within cubic $ASiCl_3$ systems, suggesting possible temperature-driven phase transitions or symmetry-lowering distortions. Taken together, these results not only advance our fundamental understanding of the mechanical and vibrational properties of these complex materials but also provide valuable guidelines for their selection and optimization in technological applications, where mechanical resilience and thermal stability are critical performance factors.

Bibliography

[**1**] J. Rychlewski, *Journal of Applied Mathematics and Mechanics*, 1984, 48, 303–314.
[**2**] C. S. G. Cousins, *Journal of Physics C: Solid State Physics*, 1978, 11, 4881.
[**3**] Y. Li, Y. Gao, B. Xiao, T. Min, Z. Fan, S. Ma and L. Xu, *J Alloys Compd*, 2010, 502, 28–37.
[**4**] J. Wang, J. Li, S. Yip, D. Wolf and S. Phillpot, *Physica A: Statistical Mechanics and its Applications*, 1997, 240, 396–403.
[**5**] M. H. B. M. Shariff, *Rubber Chemistry and Technology*, 2000, 73, 1–18.
[**6**] S. Doll and K. Schweizerhof, *J Appl Mech*, 2000, 67, 17–21.
[**7**] A. G. Khachaturyan, S. Semenovskaya and T. Tsakalakos, *Phys Rev B*, 1995, 52, 15909.
[**8**] E. Ziambaras and E. Schröder, *Phys Rev B*, 2003, 68, 064112.
[**9**] A. S. Verma and A. Kumar, *J Alloys Compd*, 2012, 541, 210–214.
[**10**] R. Goldstein, V. Gorodtsov, D. Lisovenko and ipmnetru AYu, *Letters on Materials*, 2012, 2, 21–24.
[**11**] M. Dacorogna, J. Ashkenazi and M. Peter, *Phys Rev B*, 1982, 26, 1527.
[**12**] J. Turley and G. Sines, *J Phys D Appl Phys*, 1971, 4, 264.
[**13**] J. M. Zhang, Y. Zhang, K. W. Xu and V. Ji, *Chinese Physics B*, 2008, 17, 1565.
[**14**] J. M. Zhang, Y. Zhang, K. W. Xu and V. Ji, *Journal of Physics and Chemistry of Solids*, 2007, 68, 503–510.
[**15**] T. Ungár, I. Dragomir, Á. Révész and A. Borbély, *urn:issn:0021-8898*, 1999, 32, 992–1002.
[**16**] O. N. Senkov and D. B. Miracle, *Sci Rep*, 2021, 11, 1–4.
[**17**] X. Qian and R. Yang, *Phys Rev B*, 2018, 98, 224108.
[**18**] J. F. Scott, *Rev Mod Phys*, 1974, 46, 83.
[**19**] G. P. Srivastava, *The Physics of Phonons*, DOI:10.1201/9781003141273.

[**20**] S. Mei, C. J. Foss, L. N. Maurer, O. Jonasson, Z. Aksamija and I. Knezevic, *IEEE International Reliability Physics Symposium Proceedings*, 2017, 6A1.1-6A1.10.
[**21**] H. S. Kim, S. D. Kang, Y. Tang, R. Hanus and G. Jeffrey Snyder, *Mater Horiz*, 2016, 3, 234–240.
[**22**] A. Togo, L. Chaput, T. Tadano and I. Tanaka, *Journal of Physics: Condensed Matter*, 2023, 35, 353001.
[**23**] Y. Wang and P. Mora, *J Mech Phys Solids*, 2008, 56, 3459–3474.

CHAPTER V

Thermoelectric Properties

V.1 Introduction

Thermoelectric materials have garnered significant attention due to their unique ability to convert heat into electricity, offering a promising solution for energy harvesting and waste heat recovery. This direct energy conversion process is vital for developing sustainable technologies that can efficiently utilize otherwise lost energy in industrial processes, automotive systems, and even everyday electronic devices. Thermoelectric materials have applications ranging from power generation to solid-state cooling, highlighting their versatile potential across various industries. The purpose of this chapter is to provide an in-depth analysis of thermoelectric properties, focusing on the theoretical and practical aspects of these materials. By exploring how thermoelectric materials operate and their potential applications, this chapter seeks to emphasize their growing importance in the field of energy conversion and sustainability. In this work, structural and electronic optimization was performed on an initial set of twenty-five compounds to evaluate their stability and fundamental electronic properties. These materials have already been reported in eleven international publications in renowned journals, attesting to their scientific interest. Based on the results of this first phase, two compounds were selected for an in-depth thermoelectric investigation. This choice resulted from a comparative analysis of calculated parameters such as band gap nature and magnitude, density of states near the Fermi level, and crystal symmetry, indicating promising thermoelectric potential

V.2 Thermoelectricity

The various thermoelectric effects, including the Seebeck effect, the Peltier effect, and the Thomson effect, were discovered in the 19th century. Initially, these effects were observed in metallic conductors, and later, in semiconductors **[1]**.

V.2.1 The Seebeck Effect

The Seebeck effect, first observed by German physicist Thomas Johann Seebeck in 1821, involves the generation of an electric current when heat is transferred across the junction between two different conductors or semiconductors. When a temperature gradient is applied between the two materials, a potential difference is created at the junction **[1]**. This phenomenon

is linked to an intrinsic property of the materials, historically referred to as the thermoelectric power and now known as the Seebeck coefficient (**S**). The Seebeck effect can be described by the following equation [2].

$$\boldsymbol{E = S_{AB} \cdot \nabla T} \qquad (\mathbf{V.1})$$

Where $\mathbf{S_{AB}}$ is the difference in the Seebeck coefficients of the two materials (**A** and **B**), and $\boldsymbol{\nabla T}$ is the temperature gradient across the junction. The induced electric field, **E**, is proportional to the temperature gradient, with the proportionality constant being the Seebeck coefficient, which characterizes the thermoelectric response of the materials.

V.2.2 The Peltier Effect

In 1834, the French physicist Jean Peltier discovered the reverse thermoelectric effect, known as the Peltier effect. This effect occurs when an electric current is passed through the junction of two different materials [3]. Depending on the direction of the current, thermal energy is either absorbed or released at the junction. Essentially, when a current flows across the interface, heat is transferred, causing either cooling or heating at the junction. The amount of heat absorbed or released, **Q** can be expressed by the following equation [4].

$$\mathbf{Q = \Pi_{AB} \cdot I} \qquad (\mathbf{V.2})$$

Where $\mathbf{\Pi_{AB}}$, is the Peltier coefficient that characterizes the strength of the effect for the specific materials, and **I** is the electric current. The Peltier effect is the basis for thermoelectric cooling and heating applications, where heat can be controlled by adjusting the current.

V.2.3 The Thomson Effect

The Seebeck effect connects a temperature difference with a voltage difference, and the Peltier effect links an applied current to the heat absorbed or released at the junction of two materials. In 1851, William Thomson (later known as Lord Kelvin) identified another thermoelectric phenomenon, now known as the Thomson effect. He observed that when a conductor is exposed to a temperature gradient and carries an electric current, heat is either absorbed or released within the conductor itself. This heat exchange is proportional to both the

applied current **I** and the temperature gradient $\frac{dT}{dx}$ within a small segment of the conductor. The Thomson effect can be described by the following relationship [5,6].

$$\frac{dQ}{dx} = h \cdot I \cdot \frac{dT}{dx} \quad (\mathbf{V.3})$$

Where, $\frac{dQ}{dx}$ is the rate of heat exchange along the conductor, **h** is the Thomson coefficient, and $\frac{dT}{dx}$ is the temperature gradient. Thomson also demonstrated that there is a direct relationship between the Seebeck, Peltier, and Thomson effects. He established the following equations linking the Seebeck coefficient S_{AB}, the Peltier coefficient Π_{AB}, and the Thomson coefficient **h** [5].

$$\Pi_{AB} = \int S_{AB}\, dT \quad (\mathbf{V.4})$$

$$h = S_A - S_B \quad (\mathbf{V.5})$$

Here, S_A and S_B are the Seebeck coefficients of materials **A** and **B**, respectively. This shows that these thermoelectric effects are interconnected and can be understood as different aspects of the same underlying phenomenon.

V.2.4 Transport Equations

The thermoelectric transport phenomena in p-type and n-type semiconductor legs are governed by coupled electrical and thermal processes, which are captured by a set of fundamental transport equations [7]. These equations quantify how heat flux and temperature gradients develop inside each leg under the combined influence of electrical current, material properties, and boundary conditions. Starting with the temperature gradient inside the legs, equations (IV.6) and (IV.7) describe how Joule heating alters the otherwise linear temperature distribution caused by the imposed hot and cold side temperatures. Specifically, the thermal conduction term $\kappa A \frac{dT}{dz}$ in each leg balances the internal volumetric heat generation due to Joule heating, expressed as $\frac{I^2\rho}{A}$ spread along the length L. The temperature gradient in the p-type leg is therefore [8].

$$\kappa_p A_p \frac{dT}{dz} = -\frac{I^2 \rho_p \left(z - \frac{1}{2} L_p\right)}{A_p} + \frac{\kappa_p A_p (T_h - T_c)}{L_p} \quad (\mathbf{V.6})$$

Similarly, the n-type leg gradient is.

$$\kappa_n A_n \frac{dT}{dz} = -\frac{I^2 \rho_n \left(z - \frac{1}{2} L_n\right)}{A_n} + \frac{\kappa_n A_n (T_h - T_c)}{L_n} \quad (\mathbf{V.7})$$

These expressions reveal a superposition of two effects: the linear temperature gradient resulting from the fixed boundary temperatures at the hot and cold ends, and a parabolic component due to Joule heating, which peaks at the leg midpoint $\frac{1}{2}\boldsymbol{L}$. The parabolic term reduces the steepness of the temperature gradient near the center and indicates a localized temperature rise caused by internal resistance to current flow. This non-uniform temperature distribution is critical for accurately predicting device performance, as it directly influences the Seebeck effect and thermal losses. The total heat flux at the interface between p-type and n-type materials, typically located at $\boldsymbol{z = 0}$, is given by equation (IV.8) **[9]**.

$$Q_t = (S_p - S_n) I T_f - \kappa \Delta T - \frac{1}{2} I^2 R \quad (\mathbf{V.8})$$

This equation encapsulates the net heat transferred at the junction, balancing three terms. The first, $(S_p - S_n) I T_f$, corresponds to the useful Peltier heat transported by the current, with T_f representing the effective junction temperature, usually approximated as an average between T_c and T_h. The second term, $\kappa \Delta T$ accounts for conductive heat leakage through the device due to the temperature difference $\Delta T = T_h - T_c$. The last term, $\frac{1}{2} I^2 R$ describes Joule heating losses inside the device, where only half of the heat dissipated is considered at the cold side because the other half appears at the hot side. This highlights the fundamental tradeoff in thermoelectric devices: while the electrical current drives useful heat pumping, it simultaneously generates resistive heating that counteracts cooling. The device's overall thermal and electrical transport characteristics are quantified by the effective thermal conductance **K** and electrical resistance R, expressed as the sums of contributions from each leg **[10]**.

$$\mathbf{K} = \frac{\boldsymbol{\kappa_p A_p}}{\boldsymbol{L_p}} + \frac{\boldsymbol{\kappa_n A_n}}{\boldsymbol{L_n}} \qquad (\mathbf{V.9})$$

$$\boldsymbol{R} = \frac{\boldsymbol{L_p \rho_p}}{\boldsymbol{A_p}} + \frac{\boldsymbol{L_n \rho_n}}{\boldsymbol{A_n}} \qquad (\mathbf{V.10})$$

Here, the terms $\frac{\boldsymbol{\kappa A}}{\boldsymbol{L}}$ and $\frac{\boldsymbol{L\rho}}{\boldsymbol{A}}$ represent the thermal conductance and electrical resistance of each leg, respectively. These parameters are pivotal in device design because they control how easily heat and current flow through the materials. Minimizing $\boldsymbol{R}$ reduces Joule heating losses, while minimizing $\mathbf{K}$ limits conductive heat leakage, both of which improve device efficiency. The electrical work $\boldsymbol{W}$ needed to maintain current $\boldsymbol{I}$, is given by [11]:

$$\boldsymbol{W = I\left[\left(S_p - S_n\right) \cdot \Delta T + IR\right]} \qquad (\mathbf{V.11})$$

This expression includes two components: the voltage generated by the Seebeck effect across the temperature difference $\boldsymbol{\Delta T}$, and the voltage drop due to the internal resistance $\boldsymbol{R}$. The work done on the device must overcome both to sustain current flow. The efficiency or coefficient of performance (COP) of the thermoelectric cooler is defined as the ratio of heat removed at the cold side to the electrical power input [11].

$$\boldsymbol{\varepsilon_c = \frac{Q_t}{W} = \frac{\left(S_p - S_n\right) I T_f - K \Delta T - \frac{1}{2} I^2 R}{I\left[\left(S_p - S_n\right) \cdot \Delta T + IR\right]}} \qquad (\mathbf{V.12})$$

This equation reflects how the useful Peltier cooling, thermal conduction losses, and Joule heating together determine the device's cooling performance relative to input power. In more practical scenarios, additional parasitic resistances r exist, leading to a modified efficiency expression [12,13].

$$\boldsymbol{\varepsilon_p = \frac{W_{\text{useful}}}{Q} = \frac{I \cdot \left[\left(S_p - S_n\right) \cdot \Delta T + IR\right]}{\left(S_p - S_n\right) I T_f - K \Delta T - \frac{1}{2} I^2 (R + r)}} \qquad (\mathbf{V.13})$$

This formulation accounts for extra resistive losses not included in the ideal model, providing a more realistic efficiency estimate for device operation. The quality of thermoelectric materials is often assessed by the figure of merit $\boldsymbol{Z}$, which combines the Seebeck coefficient,

electrical resistivity, and thermal conductivity. For a thermoelectric couple, this is expressed as [14].

$$Z_{pn} = \frac{\left(S_n - S_p\right)^2}{\left(\sqrt{\kappa_p \rho_p} + \sqrt{\kappa_n \rho_n}\right)^2} \quad (\mathbf{V.14})$$

This expression shows that maximizing the difference in Seebeck coefficients and minimizing the combined resistive and thermal losses leads to better device performance. For a single thermoelectric material, the figure of merit is [14,15]:

$$Z = \frac{S^2}{\rho \cdot \kappa} = \frac{S^2 \sigma}{\kappa} \quad (\mathbf{V.15})$$

Where $\sigma = 1/\rho$ is the electrical conductivity. This ratio encapsulates the intrinsic trade-off among the Seebeck effect, electrical transport, and thermal conduction. Finally, the dimensionless figure of merit ZT, which is temperature-dependent and widely used as a benchmark for thermoelectric materials, is given by [16].

$$ZT = \frac{S^2 \sigma T}{\kappa_e + \kappa_l} \quad (\mathbf{V.16})$$

Here, the total thermal conductivity is split into electronic κ_e and lattice κ_l contributions. A high ZT signifies that a material can efficiently convert heat to electricity or vice versa, driving ongoing research efforts to engineer materials with high Seebeck coefficients, high electrical conductivity, and low thermal conductivity.

V.3 Boltzmann Transport Theory in Thermoelectric Materials

The Boltzmann transport equation (BTE) is a fundamental framework used to describe the behavior of charge carrier's electrons and holes in thermoelectric materials under the influence of external fields and temperature gradients. It provides a detailed description of how the distribution of carriers evolves in time and space, enabling the prediction of key transport properties such as electrical conductivity, Seebeck coefficient, and thermal conductivity. The electrical current density **J** in a material can be expressed as the sum over all charge carriers, where each carrier contributes according to its distribution function f and velocity v [17].

$$\mathbf{J} = e\sum \boldsymbol{f} \cdot \mathbf{v} = \boldsymbol{\sigma} \cdot \mathbf{E} \qquad (\mathbf{V.17})$$

Here, $\boldsymbol{e}$ is the elementary charge, $\boldsymbol{\sigma}$ is the electrical conductivity tensor, and $\mathbf{E}$ is the applied electric field. This equation succinctly connects microscopic carrier dynamics to macroscopic electrical response. The time evolution of the distribution function $\boldsymbol{f}(\mathbf{r}, \mathbf{p}, \boldsymbol{t})$, which represents the probability of finding a carrier at position r with momentum p at time $\boldsymbol{t}$, is governed by the Boltzmann transport equation **[18]**.

$$\frac{\partial \boldsymbol{f}}{\partial \boldsymbol{t}} + \frac{\boldsymbol{d}\mathbf{r}}{\boldsymbol{dt}} \cdot \nabla_{\mathrm{r}} \boldsymbol{f} + \frac{\boldsymbol{d}\mathbf{p}}{\boldsymbol{dt}} \cdot \nabla_{\mathrm{p}} \boldsymbol{f} = \left(\frac{\partial \boldsymbol{f}}{\partial \boldsymbol{t}}\right)_{\boldsymbol{c}} \qquad (\mathbf{V.18})$$

This equation balances the change in distribution due to particle motion in real and momentum space (left side) against the change due to collisions or scattering events (right side) denoted by $\left(\frac{\partial \boldsymbol{f}}{\partial \boldsymbol{t}}\right)_{\boldsymbol{c}}$. Because solving the full BTE is often complex, a common approach is to use the relaxation time approximation (RTA). It assumes that after a disturbance, the distribution function relaxes exponentially back to its equilibrium state $\boldsymbol{f_0}$ over a characteristic timescale $\boldsymbol{\tau}$.

$$\frac{\partial \boldsymbol{f}}{\partial \boldsymbol{t}} = \frac{\boldsymbol{f} - \boldsymbol{f_0}}{\boldsymbol{\tau}} \qquad (\mathbf{V.19})$$

This implies the deviation $\boldsymbol{f} - \boldsymbol{f_0}$ decays as.

$$\boldsymbol{f} - \boldsymbol{f_0} = \boldsymbol{C}\boldsymbol{e}^{-\frac{\boldsymbol{t}}{\boldsymbol{\tau}}} \qquad (\mathbf{V.20})$$

Where $\boldsymbol{C}$ is a constant determined by initial conditions. Under a small-applied electric field and steady-state conditions, the non-equilibrium distribution can be linearized as.

$$\boldsymbol{f} = \boldsymbol{f_0} + \boldsymbol{e}\left(-\frac{\partial \boldsymbol{f_0}}{\partial \boldsymbol{\varepsilon}}\right)\mathbf{v} \cdot \mathbf{E} \qquad (\mathbf{V.21})$$

Where $\boldsymbol{\varepsilon}$ is the carrier energy, and the derivative $-\frac{\partial \boldsymbol{f_0}}{\partial \boldsymbol{\varepsilon}}$ reflects how carriers near the Fermi surface contribute most significantly to transport. From this, the electrical conductivity $\boldsymbol{\sigma}$ can be formulated as a sum over all carrier states weighted by their velocity squared and scattering time.

$$\boldsymbol{\sigma} = \boldsymbol{e}^2 \sum \left(-\frac{\partial \boldsymbol{f_0}}{\partial \boldsymbol{\varepsilon}}\right) \boldsymbol{v}^2 \boldsymbol{\tau} \qquad (\mathbf{V.22})$$

In practical materials, this sum is converted into an integral over energy and crystal momentum k in the Brillouin zone, leading to.

$$\boldsymbol{\sigma(\varepsilon) = \frac{e^2}{N\Omega}\int d\varepsilon\left(-\frac{\partial f_0}{\partial \varepsilon}\right)\sum_{n,k}\tau_{n,k}\,\vec{v}_{n,k}\otimes\vec{v}_{n,k}\delta\left(\varepsilon-\varepsilon_{n,k}\right)} \qquad \mathbf{(V.23)}$$

Where $\boldsymbol{N}$ is the number of sampled k-points, $\boldsymbol{\Omega}$ the unit cell volume, $\boldsymbol{\tau_{n,k}}$ the relaxation time for band $\boldsymbol{n}$ and wavevector $\mathbf{k}$, and $\boldsymbol{\delta}$ is the Dirac delta function ensuring integration only over states at energy $\boldsymbol{\varepsilon}$. The velocity $\boldsymbol{\vec{v}_{n,k}}$ of carriers is obtained directly from the electronic band structure $\boldsymbol{\varepsilon_{n,k}}$ as.

$$\boldsymbol{\vec{v}_{n,k} = \frac{1}{\hbar}\frac{\partial \varepsilon_{n,k}}{\partial \mathbf{k}}} \qquad \mathbf{(V.24)}$$

Linking quantum mechanical band theory with semiclassical transport. When a temperature gradient $\boldsymbol{\nabla T}$ exists alongside an electric field, the total charge current density is influenced not only by electrical forces but also by thermal diffusion of carriers. This leads to the generalized transport relation

$$\boldsymbol{\mathbf{J} = \sigma\mathbf{E} - \sigma S\nabla T} \qquad \mathbf{(V.25)}$$

Where $\boldsymbol{S}$ is the Seebeck coefficient, quantifying the voltage generated per unit temperature gradient. The heat current density $\mathbf{J_q}$ is related to the entropy flux $\mathbf{J_S}$ as

$$\boldsymbol{\mathbf{J} = T\mathbf{J}_S = ST\mathbf{J} - \kappa\nabla T} \qquad \mathbf{(V.26)}$$

With $\boldsymbol{\kappa}$ representing the electronic thermal conductivity. Using Onsager reciprocal relations, the Seebeck coefficient and electronic thermal conductivity can be rigorously expressed via integrals over the electronic structure as:

$$\boldsymbol{S = \frac{ek_B}{N\Omega}\sigma^{-1}\int d\varepsilon\left(-\frac{\partial f_0}{\partial \varepsilon}\right)\left(\frac{\varepsilon-\mu}{k_BT}\right)\sum_{n,k}\tau_{n,k}\,\vec{v}_{n,k}\otimes\vec{v}_{n,k}\delta\left(\varepsilon-\varepsilon_{n,k}\right)} \qquad \mathbf{(V.27)}$$

$$\boldsymbol{\kappa_e = \frac{k_B^2T}{N\Omega}\int d\varepsilon\left(-\frac{\partial f_0}{\partial \varepsilon}\right)\left(\frac{\varepsilon-\mu}{k_BT}\right)^2\sum_{n,k}\tau_{n,k}\,\vec{v}_{n,k}\otimes\vec{v}_{n,k}\delta\left(\varepsilon-\varepsilon_{n,k}\right) - T\sigma S^2} \qquad \mathbf{(V.28)}$$

Where $\boldsymbol{\mu}$ is the chemical potential and $\boldsymbol{k_B}$ the Boltzmann constant. These equations establish a direct link between microscopic electronic structure details such as band energies, carrier velocities, and scattering times and macroscopic transport coefficients measurable in experiments. The Boltzmann transport formalism thus forms the theoretical foundation for predicting and optimizing the performance of thermoelectric materials, guiding the design of new compounds with enhanced efficiency for energy conversion applications.

V.4 Results and Discussion

V.4.1 Seebeck Coefficient (S)

For Ba_2InOsO_6, the GGA results **Figure V.1 (a)** show that the Seebeck coefficient remains zero below 175 K, indicating negligible carrier excitation at low temperature. As the temperature increases beyond this point, **S** drops sharply to -2.59 µV/K and then gradually increases to -1.60 µV/K at room temperature (300 K) and -0.73 µV/K at 800 K. This trend reflects a typical n-type thermoelectric behavior, where electron carriers dominate transport, and their thermal activation increases with temperature **[19]**. The GGA+U approximation **Figure V.1 (b)** yields a similar overall trend, with slightly lower magnitudes: S reaches -2.61 µV/K at 175 K, -1.74 µV/K at 300 K and -0.74 µV/K at 800 K, indicating that electron-electron correlations slightly reduce the thermopower but maintain the same conduction mechanism.

Under the mBJ+U functional **Figure V.1(c)**, a different behavior is observed: the Seebeck coefficient remains zero until 375 K, after which it sharply decreases to -2.86 µV/K and increases steadily to -1.42 µV/K at 800 K. The delayed onset of non-zero values indicates that mBJ+U predicts a larger band gap, requiring higher thermal energy for carrier excitation **[20]**. The mBJ+U+SOC results **Figure V.1 (d),** significantly alters the thermoelectric response. **S** is no longer zero at low temperature, starting at -0.16 µV/K at 50 K and showing a shallow decrease to -0.26 µV/K at 300 K before slightly increasing to -0.24 µV/K at 800 K. This muted thermoelectric response and weak temperature dependence suggest that spin-orbit coupling modifies the electronic structure by reducing band asymmetry or introducing degeneracies, leading to a lower Seebeck magnitude **[21]**. Nonetheless, Ba_2InOsO_6 consistently displays n-type conduction across all approximations, with the transport properties being strongly influenced by the functional choice and the inclusion of SOC.

In the case of Sr_2MnSbO_6, which crystallizes in the tetragonal phase, the Seebeck coefficient was analyzed in two crystallographic directions (X and Z) due to anisotropy. Under the GGA approximation **Figure V.1 (a)**, both directions exhibit nearly identical thermoelectric behavior. The Seebeck coefficient remains zero below 250 K and then shows a sharp drop to -2.59 µV/K at 250 K, followed by a gradual increase to -0.94 µV/K at 800 K. This behavior again reflects n-type transport, with similar thermopower in both directions, indicating isotropic electronic behavior within the studied range **[19]**. However, when the Hubbard U correction is applied **Figure V.1 (b)**, the sign of the Seebeck coefficient changes, indicating a switch to p-type behavior **[19]**. S remains zero below 250 K, but then increases sharply to +2.85 µV/K at 250 K, followed by a decrease with increasing temperature. At 800 K, the Seebeck coefficient reaches +1.04 µV/K in the X direction and +0.99 µV/K in the Z direction, suggesting weak but measurable anisotropy in hole-dominated transport.

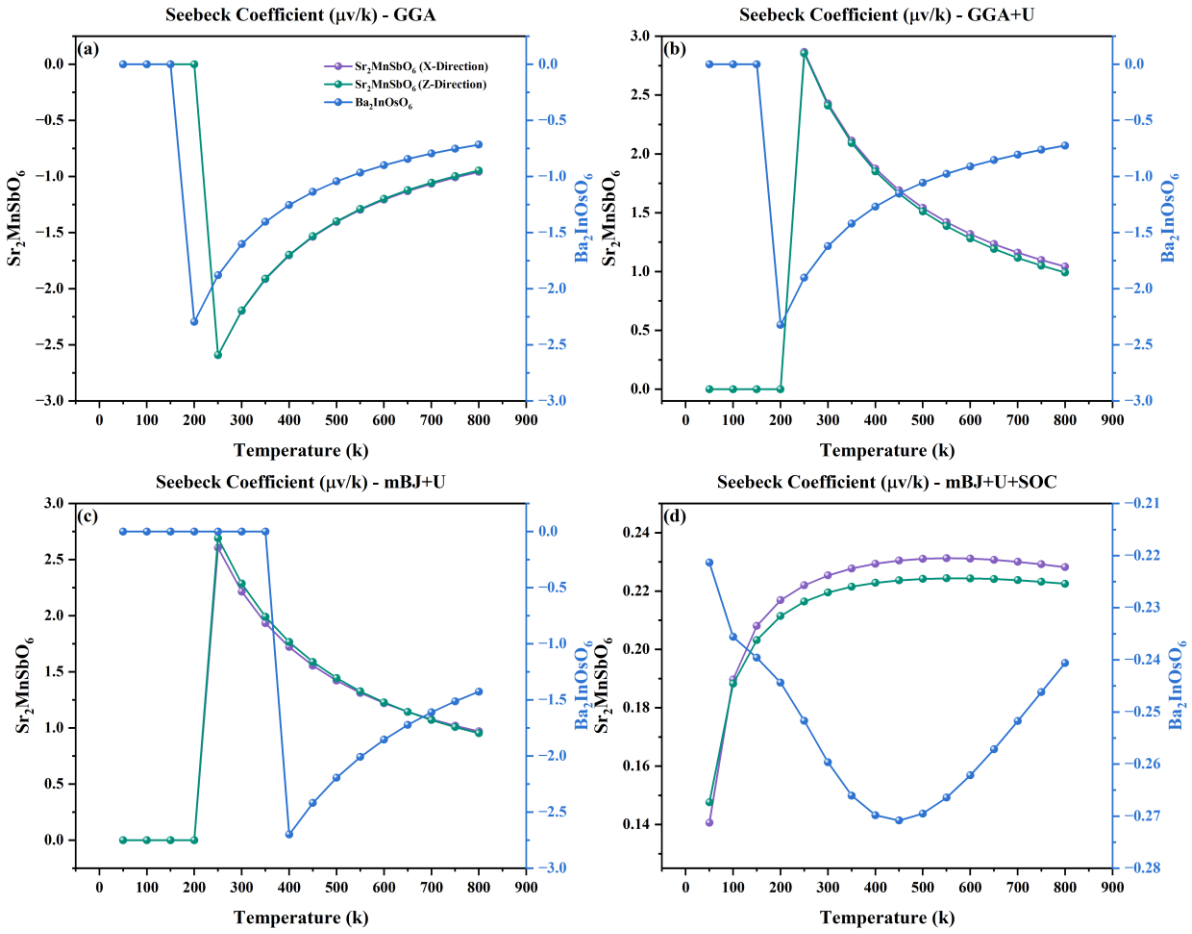

Figure V.1. Seebeck Coefficient of Double Perovskite Compounds Ba_2InOsO_6 and Sr_2MnSbO_6 under various approximations, **(a)** GGA, **(b)** GGA+U, **(c)** mBJ+U, and **(d)** mBJ+U+SOC

The mBJ+U approximation **Figure V.1(c),** maintains this p-type character, with the Seebeck coefficient reaching +2.60 μV/K (X direction) and +2.69 μV/K (Z direction) at 300 K, followed by a gradual decrease to about +0.95 μV/K at 800 K for both directions. This confirms the enhancement of the transport gap and stabilization of hole-type carriers in the mBJ+U approach. Upon including SOC **Figure V.1 (d)**, the overall positive thermopower is preserved, but the directional anisotropy becomes more apparent. At low temperature (50 K), the Seebeck coefficient is +0.14 μV/K in the X direction and +0.15 μV/K in the Z direction. As temperature increases, the values diverge slightly: +0.22 μV/K (X) and +0.21 μV/K (Z) at 300 K, and +0.23 μV/K (X) versus +0.22 μV/K (Z) at 800 K. These small but consistent differences suggest that spin-orbit coupling subtly affects the electronic band curvature differently along each axis, leading to a modest directional dependence in thermoelectric performance **[21]**.

V.4.2 The Electrical Conductivity (σ/τ)

The temperature-dependent electrical conductivity divided by relaxation time, σ/τ, expressed in units of $(\Omega \cdot cm \cdot s)^{-1}$, was analyzed for Ba_2InOsO_6 in its cubic phase using four different computational schemes: GGA, GGA+U, mBJ+U, and mBJ+U+SOC, as shown in **Figure V.2(a–d)**. Under the GGA approximation **Figure V.2 (a)**, the electrical conductivity remains zero until approximately 150 K. At 175 K, it begins to increase, reaching 1.3×10^{6} $(\Omega \cdot cm \cdot s)^{-1}$. This value continues to rise sharply with temperature, reaching 3.0×10^{11} at 300 K and 2.84×10^{16} $(\Omega \cdot cm \cdot s)^{-1}$ at 800 K. This strong temperature dependence is consistent with semiconducting behavior, where thermal excitation significantly increases the number of charge carriers. The GGA+U method **Figure V.2 (b),** yields a similar profile, maintaining zero conductivity below 150 K, followed by a rapid increase from 175 K. The values closely mirror those obtained with GGA, indicating that the on-site Coulomb interaction (U) does not drastically alter the carrier activation trend but may slightly affect the carrier concentration **[21]**.

The mBJ+U approximation **Figure V.2(c)** predicts a larger transport gap, as indicated by the conductivity remaining nearly zero until 375 K. At this temperature, σ/τ reaches 3.54×10^{6} $(\Omega \cdot cm \cdot s)^{-1}$ and continues to rise with temperature, reaching 1.22×10^{13} $(\Omega \cdot cm \cdot s)^{-1}$ at 800 K. This delayed onset is in agreement with the Seebeck coefficient behavior under the same approximation and reflects the sensitivity of transport properties to the size of the predicted

band gap. A distinctly different behavior is observed with the inclusion of spin–orbit coupling (SOC) in the mBJ+U+SOC approximation **Figure V.2 (d)**. In this case, the electrical conductivity is already significant at very low temperatures, starting with a high value of 3.26×10^{16} $(\Omega\cdot cm\cdot s)^{-1}$ at 50 K. This value increases further to 4.29×10^{17} at 300 K and reaches a maximum of 2.39×10^{18} $(\Omega\cdot cm\cdot s)^{-1}$ at 800 K. The absence of a thermal activation threshold and the high conductivity values even at low temperatures indicate a transition toward metallic-like behavior. This suggests that SOC significantly alters the band structure likely narrowing the band gap or causing band overlap, which leads to a continuous increase in carrier density and mobility **[22]**.

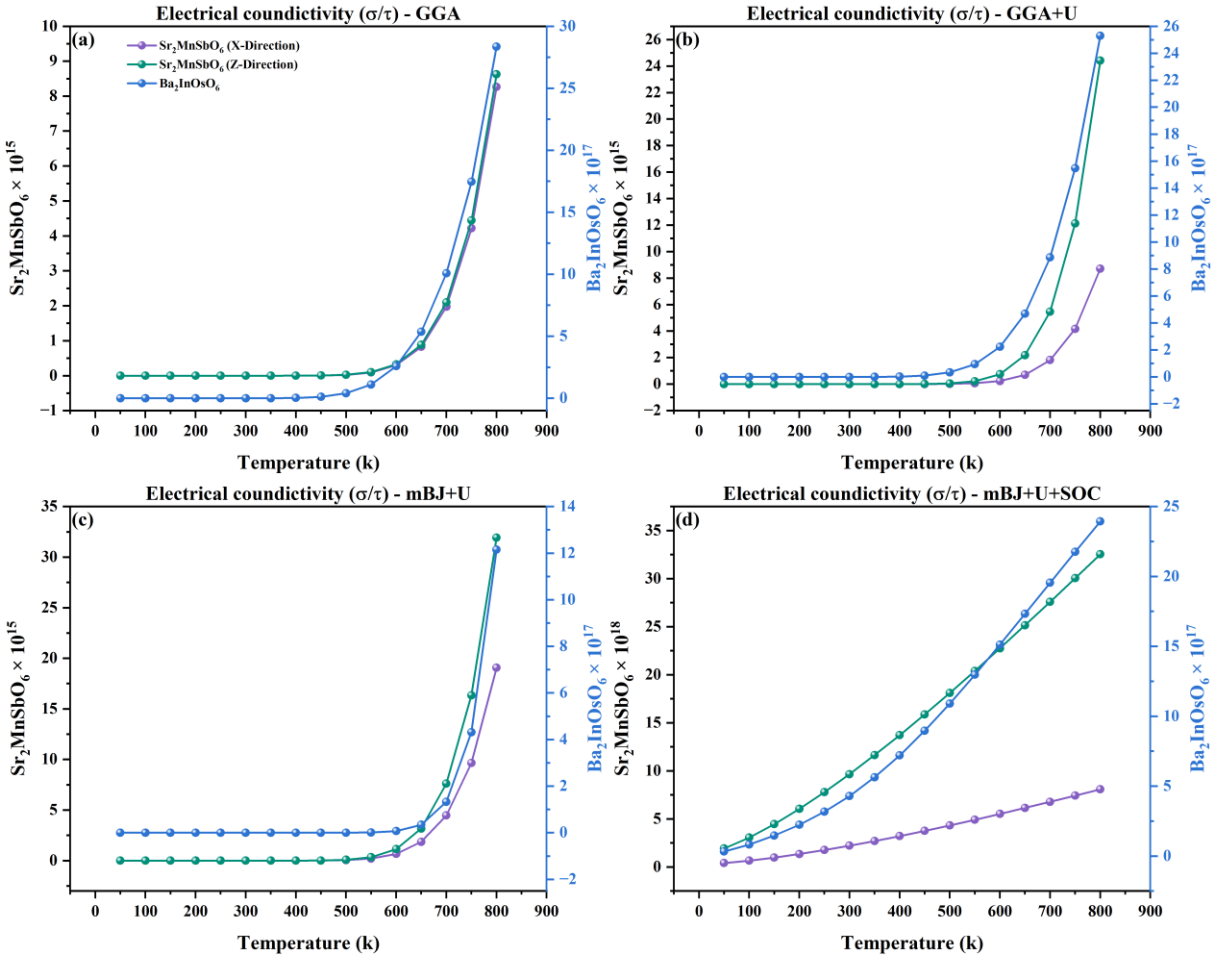

Figure V.2. The Electrical Conductivity of Double Perovskite Compounds Ba_2InOsO_6 and Sr_2MnSbO_6 under various approximations, **(a)** GGA, **(b)** GGA+U, **(c)** mBJ+U, and **(d)** mBJ+U+SOC

For Sr_2MnSbO_6, which crystallizes in a tetragonal phase, the electrical conductivity was evaluated along both the X and Z crystallographic directions. Under the GGA, GGA+U, and mBJ+U approximations **Figures V.2(c)**, σ/τ is zero below 150 K for both directions, indicating semiconducting character. Above this threshold, conductivity increases with temperature. At 300 K, the GGA approximation gives a conductivity of 9.38×10^{6} $(\Omega\cdot cm\cdot s)^{-1}$, while the GGA+U value is substantially higher at 9.80×10^{16} $(\Omega\cdot cm\cdot s)^{-1}$. The mBJ+U approximation yields a value of 1.62×10^{7} $(\Omega\cdot cm\cdot s)^{-1}$ at 300 K for both directions, consistent with its prediction of a larger band gap. Directional differences become more apparent upon including SOC in the mBJ+U+SOC approximation **Figure V.2 (d)**. At 300 K, the conductivity in the X direction is 1.76×10^{17} $(\Omega\cdot cm\cdot s)^{-1}$, while in the Z direction it is notably higher at 7.79×10^{17} $(\Omega\cdot cm\cdot s)^{-1}$. This anisotropy becomes increasingly pronounced at higher temperatures. At 800 K, the conductivity reaches 8.26×10^{14} $(\Omega\cdot cm\cdot s)^{-1}$ for GGA-X, 8.62×10^{14} for GGA-Z, 8.71×10^{14} for GGA+U-X, and 2.44×10^{15} $(\Omega\cdot cm\cdot s)^{-1}$ for GGA+U-Z. For mBJ+U, the conductivity is 1.91×10^{15} $(\Omega\cdot cm\cdot s)^{-1}$ in the X direction and 3.19×10^{15} in the Z direction. With mBJ+U+SOC, the conductivity significantly increases to 8.08×10^{17} $(\Omega\cdot cm\cdot s)^{-1}$ along X direction and 3.25×10^{18} along Z direction, confirming a strong directional anisotropy induced by SOC at high temperatures. These results suggest that SOC not only increases the conductivity by modifying the band structure but also affects the band curvature differently along each crystallographic axis, leading to anisotropic transport.

V.4.3 The Electronic Thermal Conductivity

The electronic part of thermal conductivity divided by relaxation time (**κe/τ**), as a function of temperature, was calculated for Ba_2InOsO_6 in its cubic phase using four different exchange-correlation approximations: GGA, GGA+U, mBJ+U, and mBJ+U+SOC, shown in **Figure V.3 (a–d)**. The thermal conductivity trend follows the same pattern observed for the electrical conductivity and Seebeck coefficient. For both GGA and GGA+U **Figure V.3 (a)** and **Figure V.3 (b)**, the thermal conductivity remains null at low temperatures, indicating absence of thermally activated carriers **[23]**. It starts increasing with temperature and reaches approximately 2.32×10^{8} $(W\cdot K^{-1}\cdot cm^{-1}\cdot s^{-1})$ at 300 K for GGA and 1.83×10^{8} for GGA+U. The values continue rising, reaching 1.19×10^{13} and 1.09×10^{13}, respectively, at 800 K. These results

indicate a thermally driven increase in carrier concentration, and the similarity with the electrical conductivity behavior reflects their direct relation via the Wiedemann-Franz law **[24]**.

In the mBJ+U approximation **Figure V.3(c)**, a larger transport gap delays the onset of thermal conductivity, remaining negligible until 375 K. After this point, (**κe/τ**) starts rising and reaches 1.99×10^{10} ($W\cdot K^{-1}\cdot cm^{-1}\cdot s^{-1}$) at 800 K. This delayed activation is in line with the behavior of the Seebeck and electrical conductivity under the same approximation, again reinforcing the prediction of a larger band gap. When spin-orbit-coupling (SOC) is included, **Figure V.3 (d)**, the behavior changes substantially. The conductivity is no longer null at low temperatures and starts at 1.13×10^{11} at 50 K, increases to 1.19×10^{11} at 300 K, and reaches 1.31×10^{14} ($W\cdot K^{-1}\cdot cm^{-1}\cdot s^{-1}$) at 800 K. This significant increase and the absence of a temperature threshold suggest that SOC strongly modifies the band structure, enhancing electronic contributions to thermal transport even at cryogenic temperatures, likely due to enhanced carrier mobility and possible band overlap.

For Sr_2MnSbO_6, which adopts a tetragonal phase, the electrothermal conductivity was calculated along both X and Z directions. Under the GGA, GGA+U, and mBJ+U approximations **Figures V.3 (a–c)**, (**κe/τ**) remains zero below 200 K in both directions, consistent with a semiconducting ground state. Above 200 K, conductivity begins to rise and reaches nearly identical values in both directions at room temperature. At 300 K, the thermal conductivity is 1.77×10^{5} for GGA, 1.53×10^{5} for GGA+U, and 4.08×10^{5} ($W\cdot K^{-1}\cdot cm^{-1}\cdot s^{-1}$) for mBJ+U. These similar values along X and Z directions suggest minimal anisotropy at this temperature range. However, upon inclusion of SOC **Figure V.3 (d)**, a clear directional dependence emerges. At 300 K, the X direction exhibits a value of 4.64×10^{12}, while the Z direction reaches 1.93×10^{13}, indicating that SOC introduces significant band structure anisotropy that strongly affects the thermal transport.

This anisotropy becomes even more pronounced at higher temperatures. At 800 K, the full set of values shows a significant divergence between directions: for GGA, the conductivity is 6.20×10^{11} (X) and 6.29×10^{11} (Z); for GGA+U, it increases to 7.70×10^{11} (X) and 1.94×10^{12} (Z); for mBJ+U, values are 1.46×10^{12} (X) and 2.35×10^{12} (Z). With SOC (mBJ+U+SOC), the difference becomes particularly striking: 4.44×10^{13} in the X direction versus 1.72×10^{14}

($W \cdot K^{-1} \cdot cm^{-1} \cdot s^{-1}$) in the Z direction. These results confirm that SOC plays a dominant role in altering the electronic structure to favor directional transport properties, likely due to lifting of band degeneracies and enhancement of effective masses differently along the crystallographic axes.

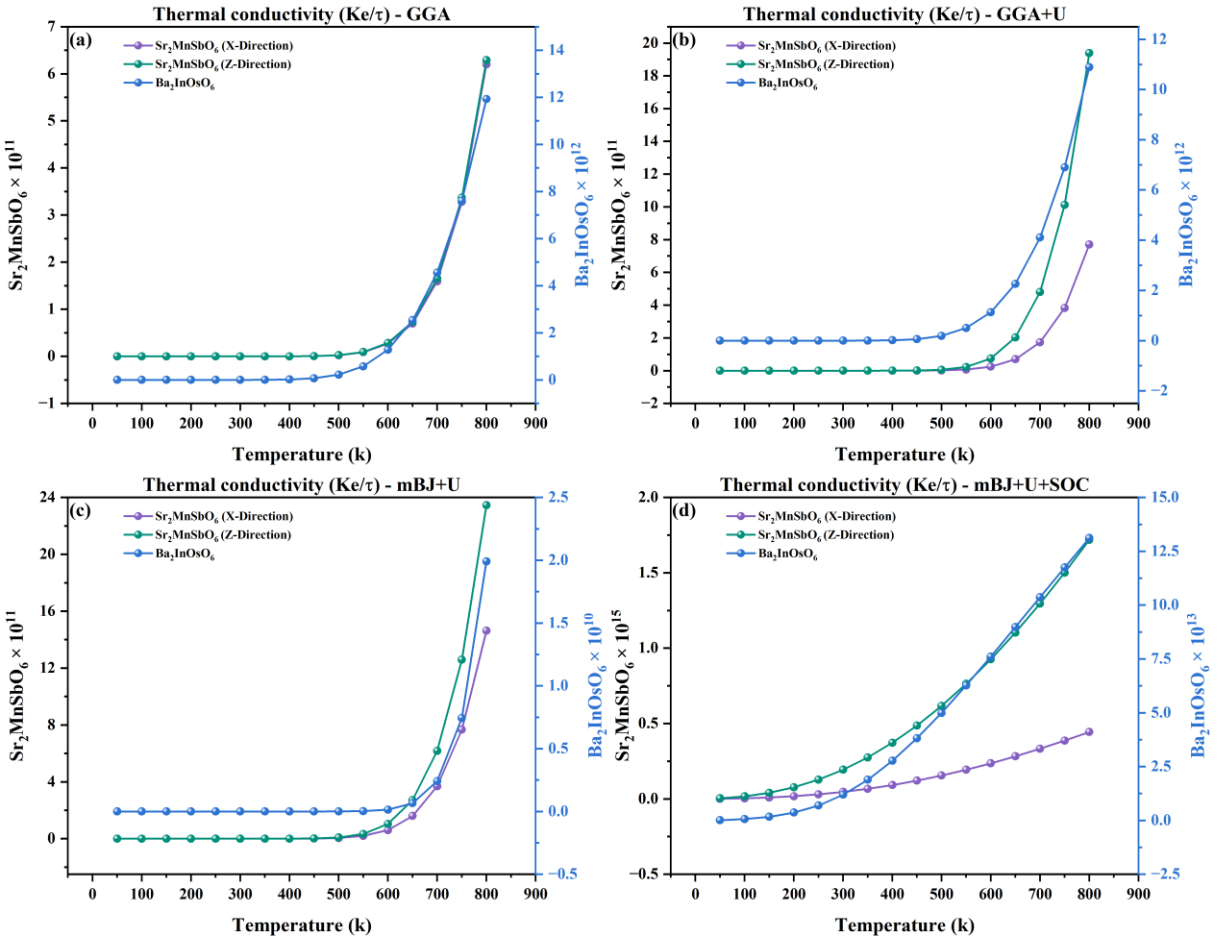

Figure V.3. The electronic part of Thermal Conductivity of Double Perovskite Compounds Ba_2InOsO_6 and Sr_2MnSbO_6 under various approximations, **(a)** GGA, **(b)** GGA+U, **(c)** mBJ+U, and **(d)** mBJ+U+SOC

V.4.4 The figure of merit (ZT)

The figure of merit (**ZT**), was calculated for both Ba_2InOsO_6 and Sr_2MnSbO_6 across various temperature ranges (50 K to 800 K) and under different approximations: GGA, GGA+U, mBJ+U, and mBJ+U+SOC, as shown in **Figures V.4 (a–d)**. For Ba_2InOsO_6 in the cubic phase, the results using GGA, GGA+U, and mBJ+U demonstrate a decreasing trend in (**ZT**) as temperature increases. Although the decrease is not drastic, all approximations show

(**ZT**) values ranging from 0.99 to 0.94 across the entire temperature range, from 50 K to 800 K. This suggests that the material maintains a relatively stable thermoelectric performance within the given range, with no significant enhancement observed in the figure of merit. In contrast, when spin–orbit coupling (SOC) is applied **Figure V.4 (d)**, the trend changes significantly. The (**ZT**) value initially starts at 0.51 at 50 K, then increases sharply to 0.74 at 200 K. After a slight decrease around room temperature (0.72), (**ZT**) rises again to reach 0.84 at 800 K, reflecting an improvement in thermoelectric efficiency with increasing temperature due to the influence of SOC. This behavior suggests that SOC enhances the material's performance by affecting the electronic structure, likely through a reduction in thermal conductivity or improvement in carrier mobility.

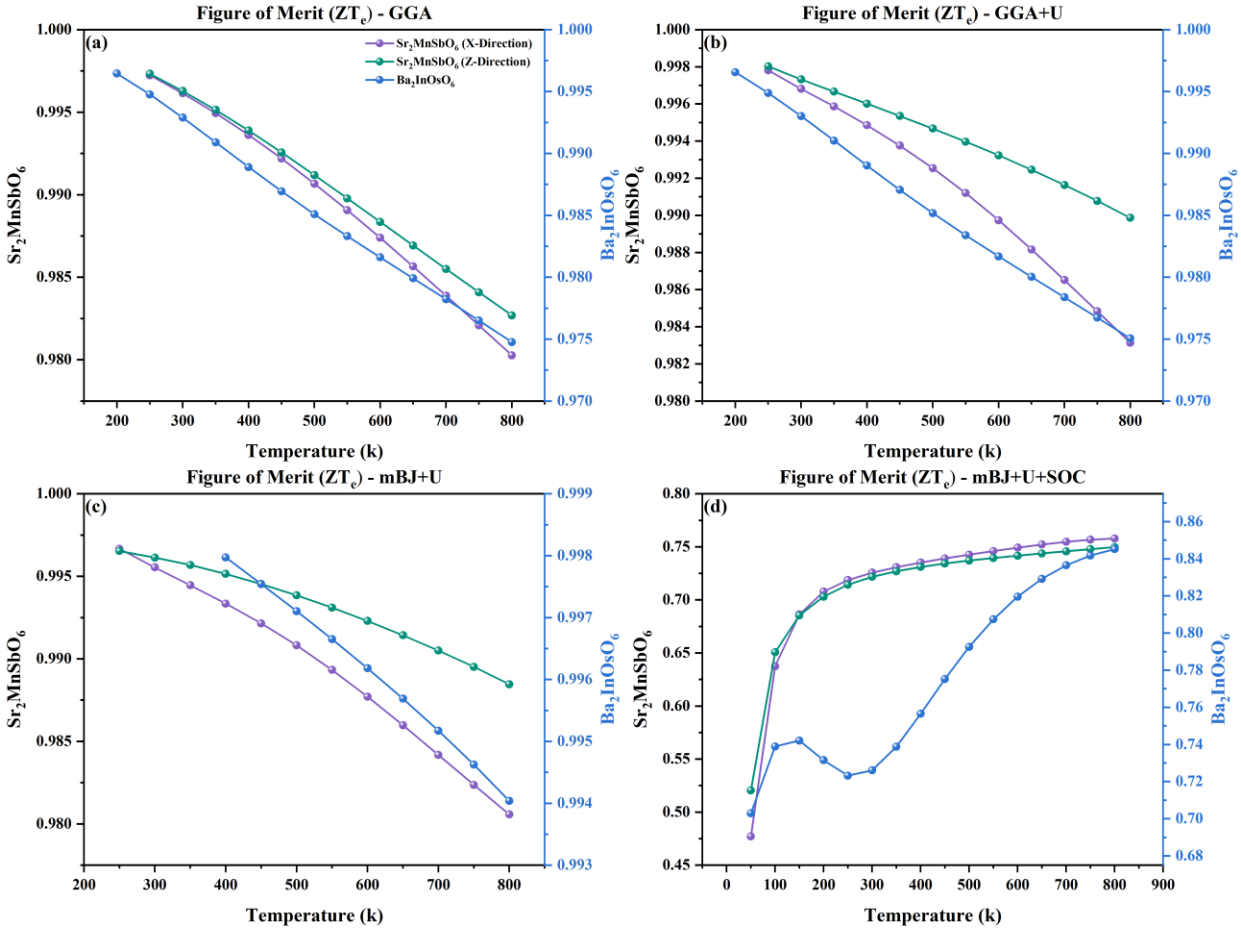

Figure V.4. The electronic part of Thermal Conductivity of Double Perovskite Compounds Ba_2InOsO_6 and Sr_2MnSbO_6 under various approximations, **(a)** GGA, **(b)** GGA+U, **(c)** mBJ+U, and **(d)** mBJ+U+SOC

For Sr_2MnSbO_6 in the tetragonal phase, the trend is similar but with some differences in the directional dependence of (**ZT**). In both the X and Z directions, the GGA, GGA+U, and mBJ+U approximations **Figures V.4 (a–c)** show nearly identical behavior. The (**ZT**) values for the X direction range between 0.998 and 0.983, while in the Z direction, the values range between 0.998 and 0.992. These values indicate a slight directional dependence, with the Z direction performing marginally better in all three approximations. However, this difference is not significant enough to greatly affect the overall performance of the material. After applying SOC **Figure V.4 (d)**, both directions exhibit a clear increase in (**ZT**) with temperature, similar to the behavior observed for Ba_2InOsO_6. At 50 K, (ZT) starts at 0.47, rises to 0.72 at 300 K, and further increases to 0.75 at 800 K. Interestingly, the difference between the X and Z directions remains minimal, suggesting that the influence of SOC on the directional dependence of the thermoelectric properties is not as pronounced as in Ba_2InOsO_6.

V.5 Conclusion

This chapter has provided an in-depth analysis of the thermoelectric properties of materials, focusing on the theoretical and practical aspects that govern their performance in energy conversion applications. Through the examination of key thermoelectric effects Seebeck, Peltier, and Thomson this chapter has highlighted how these phenomena underpin the conversion of heat into electricity, making thermoelectric materials crucial for sustainable technologies aimed at energy harvesting and waste heat recovery. A detailed study of compounds like Ba_2InOsO_6 and Sr_2MnSbO_6 has demonstrated how different computational approximations (such as GGA, GGA+U, mBJ+U, and mBJ+U+SOC) affect their thermoelectric characteristics, including the Seebeck coefficient, electrical conductivity, thermal conductivity, and the figure of merit (**ZT**). The results indicate that spin-orbit coupling (SOC) significantly influences the electronic structure, enhancing carrier mobility and modifying thermal transport properties, thereby improving the overall thermoelectric performance, especially at higher temperatures. The chapter also emphasized the directional anisotropy observed in Sr_2MnSbO_6, which became more pronounced when SOC was included, indicating the importance of considering crystallographic directionality in material design. Moreover, while Ba_2InOsO_6 exhibited relatively stable thermoelectric performance, the inclusion of SOC led to notable improvements in its figure of merit, particularly at elevated

temperatures. These findings underscore the necessity of optimizing material properties, particularly by engineering electronic structure, to enhance the efficiency of thermoelectric devices. Future advancements in this field will likely involve tailored materials with improved thermoelectric properties, providing promising solutions for energy conversion technologies in diverse applications, from industrial waste heat recovery to solid-state cooling systems. Thus, this chapter not only advances our understanding of thermoelectric materials but also lays the groundwork for future research and development aimed at creating more efficient and sustainable thermoelectric systems.

Bibliography

[**1**] Brostow, Granowski, Hnatchuk, Sharp & White, *Journal of Materials Education*, 2014, **36**, 175–186.

[**2**] Uchida, Takahashi, Harii, Ieda, Koshibae, Ando, Maekawa & Saitoh, *Nature*, 2008, **455**, 778–781.

[**3**] Bai, Liu, Liu, Sun, Lian & Liu, *Phys Teach*, 2022, **60**, 586–587.

[**4**] Buchelnikov, Sokolovskiy, Matyunina & Enenko, *Physics of Metals and Metallography*, 2024, **125**, 1814–1820.

[**5**] Sandoz-Rosado, Weinstein & Stevens, *International Journal of Thermal Sciences*, 2013, **66**, 1–7.

[**6**] Huang, Yen & Wang, *Int J Heat Mass Transf*, 2005, **48**, 413–418.

[**7**] Manzanares, Jokinen & Cervera, *Journal of Non-Equilibrium Thermodynamics*, 2015, **40**, 211–227.

[**8**] Alghamdi, Maduabuchi, Albaker, Alatawi, Alsenani, Alsafran, AlAqil & Alkhedher, *J Therm Anal Calorim*, 2024, **149**, 5341–5365.

[**9**] Cheng, Huang & Cheng, *Int J Heat Mass Transf*, 2010, **53**, 2001–2011.

[**10**] Sobrino, Eich, Stefanucci, D'Agosta & Kurth, *Phys Rev B*, 2021, **104**, 125115.

[**11**] Price, *Physical Review*, 1956, **104**, 1223.

[**12**] Multiphase Flow and Fluidization | ScienceDirect, https://www.sciencedirect.com/book/9780080512266/multiphase-flow-and-fluidization, (accessed 2 August 2025).

[**13**] Harman, Cahn & Logan, *J Appl Phys*, 1959, **30**, 1351–1359.

[**14**] Mahan & D., *JAP*, 1989, **65**, 1578–1583.

[**15**] Snyder & Snyder, *Energy Environ Sci*, 2017, **10**, 2280–2283.

[**16**] Nemir & Beck, *J Electron Mater*, 2010, **39**, 1897–1901.

[**17**] Deterministic Solvers for the Boltzmann Transport Equation - Sung-Min Hong, Anh-Tuan Pham, Christoph Jungemann - Google Books, https://books.google.dz/books?hl=en&lr=&id=AhHGGsO2HDwC&oi=fnd&pg=PR3&dq=boltzmann+transport+equations&ots=usJSX4liCB&sig=oUW3VUalYSLwfK0iWzJKV2F1NQU&redir_esc=y#v=onepage&q=boltzmann%20transport%20equations&f=false, (accessed 2 August 2025).

[**18**] Péraud, Landon & Hadjiconstantinou, *Annual Review of Heat Transfer*, 2014, **17**, 205–265.

[**19**] Farhadi, Zabihi, Lugoloobi & Liu, *Solar Energy*, 2022, **233**, 11–17.

[**20**] Muchtar, Srinivasan, Tonquesse, Singh, Soelami, Yuliarto, Berthebaud & Mori, *Adv Energy Mater*, 2021, **11**, 2101122.

[**21**] Gmitra, Konschuh, Ertler, Ambrosch-Draxl & Fabian, *Phys Rev B Condens Matter Mater Phys*, 2009, **80**, 235431.
[**22**] Ali, Alam, Ali, Dar, Khan, Murtaza & Laref, *Int J Quantum Chem*, 2020, **120**, e26141.
[**23**] Zhong, Yin, Chen, Gao & Wang, *ACS Appl Mater Interfaces*, 2020, **12**, 26276–26285.
[**24**] Chen & Podloucky, *Phys Rev B Condens Matter Mater Phys*, 2013, **88**, 045134.

CHAPTER VI

Optical Properties

VI.1 Introduction

This chapter explores the optical properties of various perovskite materials, focusing on the theoretical background and the equations that govern their interaction with electromagnetic radiation. The complex dielectric function plays a pivotal role in determining a material's optical behavior, and its components namely, the real and imaginary parts are fundamental for calculating optical constants such as refractive index, extinction coefficient, absorption coefficient, and energy loss function. First-principles calculations are employed to investigate these properties across a range of materials, including $ASiCl_3$, A_3SbAs, A_3BiI_3, and $Rb_2Pt_{1-x}Pd_xBr_6$, in the near-infrared (NIR), visible, and ultraviolet (UV) regions. By analyzing the frequency-dependent behavior of the dielectric function, we aim to gain deeper insights into the optical characteristics of these materials and their potential for applications in optoelectronics, photonics, and energy harvesting technologies. In this work, structural and electronic optimization was carried out on an initial set of fourteen compounds to assess their stability and fundamental electronic properties. These materials have already been the subject of eleven international publications in renowned journals, highlighting their scientific interest. Based on these results, four compounds were selected for in-depth optical investigation. This choice followed a rigorous comparative analysis of key parameters, such as crystal stability (formation energy, structural cohesion), band gap width, and the nature of electronic transitions (direct or indirect).

VI.2 Complex Dielectric Function

The complex dielectric function plays a central role in the theoretical description of how a material interacts with electromagnetic radiation. In solid-state physics and materials science, it serves as a fundamental link between a material's electronic structure and its optical behavior. From a microscopic perspective, the dielectric function arises from the linear response of the electron system to an external perturbation, such as an applied electric field associated with an incident photon. It describes how the internal polarization of the medium screens the external field, influencing the propagation of electromagnetic waves within the material. Mathematically, it is a frequency-dependent complex function denoted as **[1]**.

$$\boldsymbol{\varepsilon(\omega) = \varepsilon_1(\omega) + i\varepsilon_2(\omega)} \qquad \textbf{(VI. 1)}$$

Where $\boldsymbol{\omega}$ is the angular frequency of the incident light. In first-principles calculations, the dielectric function is evaluated using time-dependent perturbation theory within the

independent particle approximation (IPA) or the more accurate random phase approximation (RPA), which includes many-body effects without electron-hole interactions.

VI.2.1 Real Part of the Dielectric Function $\boldsymbol{\varepsilon_1(\omega)}$

The real part of the complex dielectric function, denoted as $\boldsymbol{\varepsilon_1(\omega)}$, describes the dispersive response of a material to an external electromagnetic field. Physically, it represents the material's ability to polarize in response to the oscillating electric field of incident radiation, thereby affecting the phase velocity of the propagating wave. In essence, $\boldsymbol{\varepsilon_1(\omega)}$ governs how light bends and slows down as it travels through the medium. In the low-frequency limit, the static dielectric constant $\boldsymbol{\varepsilon_1(0)}$ provides crucial information about the polarizability of the system in the absence of absorption. A high value of $\boldsymbol{\varepsilon_1(0)}$ generally indicates a strong polarization response, which is often associated with high lattice or electronic polarizability. This is particularly relevant in semiconducting and insulating materials, where ionic displacements and electronic cloud deformation contribute significantly to the dielectric screening [2].

Importantly, the behavior of $\boldsymbol{\varepsilon_1(\omega)}$ is not computed directly in first-principles methods. Instead, it is derived from the imaginary part $\boldsymbol{\varepsilon_2(\omega)}$ via the Kramers-Kronig relations, which ensure that causality is preserved in the optical response [3].

$$\boldsymbol{\varepsilon_1(\omega) = 1 + \frac{2}{\pi}\mathcal{P}\int_0^{\infty} \frac{\omega'\varepsilon_2(\omega')}{\omega'^2 - \omega^2}\, d\omega'} \qquad \textbf{(VI. 2)}$$

Where $\boldsymbol{\mathcal{P}}$ denotes the principal value of the integral. This relationship guarantees that the real and imaginary components of the dielectric function are not independent but are interlinked through fundamental physical constraints.

VI.2.2 Imaginary Part of the Dielectric Function $\boldsymbol{\varepsilon_2(\omega)}$

The imaginary part of the complex dielectric function, denoted $\boldsymbol{\varepsilon_2(\omega)}$, quantifies the absorptive behavior of a material when subjected to an external electromagnetic field. It represents the dissipation of electromagnetic energy due to electronic excitations, particularly interband transitions, and is directly related to the material's ability to absorb photons at specific energies. In the framework of linear response theory and within the independent particle

approximation (IPA), $\boldsymbol{\varepsilon_2(\omega)}$ can be computed directly from first-principles using the following expression [1].

$$\boldsymbol{\varepsilon_2^{\alpha\beta}(\omega) = \frac{4\pi^2 e^2}{\Omega} \lim_{q\to 0} \frac{1}{q^2} \sum_{k,v,c} 2\, w_k \delta(E_{ck} - E_{vk} - \hbar\omega) \left\langle u_{ck+e_\alpha q} | u_{vk} \right\rangle \left\langle u_{vk} | u_{ck+e_\beta q} \right\rangle} \quad \textbf{(VI. 3)}$$

where $\mathbf{v}$ and $\mathbf{c}$ denote valence and conduction band states, respectively; $\mathbf{k}$ are the wavevectors in the Brillouin zone; $\mathbf{w_k}$ are the corresponding weights; $\boldsymbol{\Omega}$ is the unit cell volume; and $\boldsymbol{\alpha, \beta}$ refer to Cartesian directions of the electric field polarization. The delta function enforces energy conservation, ensuring that only transitions with photon energies matching the band-to-band energy difference contribute to $\boldsymbol{\varepsilon_2(\omega)}$. The spectral features of $\boldsymbol{\varepsilon_2(\omega)}$ are closely tied to the electronic structure of the material. Peaks in $\boldsymbol{\varepsilon_2(\omega)}$ correspond to regions in the energy spectrum where high densities of allowed electronic transitions occur. These features are influenced by the joint density of states (JDOS), and the transition dipole matrix elements, both of which are determined by the nature of the band structure and the symmetry of the wavefunctions involved [3].

VI.3 Derived Optical Constants

Once the complex dielectric function $\boldsymbol{\varepsilon(\omega)}$ is obtained, a set of important optical constants can be derived. These constants provide physical insights into how electromagnetic waves propagate through and interact with the material. Using well-established mathematical relations, one can compute the refractive index, extinction coefficient, reflectivity, absorption coefficient, and energy loss function. Each of these quantities reveals specific aspects of the optical behavior, such as transparency, reflectance, and electronic excitation characteristics. In the following subsections, we present a detailed analysis of each of these optical parameters as derived from first-principles calculations.

VI.3.1 Complex Refractive Index

The complex refractive index provides a comprehensive description of the propagation of electromagnetic radiation in a medium by accounting for both the phase shift and the attenuation of light. It is defined as [4]:

$$\tilde{\mathbf{n}}(\boldsymbol{\omega}) = \mathbf{n}(\boldsymbol{\omega}) + \mathbf{ik}(\boldsymbol{\omega}) \quad (\mathbf{VI.4})$$

Where, $\mathbf{n}(\boldsymbol{\omega})$ is the real part known as the refractive index, and $\mathbf{k}(\boldsymbol{\omega})$ is the imaginary part, referred to as the extinction coefficient. This complex quantity is derived from the frequency-dependent dielectric function and links theoretical calculations with experimentally accessible optical parameters. Its accurate evaluation provides essential insights for applications in photonics, photovoltaics, and transparent electronics. In the following subsections, each component of $\tilde{\mathbf{n}}(\boldsymbol{\omega})$ is analyzed separately, with emphasis on its physical significance and behavior in perovskite materials **[4-6]**.

VI.3.1.1 Real Part: Refractive Index

The real part of the complex refractive index, $\mathbf{n}(\boldsymbol{\omega})$, determines the phase velocity of light within the material and governs optical phenomena such as refraction, waveguiding, and dispersion. It reflects the extent to which light slows down as it traverses the medium, and its spectral variation is closely linked to the underlying electronic structure. Mathematically, $\mathbf{n}(\boldsymbol{\omega})$ is obtained from the dielectric function as **[4]**.

$$\mathbf{n}(\boldsymbol{\omega}) = \sqrt{\frac{|\boldsymbol{\varepsilon}(\boldsymbol{\omega})| + \boldsymbol{\varepsilon}_1(\boldsymbol{\omega})}{\mathbf{2}}} \quad (\mathbf{VI.5})$$

Where

$$|\boldsymbol{\varepsilon}(\boldsymbol{\omega})| = \sqrt{\boldsymbol{\varepsilon}_1^2(\boldsymbol{\omega}) + \boldsymbol{\varepsilon}_2^2(\boldsymbol{\omega})} \quad (\mathbf{VI.6})$$

In the low-energy regime, the static value $\mathbf{n}(\mathbf{0})$ is a key parameter for optical design, especially for antireflection coatings and multilayer structures. Materials with high $\mathbf{n}$ values tend to exhibit strong light confinement, which is advantageous in photonic devices. In perovskites, the refractive index can be modulated by composition, phase, and electronic configuration, allowing for tunable dispersion across visible and ultraviolet regions. The evolution of $\mathbf{n}(\boldsymbol{\omega})$ with photon energy provides insight into the density and nature of optical transitions. Peaks and variations in its dispersion curve often correspond to strong interband activity, offering clues about band symmetry and transition probabilities.

VI.3.1.2 Imaginary Part: Extinction Coefficient

The imaginary part of the complex refractive index, $\mathbf{k(\omega)}$, describes the attenuation of electromagnetic wave intensity due to absorption as it propagates through the material. It is directly associated with optical losses arising from electronic excitations and provides valuable information on the absorption profile of the material. It is calculated from the dielectric function using the expression [4].

$$\mathbf{k(\omega)} = \sqrt{\frac{|\boldsymbol{\varepsilon(\omega)}| - \boldsymbol{\varepsilon_1(\omega)}}{\mathbf{2}}} \qquad (\mathbf{IV.7})$$

In energy regions below the fundamental band gap, $\mathbf{k(\omega)}$ is effectively zero, indicating transparency. Once the photon energy surpasses the threshold for interband transitions, $\mathbf{k(\omega)}$ increases, reflecting the onset of significant light absorption. This absorption is influenced by the joint density of states and the oscillator strength of transitions between occupied and unoccupied states. In complex oxides and perovskites, pronounced features in $\mathbf{k(\omega)}$ spectra result from transitions involving metal-oxygen hybridized orbitals. These features define the spectral regions of optical activity and are crucial for tailoring materials for applications such as UV-blocking layers, light-absorbing coatings, and photodetectors. Together, $\mathbf{n(\omega)}$ and $\mathbf{k(\omega)}$ fully characterize the amplitude and phase behavior of light within the material, providing the foundation for understanding and engineering advanced optical functionality [6].

VI.3.2 Absorption Coefficient $\boldsymbol{\alpha(\omega)}$

The absorption coefficient $\boldsymbol{\alpha(\omega)}$ quantifies the attenuation of electromagnetic radiation as it propagates through a medium due to photon absorption. It represents the rate at which light intensity decreases with penetration depth and is one of the most direct indicators of a material's optical absorption strength at a given photon energy. Defined as a function of angular frequency $\boldsymbol{\omega}$, the absorption coefficient is related to the extinction coefficient $\mathbf{k(\omega)}$ through the following expression [7].

$$\boldsymbol{\alpha(\omega)} = \frac{\mathbf{2\omega k(\omega)}}{\mathbf{c}} \qquad (\mathbf{VI.8})$$

Where **c,** is the speed of light in vacuum. This relation enables the calculation of $\boldsymbol{\alpha(\omega)}$ from the dielectric function via its connection to the complex refractive index. At photon energies below the electronic transition threshold typically the band gap in insulating and semiconducting systems the absorption coefficient remains close to zero, indicating that the material is effectively transparent in that region. As the photon energy increases and surpasses the threshold for allowed interband transitions, $\boldsymbol{\alpha(\omega)}$ rises sharply. This increase marks the onset of significant optical absorption and provides insight into the material's electronic structure. The behavior of $\boldsymbol{\alpha(\omega)}$ across the electromagnetic spectrum reflects both the availability of electronic states and the strength of transition matrix elements. Sharp onsets or steep absorption edges are often associated with direct transitions between well-defined energy bands, while more gradual increases may indicate indirect or forbidden transitions that require phonon assistance or involve weak oscillator strengths. The profile of $\boldsymbol{\alpha(\omega)}$ is essential for assessing a material's suitability in optical and optoelectronic applications. For example, materials with high absorption in the visible range are desirable for photodetection and energy harvesting, whereas low absorption is preferred for transparent optical coatings and window layers. In addition to identifying absorption thresholds, the magnitude and bandwidth of peaks in $\boldsymbol{\alpha(\omega)}$ inform on the intensity and spectral selectivity of light–matter interactions. These characteristics are critical in determining light penetration depth, optical efficiency, and frequency selectivity in both passive and active photonic systems **[8]**.

VI.3.3 Reflectivity $\mathbf{R(\omega)}$

Reflectivity $\boldsymbol{R(\omega)}$ is a fundamental optical property that describes the proportion of incident electromagnetic radiation reflected at the surface of a material. It is an essential quantity in optics and photonics, directly linked to how efficiently a material reflects light as a function of photon energy. Reflectivity is calculated from the complex refractive index $\boldsymbol{\tilde{n}(\omega)}$ using the Fresnel equations. For normal incidence, the reflectivity **[9]** is given by.

$$\mathbf{R(\omega)} = \left|\frac{\tilde{\mathbf{n}}(\boldsymbol{\omega}) - \mathbf{1}}{\tilde{\mathbf{n}}(\boldsymbol{\omega}) + \mathbf{1}}\right|^{\mathbf{2}} = \frac{(\mathbf{n}(\boldsymbol{\omega}) - \mathbf{1})^{\mathbf{2}} + \mathbf{k}^{\mathbf{2}}(\boldsymbol{\omega})}{(\mathbf{n}(\boldsymbol{\omega}) + \mathbf{1})^{\mathbf{2}} + \mathbf{k}^{\mathbf{2}}(\boldsymbol{\omega})} \qquad (\mathbf{VI.9})$$

This expression accounts for both the phase mismatch (through $\mathbf{n(\omega)}$) and absorption losses (through $\mathbf{k(\omega)}$) encountered by the incoming wave at the interface. The spectral behavior

of $\mathbf{R(\omega)}$ is governed by the electronic structure and optical response of the material. At low photon energies particularly below the absorption threshold the reflectivity tends to be moderate and primarily influenced by dispersion. As the photon energy increases and electronic transitions become active, the reflectivity can rise sharply, especially in regions where $\mathbf{k(\omega)}$ becomes large. This corresponds to strong absorption and higher surface impedance mismatch.

In highly dispersive or metallic materials, reflectivity may approach unity over specific frequency ranges, indicating strong opposition to electromagnetic wave penetration. Conversely, materials designed for optical transparency or anti-reflective applications aim to minimize $\mathbf{R(\omega)}$ over designated spectral windows. Reflectivity is not only critical in determining the visual appearance and surface brightness of materials but also plays a key role in the performance of optical devices such as mirrors, coatings, filters, and multilayer stacks. Its calculation from first-principles allows for predictive modeling of optical interface behavior without relying on empirical input. Therefore, the analysis of $\mathbf{R(\omega)}$ complements other optical parameters by offering a surface-sensitive view of light–material interaction, which is particularly important in layered, stratified, or nanostructured systems where interface effects dominate **[10]**.

VI.3.4 Energy Loss Function $\mathbf{L(\omega)}$

The energy loss function $\mathbf{L(\omega)}$ characterizes the energy dissipated by a fast-moving charged particle typically an electron as it traverses a material. It reflects the collective excitation behavior of the electron system, particularly the response of valence electrons to external perturbations, and is crucial for interpreting spectroscopic techniques such as electron energy loss spectroscopy (EELS). Defined in terms of the complex dielectric function $\boldsymbol{\varepsilon(\omega)}$, the energy loss function is given by **[11]**.

$$\mathbf{L(\omega) = Im\left[-\frac{1}{\varepsilon(\omega)}\right]} \qquad \mathbf{(VI.10)}$$

This expression quantifies how strongly the medium resists the passage of high-energy electrons by inducing polarization, resulting in energy transfer from the electron to the material. The spectral features of $\mathbf{L(\omega)}$ are typically characterized by well-defined peaks that correspond to plasmon resonances, where electrons oscillate collectively at a characteristic frequency. The

main plasmon peak often occurs at the frequency where the real part of the dielectric function $\boldsymbol{\varepsilon_1(\omega)}$ crosses zero and the imaginary part $\boldsymbol{\varepsilon_2(\omega)}$ is small but finite. This condition indicates that the system supports longitudinal charge oscillations with minimal damping.

In addition to plasmon peaks, secondary features in $\mathbf{L(\omega)}$ may arise from interband transitions or surface-related excitations, particularly in thin films and nanostructures. These peaks can provide detailed insight into the electronic structure and energy-level distribution within the material. From a practical standpoint, the energy loss function is an important tool for assessing optical losses in high-frequency or high-energy regimes. It is also central to the design of materials for applications such as shielding, beam propagation in electron optics, and dielectric response modeling at nanoscales. Unlike reflectivity or absorption, which describe transverse electromagnetic wave interactions, $\mathbf{L(\omega)}$ provides information about longitudinal excitation modes. Its accurate evaluation therefore complements the optical constants discussed previously, offering a broader understanding of both surface and bulk electronic dynamics **[12]**.

VI.4 Results and Discussion

VI.4.1 Dielectric function

VI.4.1.1 Real part

In this section, we explore the dielectric function $\boldsymbol{\varepsilon_1}$ of various materials across different energy ranges, including the static dielectric permittivity $\boldsymbol{\varepsilon_1(\omega 0)}$ as well as their dynamic behavior in the near-infrared (NIR) ~0 to 1.63 eV, visible ~1.63 to 3.26 eV, and ultraviolet (UV) +3.26 eV regions. The analysis of $\boldsymbol{\varepsilon_1}$ provides insight into the material's ability to polarize in response to an external electric field and its interaction with electromagnetic radiation. By interpreting $\boldsymbol{\varepsilon_1}$ over a wide range of photon energies, we can gain a deeper understanding of the material's optoelectronic, plasmonic, and dielectric properties, which are crucial for a variety of applications.

For $LiSiCl_3$, $RbSiCl_3$, and $CsSiCl_3$ perovskites **Figure VI.1(a)**, the $\boldsymbol{\varepsilon_1}$ values at 0 eV $\boldsymbol{\varepsilon_1(0)}$ are 12.25, 7.82, and 102.55, respectively, indicating that $CsSiCl_3$ exhibits the strongest polarization at zero frequency. This suggests that $CsSiCl_3$ is particularly suitable for applications that require high dielectric responses **[13]**. In the optical range, $CsSiCl_3$ shows a sharp decrease in $\boldsymbol{\varepsilon_1}$ until it reaches negative values at around 0.85 eV, before rising again. It also exhibits a

peak in the visible energy range around 2.16 eV with a value of 2.77, followed by a second peak in the UV range around 3.51 eV with a value of 4.46, and a third peak in the UV range around 4.64 eV with a value of 2.97. $RbSiCl_3$ shows a moderate increase in $\boldsymbol{\varepsilon_1}$, peaking in the NIR range (around 1.08 eV) with a value of 8.20 before decreasing. $LiSiCl_3$ shows two peaks in the NIR range: the first at around 1.70 eV with a value of 14.40 and the second at around 1.20 eV with a value of 6.10, before transitioning to negative values between 1.20 eV and 1.70 eV. $LiSiCl_3$ then continues to increase in the visible and UV ranges, showing a peak around 4.64 eV with a value of 2.97.

For A_3SbAs (A = Ba, Sr, Ca) antiperovskites **Figure VI.1(b)**, the $\boldsymbol{\varepsilon_1}$ values at 0 eV range from 10.12 for Ca_3SbAs, 9.23 for Ba_3SbAs, and 8.94 for Sr_3SbAs, with Ca_3SbAs showing the strongest polarization. In the NIR range, Ca_3SbAs exhibits the highest interaction with photons, peaking at around 1.29 eV with a value of 14.18, followed by Sr_3SbAs and Ba_3SbAs, with values of 12.29 at 1.08 eV and 11.99 at 1.39 eV, respectively. In the visible range, all materials maintain positive $\boldsymbol{\varepsilon_1}$ values, but Ba_3SbAs becomes negative at around 2.80 eV, indicating a plasmonic response **[13,14]**. In the UV range, Ba_3SbAs becomes positive again at around 3.32 eV and turns negative at around 4.29 eV, while Sr_3SbAs and Ca_3SbAs show negative ε_1 values around 3.30 eV and 3.34 eV, respectively. At higher photon energies around 13.5 eV, all materials return to positive values, indicating normal dielectric behavior **[15]**.

For A_3BiI_3 (A = Ba, Sr, Ca) derivative antiperovskites **Figure VI.1(c)**, the $\boldsymbol{\varepsilon_1}$ values at 0 eV are 5.98 for CA_3BiI_3, 6.27 for Sr_3BiI_3, and 5.81 for Ba_3BiI_3, suggesting significant static dielectric responses that indicate strong polarization in all three materials **[13]**. Among them, Sr_3BiI_3 shows the highest static dielectric permittivity at zero frequency. In the visible range, all three materials show a steady increase in $\boldsymbol{\varepsilon_1}$, reflecting a strong interaction with visible light, which is beneficial for optoelectronic applications. This trend suggests that these materials can be used in devices that require effective light absorption and polarization in the visible spectrum **[14]**. In the NIR range, the dielectric function values are lower compared to the visible range, indicating a weaker interaction with NIR radiation. This behavior suggests that these materials may not be as efficient for applications that depend on NIR light, such as certain photodetectors. However, in the UV range (above 3.26 eV), all three materials exhibit a significant increase in $\boldsymbol{\varepsilon_1}$, showing a strong response to UV light. Specifically, in the UV range, Ba_3BiI_3, CA_3BiI_3, and

Sr_3BiI_3 show substantial increases in $\boldsymbol{\varepsilon_1}$, with CA_3BiI_3 reaching a maximum value around 3.26 eV. This strong UV response makes these materials suitable for UV photodetection and other high-energy applications **[15]**.

Our study also focuses on the dielectric function of $Rb_2Pt_{1-x}Pd_xBr_6$ (x = 0.00, 0.25, 0.50, 0.75, and 1.00), evaluated in the energy range from 0 to 11 eV, as illustrated in **Figure VI.1(d)**. The static dielectric constant $\boldsymbol{\varepsilon_1(0)}$, which represents the material's dielectric permittivity at zero frequency, plays a pivotal role in determining excitonic effects and screening behavior in simulations. The calculated $\boldsymbol{\varepsilon_1(0)}$ values increase gradually with Pd concentration: 3.35 for x = 0.00, 3.55 for x = 0.25, 3.68 for x = 0.50, 3.84 for x = 0.75 and reach 4.50 for x = 1.00. This increase suggests that Pd incorporation enhances the polarization ability of the material, making it more suitable for applications that rely on strong dielectric responses **[13]**. In NIR region, $\boldsymbol{\varepsilon_1}$ increases for all compositions and continues to rise into the visible range, where distinct peaks are observed. For x = 0.00, $\boldsymbol{\varepsilon_1}$ peaks at 5.87 around 2.64 eV, indicating significant polarization at this photon energy. For x = 0.25, two notable peaks are seen: the first at 5.10 at 1.95 eV, and the second at 4.64 at 2.73 eV. Similarly, for x = 0.50, the first peak is observed at 1.95 eV with a value of 5.89, and the second peak appears at 2.73 eV with a value of 4.97. For x = 0.75, the material shows a prominent peak of 6.70 at 1.92 eV, suggesting an enhanced polarizability at this concentration. For x = 1.00, the highest $\boldsymbol{\varepsilon_1}$ peak of 8.12 is found at 1.77 eV, indicating the maximum polarization capability at this Pd concentration, making this material particularly effective in the NIR region **[14]**. In UV region, $\boldsymbol{\varepsilon_1}$ begins to oscillate, decreasing and increasing until it becomes negative in the range between approximately 3.77 eV and 5.27 eV, indicative of plasmonic resonance. This oscillatory behavior signifies a complex interaction with high-energy photons, where the material's dielectric response shifts as a result of collective oscillations of the charge carriers. After this plasmonic resonance range, ε_1 returns to positive values, demonstrating normal dielectric behavior at higher photon energies, which is typical for materials that do not exhibit active plasmonic effects beyond a certain energy threshold **[14, 15]**.

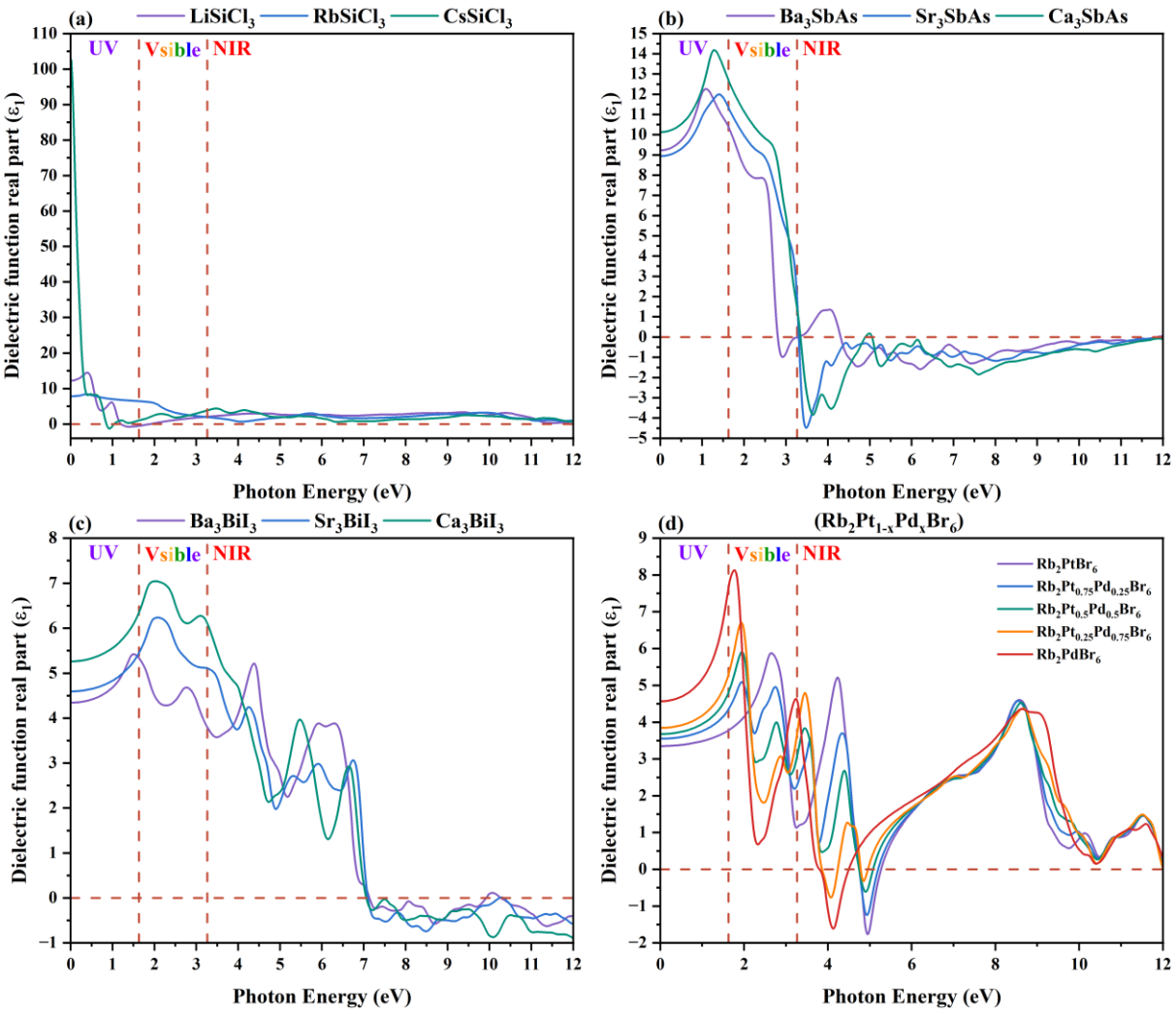

Figure VI.1. Dielectric Function ε₁ of Various Perovskite Compounds (a) $ASiCl_3$ (b) A_3SbAs (c) A_3BiI_3 and (d) $Rb_2Pt_{1-x}Pd_xBr_6$

VI.4.1.2 Imaginary part of the dielectric function

In the analysis of the imaginary part of the dielectric function, $\boldsymbol{\varepsilon_2}$, for various materials across different energy ranges, the behavior of the compounds reveals important insights into their optical absorption properties, particularly in the near-infrared (NIR), visible, and ultraviolet (UV) regions.

For $CsSiCl_3$, as shown in **Figure VI.2(a)**, the first peak occurs at 0.10 eV with a value of 67.51, indicating a significant increase in absorption at low energies. This large initial peak suggests that $CsSiCl_3$ strongly absorbs photons in the low-energy range **[16]**. Following this, there is a sharp decrease in absorption, with the second peak appearing at 0.73 eV, where $\boldsymbol{\varepsilon_2}$

reaches 23.54. A third peak emerges in the visible range at 2.35 eV with a value of 5.17, indicating moderate absorption in the visible region. After this point, the $\boldsymbol{\varepsilon_2}$ curve stabilizes, with fluctuations that eventually merge into a steady region as the energy moves into the far UV range, suggesting that $CsSiCl_3$ becomes less responsive to higher-energy photons **[17]**. $RbSiCl_3$ shows a different absorption pattern. Its first peak appears in the NIR range at 0.47 eV with a value of 1.75. As the photon energy increases, it reaches a second peak at 2.15 eV in the visible range, where $\boldsymbol{\varepsilon_2}$ rises to 5.51. Unlike $CsSiCl_3$, the increase in absorption is more gradual, and after the peak, $RbSiCl_3$ starts to decrease more slowly as it enters the UV range, showing a less pronounced shift in absorption. For $LiSiCl_3$, two peaks are observed in the NIR range: the first at 0.56 eV with a value of 11.99 and the second at 1.09 eV with a value of 10.11. These peaks indicate that $LiSiCl_3$ absorbs well in the NIR range. However, after these peaks, the absorption sharply decreases as it approaches zero in the visible range, followed by a slight increase in the UV range around 4 eV. The absorption remains low for the rest of the UV spectrum, showing limited effectiveness in the higher-energy regions.

Moving to the A_3SbAs compounds, as shown in **Figure VI.2(b)**, none of the materials exhibit peaks in the NIR range, indicating minimal absorption in that region. Instead, all compounds show their first peaks in the visible to UV transition. For Ba_3SbAs, the first peak is observed at 2.69 eV with a value of 10.04, suggesting moderate absorption in the visible range [17]. Ca_3SbAs peaks at a higher energy of 3.10 eV with a value of 15.42, indicating stronger absorption in the visible range compared to $B_{A3}SbAs$. Sr_3SbAs is unique, as its first peak appears in the early UV region at 3.29 eV with a value of 15.52, highlighting a shift towards higher energy absorption compared to the other two materials. After these peaks, all three materials exhibit a sharp decrease in absorption as the photon energy increases, indicating that they become less effective at absorbing photons at higher energies **[18]**. This behavior suggests that while these materials are efficient at absorbing visible and early UV light, they are less responsive to higher-energy UV light, with absorption rapidly diminishing in the far UV range. This trend makes the A_3SbAs compounds suitable for applications that require absorption in the visible to early UV regions, such as in optoelectronics and UV photodetectors **[19]**.

For the A_3BiI_3 series, shown in **Figure VI.2(c)**, all compounds exhibit their first peaks in the visible range, with Ca_3BiI_3 and Sr_3BiI_3 each showing a single peak. Ca_3BiI_3 peaks at 2.57

eV with a value of 2.87 and Sr_3BiI_3 peaks at 2.54 eV with a value of 2.44. Ba_3BiI_3, however, shows two peaks in the visible range: one at 1.91 eV with a value of 1.79 and another at 3.09 eV with a value of 2.43. This indicates that Ba_3BiI_3 has a broader absorption profile in the visible range compared to the others **[17]**. In the mid-UV range, all compounds show their highest peaks. Ba_3BiI_3 reaches a value of 6.37 at 6.69 eV, Sr_3BiI_3 peaks at 6.46 at 6.97 eV, and Ca_3BiI_3 peaks at 6.24 at 6.86 eV. After these peaks, all materials experience a sharp decrease in $\boldsymbol{\varepsilon_2}$, indicating less efficient absorption at higher energies. This behavior suggests that the compounds are highly responsive to visible and mid-UV light, with diminishing absorption in the higher-energy UV region **[19]**.

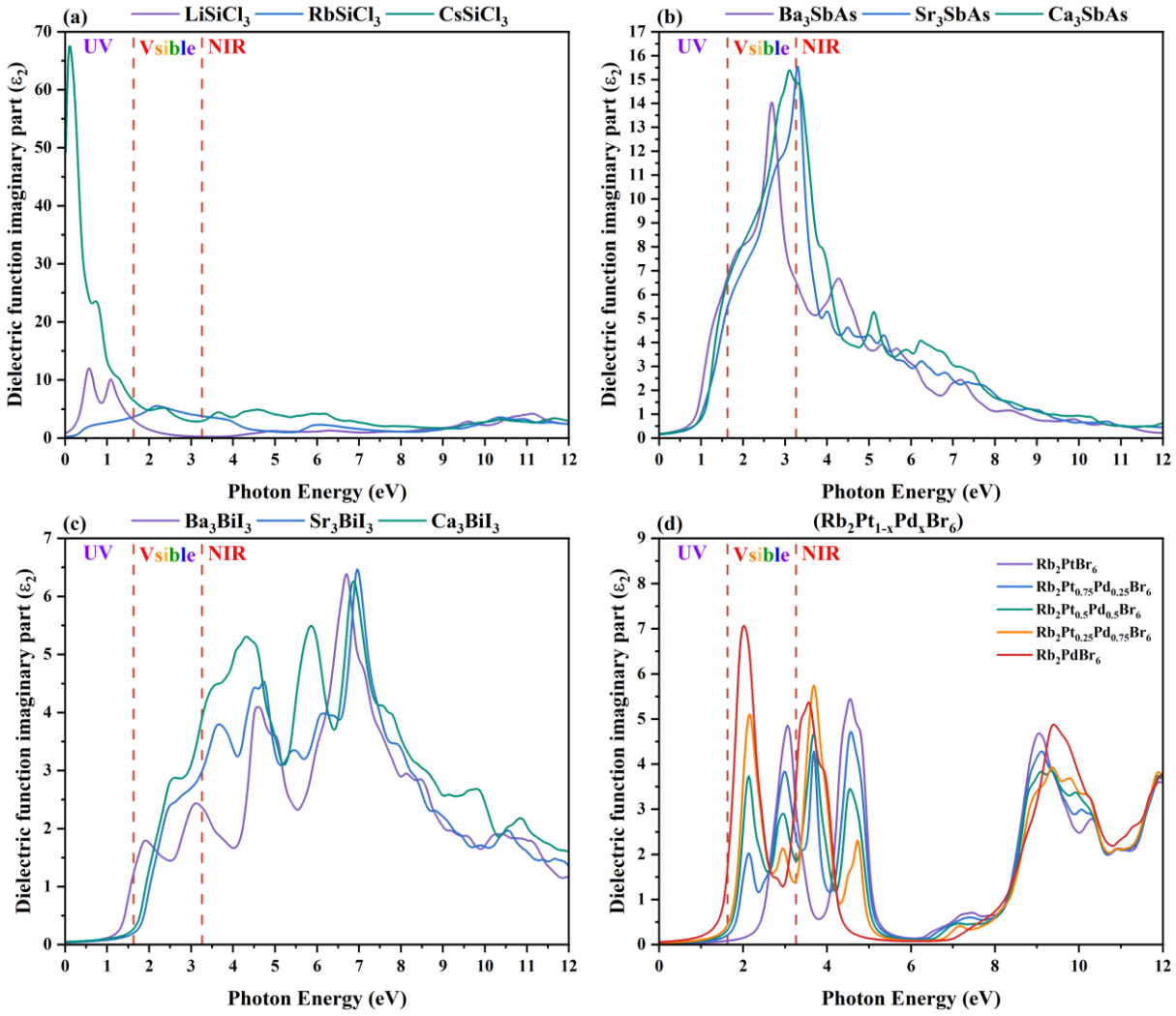

Figure VI.2. Dielectric Function ε2 of Various Perovskite Compounds (a) $ASiCl_3$ (b) A_3SbAs (c) A_3BiI_3 and (d) $Rb_2Pt_{1-x}Pd_xBr_6$.

Finally, for $Rb_2Pt_{1-x}Pd_xBr_6$, as shown in **Figure VI.2(d)**, the $\boldsymbol{\varepsilon_2}$ values remain low in the NIR range for all compositions, below 0.5, indicating minimal absorption in this region. As the photon energy increases into the visible and UV regions, $\boldsymbol{\varepsilon_2}$ rises sharply, with the highest value observed for Rb_2PdBr_6 (x = 1.00) at 2.01 eV, reaching 7.07. This indicates significant absorption in the visible range. The other compositions show peaks in the UV region, with Rb_2PtBr_6 (x = 0.00) peaking at 4.53 eV with a value of 5.46, $Rb_2Pt_{0.75}Pd_{0.25}Br_6$ (x = 0.25) at 4.52 eV with a value of 4.72, and $Rb_2Pt_{0.5}Pd_{0.5}Br_6$ (x = 0.50) at 3.66 eV with a value of 4.62. $Rb_2Pt_{0.25}Pd_{0.75}Br_6$ (x = 0.75) peaks at 3.66 eV with a value of 5.73. Beyond 4.6 eV, $\boldsymbol{\varepsilon_2}$ decreases sharply for all compositions, indicating a reduction in absorption, before a second increase near 6.7 eV, suggesting complex interband transitions. This behavior emphasizes the strong light-matter interaction, particularly in the UV range, making these materials suitable for applications in photodetectors and optoelectronics **[19]**.

VI.4.2 Complex Refractive Index

The refractive index trends observed in the figures for the four different perovskite series exhibit patterns that closely mirror the behavior of the real part of the dielectric function, ε_1. This similarity arises because the refractive index (n) is directly related to ε_1 through the equation $\boldsymbol{n = \sqrt{\varepsilon_1}}$. As ε_1 increases, the refractive index increases, and vice versa, leading to similar peak positions and overall trends in both quantities.

For the $ASiCl_3$ (A = Cs, Rb, Li) series, as shown in **Figure IV.3(a)**, the refractive index shows a sharp contrast across the different alkali metal compositions in the near-infrared (NIR) energy range. The Cs-based compound exhibits the highest refractive index value of around 10 at 0 eV, reflecting strong polarization, while the Rb-based and Li-based compounds show lower values of 2.8 and 3.5, respectively, before decreasing. These differences suggest that Cs has a stronger optical response compared to Rb and Li in the studied energy range.

Moving to the A_3SbAs (A = Ba, Sr, Ca) serie, as shown in **Figure IV.3(b)**, the refractive index exhibits a trend similar to ε_1, with all compounds showing a peak in the NIR range. The refractive index values for this peak range from 3.5 to 3.8, followed by a second, smaller peak in the visible range, before decreasing across the UV spectrum. This indicates that the

compounds have good optical response in the NIR region but a less pronounced response in the UV.

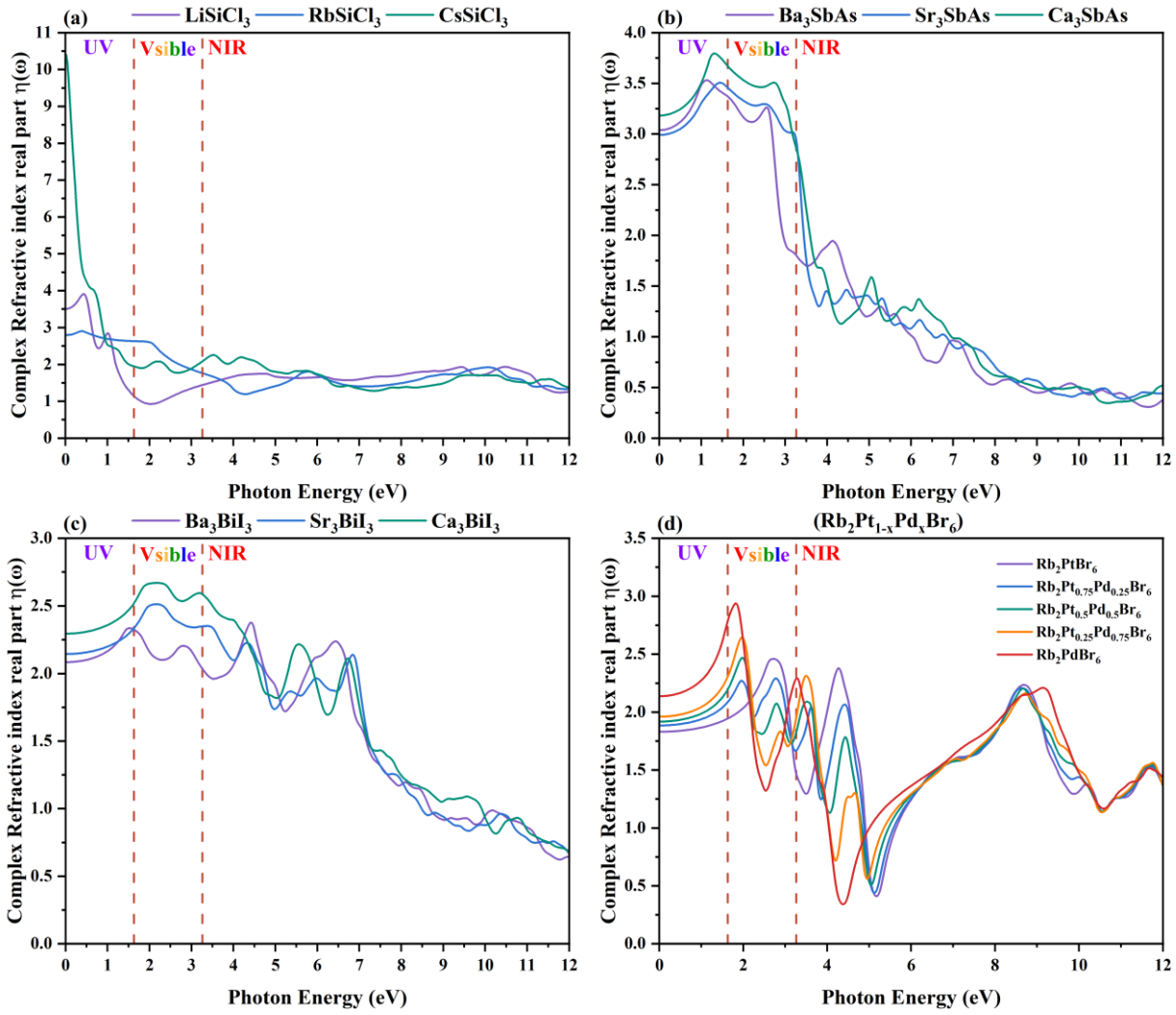

Figure VI.3. Dielectric Function ε2 of Various Perovskite Compounds (a) $ASiCl_3$ (b) A_3SbAs (c) A_3BiI_3 and (d) $Rb_2Pt_{1-x}Pd_xBr_6$

In the A_3BiI_3 (A = Ba, Sr, Ca) serie, as shown in **Figure IV.3(c)**, the refractive index trend is also similar to ε_1, but with some notable variations based on the specific alkali metal used. The Ba-based compound shows a significant peak in the NIR region, followed by a smaller peak in the visible range, which indicates a strong polarization in the NIR. In contrast, the Sr-based compound exhibits peaks primarily in the visible range, with the second smaller peak appearing in the early UV range. The Ca-based compound shows the largest peaks in both the early and late visible range, suggesting a more complex response to light across the visible spectrum.

Lastly, the $Rb_2Pt_{1-x}Pd_xBr_6$ alloys (x = 0, 0.25, 0.5, 0.75, 1), as shown in **Figure IV.3(d)**, show a different pattern. For these compounds, the refractive index first peaks in the visible range and exhibits several smaller peaks in the UV range before gradually decreasing in the late UV spectrum. This suggests a strong optical response in the visible region with additional fine structure in the UV range, likely due to the varying concentrations of Pd in the alloy, which may introduce different electronic or vibrational modes affecting the light-matter interaction.

VI.4.3 Absorption coefficient

In the absorption spectra shown across the four panels, each compound demonstrates distinct absorption behavior in the UV, visible, and NIR regions.

Figure VI.4(a) presents the absorption data for $LiSiCl_3$, $RbSiCl_3$, and $CsSiCl_3$. In the UV region, $CsSiCl_3$ exhibits the highest absorption coefficient, peaking at approximately 81.82 × 10^4 cm^{-1}, while $RbSiCl_3$ and $LiSiCl_3$ show lower absorption coefficients, ranging from 60 to 70 × 10^4 cm^{-1}. This suggests that $CsSiCl_3$ is the most efficient in absorbing UV light. In the visible region, all three materials experience a significant drop in absorption. $LiSiCl_3$ shows values ranging from 3 to 23 × 10^4 cm^{-1}, $RbSiCl_3$ drops from 11 to 35 × 10^4 cm^{-1}, and $CsSiCl_3$ ranges from 23 to 27 × 10^4 cm^{-1}. This indicates that $LiSiCl_3$ maintains some stability across the visible range, while $CsSiCl_3$ and $RbSiCl_3$ perform moderately, with $RbSiCl_3$ experiencing a sharper drop. In the NIR region, absorption decreases further, with $LiSiCl_3$ and $CsSiCl_3$ maintaining slightly higher values (around 25 × 10^4 cm^{-1}), while $RbSiCl_3$ drops below 8 × 10^4 cm^{-1}. This suggests that $RbSiCl_3$ is less effective in absorbing light across the entire spectrum compared to $LiSiCl_3$ and $CsSiCl_3$.

Figure VI.4(b) shows the absorption spectra for Ba_3SbAs, Sr_3SbAs, and Ca_3SbAs. In the UV region, Ca_3SbAs exhibits the highest absorption coefficient, peaking at 120 × 10^4 cm^{-1}, followed by Sr_3SbAs at 104 × 10^4 cm^{-1} and Ba_3SbAs at 101 × 10^4 cm^{-1}. This indicates that Ca_3SbAs is the best performer in the UV region. In the visible region, all materials experience a sharp decline in absorption. Ba_3SbAs shows the highest value in this region, with absorption ranging from 70 to 84 × 10^4 cm^{-1}, while Sr_3SbAs and Ca_3SbAs decrease to 17 × 10^4 cm^{-1} by the end of the visible region. This suggests that while Ba_3SbAs performs better in the visible range, all three materials still experience significant reductions in absorption. In the NIR region,

absorption further decreases, with Ba_3SbAs at 11 × 10^4 cm^{-1}, Sr_3SbAs at 9 × 10^4 cm^{-1}, and Ca_3SbAs at 10 × 10^4 cm^{-1}. This shows that these compounds have limited potential in the NIR region and are primarily useful for UV-based applications.

Figure VI.4(c) presents the absorption spectra for Ba_3BiI_3, Sr_3BiI_3, and Ca_3BiI_3. In the UV region, Sr_3BiI_3 shows the highest absorption, peaking at 122 × 10^4 cm^{-1}, followed by Ca_3BiI_3 at 118 × 10^4 cm^{-1} and Ba_3BiI_3 at 111 × 10^4 cm^{-1}. These results suggest that Bi-based compounds are generally good absorbers in the UV region. In the visible range, all three materials show a significant decline in absorption, with Ba_3BiI_3 performing better due to its more stable absorption values ranging from 5 to 14 × 10^4 cm^{-1}. Sr_3BiI_3 and Ca_3BiI_3 drop more sharply, with Sr_3BiI_3 reaching as low as 3 × 10^4 cm^{-1} and Ca_3BiI_3 ranging from 3 to 25 × 10^4 cm^{-1}. In the NIR region, the absorption of all compounds is quite low, with Sr_3BiI_3 and Ca_3BiI_3 at around 1 × 10^4 cm^{-1}, and Ba_3BiI_3 at approximately 4 × 10^4 cm^{-1}. These results indicate that although the Bi-based compounds are efficient in the UV region, they are not well-suited for applications requiring strong performance in the visible or NIR regions.

Figure VI.4(d) focuses on $Rb_2Pt_{1-x}Pd_xBr_6$ with varying Pd concentrations (x = 0, 0.25, 0.5, 0.75, and 1). At x = 0 (pure Rb_2PtBr_6), the absorption coefficient peaks in the UV region at about 82 × 10^4 cm^{-1}. As Pd is introduced, the absorption shifts towards the visible region, and the UV absorption decreases. At x = 0.5, the UV absorption drops to 57 × 10^4 cm^{-1}, and at x = 1, it drops to around 62 × 10^4 cm^{-1}. This shift towards visible absorption is due to the modification of electronic properties with Pd doping. In the visible region, absorption increases as the Pd concentration rises, with values ranging from 10.31 × 10^4 cm^{-1} at x = 0.25 to 34.26 × 10^4 cm^{-1} at x = 1. This suggests that increasing Pd content enhances the material's absorption in the visible region, which could make it more suitable for visible-light applications. However, in the NIR region, absorption remains low for all concentrations, not exceeding 4 × 10^4 cm^{-1}. This indicates that while Pd doping improves the absorption in the visible range, the material does not significantly absorb in the NIR region.

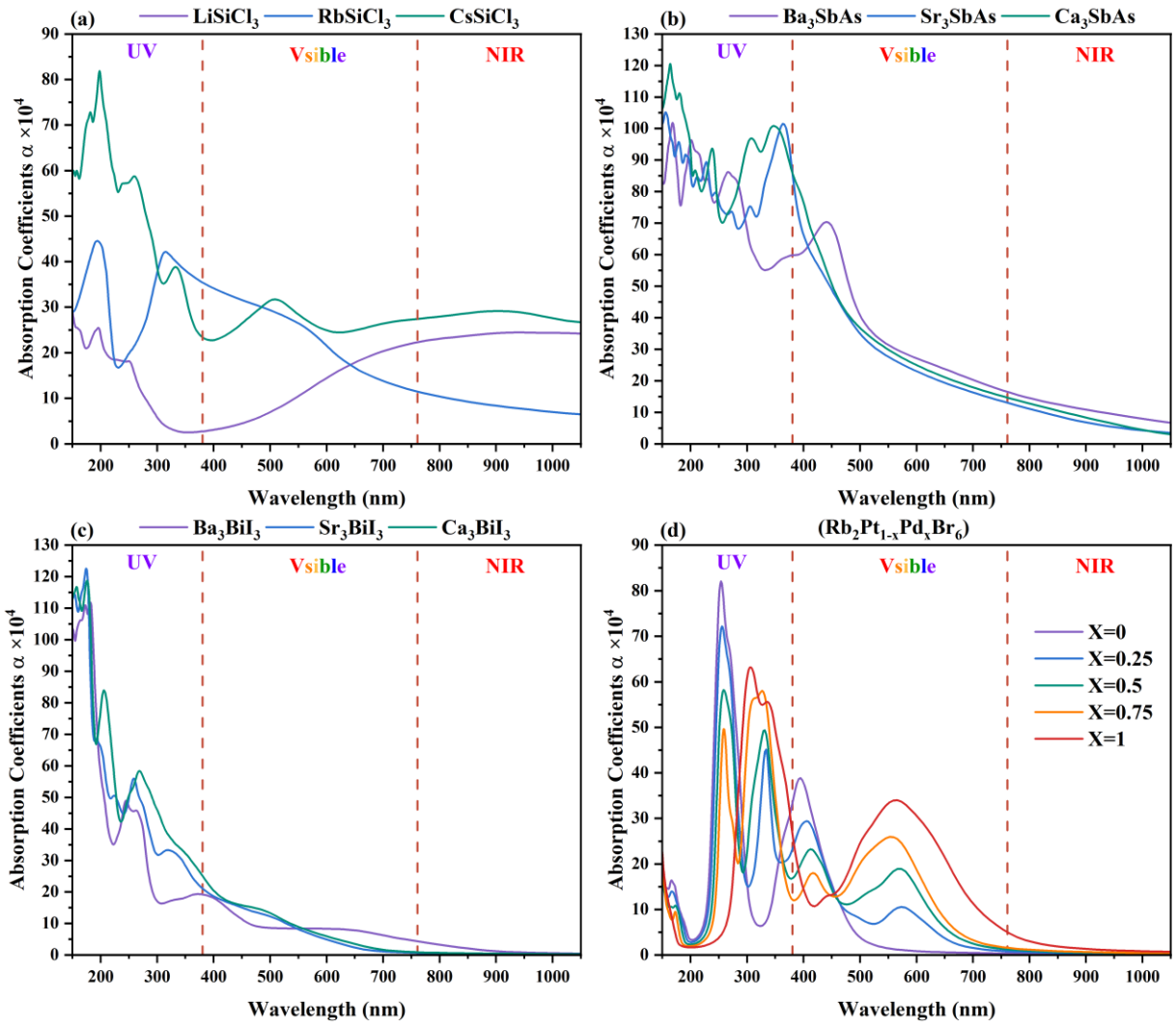

Figure VI.4. Absorption Coefficients of Various Perovskite Compounds (a) $ASiCl_3$ (b) A_3SbAs (c) A_3BiI_3 and (d) $Rb_2Pt_{1-x}Pd_xBr_6$.

VI.4.4 Reflectivity

Reflectivity of different perovskite materials is analyzed for various compositions across three regions: the Near-Infrared (NIR), Visible, and Ultra-Violet (UV) regions.

Starting with the $ASiCl_3$ series (A = Li, Rb, Cs) as depicted in **Figure VI.5(a)**, we observe that $RbSiCl_3$ and $LiSiCl_3$ exhibit nearly identical performance in the NIR region, maintaining a high reflectivity below 0.40. However, $CsSiCl_3$ shows a weaker performance, with a maximum reflectivity just under 0.70 and a minimum around 0.35. In the visible region, all compounds perform similarly, with maximum reflectivity values around 0.25. $LiSiCl_3$ stands

out with a remarkable drop in reflectivity, reaching as low as 0.025. Moving into the UV region, all compounds show reflectivity below 0.23, indicating a significant increase in absorption. The low reflectivity in the UV region makes them promising for other optoelectronic applications that require efficient absorption in this range.

Next, the A_3SbAs series (A = Ba, Sr, Ca), plotted in **Figure VI.5(b)**, reveals that the compounds exhibit very similar behavior across all regions with only slight differences in performance. In the NIR region, all compounds show reflectivity values between 0.25 (lower bound) and 0.35 (higher bound). In the visible region, reflectivity increases slightly to reach a maximum of 0.45, continuing to rise as we move into the early UV region, reaching a peak reflectivity value of 0.55 before beginning to decline around 4.5 eV, with a final value of 0.43. These compounds exhibit a relatively stable reflectivity profile across the entire range.

Moving on to the A_3BiI_3 series (A = Ba, Sr, Ca), shown in **Figure VI.5(c)**, this series demonstrates superior performance compared to the previous two, $ASiCl_3$ and A_3SbAs. In the NIR region, it maintains a low reflectivity with a maximum of 0.18. As we transition to the visible region, Ba_3BiI_3 shows a slightly higher maximum reflectivity of 0.22, but Ba_3BiI_3 emerges as the most promising compound, showing the lowest reflectivity of 0.16 across the entire visible range. This suggests that Ba_3BiI_3 could be an excellent candidate for use as an active layer in solar cells due to its low reflectivity across both the visible and NIR regions. In the UV region, the reflectivity increases but remains low, peaking at 0.35, indicating minimal reflection and greater absorption, ideal for optoelectronic applications **[20]**.

Finally, the double perovskite alloys $Rb_2Pt_{1-x}Pd_xBr_6$ with varying concentrations (0, 0.25, 0.5, 0.75, and 1), shown in **Figure VI.5(d)**, exhibit an interesting trend. In the NIR region, all concentrations show low reflectivity, with a maximum value around 0.20. Reflectivity increases slightly in the visible region, reaching a maximum value of 0.29. However, the most intriguing feature of this series is the noticeable drop in reflectivity between 4.5 eV and 6 eV, where the reflectivity becomes almost negligible, approaching a value of 0. This behavior suggests that the double perovskite alloys could be tuned for specific optical properties, making them potentially useful in devices that require minimal reflectivity in certain energy ranges **[21].**

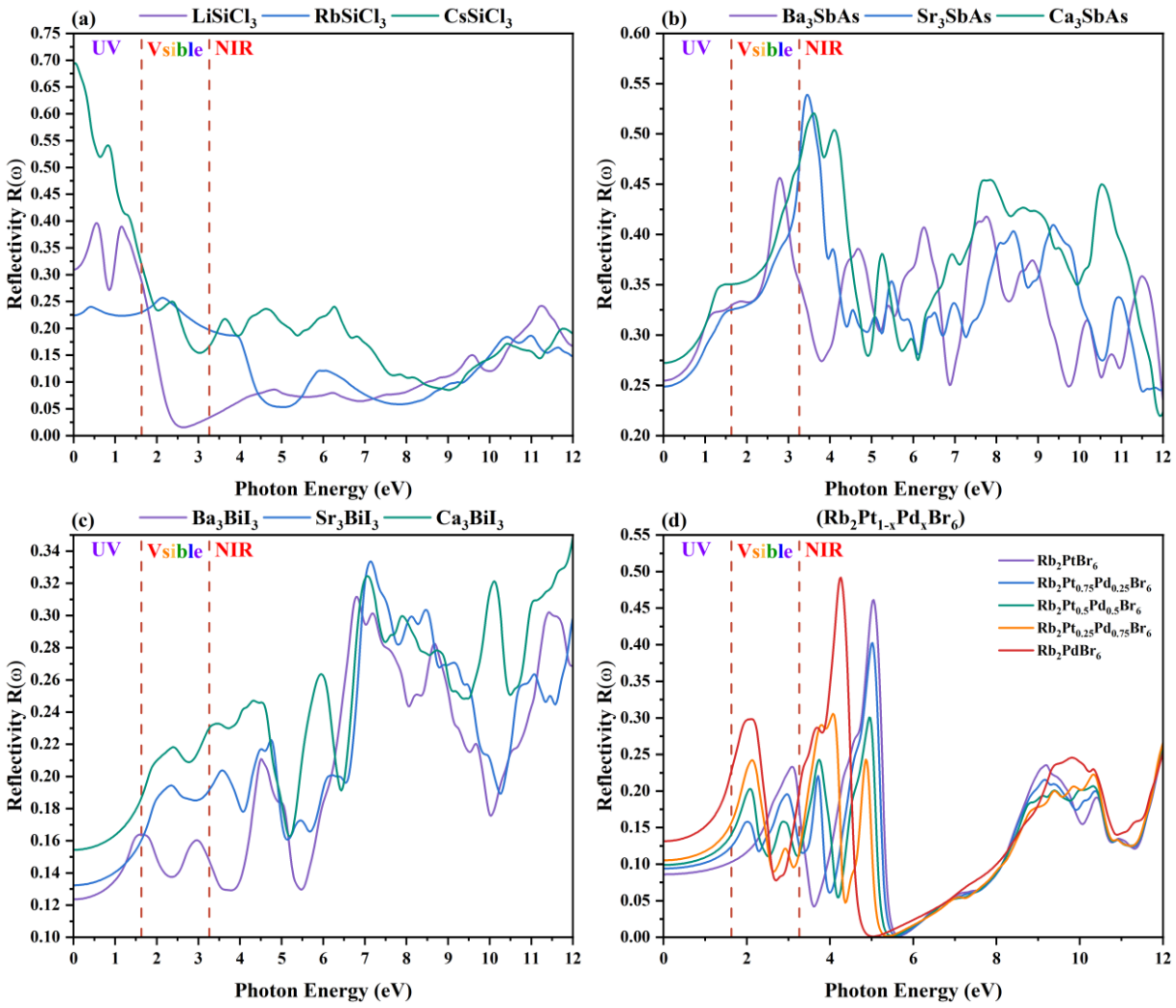

Figure VI.5. Reflectivity of Various Perovskite Compounds (a) $ASiCl_3$ (b) A_3SbAs (c) A_3BiI_3 and (d) $Rb_2Pt_{1-x}Pd_xBr_6$.

VI.4.5 Energy Loss

In the energy loss trends for the different perovskite series shown in **Figures VI.6(a-d)**, each series exhibits distinct behaviors across the NIR, visible, and UV regions. Starting with the $ASiCl_3$ series (A=Li, Rb, Cs) plotted in **Figure VI.6(a)**, all three compounds demonstrate similar trends in the NIR region, with energy loss values remaining below 0.10, indicating minimal absorption or scattering in this range. However, in the visible region, $RbSiCl_3$ and $CsSiCl_3$ show lower energy losses, not exceeding 0.20, suggesting efficient transmission of visible light, while $LiSiCl_3$ exhibits a significant peak in energy loss at 0.75, possibly due to stronger electronic transitions or absorption in this range. In the UV region, $LiSiCl_3$ shows a

decrease in energy loss to a maximum of 0.30, implying a shift in its behavior compared to the visible region. In contrast, $RbSiCl_3$ and $CsSiCl_3$ show an increase in energy loss, reaching values between 0.40 and 0.45, suggesting increasing absorption as energy transitions into the UV.

Moving to the A_3SbAs series (A=Ba, Sr, Ca) shown in **Figure VI.6(b)**, the compounds in the NIR region show almost negligible energy loss, with values close to zero, indicating low interaction with light in this region. In the visible range, the compounds display a similar trend, reaching a maximum energy loss of around 0.20. However, as the energy shifts toward the UV region, energy loss begins to increase significantly, starting at approximately 0.20 around 4 eV and rising sharply to exceed 2 at the high-energy UV region near 12 eV, indicating stronger absorption in the UV.

For the Ba_3BiI_3 series (A=Ba, Sr, Ca) shown in **Figure VI.6(c)**, all compounds show a similar trend, with negligible energy loss in the NIR region, close to zero. In the visible range, energy loss is low, not exceeding 0.11, which suggests that these materials have minimal absorption or scattering of visible light. As with the previous series, the energy loss increases in the UV region but remains relatively low, not exceeding 0.8 in the far UV range around 12 eV, indicating that these materials absorb UV light moderately but do not exhibit significant energy loss even at higher energies.

Finally, in the double perovskite alloys $Rb_2Pt_{1-x}Pd_xBr_6$, shown in **Figure VI.6(d)** with varying concentrations (0, 0.25, 0.5, 0.75, and 1), all concentrations show negligible energy loss in the NIR region. In the visible range, the energy loss does not exceed 0.4, indicating low absorption or scattering. However, these alloys exhibit notable high energy loss in the UV region between 4.5 and 6 eV, with energy losses reaching up to 3. This is the same region where zero reflectivity is observed in **Figure VI.5(d)**, suggesting a significant interaction between the material and the incident UV light in this energy range, possibly due to electronic transitions or absorption processes that are not reflected. After this peak, the energy loss decreases, staying below 0.5 in the rest of the studied UV region, showing a shift in the material's behavior as the energy continues to increase.

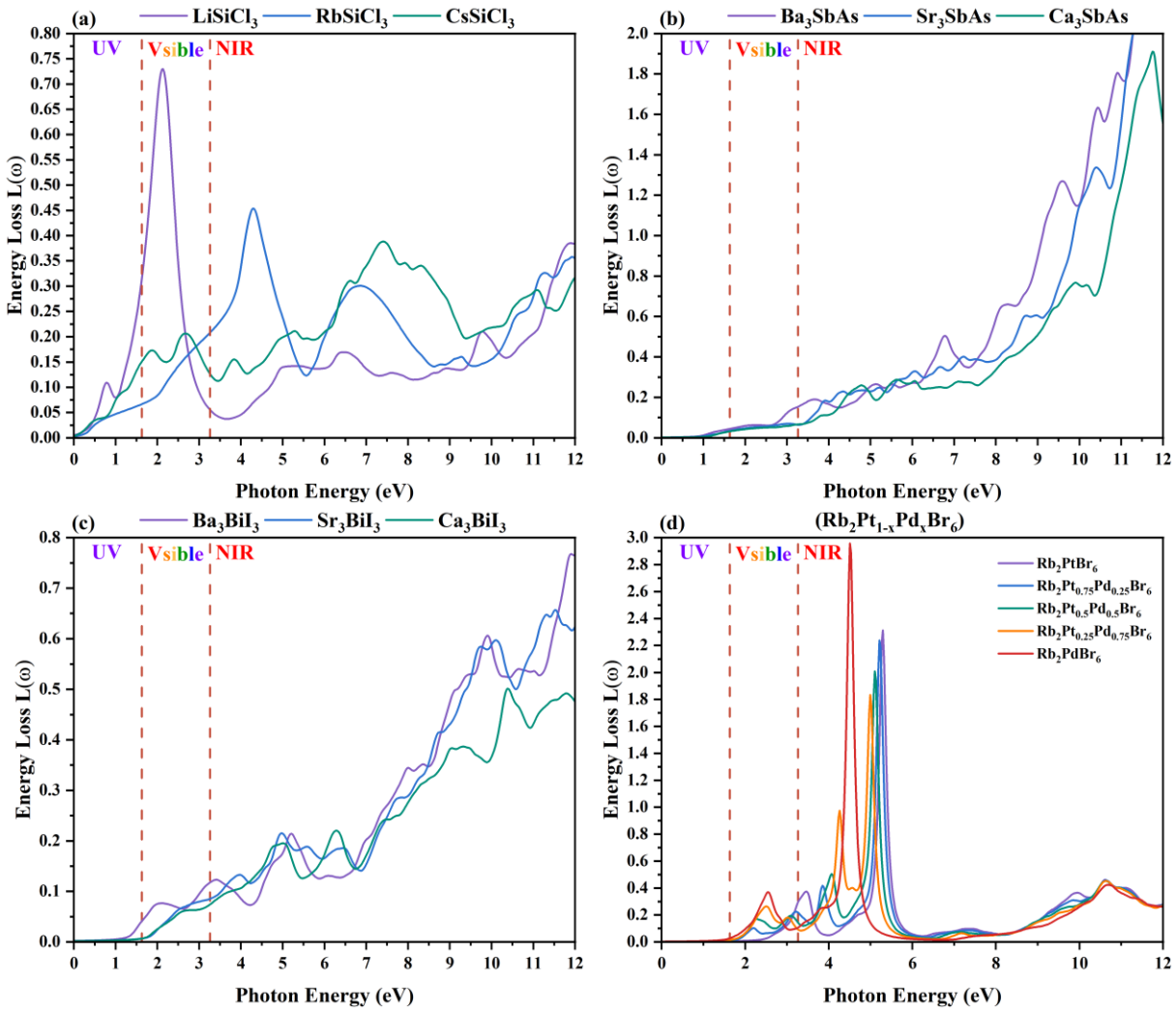

Figure VI.6. Energy Loss of Various Perovskite Compounds (a) $ASiCl_3$ (b) A_3SbAs (c) A_3BiI_3 and (d) $Rb_2Pt_{1-x}Pd_xBr_6$.

VI.5 Conclusion

This chapter has provided a comprehensive analysis of the optical properties of several perovskite materials, revealing important insights into their behavior in response to electromagnetic radiation across the NIR, visible, and UV regions. The study of the complex dielectric function, including both its real and imaginary parts, has allowed for a detailed examination of key optical characteristics such as refractive index, absorption coefficient, reflectivity, and energy loss. The results highlight the distinct optical behaviors of materials like $CsSiCl_3$, Ba_3SbAs, and $Rb_2Pt_{1-x}Pd_xBr_6$, which exhibit significant absorption in the UV region, tailored refractive indices, and unique reflectivity profiles. These findings suggest that these materials are highly suitable for applications in

photodetectors, solar cells, and transparent electronics. By utilizing first-principles calculations, this study demonstrates the importance of theoretical methods in predicting and optimizing the optical properties of materials, paving the way for the design of advanced optical devices. Ultimately, the insights gained here contribute to the ongoing development of next-generation materials with tailored optical functionalities for a variety of technological applications.

Bibliography

[1] J. N. Hilfiker and T. Tiwald, Springer Series in Optical Sciences, 2018, 212, 115–153.
[2] V. B. Bobrov and S. A. Trigger, J Phys A Math Theor, 2010, 43, 365002.
[3] H. Kuzmany, Solid-State Spectroscopy, 1998, 101–120.
[4] N. Piri, A. Shams-Nateri and J. Mokhtari, Color Res Appl, 2016, 41, 477–483.
[5] B. J. Sumlin, Y. W. Heinson, N. Shetty, A. Pandey, R. S. Pattison, S. Baker, W. M. Hao and R. K. Chakrabarty, J Quant Spectrosc Radiat Transf, 2018, 206, 392–398.
[6] S. M. K. Skiles, T. Painter and G. S. Okin, Journal of Glaciology, 2017, 63, 133–147.
[7] C. Hu, F. E. Muller-Karger and R. G. Zepp, Limnol Oceanogr, 2002, 47, 1261–1267.
[8] C. Hu, F. E. Muller-Karger and R. G. Zepp, Limnol Oceanogr, 2002, 47, 1261–1267.
[9] M. Sparks, JOSA, Vol. 67, Issue 11, pp. 1590-1594, 1977, 67, 1590–1594.
[10] O. S. Heavens, Reports on Progress in Physics, 1960, 23, 1.
[11] M. F. Al-Mudhaffer, M. A. Nattiq and M. A. Jaber, Scholars Research Library Archives of Applied Science Research, 2012, 1731–7140.
[12] H. R. Philipp and H. Ehrenreich, Physical Review, 1963, 129, 1550.
[13] Y. Wang, W. Jie, C. Yang, X. Wei, J. Hao, Y. B. Wang, C. Yang, X. H. Wei, W. J. Jie and J. H. Hao, Adv Funct Mater, 2019, 29, 1808118.
[14] B. Zhang, H. Zhang, J. Lin and X. Cheng, Int J Quantum Chem, 2020, 120, e26232.
[15] W. D. Mesquita, S. R. de Jesus, M. C. Oliveira, R. A. P. Ribeiro, M. R. de Cássia Santos, M. G. Junior, E. Longo and M. F. do Carmo Gurgel, Theor Chem Acc, 2021, 140, 1–12.
[16] J. Laali, A. Hamedani, G. Alahyarizadeh and A. Minuchehr, Superlattices Microstruct, 2020, 143, 106551.
[17] J. Laali, A. Hamedani, G. Alahyarizadeh and A. Minuchehr, Superlattices Microstruct, 2020, 143, 106551.
[18] S. Idrissi, H. Labrim, L. Bahmad and A. Benyoussef, Chem Phys Lett, 2021, 766, 138347.
[19] F. T. Zahra, M. M. Islam, M. M. Hasan, M. R. Islam and S. Ahmad, Journal of Physics and Chemistry of Solids, 2024, 191, 112037.
[20] V. B. Parmar, D. Raval, S. K. Gupta, P. N. Gajjar and A. M. Vora, Mater Today Proc, DOI:10.1016/J.MATPR.2023.01.410.
[21] B. Farhadi, F. Zabihi, I. Lugoloobi and A. Liu, Solar Energy, 2022, 233, 11–17.

CHAPTER VII

Perovskite in Embedded Systems

VII.1 Introduction

This chapter explores the integration of Perovskite Solar Cells (PSCs) into embedded systems, with a focus on their application in solar-powered embedded systems, particularly in the context of autonomous devices. Embedded systems are specialized computing units designed to perform dedicated tasks, and when powered by renewable energy sources like solar cells, they present a sustainable solution for devices operating in remote or off-grid environments. The chapter delves into the properties and working principles of PSCs, highlighting their advantages over traditional silicon-based solar cells, such as higher efficiency, lower production costs, and flexibility. Additionally, it examines the challenges faced by PSCs, particularly related to their stability and environmental concerns, while also showcasing simulation tools like SCAPS-1D to model their performance. The chapter concludes by discussing the integration of PSCs into real-world applications, particularly in agricultural drones, demonstrating how these cells can contribute to the autonomy and sustainability of embedded systems.

VII.2 Applications of Solar Cells in Embedded Systems

VII.2.1 Definition and Role of Embedded Systems

An embedded system is a specialized computing system designed to perform dedicated functions within a larger system. Unlike general-purpose computers, embedded systems are optimized for specific tasks and operate with limited resources such as memory, processing power, and storage. These systems are commonly found in devices such as household appliances, medical equipment, automotive systems, industrial machines, and consumer electronics. Their role is crucial in ensuring that the devices they control perform with high efficiency, reliability, and real-time responsiveness **[1]**. Embedded systems are typically characterized by real-time operation, energy efficiency, and stability. The design of these systems often requires considerations for hardware and software integration, where software is tightly coupled with the hardware to optimize performance and functionality **[2]**. For a visual understanding of embedded systems, refer to **Figure VII.1**, which illustrates the structure of a typical embedded system, highlighting its interaction with various hardware components and sensors.

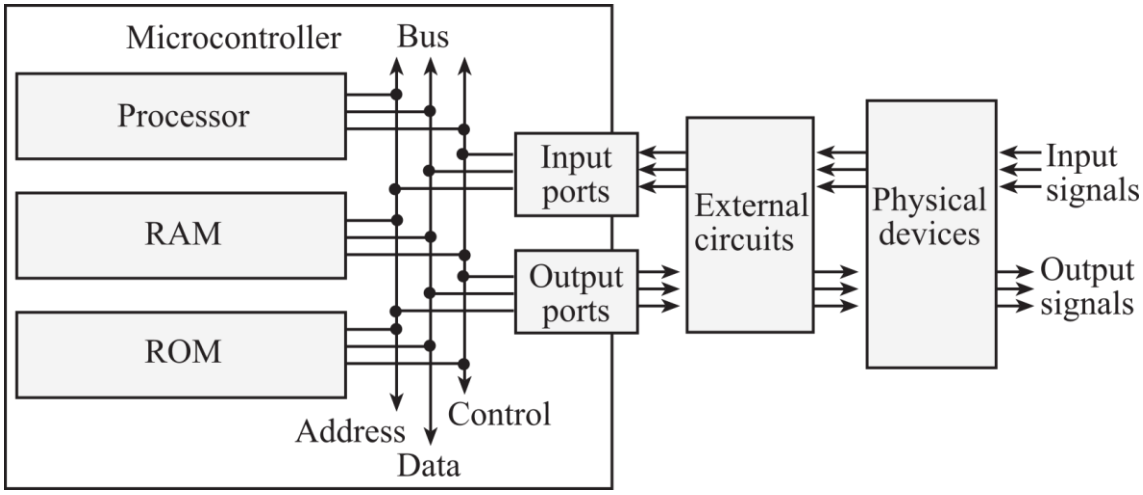

Figure VII.1. Structure of a typical embedded system

VII.2.2 Powering Embedded Systems with Solar Energy

Powering embedded systems with solar energy is an innovative solution to provide sustainable and eco-friendly energy for low-power devices. These systems are independent of human interaction and are designed to operate autonomously in remote or off-grid locations, where conventional power sources are unavailable or impractical. Solar-powered embedded systems rely on photovoltaic cells to convert sunlight into electrical energy, which is then used to power sensors, communication modules, or processing units. Examples of such systems include solar-powered weather stations, autonomous drones, and smart irrigation systems **[3]**. These systems offer the advantage of long-term operation without the need for frequent battery replacements or external power sources, ensuring minimal human intervention. As we see in **Figure VII.2**, the integration of solar panels with embedded systems is shown, demonstrating the energy conversion and storage process for continuous, independent system operation **[4]**.

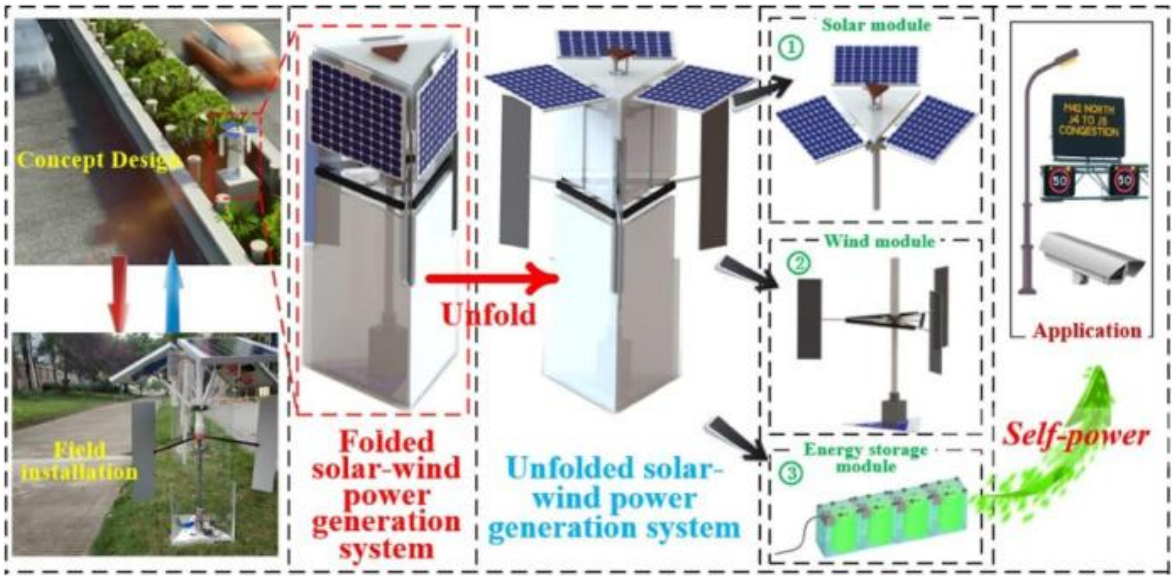

Figure VII.2. Integration of solar panels with embedded systems

VII.3 Perovskite Solar Cells (PSCs)

VII.3.1 Definition of Perovskite Solar Cells (PSCs)

Perovskite Solar Cells (PSCs) are a type of solar cell that utilizes perovskite-structured compounds as the light-absorbing material. These materials have a unique crystalline structure that enables efficient light absorption and conversion into electricity **[5]**. PSCs have gained significant attention in the field of solar energy due to their high-power conversion efficiency, low production costs, and ease of fabrication compared to traditional silicon-based solar cells. They are lightweight, flexible, and can be made using solution-based processes, making them suitable for a wide range of applications, from portable devices to large-scale solar installations. The development of perovskite solar cells has the potential to revolutionize the solar energy industry due to their promising performance and scalability **[6].**

VII.3.2 Working Principle of Perovskite Solar Cells (PSCs)

Perovskite Solar Cells (PSCs) operate based on the principle of converting sunlight into electricity through the photovoltaic effect. When light strikes the perovskite layer, it excites electrons, creating electron-hole pairs **[7]**. These charge carriers are then separated by an internal electric field and collected by the electrodes, generating electrical current. The perovskite material, often a combination of organic and inorganic compounds, plays a key role in this

process by efficiently absorbing light across a wide range of the solar spectrum. The simplicity of the PSC structure, which typically consists of a transparent electrode, a perovskite absorber layer, and a back electrode, allows for effective energy conversion. As we see in **Figure VII.3**, the diagram illustrates the layered structure of a typical PSC and the movement of charge carriers during operation **[8]**.

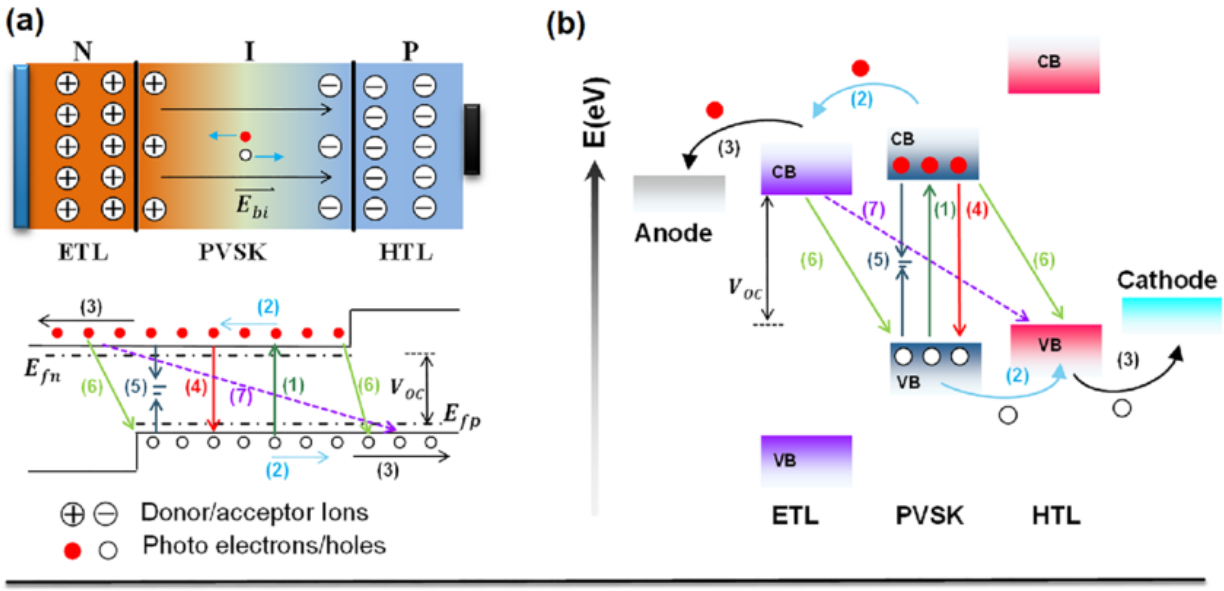

Figure VII.3. Layered structure of a typical PSC and the movement of charge carriers during operation

VII.3.3 Types of Perovskite Solar Cell (PSC) Architectures

Perovskite Solar Cells (PSCs) are typically designed using two main types of structures: n-i-p and p-i-n, referring to the arrangement of layers in the cell. In the n-i-p structure, the electron transport layer (n-type) is positioned on top of the perovskite absorber layer, followed by the hole transport layer (p-type). This configuration is commonly used for its high efficiency and ease of fabrication. On the other hand, the p-i-n structure reverses this order, with the hole transport layer (p-type) placed on top of the perovskite layer, and the electron transport layer (n-type) at the back. This design offers better stability and charge carrier dynamics.

Additionally, PSCs can be fabricated using mesoporous or planar architectures. In mesoporous PSCs, the perovskite layer is deposited on a porous scaffold material, such as titanium dioxide (TiO_2), which helps facilitate better charge transport and collection. Planar PSCs use a flat substrate without the mesoporous layer, offering simpler manufacturing

processes, though they often require more precise control of the perovskite deposition. As we see in **Figure VII.4**, the diagram illustrates both n-i-p and p-i-n structures.

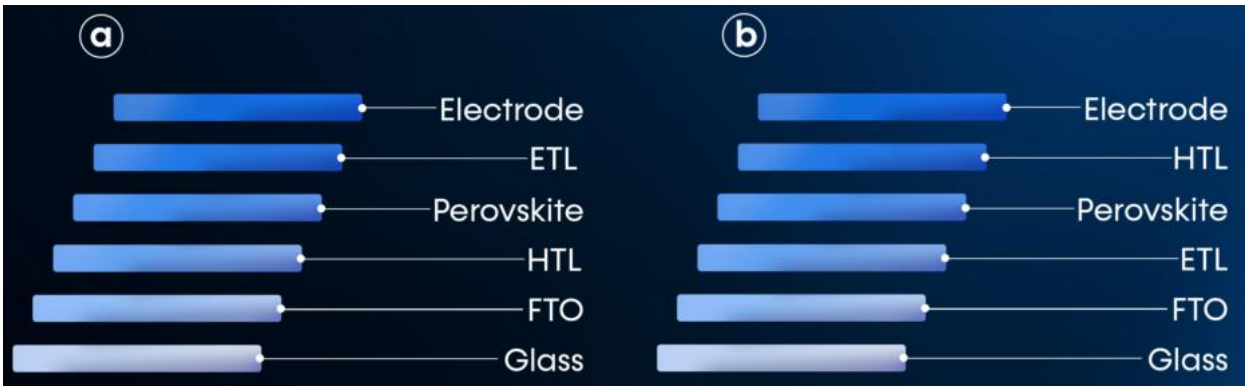

Figure VII.4. Diagram illustrates both n-i-p and p-i-n structures

VII.3.4 Challenges and Stability Issues of Perovskite Solar Cells (PSCs)

Despite their high efficiency and low-cost fabrication, Perovskite Solar Cells (PSCs) face several challenges, particularly regarding their stability and long-term performance. One of the main issues is the degradation of the perovskite material when exposed to moisture, oxygen, and ultraviolet (UV) light, which can cause the cell's efficiency to decline over time. Additionally, thermal instability is a concern, as high temperatures can lead to the breakdown of the perovskite layer. Another challenge is the use of toxic materials in some PSCs, such as lead, which raises environmental and health concerns. Researchers are working on developing more stable and environmentally friendly materials, improving encapsulation techniques, and enhancing the overall durability of the cells. Overcoming these stability issues is crucial for the widespread commercialization of PSCs in real-world applications **[9]**.

VII.4 Review of SCAPS-1D Simulation Tool

VII.4.1 Introduction to SCAPS-1D

SCAPS-1D (Solar Cell Capacitance Simulator) is a simulation tool developed by the University of Gent, Belgium, primarily designed for modeling thin-film solar cells. It allows users to simulate the electrical and optical behavior of various solar cell structures. SCAPS-1D operates based on several fundamental equations, including Poisson's equation, continuity equations for electrons and holes, drift-diffusion equations, recombination equations, and

current-voltage (I-V) characteristics. These equations enable the software to predict the performance of solar cells under different operating conditions **[10].**

VII.4.2 Governing Equations

In solar cell simulations, one of the fundamental equations is Poisson's equation, which describes the relationship between the electrostatic potential and the charge distribution in a semiconductor. This equation is essential for modeling the electric fields within the solar cell and is particularly crucial for understanding how charges accumulate and how they influence the movement of charge carriers such as electrons and holes. Poisson's equation is given by **[11]**:

$$\frac{\mathbf{d^2\psi(x)}}{\mathbf{dx^2}} = -\frac{\mathbf{q}}{\boldsymbol{\varepsilon}\mathbf{(x)}}[\mathbf{p(x)} - \mathbf{n(x)} + \mathbf{N_D^+} - \mathbf{N_A^-} + \boldsymbol{\rho}_{\mathbf{def}}\mathbf{(x)}] \qquad \textbf{(VII. 1)}$$

Where $\boldsymbol{\psi}\mathbf{(x)}$ is the electrostatic potential, $\mathbf{q}$ is the elementary charge, $\boldsymbol{\varepsilon}\mathbf{(x)}$ is the position-dependent dielectric permittivity, $\mathbf{p(x)}$ and $\mathbf{n(x)}$ are the hole and electron concentrations, $\mathbf{N_D^+}$ and $\mathbf{N_A^-}$ are the densities of ionized donors and acceptors, and $\boldsymbol{\rho}_{\mathbf{def}}\mathbf{(x)}$ accounts for the charge density due to defects or traps. This equation plays a pivotal role in determining the electric field within the device, which, in turn, affects the transport of carriers across the solar cell layers. By solving Poisson's equation, SCAPS-1D can accurately model how the device's built-in electric field influences carrier behavior, thus providing insights into the performance and efficiency of the solar cell.

The continuity equations for electrons and holes describe the conservation of charge carriers within a semiconductor. These equations account for the generation, recombination, and transport of electrons and holes, which are crucial for understanding the dynamics of charge carriers in a solar cell. The continuity equations are essential for modeling how the carrier concentration evolves over time and space within the device. For electrons, the continuity equation is **[12]**.

$$\frac{\mathbf{1}}{\boldsymbol{q}}\frac{\boldsymbol{dJ_n(x)}}{\boldsymbol{dx}} = \boldsymbol{G(x)} - \boldsymbol{R(x)} \qquad \textbf{(VII. 2)}$$

For holes, the continuity equation is:

$$-\frac{1}{q}\frac{dJ_p(x)}{dx} = G(x) - R(x) \qquad \textbf{(VII. 3)}$$

Where **Jn** and **Jp** are the electron and hole current densities, **G(x)** is the position-dependent photogeneration rate, and **R(x)** represents the total recombination rate including Shockley-Read-Hall (SRH), radiative, and Auger processes. These equations describe how carriers move, recombine, and are generated within the solar cell.

VII.4.3 Required Inputs and Output Parameters

In SCAPS-1D simulations, the required inputs are the material properties, device structure, and operating conditions that define the solar cell. These inputs include the semiconductor layer thicknesses, doping concentrations, carrier mobilities, recombination coefficients, and light intensity. Additionally, boundary conditions such as the applied voltage or external illumination are specified. These inputs are essential for setting up the simulation and obtaining realistic results **[13]**.

The output parameters of the simulation provide crucial performance metrics of the solar cell. These include the current-voltage **(I-V)** characteristics, open-circuit voltage **(V_{OC})**, short-circuit current **(I_{SC})**, fill factor **(FF)**, and power conversion efficiency **(PCE)**. Other important outputs might include the carrier concentrations, electric fields, and recombination rates, which help in analyzing the internal behavior and efficiency-limiting processes within the device. These parameters allow for a comprehensive understanding of the solar cell's performance under various conditions **[14].**

VII.5 Results and Discussion

VII.5.1 SCAPS-1D Simulation of Perovskite Solar Cell

VII.5.1.1 Device construction and simulation techniques

To assess the photovoltaic performance of the $Rb_2Pt_{1-x}PdxBr_6$ alloyed double perovskite absorber, numerical simulations were carried out using SCAPS-1D. The simulation focused on a conventional five-layer architecture consisting of FTO/SnS_2/$Rb_2Pt_{1-x}PdxBr_6$/MoO_3/Au, where FTO serves as the transparent front contact, SnS_2 is the electron transport layer (ETL), MoO_3 is

the hole transport layer (HTL), and Au is the back contact. This structure is depicted in **Figure VII.5**.

The device simulation was conducted under standard AM1.5G illumination, with an incident power of 1000 W/m² and a constant temperature of 300 K. The absorber layer thickness was varied to optimize photogeneration and carrier collection, while the transport layers were kept at fixed, optimized values based on existing literature. The electronic and optical parameters for each material, such as band gap, electron affinity, carrier mobilities, and defect densities, were based on experimental data and theoretical calculations, as summarized in **Tables VII.1** and **VII.2**.

The simulations were designed to evaluate the influence of varying the composition of the $Rb_2Pt_{1-x}PdxBr_6$ absorber material. Key performance metrics were extracted from the simulations, including the current-voltage **(I-V)** characteristics, short-circuit current, open-circuit voltage, fill factor, and power conversion efficiency. Additionally, the external quantum efficiency **(EQE)** was calculated, providing insight into the spectral response of the device.

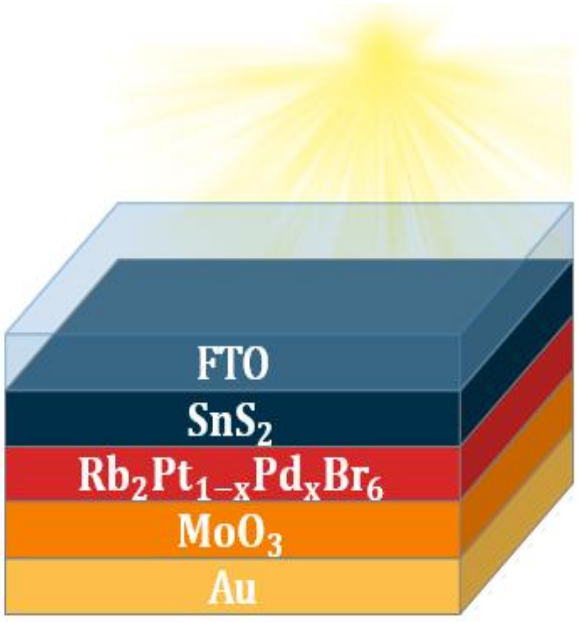

Figure VII.5. Schematic Representation of the Device Architecture for the Five Photovoltaic Devices

Table VII.1: Material Parameters of FTO, MoO_3, SnS_2, and $Rb_2Pt_{1-x}Pd_xBr_6$ for SCAPS-1D Device Simulation

Parameter	FTO	ETL	Absorber Layer ($Rb_2Pt_{1-x}Pd_xBr_6$)					HTL
		SnS_2	X = 0	X = 0.25	X = 0.5	X = 0.75	X = 1	MoO_3
Thickness (μm)	0.20	0.05	0.45	0.45	0.45	0.45	0.45	0.15
Band Gap (eV)	3.6	2.24	2.18	1.69	1.52	1.44	1.20	3.0
Electron Affinity (eV)	4.5	4.24	4.11	4.06	4.02	3.97	3.95	2.5
Dielectric Constant (ε_r)	10	10	3.35	3.55	3.68	3.84	4.56	12.5
CB effective density of states N_C	2×10^{18}	2.2×10^{18}	1.53×10^{19}	1.83×10^{19}	8.31×10^{18}	1.72×10^{19}	1.59×10^{19}	2.2×10^{18}
VB effective density of states N_v	1.8×10^{19}	1.8	9.36×10^{18}	1.23×10^{19}	8.73×10^{18}	8.52×10^{18}	9.59×10^{18}	1.9×10^{19}
Electron Mobility ($cm^2/V\cdot s$)	100	50	50	50	50	50	50	25
Hole Mobility ($cm^2/V\cdot s$)	20	50	25	25	25	25	25	100
Doping Type	n-type	n-type	intrinsic	intrinsic	intrinsic	intrinsic	intrinsic	p-type
Doping Concentration (cm^{-3})	10^{18}	10^{17}	10^{15}	10^{15}	10^{15}	10^{15}	10^{15}	10^{18}
Defect Density (cm^{-3})	10^{14}	10^{14}	10^{14}	10^{14}	10^{14}	10^{14}	10^{14}	10^{14}

Table VII.2: Interface Parameters for Solar Cell Devices

Parameters	Absorber/ETL	HTL/Absorber
Defect type	neutral	neutral
σ_e (cm^2)	1×10^{19}	1×10^{19}
σ_h (cm^2)	1×10^{19}	1×10^{19}
E_r	0.6	0.6
Interface defect density, n_t	10^{11}	10^{11}
Energetic distribution	single	single
Working temperature (K)	300	300

VII.5.1.2 Energy Band Alignment and Interfacial Offset Analysis

The energy band diagram, shown in **Figure VII.6**, depicts the vertical structure of the proposed solar cell device, consisting of the layers MoO_3 (HTL), $Rb_2Pt_{1-x}PdxBr_6$ (Absorber), SnS_2 (ETL), and FTO. Simulations were conducted for various doping concentrations of $x = \mathbf{0.0, 0.25, 0.5, 0.75, 1.0}$. The diagram clearly illustrates the conduction band **($\mathbf{E_c}$)**, valence band **($\mathbf{E_v}$)**, and the Fermi levels for both electrons **($\mathbf{F_n}$)** and holes **($\mathbf{F_p}$).** The alignment of these bands at the interfaces between layers plays a crucial role in determining the efficiency of charge carrier separation and transport.

As the doping concentration of Pd increases, the bandgap of the absorber layer can be tuned, with values ranging from 2.24 eV at $x = 0$ to 1.44 eV at $x = 1$. This tunability in bandgap is key for optimizing light absorption and adjusting the device's spectral response. Specifically, the bandgap values for each absorber composition are as follows: $x = 0$ yields $E_g = 2.24$ eV, $x = 0.25$ gives $E_g = 2.18$ eV, $x = 0.5$ shows $E_g = 1.69$ eV, $x = 0.75$ results in $E_g = 1.52$ eV, and $x = 1.0$ corresponds to $E_g = 1.44$ eV. This variation shifts the absorption window from the near-ultraviolet to the visible spectrum, providing flexibility for both single-junction and tandem solar cell designs.

To assess the interfacial charge transport, the conduction band offset (CBO) at the absorber/ETL interface ($Rb_2Pt_{1-x}PdxBr_6/SnS_2$) and the valence band offset (VBO) at the HTL/absorber interface ($MoO_3/Rb_2Pt_{1-x}PdxBr_6$) were calculated. The CBO is crucial for determining the efficiency of electron extraction, while the VBO impacts hole extraction. The CBO values were found to increase with Pd content: for $x = 0$, 0.25, 0.5, 0.75, and 1.0, the values were 0.26 eV, 0.39 eV, 0.44 eV, 0.48 eV, and 0.55 eV, respectively. A slightly positive CBO (around 0.3 eV) is ideal for facilitating electron transport while hindering hole movement. However, as Pd concentration increases, a higher CBO may impede electron transport due to the larger barrier.

Similarly, the VBO values for the absorber/HTL interface were calculated as -1.00 eV, -1.08 eV, -1.16 eV, -1.20 eV, and -1.24 eV for $x = 0,0.25,0.5,0.75$, and 1.0, respectively. These increasingly negative VBO values create a deep barrier at the HTL/absorber interface, which

promotes hole extraction but may also lead to higher recombination rates at the interface, especially at higher Pd concentrations.

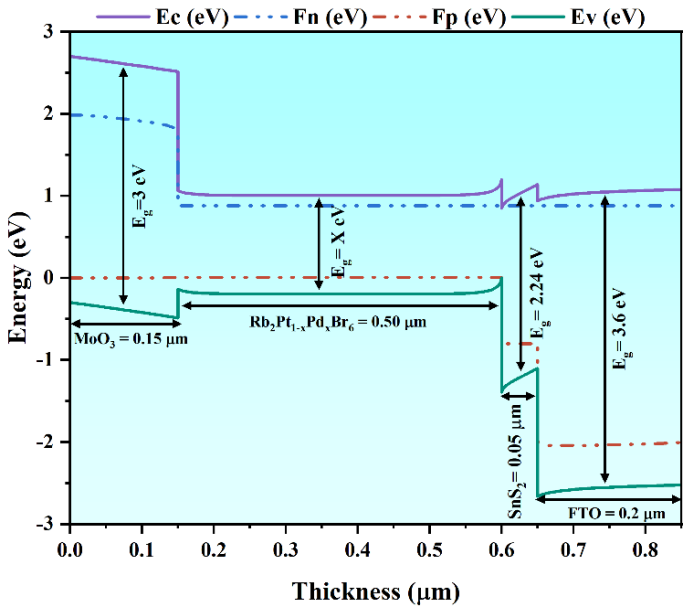

Figure VII.6. Band Diagram of the Photovoltaic Devices

VII.5.1.3 Photovoltaic Performance Analysis

Figure VII.7 illustrates the current density-voltage (J-V) characteristics of five solar cell devices employing $Rb_2Pt_{1-x}Pd_xBr_6$ double perovskite absorbers, where the Pd concentration (x) varies from 0 to 1 in steps of 0.25. As expected for typical photovoltaic behavior, all devices exhibit a negative current density in the fourth quadrant under illumination, indicating power generation. The short-circuit current density (J_{SC}) corresponds to the current value at zero voltage (V = 0), and the open-circuit voltage (V_{OC}) is the voltage at which the current becomes zero. For Device I (x = 0), the J_{SC} is approximately 9.01 mA/cm², and the V_{OC} is 1.37 V. Device II (x = 0.25) shows a significantly higher J_{SC} of 19.72 mA/cm² with a V_{OC} of 1.28 V, indicating improved light absorption and carrier collection with partial Pd substitution. Device III (x = 0.5) achieves a further enhanced J_{SC} of 24.77 mA/cm² with a V_{OC} of 1.14 V, reflecting an optimal balance between absorption and charge transport. Device IV (x = 0.75) exhibits a higher J_{SC} of 27.60 mA/cm², although the V_{OC} decreases to 1.05 V, suggesting increased recombination losses at elevated Pd content. Device V (x = 1) achieves the maximum J_{SC} of approximately 32.07 mA/cm² but experiences a significant drop in V_{OC} to 0.82 V, indicating that full Pd substitution,

while beneficial for photocurrent generation, compromises voltage due to increased non-radiative recombination or unfavorable band alignment. All extracted photovoltaic parameters are summarized in **Table VII.3**. Comparatively, the substitution of Pt by Pd consistently enhances current generation across the composition range due to improved optical absorption or better carrier dynamics, as evidenced by the increasing J_{SC}. However, the V_{OC} trend reveals a trade-off, where higher Pd content leads to voltage deterioration. From a device optimization standpoint, Device III (x = 0.5) offers the most balanced performance, combining a high J_{SC} with a moderate V_{OC}, thereby achieving the highest power conversion efficiency (PCE).

The external quantum efficiency (EQE) spectra of the five investigated solar cell devices, plotted in the spectral range of 300 to 900 nm, reveal key insights into the light-harvesting capabilities of each structure across varying wavelengths. At lower wavelengths (300-400 nm), the EQE increases progressively for all devices, with the highest efficiency consistently observed in the device with the fifth concentration level. This early spectral region highlights the superior photon conversion efficiency of this device in the ultraviolet-blue range. Between 400 and 550 nm, the EQE values for all devices continue to rise, albeit at varying rates, converging toward a common trend. Notably, the fifth device maintains its performance lead, indicating an optimized absorption and carrier collection efficiency likely due to favorable material quality or band alignment. The spectral region between 550 and 590 nm marks the peak EQE response for all devices. At 570 nm, the highest EQE is recorded, reaching approximately 96.17% for the third device, and marginally lower values for the others. This narrow band represents the optimal operating window of the devices, where photo-generated carriers are most efficiently collected **[15, 16]**. The consistency in peak values across devices suggests that all architectures possess similarly effective photon absorption and charge transport mechanisms in this range, possibly governed by intrinsic material properties rather than external structural differences. Beyond 590 nm, a notable trend emerges the EQE curves of all five devices begin to converge, exhibiting minimal variation across the near-infrared region. This convergence implies that, at longer wavelengths, the differences in device configuration or concentration no longer significantly affect carrier generation or collection. Instead, the limiting factor is likely the reduced photon energy in this spectral region, which may fall below the bandgap threshold of some layers, thereby reducing the absorption probability. Toward the end of the spectrum (above 750 nm), a steep decline in EQE is observed for all devices, eventually approaching

negligible values beyond 780 nm. This decline corresponds to the long-wavelength limit of photon absorption, where insufficient photon energy fails to excite electrons across the bandgap, thus terminating effective charge carrier generation. Minor residual EQE values in this region may be attributed to sub-bandgap absorption or defect-assisted transitions, more prominent in the fifth device, which shows slightly higher EQE in the tail region **[17, 18]**.

The fill factor (FF) is a vital performance metric in solar cell evaluation, representing the ratio of the maximum obtainable power to the product of open-circuit voltage (V_{OC}) and short-circuit current density (J_{SC}). Mathematically, it is defined as **[19]**:

$$\mathbf{FF} = \frac{\boldsymbol{P}_{\mathbf{max}}}{\boldsymbol{V}_{\mathbf{oc}} \times \boldsymbol{J}_{\mathbf{sc}}} \qquad (\mathbf{VII.4})$$

A higher FF signifies lower internal resistive losses and better carrier extraction efficiency. From **Table VII.3**, the FF values for the five devices range from 77.56% to 84.79%. The highest FF of 84.79% is observed in Device-II ($Rb_2Pt_{0.75}Pd_{0.25}Br_6$), suggesting this composition yields an optimal balance between series and shunt resistance, promoting efficient charge transport and minimal recombination losses. Device-III and Device-IV also maintain relatively high FFs of 83.45% and 82.69%, respectively, indicating good electrical characteristics across intermediate alloying concentrations. Notably, Device-V (Rb_2PdBr_6), despite demonstrating the highest short-circuit current density (32.07 mA/cm²), exhibits a reduced FF of 77.56%, suggesting the presence of increased resistive losses or charge recombination at higher Pd content.

The power conversion efficiency (PCE) quantifies the effectiveness of a solar cell in converting incident light into electrical energy and is calculated as **[20]**:

$$\mathbf{PCE} = \frac{\boldsymbol{V}_{\mathbf{oc}} \times \boldsymbol{J}_{\mathbf{sc}} \times \mathbf{FF}}{\boldsymbol{P}_{\mathbf{in}}} \qquad (\mathbf{VII.5})$$

Where P_{in} is the incident solar power, typically 100 mW/cm² under standard AM1.5G conditions. The PCE values obtained range from 10.10% to 24.04%. Device-I (Rb_2PtBr_6) demonstrates the lowest PCE (10.10%), constrained primarily by a low J_{SC} of 9.01 mA/cm² despite a relatively high V_{OC} (1.37 V) and FF (81.58%). Upon partial substitution of Pt with Pd, Device-II exhibits a significant enhancement in all photovoltaic parameters, culminating in a

PCE of 21.53%. The PCE reaches its peak value of 24.04% in Device-IV ($Rb_2Pt_{0.25}Pd_{0.75}Br_6$), where a well-optimized J_{SC} (27.60 mA/cm²), reasonable V_{OC} (1.05 V), and high FF (82.69%) synergistically yield the most efficient energy conversion. Device-V, although having the highest J_{SC}, records a slightly lower PCE (22.16%) due to its diminished V_{OC} (0.82 V) and FF, highlighting the trade-offs associated with complete substitution of Pt by Pd.

Table VII.3: Photovoltaic Performance Parameters of the Devices I to V

Absorber Material	V_{OC} (V)	FF (%)	J_{SC} (mA/cm^{-2})	PCE (%)
Device-I (Rb_2PtBr_6)	1.37	81.58	9.01	10.10
Device-II ($Rb_2Pt_{1-0.25}Pd_{0.25}Br_6$)	1.28	84.79	19.72	21.53
Device-III ($Rb_2Pt_{1-0.5}Pd_{0.5}Br_6$)	1.14	83.45	24.77	23.74
Device-IV ($Rb_2Pt_{1-0.75}Pd_{0.75}Br_6$)	**1.05**	**82.69**	**27.60**	**24.04**
Device-V (Rb_2PdBr_6)	0.82	77.56	32.07	22.16

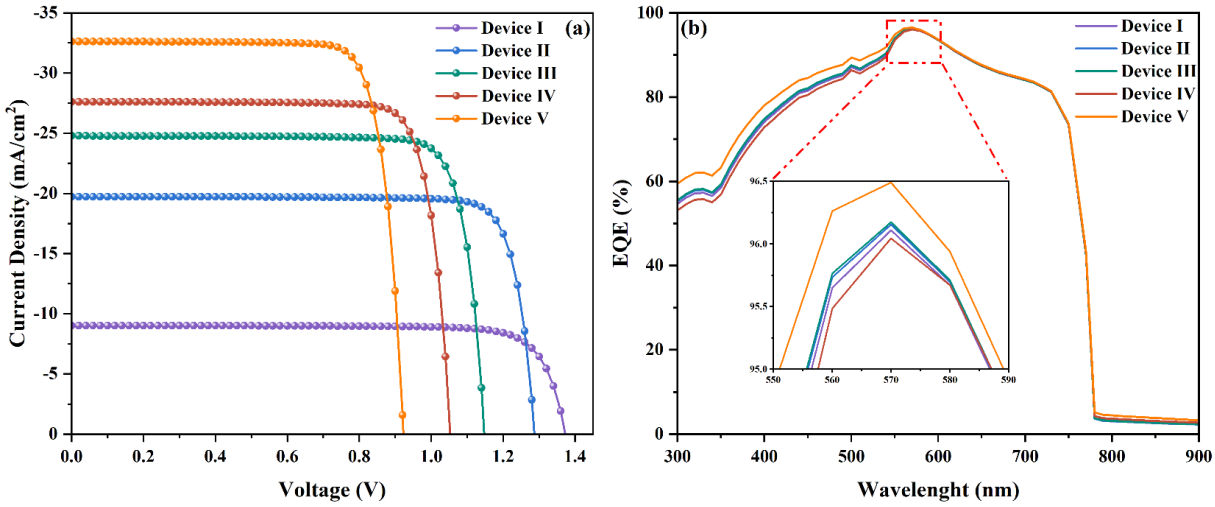

Figure VII.7. (a) Current-Voltage J-V Characteristics and (b) External Quantum Efficiency EQE for the Five Devices

VII.5.2 Integration of PSC in Embedded System

The integration of a Perovskite Solar Cell (PSC) into the embedded system of an agricultural quadcopter represents a significant step toward achieving energy autonomy and reducing human intervention in field operations. In this design, the PSC is strategically positioned on the upper surface of the quadcopter, as illustrated in **Figure VII.8**, to maximize solar energy capture during flight and idle periods. The harvested solar energy is used to charge

the onboard battery and directly supplement the power requirements of the quadcopter's embedded systems, thereby reducing dependency on ground-based charging infrastructure. This approach not only extends operational endurance but also enhances the sustainability of agricultural spraying missions, where the quadcopter is deployed to distribute agrochemical products for crop protection, pest control, and fertilization. By leveraging the high efficiency and lightweight properties of perovskite solar technology, the proposed system ensures a self-powered, power-independent solution that aligns with modern precision agriculture goals.

Figure VII.8. 3D View of Simulated Agricultural Quadcopter with Integrated Solar Panel

Following the comprehensive characterization of the five perovskite solar cell prototypes presented in Section VII.5.1, it was determined that Device 4 delivered the most favorable performance parameters for integration into the quadcopter's embedded power system. This device, based on the composition $Rb_2Pt_{1-0.75}Pd_{0.75}Br_6$, demonstrated under standard test conditions AM 1.5G, 1000 W/m², active area = 1 cm² an open-circuit voltage (V_{OC}) of 1.05 V, a short-circuit current density (J_{SC}) of 27.60 mA/cm², and a fill factor (FF) of 82.69 %, yielding a power conversion efficiency (PCE) of 24.04 %. The corresponding maximum output power can be calculated as **[21]**:

$$P_{max} = V_{OC} \times J_{SC} \times FF \approx 1.05 \times 27.60\,\text{mA} \times 0.8269 \approx 23.98\,\text{mW} \quad \textbf{(VII.6)}$$

per cell of 1 cm² active area. This high output power, combined with the lightweight nature of the perovskite layer, makes the device highly suitable for airborne energy harvesting. To meet the operational voltage and current requirements of the quadcopter encompassing both battery charging and direct powering of low-voltage embedded electronics multiple cells will be interconnected in series and/or parallel. Furthermore, the integration of a maximum power point tracking (MPPT) charge controller, modeled in Section 6.1, will ensure that the PSC array operates consistently at peak efficiency under varying environmental conditions, enabling a self-powered agricultural spraying platform with minimal human intervention.

VII.5.2.1 Modeling of Charge Controller Circuit

a- Mission assumptions for our prototype

In this section, we outline the mission assumptions for the quadcopter prototype, focusing on the battery charging process using perovskite solar cells. The quadcopter is designed to cover a field of 1.08 hectares, with a total weight ranging between 4.5 kg and 5.5 kg. The quadcopter is powered by a Li-Po 22,000 mAh 6S (22.2 V) 25C battery, which is charged at stations strategically placed along the field's border. These stations are primarily powered by solar cells and include human intervention for urgent situations. The goal is to use perovskite solar cells for recharging the battery, with the power generation and panel dimensions optimized through MATLAB modeling.

b- Perovskite Solar Cell Design and Optimization

The perovskite solar cells used in the quadcopter charging stations are designed to achieve a target power output of 30 W. To determine the optimal panel dimensions and the number of cells required, we need to ensure that the system delivers the desired voltage and current.

- **Series Configuration**: The number of cells connected in series is calculated to meet the required voltage. The voltage per cell under open-circuit conditions (V_{OC}) is 1.05 V, and the target voltage (V_{target}) is 18.8 V. Therefore, the number of cells in series (n_{series}) is determined as **[22]**.

$$\boldsymbol{n_{\text{series}} = \left\lceil \frac{V_{\text{target}}}{V_{\text{oc}}} \right\rceil = \left\lceil \frac{18.8}{1.05} \right\rceil = 18} \qquad \textbf{(VII. 7)}$$

- **Parallel Configuration**: To achieve the desired current of at least 100 mA, the number of parallel strings of cells ($n_{parallel}$) is calculated based on the current per cell (I_{cell}), which is $I_{cell} = J_{sc} \times \text{area} = 27.60\,\text{mA/cm}^2 \times 1\,\text{cm}^2 = 27.60\,\text{mA}$. The number of parallel strings required is **[22]**.

$$\boldsymbol{n_{\text{parallel}} = \left\lceil \frac{I_{\text{target}}}{I_{\text{cell}}} \right\rceil = \left\lceil \frac{300}{27.60} \right\rceil = 11} \qquad \textbf{(VII. 8)}$$

Thus, the total number of cells required is the product of the number of cells in series and the number of parallel strings **[22]**.

$$\boldsymbol{n_{\text{total}} = n_{\text{series}} \times n_{\text{parallel}} = 18 \times 11 = 198} \qquad \textbf{(VII. 9)}$$

The resulting total active area of the module is 198 cm² (e.g., 18.0 cm × 11.0 cm), as shown in **Figure VII.9**. With these dimensions, the theoretical output of the solar module is estimated as follows:

- **Open-circuit voltage (V_{OC})**: 18.9 V (calculated as 18×1.05 V).
- **Maximum current (I_{max})** : 303.6 mA (calculated as 11×27.60 mA).

- **Estimated maximum power output (P_{total})**: 47.47 W, calculated using the following formula.

$$\mathbf{P_{total} = V_{total} \times I_{total} \times FF} \qquad (\mathbf{VII.10})$$

This estimated maximum power indicates that the module can provide enough energy for a drone's battery charging system.

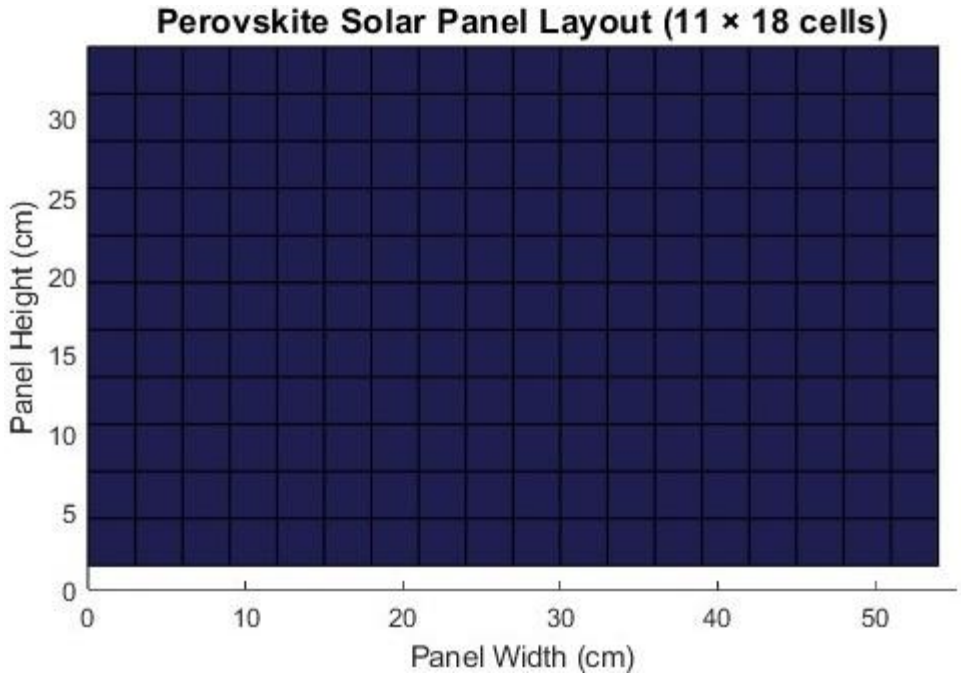

Figure VII.9. Layout of Perovskite Solar Panel (11 × 18 Cells) for Drone Battery Charging

c- Charging System Design

Building upon the previous work where the perovskite solar cell model was developed and simulated in MATLAB to predict the photovoltaic (PV) output, this section focuses on implementing the Maximum Power Point Tracking (MPPT) system for optimizing the power extracted from the perovskite solar panel. The MATLAB model provided crucial insights into the behavior of the solar panel under various environmental conditions, including irradiance and temperature changes. These insights serve as the foundation for designing the MPPT system, which will control the power extraction from the panel in real-time.

In this section, the PV output derived from the MATLAB simulation is applied to a MPPT charging circuit implemented with an Arduino Uno microcontroller. The primary objective of this MPPT system is to dynamically adjust the operating point of the solar panel to maximize its power output, ensuring the most efficient use of the harvested solar energy. The PV panel used in this system is based on the TDC_M20_36 model, which is controlled through an Arduino board for real-time MPPT operation.

The circuit diagram of the system is shown in **Figure VII.10(a)**, illustrating the integration of the PV panel, Arduino Uno, and the supporting components. The PV panel generates a variable output in terms of voltage and current, which are monitored by the Arduino Uno via a current sensor (INA169), depicted in **Figure VII.10(b)**, and a voltage sensor (B25), shown in **Figure VII.10(c)**. These sensors provide real-time data to the Arduino, enabling it to calculate the power output from the PV panel. Based on this data, the microcontroller adjusts the MOSFET (Q1) in the DC-DC converter circuit, ensuring the panel operates at its maximum power point.

The DC-DC converter, comprising components like the inductor (L), capacitors (C0 and C1), and diode (D1), regulates the output voltage to the load while optimizing power extraction from the PV panel. The MOSFET is controlled by the TC4420 driver, which interfaces with the Arduino to manage the switching operation. By adjusting the duty cycle of the MOSFET, the system ensures that the PV panel operates at its optimal power point under varying conditions.

The LCD display in **Figure VII.10(d)** is connected to the Arduino to provide real-time system feedback, such as voltage, current, and power output. This visual display allows for easy monitoring of the system's performance, ensuring that the MPPT algorithm is effectively tracking and adjusting the power extraction in response to changing environmental conditions.

The MPPT algorithm's effectiveness can be assessed through the analogue analysis section, which demonstrates how the panel's power output varies over time as it adjusts to different irradiance levels. This system, designed using the insights from the MATLAB simulation, shows the feasibility and efficiency of employing Arduino-based control for optimizing the power output of solar energy systems.

Finally, this circuit will be integrated with a drone flight controller, which is also based on an Arduino platform. This integration will enable the drone to harness solar energy during flight, thereby extending its operational time and providing a sustainable power source, particularly in remote or off-grid areas where access to conventional power sources is limited.

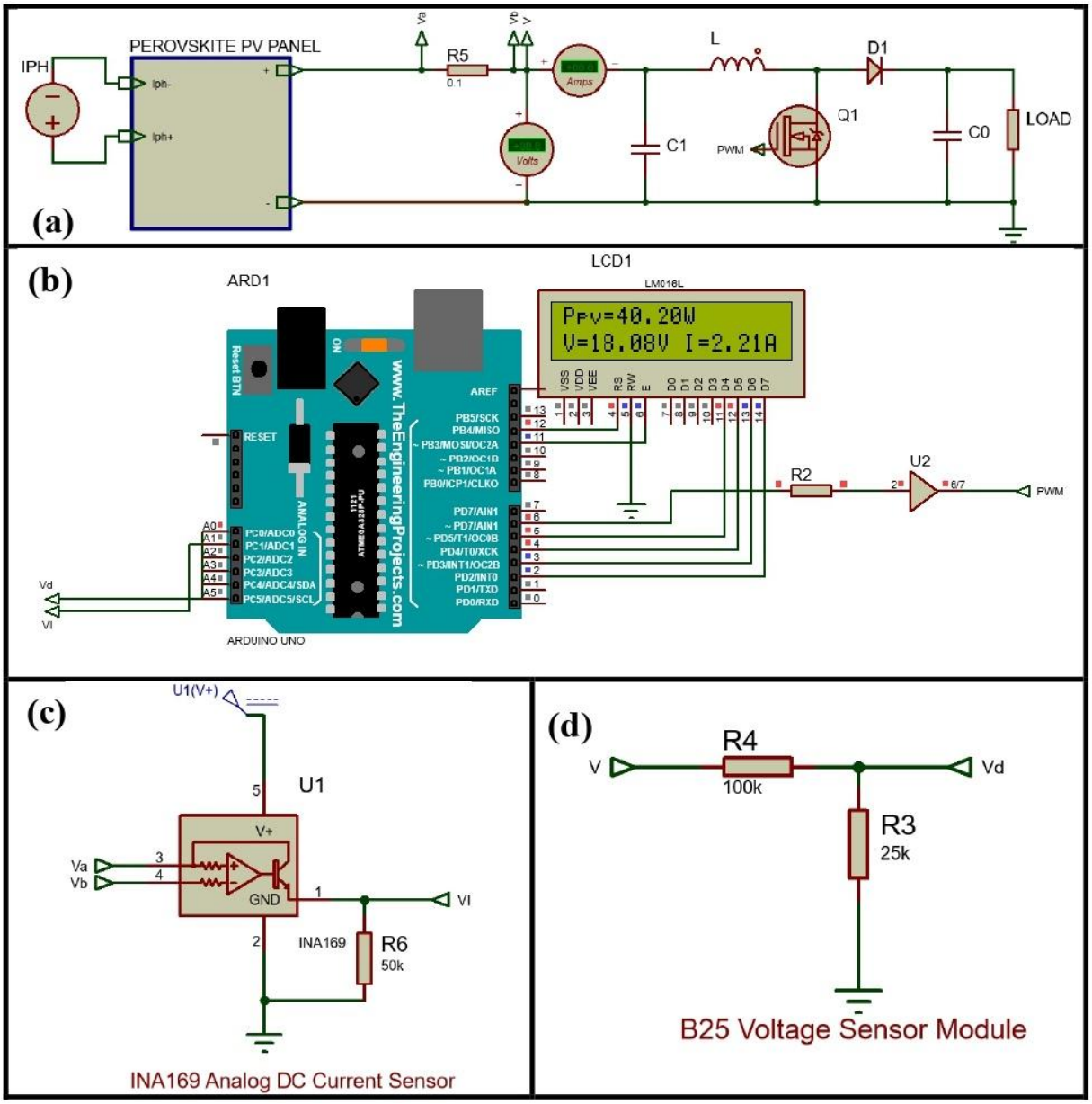

Figure VII.10. MPPT Charging Circuit with Arduino, Current and Voltage Sensor Circuits, and LCD Display for System Monitoring

VII.6 Conclusion

The integration of Perovskite Solar Cells (PSCs) into embedded systems offers a promising solution to the challenges of powering autonomous devices in remote locations. PSCs' unique properties, such as high efficiency, low cost, and flexibility, make them an ideal candidate for energy harvesting in embedded systems, particularly in applications like agricultural drones. Despite the challenges related to stability and environmental concerns, ongoing research and technological advancements continue to improve the performance and longevity of PSCs. The use of simulation tools such as SCAPS-1D provides valuable insights into optimizing the design of PSCs, further enhancing their efficiency in real-world applications. As demonstrated through the case of the agricultural quadcopter, PSCs have the potential to enable energy autonomy, reduce human intervention, and contribute to the sustainability of embedded systems, marking a significant step towards more eco-friendly and efficient technologies.

Bibliography

[**1**] R. Camposano and J. Wilberg, *Design Automation for Embedded Systems*, 1996, 1, 5–50.

[**2**] P. Marwedel, Marwedel, Peter. Embedded system design: embedded systems foundations of cyber-physical systems, and the internet of things. Springer Nature, 2021, 433.

[**3**] H. Rahmani, D. Shetty, M. Wagih, Y. Ghasempour, V. Palazzi, N. B. Carvalho, R. Correia, A. Costanzo, D. Vital, F. Alimenti, J. Kettle, D. Masotti, P. Mezzanotte, L. Roselli and J. Grosinger, *IEEE Journal of Microwaves*, 2023, 3, 237–255.

[**4**] D. Hao, L. Qi, A. M. Tairab, A. Ahmed, A. Azam, D. Luo, Y. Pan, Z. Zhang and J. Yan, *Renew Energy*, 2022, 188, 678–697.

[**5**] T. Swetha and S. P. Singh, *J Mater Chem A Mater*, 2015, 3, 18329–18344.

[**6**] J. Y. Kim, J. W. Lee, H. S. Jung, H. Shin and N. G. Park, *Chem Rev*, 2020, 120, 7867–7918.

[**7**] A. Urbina, *Journal of Physics: Energy*, 2020, 2, 022001.

[**8**] W. Wang, M. O. Tadé and Z. Shao, *Chem Soc Rev*, 2015, 44, 5371–5408.

[**9**] Y. Rong, Y. Hu, A. Mei, H. Tan, M. I. Saidaminov, S. Il Seok, M. D. McGehee, E. H. Sargent and H. Han, *Science (1979)*.

[**10**] M. Burgelman, P. Nollet and S. Degrave, *Thin Solid Films*, 2000, 361–362, 527–532.

[**11**] M. Burgelman, K. Decock, S. Khelifi and A. Abass, *Thin Solid Films*, 2013, 535, 296–301.

[**12**] W. Van Roosbroeck, *Bell System Technical Journal*, 1950, 29, 560–607.

[**13**] K. Decock, P. Zabierowski and M. Burgelman, *J Appl Phys*, DOI:10.1063/1.3686651/989544.

[**14**] K. Decock, S. Khelifi and M. Burgelman, *Thin Solid Films*, 2011, 519, 7481–7484.

[**15**] S. Moulebhar, C. Bendenia, S. Bendenia, H. Merad-Dib, S. A. Khantar and S. Merabet, *Phys Scr*, 2025, 100, 045108.

[**16**] S. Merabet, C. Bendenia, S. Bendenia, H. Merad-Dib, S. Moulebhar and S. A. Khantar, *ChemistrySelect*, 2025, 10, e202405753.

[**17**] A. A. Hassan, M. O. S. T. Sadia Islam Ria, A. Ghosh, H. A. Alrafai, A. Al Baki, S. Khalaf Alla Abdelrahim, J. Y. Al-Humaidi, R. Islam Chowdhury Robin, M. M. Rahman and M. Maniruzzaman, *Materials Science and Engineering: B*, 2024, 308, 117559.

[**18**] S. Moulebhar, C. Bendenia, H. Merad-Dib, S. Bendenia, S. Merabet and S. A. Khantar, *Physica Status Solidi (A) Applications and Materials Science*, 2025, 222, 2400654.
[**19**] M. Harun-Or-Rashid, M. F. Rahman, M. Amami, L. Ben Farhat, M. M. Islam and A. Benami, *Journal of Physics and Chemistry of Solids*, 2025, 197, 112437.
[**20**] M. Harun-Or-Rashid, K. M. Hasan, K. M. Islam, M. N. C. Onkon, A. S. Zishan, M. Elhadi, M. R. Jany, A. N. Z. Rashed and M. M. Islam, *Mater Today Commun*, 2025, 42, 111490.
[**21**] Dizaj, M. H. "Efficiency Calculation and HTL Quality Improvement in Perovskite Solar Cells." Energy Convers. 2 (2024):7.
[**22**] S. Pindado and J. Cubas, *Renew Energy*, 2017, 103, 729–738.

General Conclusion & Perspective

General Conclusion

This thesis has presented a comprehensive theoretical and computational study on the potential of perovskite, double perovskite, and antiperovskite compounds for renewable energy-powered embedded systems. Motivated by the global need for sustainable and cost-effective alternatives to conventional materials such as silicon, lithium, and III–V compounds, this research has investigated a wide range of structural, electronic, optical, elastic, and thermoelectric properties using Density Functional Theory (DFT) with advanced exchange-correlation functionals, the Full-Potential Linearized Augmented Plane Wave (FP-LAPW) method, and complementary simulation tools such as SCAPS-1D, MATLAB, and Proteus.

The results confirmed the thermodynamic stability of several studied compounds through negative formation energies and robust cohesive properties. Electronic structure analyses revealed semiconducting gaps favorable for photovoltaic applications as well as half-metallic behaviors with potential in spintronics. Elastic and vibrational studies showed that many compounds satisfy mechanical stability criteria, combining ductility, stiffness, and thermal robustness key attributes for their integration into real-world devices.

Thermoelectric investigations highlighted the promising performance of Ba_2InOsO_6 and Sr_2MnSbO_6, especially under spin–orbit coupling, with improved carrier transport and enhanced figures of merit (ZT). Optical property analyses of $ASiCl_3$, A_3SbAs, A_3BiI_3, and $Rb_2Pt_{1-x}Pd_xBr_6$ alloys revealed strong absorption and favorable dielectric behavior, confirming their suitability for solar cells, LEDs, and infrared sensors. SCAPS-1D simulations further demonstrated the potential of $Rb_2Pt_{1-x}Pd_xBr_6$ alloys in photovoltaic devices, achieving efficiencies up to 24%, thereby validating their promise for efficient and cost-effective renewable energy harvesting.

Finally, the integration of perovskite solar cells (PSCs) into embedded systems, with emphasis on agricultural and off-grid applications, demonstrated their ability to enhance energy autonomy, reduce operational costs, and minimize human intervention. While challenges remain—including long-term stability, toxicity, and environmental resilience—this work establishes a solid scientific and technological foundation for the adoption of perovskites in embedded system applications.

Perspectives

Looking forward, the findings of this thesis open several avenues for future research and technological development. On the materials side, efforts should focus on lead-free and environmentally benign perovskite compositions, as well as hybrid oxide–halide systems that combine stability with high efficiency. Machine learning–guided high-throughput DFT screening could accelerate the discovery of optimal compounds, extending beyond those investigated here.

From the device engineering perspective, improved solar cell architectures, interfacial engineering, and encapsulation strategies are needed to enhance the operational lifetime of perovskite-based devices under real-world conditions. Combining photovoltaic and thermoelectric functionalities within the same material platform may also enable multifunctional embedded systems capable of harvesting both solar and waste heat.

At the system level, integrating perovskite solar cells into embedded applications such as autonomous drones, agricultural sensors, and medical devices offers new possibilities for energy self-sufficiency. Coupling computational predictions with experimental synthesis and prototype validation will be essential to translate these findings into practical solutions.

From a societal perspective, the successful implementation of stable and non-toxic perovskite compounds could reduce dependence on scarce raw materials, lower production costs, and advance the global transition to cleaner technologies. By contributing both fundamental insights and applied strategies, this thesis provides a foundation upon which future interdisciplinary research can build, ultimately accelerating the deployment of sustainable, intelligent, and energy-efficient embedded systems.

Appendix - A

A.1 Magnetic Properties

Table A.1 and **Table A.2** presents the calculated magnetic properties of Ba_2InOsO_6 and Sr_2MnSbO_6. Ba_2InOsO_6 exhibits a net magnetic moment of 3 μB, primarily originating from the Os 5d electrons, consistent with its half-metallic nature. In contrast, Sr_2MnSbO_6 shows a larger local moment on Mn, reflecting the strong exchange interactions of 3d orbitals. The difference between the two compounds can be attributed to the variation in B-site cations (In vs. Mn, Os vs. Sb), which modifies the degree of hybridization and superexchange pathways.

Table A.1: Magnetic Moments (μ) of Ba_2InOsO_6 Under Different Approximations

Material	Approximation	μ^{Ba}	μ^{In}	μ^{Os}	μ^{O}	μ^{int}	μ^{cell}
Ba_2InOsO_6	GGA	0.01353	0.00022	1.61120	0.12051	0.64833	3.00988
	GGA + U (U = 2.84)	0.01120	-0.00122	1.72125	0.10917	0.60744	3.00489
	mBJ+U	0.00082	-0.00361	2.02885	0.09328	0.41350	3.00005
	mBJ+U+SOC	0.00090	-0.00359	1.98738	0.09126	0.40415	2.94332

Table A.2: Magnetic Moments (μ) of Sr_2MnSbO_6 Under Different Approximations

Material	Approximation	M^{Sr}	M^{Mn}	μ^{Sb}	μ^{O1}	μ^{O2}	μ^{int}	μ^{cell}
Sr_2MnSbO_6	GGA	0.00136	3.28353	0.02260	0.03129	0.03566	0.48595	4.00001
	GGA + U (U = 4)	0.00179	3.47788	0.01568	0.02098	0.00891	0.44635	4.02106
	mBJ+U	-0.00031	3.59033	0.01239	0.02566	0.01383	0.29132	4.00007
	mBJ+U+SOC	-0.00031	3.58985	0.01235	0.02549	0.01357	0.29263	3.99949

Appendix - B

B.1 Flight Controller

The flight controller **Figure B.1**, implemented on an Arduino Nano board, integrates inertial measurement unit (IMU) sensors (e.g., MPU6050) for stabilization, and distributes control signals to the ESCs to regulate the quadcopter's four motors.

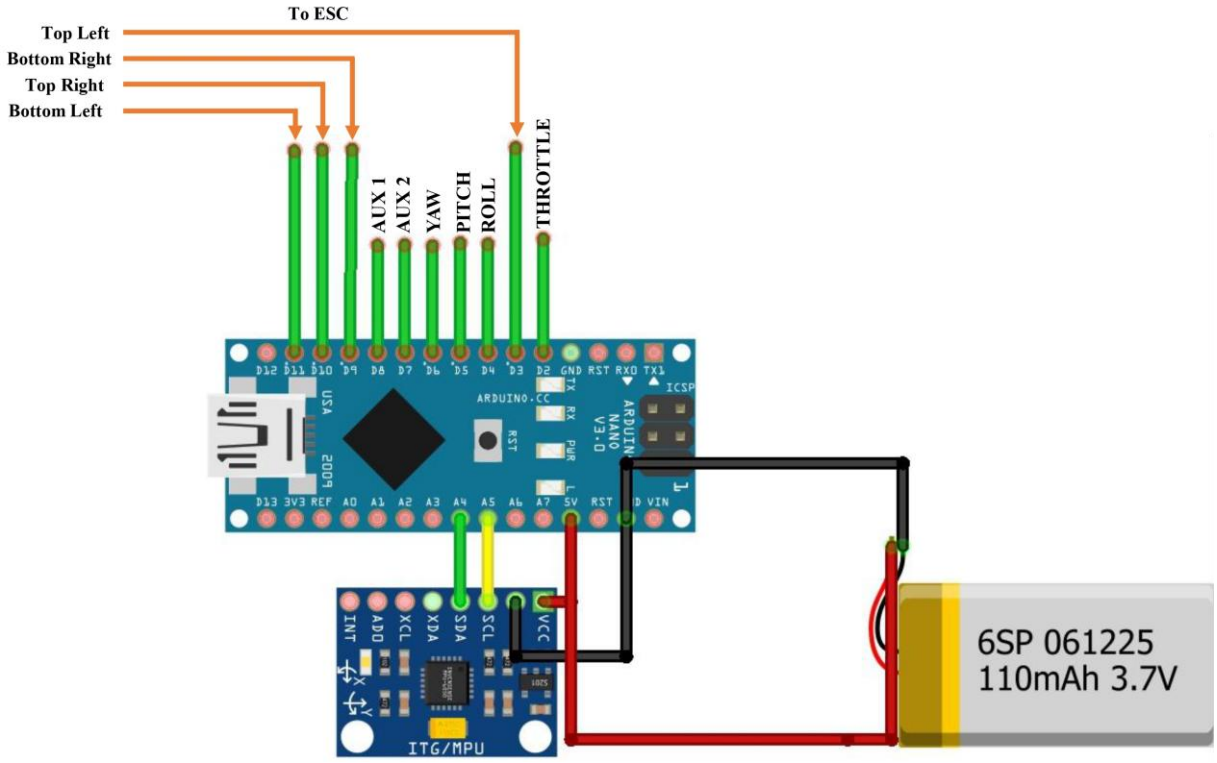

Figure B.1. Wiring schematic of the flight controller using Arduino Nano and MPU6050 sensor

B.2 Receiver Circuit

The receiver circuit employs an Arduino Nano connected to the nRF24L01 module **Figure B.2**, which decodes the received signals and forwards control commands to the electronic speed controllers (ESCs).

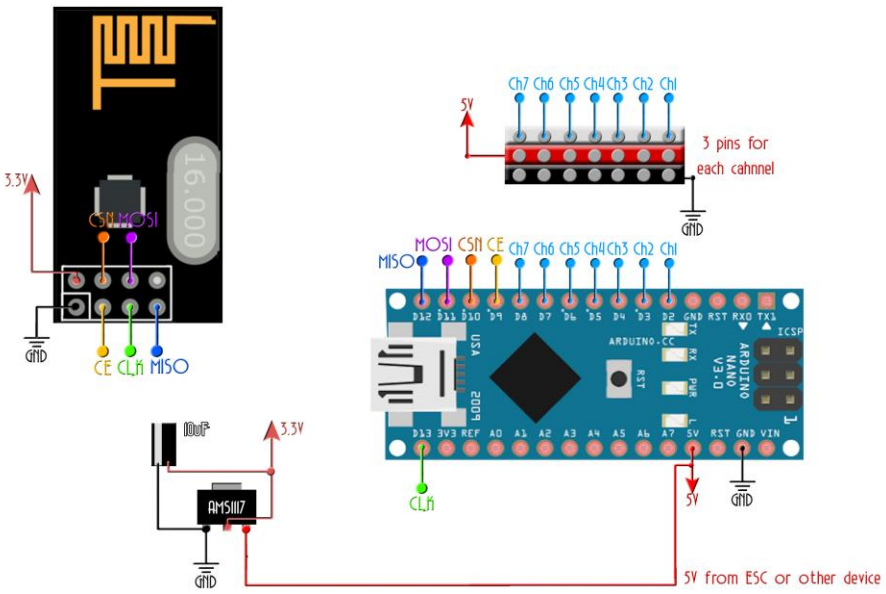

Figure B.2. Circuit diagram of the quadcopter receiver module implemented with Arduino Nano and nRF24L01

B.3 Transmitter Circuit

The transmitter circuit **Figure B.3**, integrates joystick modules with the Arduino microcontroller, which encodes user commands and transmits them via the nRF24L01 RF module.

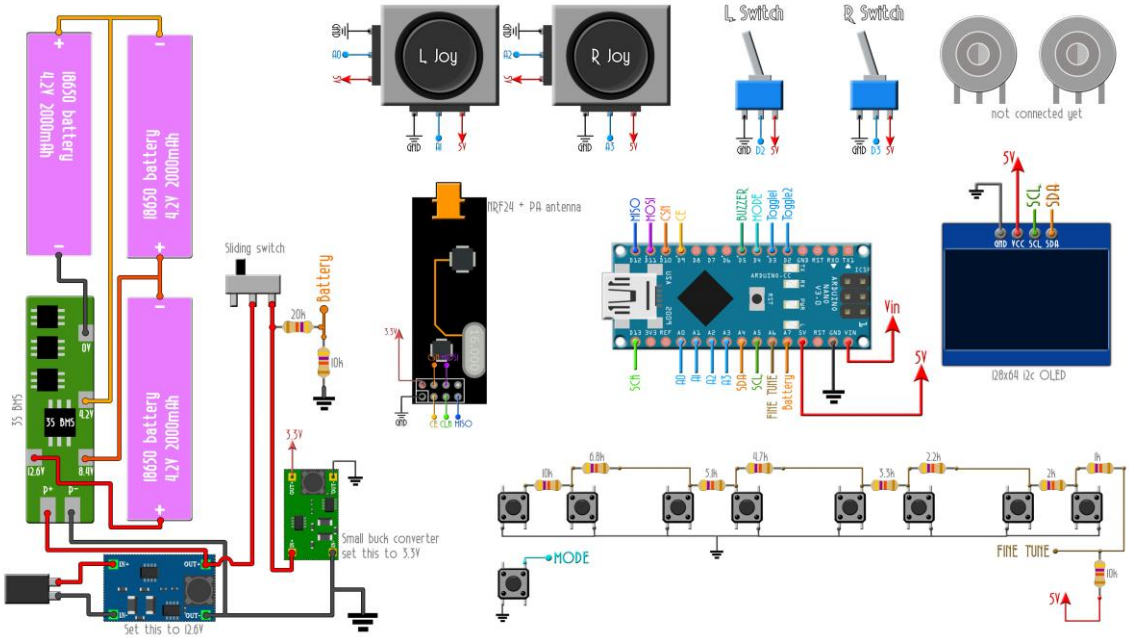

Figure B.3. Circuit diagram of the quadcopter transmitter module based on Arduino Nano and nRF24L01

B.4 Quadcopter Circuit

Figure B.4 presents the circuit diagrams of the quadcopter system developed in this research. It covers the transmitter, as well as the receiver and flight controller, which were built using Arduino microcontrollers and RF communication modules. The detailed circuit diagrams of the receiver and flight controller are provided in **Sections B.2** and **B.3**. These materials complement the discussion in **Chapter VII** and serve as a reference for reproducibility and future development.

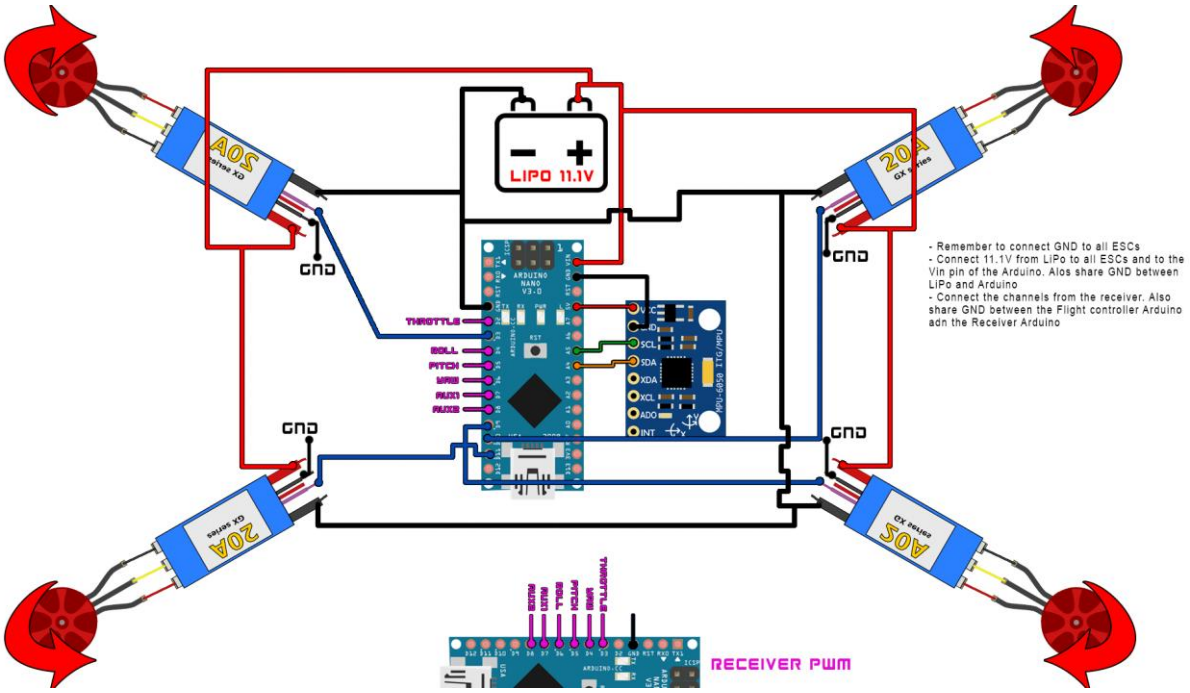

Figure B.4. Circuit diagram of the quadcopter

Optical and Quantum Electronics (2024) 56:313
https://doi.org/10.1007/s11082-023-06045-4

Structural, electronic, elastic, optical and thermoelectric properties of $ASiCl_3$ (A = Li, Rb and Cs) chloroperovskites: a DFT study

Benahmedi Lakhdar[1] · Besbes Anissa[1] · Djelti Radouan[1] · Najwa Al Bouzieh[2] · Noureddine Amrane[2]

Received: 17 August 2023 / Accepted: 4 December 2023 / Published online: 29 December 2023

Abstract

Chloroperovskites have attracted considerable attention in recent years as promising candidates for various technological applications. Their appeal lies in their appropriate optical bandgap, outstanding chemical stability, abundant availability on Earth, and non-toxic nature. In this work, we have investigated the structural, electronic, elastic, optical and thermoelectric properties of $ASiCl_3$ (A = Li, Rb and Cs) using density functional theory. The Tran–Blaha modified Becke Johnson (TB-mBJ) potential were used for exchange–correlation. The band structure profiles of the $LiSiCl_3$, $RbSiCl_3$ and $CsSiCl_3$ materials reveal a semiconductor nature with a small direct band gap of 0.28, 0.37 and 0.54 eV, respectively. The obtained negative values for formation and cohesive energies affirm the energetic and dynamic stability of these compounds. The elastic constants and mechanical parameters acquired suggest that the compounds are mechanically stable and demonstrate a ductile nature with by low stiffness. The analysis of optical parameters revealed an increasing trend in the dielectric constant, refractive index, reflectivity, and absorption coefficient in the UV domain as the A-site atom transitions from Li to Rb and then to Cs (decreasing electronegativity). In the visible spectrum, the three chloroperovskites exhibit low reflectivity, while the highest absorption coefficient is assigned to the $CsSiCl_3$ in the UV domain. The thermoelectric properties are computed with respect to chemical potential at various temperatures. At room temperature, the merit factors for $CsSiCl_3$, $RbSiCl_3$, and $LiSiCl_3$ are 0.95, 0.84, and 0.80, respectively, indicating their potential suitability for use in thermoelectric devices.

Keywords Absorption coefficient · Elastic properties · Merit factor · Optical properties · Perovskite · Semiconductor · Thermoelectric properties

✉ Djelti Radouan
Radouane.djelti@univ-mosta.dz

[1] Technology and Solids Properties Laboratory, University of Mostaganem (UMAB), Mostaganem, Algeria

[2] Physics Department, College of Science, United Arab Emirates University (UAEU), 15551 Al Ain, UAE

Journal of Magnetism and Magnetic Materials 611 (2024) 172629

Contents lists available at ScienceDirect

Journal of Magnetism and Magnetic Materials

journal homepage: www.elsevier.com/locate/jmmm

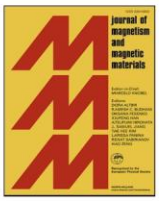

Structural, magnetic, elastic, and thermoelectric properties of Ba_2InOsO_6 double perovskite in the cubic phase: A DFT + U study with spin-orbit-coupling

Lakhdar Benahmedi *, Anissa Besbes, Radouan Djelti

Technology and Solids Properties Laboratory, Faculty of Science and Technology, Mostaganem University, Mostaganem 27000, Mostaganem, Algeria

ARTICLE INFO

Keywords:
Double perovskite
Ba_2InOsO_6
DFT
Half-metallic
Thermoelectric properties

ABSTRACT

In this study, we comprehensively investigate the structural, electronic, magnetic, elastic, and thermal properties of the double perovskite Ba_2InOsO_6 using density functional theory (DFT). Our results show that the ferromagnetic phase is the most stable, with the net magnetic moment primarily arising from the Os atom. The half-metallic behavior exhibited by Ba_2InOsO_6, characterized by a band gap of 3.62 eV in the TB-mBJ + U approximation, decreases upon the inclusion of spin–orbit coupling (SOC). This half-metallic property, coupled with the stability of the ferromagnetic phase, makes Ba_2InOsO_6 particularly suitable for spintronic applications, as it can facilitate efficient spin injection and transport. Elasticity analysis indicates moderate brittleness, while thermoelectric properties, calculated using the Boltzmann transport model, reveal n-type conductivity and notable thermopower, suggesting potential for thermoelectric applications. This work provides a solid foundation for future experimental studies and potential applications in advanced technologies.

1. Introduction

The increasing demand for advanced materials in electronics, magnetism, semiconductors, and light-absorbing technologies, such as solar cells, has driven extensive research into discovering new materials [1]. Among these, perovskite oxides (ABO_3) have garnered significant attention due to their exceptional physiochemical properties, making them ideal for applications in photovoltaics, ferromagnetism, spintronics, and thermoelectric [2,3]. These materials exhibit various functionalities, including superconductivity, diverse magnetic orders, ionic conductivity, and catalytic properties [4]. However, their application in spintronics and energy sectors is often limited by challenges such as structural and thermodynamic instability and low Curie temperature, which have spurred the search for alternative materials [5].

Double perovskites, with the general formula $A_2BB'O_6$, composed of two sublattices of single perovskites, offer enhanced structural and compositional flexibility compared to their single perovskite counterparts [6,7,8]. Particularly intriguing are double perovskite oxides containing 4d or 5d transition metal elements, which have shown unique electronic and magnetic properties, such as room-temperature magnetoresistance, high-temperature ferrimagnetism, and complex magnetic behaviors [9]. The interpenetrating B and B′ face-centered cubic (fcc) sublattices in these double perovskites contribute to their rich magnetic properties, with magnetic interactions often resulting from the interplay between intra-sublattice and inter-sublattice exchange interactions, closely linked to structural distortions [10].

In recent years, spintronics has emerged as a promising field of study, focusing on the intrinsic spin of electrons in addition to their charge. Various materials, including dilute magnetic semiconductors, single perovskites, and binary chalcogenides, have garnered significant attention due to their unique properties. However, double perovskite oxides present a compelling alternative due to their tunable electronic and magnetic characteristics, which are vital for spintronic applications [11,12]. Compounds such as Sr_2FeOsO_6 and Ca_2FeOsO_6, for example, exhibit distinct structural and magnetic characteristics, making them valuable for advanced technological applications. Sr_2FeOsO_6 crystallizes in a tetragonal structure and undergoes antiferromagnetic transitions at 140 K and 67 K, while Ca_2FeOsO_6 crystallizes in a monoclinic structure and exhibits room-temperature ferrimagnetism. The magnetic properties of these compounds are primarily governed by the exchange coupling within the Os^{5+} face-centered cubic sublattice [13,14]. Numerous double perovskites have been studied both theoretically and experimentally in this context. Compounds such as Ba_2ErReO_6 and Ba_2HoReO_6 have demonstrated promising half-metallic properties,

* Corresponding author.
E-mail address: lakhdar.benahmedi@gmail.com (L. Benahmedi).

https://doi.org/10.1016/j.jmmm.2024.172629
Received 23 September 2024; Received in revised form 23 October 2024; Accepted 28 October 2024
Available online 29 October 2024

Physica Scripta

PAPER

First-principles investigation of structural, electronic, optical, elastic, and thermoelectric properties of cubic francifluorite perovskites $FrXF_3$ (X = Si, Ge, and Sn) for optoelectronic and thermoelectric applications

RECEIVED
13 August 2024

REVISED
27 October 2024

ACCEPTED FOR PUBLICATION
12 November 2024

PUBLISHED
22 November 2024

Lakhdar Benahmedi , Anissa Besbes , Radouan Djelti , Sidahmed Bendehiba and Ali Aissani

Technology and Solids Properties Laboratory, Faculty of Science and Technology, Mostaganem University (UMAB), Algeria

E-mail: lakhdar.benahmedi@gmail.com

Keywords: francifluorite perovskites, halide perovskites, optoelectronics, thermoelectric properties, density functional theory (DFT)

Abstract

This study employs first-principles calculations based on Density Functional Theory (DFT), implemented in the Wien2k code, to investigate the structural, electronic, optical, elastic, and thermoelectric properties of $FrXF_3$ (X = Si, Ge, Sn) compounds. Various exchange–correlation functionals, including GGA-PBE, GGA-PBEsol, GGA-WC, and TB-mBJ, were utilized to achieve a comprehensive analysis. The electronic structure calculations reveal that all compounds exhibit semiconducting behavior with direct band gaps (R→R), ranging from 1.75 eV to 2.68 eV using TB-mBJ. Optical properties analysis shows strong responses in the visible to ultraviolet range, highlighting their potential for optoelectronic applications. Thermoelectric evaluations, including thermal and electrical conductivity, Seebeck coefficient, power factor, and figure of merit, indicate that $FrXF_3$ compounds possess significant thermoelectric potential, positioning them as promising candidates for thermoelectric applications.

1. Introduction

Perovskite materials, characterized by their ABX_3 crystal structure, have garnered significant attention due to their versatile properties and wide-ranging applications in various fields [1]. While research on oxide perovskites (ABO_3) has flourished, halide perovskites have emerged as a promising class of materials in areas such as optoelectronics [2]. Perovskites, have gained significant attention in recent years due to their remarkable properties and diverse applications. These materials have found widespread use across various fields, including photovoltaics, photodetectors, batteries, and light-emitting diodes (LEDs) [3–6].

In photovoltaics, perovskite solar cells have emerged as a promising alternative to traditional silicon-based solar cells, offering high power conversion efficiencies, low-cost manufacturing, and the ability to be fabricated using solution-based processes, making them an attractive option for next-generation solar technologies [1, 7–9]. Perovskites also possess excellent light-absorbing and charge-transport capabilities, which make them well-suited for use in photodetectors, employed in applications such as image sensing, optical communication, and security systems [10, 11]. Moreover, perovskite materials have shown promise in the development of high-performance batteries, particularly in the context of solid-state lithium-ion batteries, where their unique structural and electrochemical properties can contribute to improved energy density, safety, and cycle life [12].

In the field of LEDs, perovskite materials can be engineered to emit light efficiently across a wide range of the visible spectrum, enabling the fabrication of high-performance, energy-efficient displays and lighting applications. The versatility of perovskites stems from their tunable properties, which can be tailored through chemical composition and structural modifications [13]. Ongoing research and development in this field continue to explore new avenues for the application of perovskites, with the potential to drive advancements in renewable energy, optoelectronics, and energy storage technologies [14]. However, the presence of lead (Pb) in

RESEARCH ARTICLE

physica status solidi a

www.pss-a.com

Numerical Analysis of High-Efficiency Chalcogenide Perovskite Solar Cells ($InBiSe_3$/$GaBiSe_3$): Study of Single and Bilayer Configurations

Lakhdar Benahmedi, Anissa Besbes, Radouan Djelti, and Samia Moulebhar*

Chalcogenide perovskites are emerging as a promising alternative to hybrid halide perovskites for optoelectronic applications, owing to their excellent light absorption and chemical stability. This study investigates the performance of single- and dual-absorber solar cell devices using $InBiSe_3$ and $GaBiSe_3$ as absorber materials, simulated using the solar cell capacitance simulator in one dimension software. The devices employ WS_2 as the electron transport layer and CuO as the hole transport layer. For single-absorber devices, $GaBiSe_3$ achieve a power conversion efficiency (PCE) of 26.58%, with a V_{OC} of 0.94 V, a fill factor (FF) of 86.82%, and a short-circuit current density (J_{SC}) of 32.52 mA cm^{-2}. $InBiSe_3$ performs slightly lower, with a PCE of 21.44%, V_{OC} of 1.25 V, FF of 87.83%, and J_{SC} of 19.49 mA cm^{-2}. The bilayer configuration, incorporating $InBiSe_3$ as the top layer and $GaBiSe_3$ as the bottom layer, shows the highest efficiency of 30%, with a V_{OC} of 1.06 V, J_{SC} of 32.78 mA cm^{-2}, and FF of 85.97%. The study also examines the effects of temperature, shunt resistance, and series resistance on the device performance, as well as the influence of absorber layer thickness, defect density, and back contact variations.

1. Introduction

The global shift toward renewable energy, particularly solar power, is increasingly seen as a sustainable solution to meet the world's energy demands while significantly reducing the environmental impact of traditional coal-based electricity generation.[1–3] This transition is driven by the urgent need to address climate change, largely fueled by the continued reliance on fossil fuels. As a result, the development of high-performance, cost-effective solar panel technologies has become a critical priority.[4,5]

In recent years, organic–inorganic perovskites, particularly methylammonium lead iodide ($MAPbI_3$), have garnered significant attention due to their remarkable efficiency as solar cell absorber materials. $MAPbI_3$-based solar cells have achieved power conversion efficiencies (PCEs) exceeding 21%, making them one of the most promising materials in photovoltaics (PV). However, the reliance on toxic lead and stability issues under environmental stressors has raised concerns about their long-term viability.[6,7] In response, inorganic chalcogenide perovskites (CPs) are emerging as a potential replacement. These materials, characterized by the general formula ABX_3, where A is a group II cation (such as Ca^{2+}, Sr^{2+}, or Ba^{2+}), B is a group IV transition metal (such as Ti^{4+}, Zr^{4+}, or Hf^{4+}), and X is a chalcogen anion (such as S^{2-} or Se^{2-}), offer a combination of environmentally friendly, nontoxic properties and exceptional optoelectronic performance.[8] Several CPs, including barium zirconium sulfide ($BaZrS_3$), strontium zirconium sulfide ($SrZrS_3$), and barium hafnium sulfide ($BaHfS_3$), have been identified as promising candidates for PV applications due to their perovskite-type structure and bandgaps well-suited for efficient light absorption.[8–13] Among these materials, $BaZrS_3$ has attracted particular interest in experimental studies due to its lead-free composition and excellent environmental stability, making it an attractive alternative to traditional lead-based perovskites. Furthermore, research on 2D monolayer perovskites, such as $XBiSe_3$ (where X = Ga, In, Tl), has highlighted their remarkable properties, including high carrier mobility and enhanced visible light absorption, both crucial for efficient charge transport in solar cells.[14] CPs have also demonstrated superior absorption coefficients compared to widely used solar cell absorbers, such as GaAs, $CuInSe_2$, $MAPbI_3$, and Cu_2ZnSnS_4, suggesting that they may outperform many current materials used in solar technologies.[15–17]

Some recent studies on CPs have achieved efficiencies surpassing those of hybrid perovskites, signaling their potential as competitive candidates for solar energy conversion. For instance, Mercy et al. reported efficiencies reaching up to 32.58% for chalcogenide-based solar cells, specifically in $BaZr_{0.96}Ti_{0.04}S_3$-based devices, demonstrating the impressive PV properties of this lead-free material.[18] Similarly, Barman et al. investigated

L. Benahmedi, A. Besbes, R. Djelti
Technology and Solids Properties Laboratory
Faculty of Science and Technology
Mostaganem University
Mostaganem 27000, Algeria
E-mail: lakhdar.benahmedi.etu@univ-mosta.dz

S. Moulebhar
Faculty of Science and Technology
Mostaganem University
Mostaganem 27000, Algeria

The ORCID identification number(s) for the author(s) of this article can be found under https://doi.org/10.1002/pssa.202400780.

DOI: 10.1002/pssa.202400780

IOP Publishing Semiconductor Science and Technology
Semicond. Sci. Technol. **40** (2025) 025001 (23pp) https://doi.org/10.1088/1361-6641/ada17e

DFT and SCAPS-1D simulation of single-layer and bilayer perovskite solar cells: Ca_3BiI_3 and Sr_3BiI_3

Lakhdar Benahmedi[1,*], Anissa Besbes[1], Radouan Djelti[1] and Samia Moulebhar[2]

[1] Technology and Solids Properties Laboratory, Faculty of Science and Technology, Mostaganem University, 27000 Mostaganem, Algeria
[2] Faculty of Science and Technology, Mostaganem University, 27000 Mostaganem, Algeria

E-mail: lakhdar.benahmedi@gmail.com

Received 29 October 2024, revised 29 November 2024
Accepted for publication 18 December 2024
Published 31 December 2024

Abstract

This study investigates the structural, electronic, elastic, and optical properties of the inorganic perovskites Ca_3BiI_3 and Sr_3BiI_3 using density functional theory (DFT) with the Wien2k code. The optimized lattice parameters are 6.38 Å for Ca_3BiI_3 and 6.69 Å for Sr_3BiI_3. The calculated band gaps using the generalized gradient approximation-Perdew–Burke–Ernzerhof functional are 1.36 eV for Ca_3BiI_3 and 1.30 eV for Sr_3BiI_3, which increase to 1.79 eV and 1.61 eV, respectively, after applying the TB-mBJ correction. Both materials are dynamically stable, confirmed through formation energy and phonon dispersion analysis, and mechanically stable based on Born criteria. Optical analysis shows strong absorption in the visible range, with Ca_3BiI_3 slightly outperforming Sr_3BiI_3, making both candidates for photovoltaic applications. In the second part, we simulate the performance of these perovskites in single-layer and bilayer solar cells, with Ca_3BiI_3 as the top absorber and Sr_3BiI_3 as the bottom. By optimizing the bilayer device, we achieve an efficiency of up to 28.37%, with a V_{OC} of 1.36 V, a fill factor of 89.78%, and a short-circuit current density (J_{SC}) of 23.14 mA cm^{-2}.

Keywords: A_3BiI_3 perovskite, density functional theory (DFT), perovskite solar cells, bilayer device, photovoltaic efficiency

1. Introduction

Photovoltaic technology has made substantial progress with the advent of perovskite materials, which are being adopted as alternatives to traditional solar cell technologies [1–3]. In particular, halide perovskites have garnered significant attention due to their remarkable structural, electronic, and optical properties, making them promising candidates for efficient solar energy systems [4–6]. Among the various types of perovskites, the A_3MX_3 group has emerged as a notable contender for solar energy conversion, owing to its favorable attributes, such as tunable band gaps and potential for high efficiency in tandem solar cells [7].

The rapid development of perovskite solar cells (PSCs), particularly in halide-based versions, has led to impressive efficiency gains, with reported improvements from an initial 3.8% to over 25% [8, 9]. This remarkable progress is attributed to the unique properties of halide perovskites, including high absorption coefficients, long carrier diffusion lengths, and tunable band gaps. Kim *et al* initially introduced organo-halide perovskites as light absorbers in PSCs, achieving a modest efficiency of 9% [10]. Later, Chaisan *et al* demonstrated a mesoscopic PSC design with an efficiency of 14% using a two-step deposition method [11]. Following this, Zhou *et al* reported significant improvements by incorporating a TiO_2 scaffold, achieving an efficiency of 18% [12]. Heo *et al* pioneered

* Author to whom any correspondence should be addressed.

Materials Chemistry and Physics 334 (2025) 130520

Contents lists available at ScienceDirect

Materials Chemistry and Physics

journal homepage: www.elsevier.com/locate/matchemphys

First-principles investigation of physical, mechanical, thermodynamics and transport properties of tetragonal double perovskite Sr_2MnSbO_6: A DFT+U+SOC study

Lakhdar Benahmedi *, Anissa Besbes, Radouan Djelti

Technology and Solids Properties Laboratory, Faculty of Science and Technology, Mostaganem University, 27000, Mostaganem, Algeria

HIGHLIGHTS

- First-principles study of Sr_2MnSbO_6 reveals half-metallic ferromagnetic behavior.
- Mechanical analysis shows Sr_2MnSbO_6 is stable, with significant ductility and strength.
- Thermoelectric properties highlight potential for energy conversion applications.
- Spin-orbit coupling (SOC) effects incorporated for accurate electronic structure analysis.
- Sr_2MnSbO_6 is a promising candidate for spintronics and thermoelectric devices.

GRAPHICAL ABSTRACT

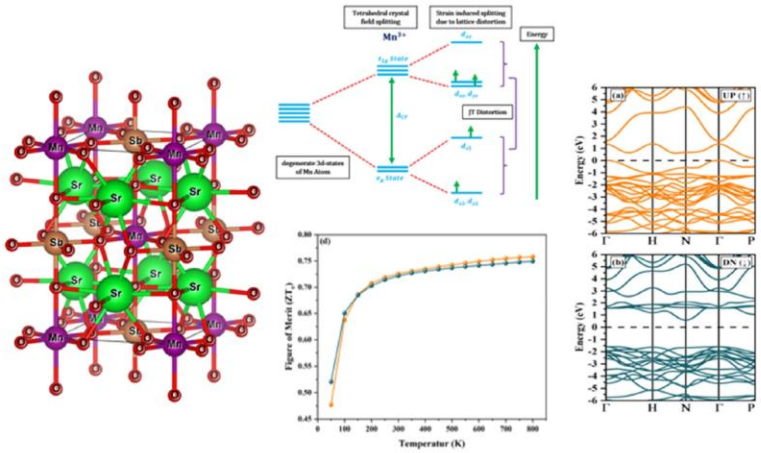

ARTICLE INFO

Keywords:
Tetragonal double perovskite
Half-metallicity
Spintronics
Thermoelectric properties
DFT

ABSTRACT

In this study, we investigate the structural, electronic, elastic, and thermoelectric properties of the tetragonal Sr_2MnSbO_6 double perovskite using the full-potential linearized augmented plane wave (FP-LAPW) method within the WIEN2k code. The calculations were performed using the generalized gradient approximation (GGA-PBE), GGA-PBE + U, and the Tran-Blaha modified Becke-Johnson (TB-mBJ) potential to correct the exchange-correlation functional. Spin-orbit coupling (SOC) was applied to account for relativistic effects. The results confirm the stability of the ferromagnetic (FM) state, as evidenced by energy optimization. Notably, the compound exhibits robust half-metallicity, characterized by a semiconductor nature in the spin-down channel and metallic behavior in the spin-up channel, which is a key feature for efficient spintronic applications such as spin filters and magnetic sensors. Thermodynamic stability is affirmed by the negative formation energy and the absence of imaginary modes in the phonon dispersion curve. Mechanical analysis indicates that Sr_2MnSbO_6 is mechanically stable, with significant anisotropy, mechanical strength, and ductility. Furthermore, the thermoelectric performance shows a high Seebeck coefficient and favorable power factor, underscoring its promising

* Corresponding author.
E-mail address: lakhdar.benahmedi@gmail.com (L. Benahmedi).

https://doi.org/10.1016/j.matchemphys.2025.130520
Received 4 December 2024; Received in revised form 5 February 2025; Accepted 8 February 2025
Available online 10 February 2025

NJC

ROYAL SOCIETY OF CHEMISTRY

PAPER

Check for updates

Cite this: *New J. Chem.*, 2025, **49**, 6741

First-principles investigation of inorganic antiperovskite A_3SbAs (A = Ba, Sr, and Ca): insights into thermoelectric and optoelectronic potential

Lakhdar Benahmedi, * Anissa Besbes, Radouan Djelti, Sidahmed Bendehiba and Ali Aissani

Received 2nd January 2025,
Accepted 22nd February 2025

DOI: 10.1039/d5nj00017c

rsc.li/njc

This study presents a comprehensive theoretical investigation of the structural, electronic, optical, thermoelectric, mechanical, phonon, and thermodynamic properties of A_3SbAs (A = Ba, Sr, and Ca) antiperovskites using first-principles density functional theory (DFT). The compounds exhibit stable cubic perovskite structures, with lattice parameters ranging from 5.49 Å for Ca_3SbAs to 6.18 Å for Ba_3SbAs. The electronic properties reveal direct band gaps, with values of 0.372 eV for Sr_3SbAs and 0.596 eV for Ca_3SbAs in the GGA-PBE approximation, increasing significantly up to 0.978 eV for Ba_3SbAs, 1.003 eV for Sr_3SbAs, and 1.195 eV for Ca_3SbAs using the TB-mBJ potential. These band gaps indicate suitability for optoelectronic applications. Optical properties show that Ba_3SbAs performs well in the near-infrared and visible ranges, while Ca_3SbAs excels in the ultraviolet range. Thermoelectric performance is also promising, with *ZT* values approaching unity at 300 K for all compounds, indicating high potential for energy conversion. Mechanical properties show that Ca_3SbAs is the most robust, while Ba_3SbAs is more flexible. Phonon dispersion confirms the dynamical stability of all compounds, and thermodynamic analysis suggests that these materials are stable under varying temperatures and pressures. The results highlight the potential of A_3SbAs antiperovskites for applications in optoelectronics and thermoelectrics, offering promising candidates for sustainable energy technologies.

1. Introduction

The relentless pursuit of advanced materials with tailored electronic, optical, and thermal properties has become a cornerstone of modern materials science, driven by the urgent need for sustainable and efficient technologies. As the global demand for energy continues to rise, the development of materials that can efficiently convert, store, and utilize energy has become a critical area of research.[1–4] Among the diverse classes of materials under investigation, antiperovskites have emerged as a highly promising family due to their structural versatility, tunable physical properties, and potential for multifunctional applications.[5] Antiperovskites, with the general formula A_3BX, where A is typically an alkaline earth or a rare earth metal, B is a transition metal or a main group element, and X is a non-metal, exhibit a crystal structure that is inversely related to the well-known perovskite structure.[6] This structural analogy, combined with their rich chemistry, allows antiperovskites to display a wide range of properties, including superconductivity, magnetism, thermoelectricity, and optoelectronic functionality, making them highly attractive for applications in energy conversion, storage, and beyond.[7]

The exploration of antiperovskites has gained significant momentum in recent years, with both theoretical and experimental studies revealing their remarkable potential in various technological domains. For instance, the antiperovskite Mn_3GaN has been extensively studied for its unique magnetic properties and phase transitions. Researchers such as Han *et al.* investigated the magnetic behavior of Mn_3GaN, revealing its potential for spintronic applications due to its tunable magnetic states and high Néel temperature.[8] The ability to control magnetic properties through chemical substitution or external stimuli makes Mn_3GaN a promising candidate for next-generation spintronic devices, which rely on the manipulation of electron spin rather than charge for information processing. Similarly, the antiperovskite $CuNCo_3$ has attracted attention for its superconducting properties. Theoretical studies by Liang *et al.* predicted that $CuNCo_3$ could exhibit high-temperature superconductivity, making it a promising candidate for quantum computing and energy transmission.[9] The discovery of high-temperature superconductors has been a long-standing goal in condensed matter physics, as they can revolutionize energy transmission by enabling lossless power transfer over long distances.

Technology and Solids Properties Laboratory, Faculty of Science and Technology, Mostaganem University, Mostaganem, 27000 Mostaganem, Algeria.
E-mail: lakhdar.benahmedi@gmail.com

Physica B 714 (2025) 417452

Contents lists available at ScienceDirect

Physica B: Condensed Matter

journal homepage: www.elsevier.com/locate/physb

First-principles study of electro-structural, mechanical, optical, and thermal properties of hexagonal chalcogenide perovskites $CsTaX_3$ (X = S, Se)

Lakhdar Benahmedi *, Anissa Besbes, Radouan Djelti

Technology and Solids Properties Laboratory, Faculty of Science and Technology, Mostaganem University, 27000, Mostaganem, Algeria

ARTICLE INFO

Keywords:
Hexagonal perovskites
Chalcogenide perovskites
DFT
Wien2K
Thermoelectric properties

ABSTRACT

This study presents a comprehensive investigation of the structural, electronic, elastic, optical, and thermoelectric properties of hexagonal chalcogenide perovskites $CsTaX_3$ (X = S, Se) using first-principles Density Functional Theory (DFT) calculations. Structural optimization using the GGA-PBE functional yields lattice constants of $a = 7.44$ Å, $c = 6.01$ Å for $CsTaS_3$, and $a = 7.71$ Å, $c = 6.14$ Å for $CsTaSe_3$. Both compounds exhibit indirect band gaps, refined using the TB-mBJ potential, with values of 0.90 eV ($CsTaS_3$) and 0.41 eV ($CsTaSe_3$). Elastic constants satisfy the Born stability criteria, and calculated bulk moduli are 52.52 GPa ($CsTaS_3$) and 46.08 GPa ($CsTaSe_3$), confirming mechanical stability. Optical properties indicate high dielectric constants, with static ε_1 values reaching 6.03 ($CsTaS_3$) and 8.06 ($CsTaSe_3$), and strong absorption in the visible region. Thermoelectric analyses reveal positive Seebeck coefficients throughout the 50–1200 K temperature range, indicating p-type conductivity, $CsTaSe_3$ exhibits a power factor of 1.85×10^{11} W/m·K^2 and a maximum ZT of 0.75, compared to 1.67×10^{11} W/m·K^2 and ZT = 0.76 for $CsTaS_3$. These findings underscore the potential of $CsTaS_3$ for high-temperature thermoelectric applications and suggest the viability of $CsTaX_3$ compounds in future energy conversion and optoelectronic technologies.

1. Introduction

The continuous demand for more efficient materials in the fields of energy conversion, optoelectronics, and thermoelectrics has prompted extensive research into the discovery and development of new materials, that can overcome the limitations of current technologies [1,2]. Among the most promising candidates in these applications are perovskite-based compounds, which have demonstrated remarkable tunability in their electronic, optical, and thermoelectric properties. These materials are characterized by the ABX_3 structure, where A and B are cations and X is an anion, typically a halide or chalcogen [3]. Over the past decade, lead halide perovskites, such as $CH_3NH_3PbI_3$ and $CsPbBr_3$, have attracted tremendous attention due to their extraordinary optoelectronic properties, including high power conversion efficiency (PCE) in photovoltaic applications, strong absorption across the visible spectrum, and tunable band gaps. These materials have revolutionized the field of solar energy conversion, with lead halide perovskite-based solar cells achieving efficiencies comparable to silicon-based technologies [4–7].

However, despite the remarkable progress, lead halide perovskites pose significant environmental and health concerns due to the inherent toxicity of lead [8]. Lead contamination is a critical issue that affects the long-term viability of these materials in commercial applications, as the degradation of lead perovskites under environmental stress can release harmful lead ions into the environment [9]. Moreover, the instability of these materials, particularly under moisture, heat, and light exposure, presents further challenges for their practical implementation. These concerns have prompted the scientific community to search for alternative perovskite materials that maintain the desirable properties of lead halide perovskites while eliminating their toxicity and enhancing their stability [10].

In response to these challenges, researchers have shifted their focus towards developing lead-free perovskite materials with comparable or superior optoelectronic and thermoelectric properties. One promising avenue of exploration has been chalcogenide perovskites, which incorporate chalcogen elements such as sulfur (S), selenium (Se), or tellurium (Te) in place of halides [11]. Chalcogenide perovskites are emerging as strong contenders for energy and optoelectronic applications due to their tunable electronic structure, excellent light absorption, and potential for enhanced stability. These materials also offer the advantage of

* Corresponding author.
E-mail address: lakhdar.benahmedi@gmail.com (L. Benahmedi).

https://doi.org/10.1016/j.physb.2025.417452
Received 17 November 2024; Received in revised form 14 May 2025; Accepted 27 May 2025
Available online 28 May 2025

Investigating the Structural, Electronic, Optical, and Thermoelectric Properties of $TlXO_3$ (X = Nb, Ta) for Low-Cost Energy Applications

L. Benahmedi*, A. Besbes and R. Djelti

Technology and Solids Properties Laboratory, Faculty of Science and Technology, Mostaganem University, 27000 Mostaganem, Algeria

Received: & Accepted: 14.03.2025

Doi: 10.12693/APhysPolA.147.393 *e-mail: lakhdar.benahmedi@gmail.com

This study explores the structural, electronic, elastic, optical, and thermoelectric properties of two novel oxide perovskites, $TlNbO_3$ and $TlTaO_3$, using density functional theory with the generalized gradient approximation and modified Becke–Johnson potential to accurately capture exchange–correlation effects. Our analysis confirms the thermodynamic stability of both compounds through assessments of cohesive energy, formation enthalpy, and phonon dispersion, indicating their cubic and dynamic stability. The band structure reveals that $TlNbO_3$ has a direct band gap of 0.17 eV, while $TlTaO_3$ exhibits a wider gap of 1.52 eV, confirming their semiconductor behavior. Elastic property calculations indicate that $TlNbO_3$ is brittle and $TlTaO_3$ is more ductile, with both materials demonstrating elastic anisotropy and a mix of metallic and covalent bonding. The density of states analysis highlights significant contributions from Tl, O, and Nb/Ta in the valence and conduction bands, emphasizing their potential in optoelectronic applications. Optical analyses further reveal high refractive indices and favorable dielectric properties, supporting their use in devices. Additionally, thermoelectric evaluations show a κ/σ ratio on the order of 10^{-5}, indicating low thermal conductivity alongside significant electrical conductivity. Notably, $TlTaO_3$ demonstrates substantial power factor values, positioning it as a promising candidate for thermal applications and energy conversion systems. Overall, this comprehensive investigation underscores the potential of $TlNbO_3$ and $TlTaO_3$ for advanced technological applications.

topics: oxide perovskites, density functional theory (DFT) calculations, band gap, thermoelectric properties

1. Introduction

The ongoing pursuit of sustainable energy solutions and efficient energy management is critical in addressing global challenges such as fossil fuel depletion and climate change [1]. As the world seeks alternatives to fossil fuels, energy storage technologies have become pivotal [2]. These technologies enable the capture and utilization of energy generated at various times, effectively addressing the intermittent nature of renewable energy sources and optimizing energy use in modern society [3]. Effective energy management supports not only industrial processes but also the performance of a wide range of electronic and electrical devices. In this context, dielectric materials and their associated technologies are essential, as they store and deliver energy rapidly, making them crucial for applications in hybrid electric vehicles, portable electronic devices, and pulse power systems [4–6].

Perovskite materials have emerged as promising candidates for addressing the global energy challenges of fossil fuel depletion and climate change [7]. The perovskite structure, characterized by its versatile ABX_3 composition, allows for incorporating a wide range of cations [8]. This adaptability results in materials with diverse and tunable properties, making perovskites highly suitable for various applications, including energy storage and conversion technologies [9, 10]. Their inherent stability, combined with unique electronic, magnetic, and optical properties, positions them as key materials in developing advanced technologies aimed at sustainable energy solutions [11–13]. Among the different classes of perovskites, oxide perovskites such as barium titanate ($BaTiO_3$) and strontium ruthenate ($SrRuO_3$) stand out due to their stability and functional versatility. These materials are integral to various applications, from capacitors and actuators to catalysts and photovoltaic systems. Their capacity to facilitate chemical reactions and absorb light makes them

Journal of Inorganic and Organometallic Polymers and Materials
https://doi.org/10.1007/s10904-025-03686-8

RESEARCH

DFT and SCAPS-1D Modeling of Ba_3BiI_3 Perovskite Solar Cells: Exploring the Influence of HTL and ETL Materials

Lakhdar Benahmedi[1] · Anissa Besbes[1] · Radouan Djelti[1] · Samia Moulebhar[2] · Ali Aissani[1] · Sidahmed Bendehiba[1]

Received: 27 January 2025 / Accepted: 23 February 2025

Abstract
In this study, we present a comprehensive analysis of the structural, electronic, and optical properties of the Ba_3BiI_3 perovskite through Density Functional Theory (DFT) calculations and SCAPS-1D simulations. The DFT calculations, utilizing the Full Potential Linearized Augmented Plane Wave (FP-LAPW) method, reveal that Ba_3BiI_3 exhibits a direct bandgap of 1.43 eV, making it a promising candidate for solar energy applications. Structural optimization shows excellent stability with negative formation and cohesive energies. To explore its photovoltaic potential, Ba_3BiI_3 was integrated into a solar cell architecture, and the influence of various hole and electron transport layers (HTL and ETL) on the device's performance was evaluated. SCAPS-1D modeling suggests that the Al/FTO/SnS_2/Ba_3BiI_3/MoO_3/Au configuration delivers optimal device performance with a power conversion efficiency (PCE) of 30.27%, a short-circuit current density (JSC) of 28.37 mA/cm², an open-circuit voltage (VOC) of 1.2367 V, and a fill factor (FF) of 88.77%. These findings highlight the potential of Ba_3BiI_3 as an efficient, lead-free alternative for next-generation perovskite solar cells. Future work will focus on experimental validation and further optimization of device structures to enhance photovoltaic performance.

Keywords Ba_3BiI_3 · Perovskite · DFT · SCAPS-1D · ETL · HTL

1 Introduction

Perovskite solar cells (PSCs) have revolutionized the photovoltaic industry in recent years, offering a promising alternative to traditional silicon-based solar cells [1, 2]. The unique properties of perovskite materials, including their high absorption coefficients, tunable bandgaps, low exciton binding energies, and defect tolerance, have contributed to their unprecedented rise in efficiency from 3.8% in 2009 to over 25.8% in 2023 [3, 4]. These advantages, coupled with the low-cost and facile fabrication processes of perovskite thin films, have positioned PSCs as a disruptive technology in renewable energy. Despite this rapid progress, the majority of high-performing PSCs rely on lead-based perovskite materials such as methylammonium lead iodide ($CH_3NH_3PbI_3$), which pose significant environmental and health hazards due to lead toxicity and its potential leaching into the environment during production, operation, or disposal [5]. This has motivated an intense search for lead-free perovskite materials that can provide comparable efficiencies while addressing environmental concerns. There have been numerous recent theoretical studies on lead-free halide double perovskites, exploring their structural, electronic, and optical properties to identify potential candidates for replacing lead-based perovskites in solar cell applications. There have been numerous recent theoretical studies on lead-free halide double perovskites, exploring their structural, electronic, and optical properties to identify potential candidates for replacing lead-based perovskites in solar cell applications. These studies have primarily focused on materials such as $Cs_2LaGaBr_6$ and $Cs_2NaGaCl_6$, which exhibit promising stability and optoelectronic properties, although their efficiency still lags behind that of lead-based counterparts [6–14].

To overcome the toxicity challenges associated with lead, researchers have explored a range of alternative materials,

✉ Lakhdar Benahmedi
lakhdar.benahmedi@gmail.com

[1] Technology and Solids Properties Laboratory, Faculty of Science and Technology, Mostaganem University, Mostaganem 27000, Mostaganem, Algeria

[2] Laboratory of Electromagnetism and Guided Optics, Faculty of Science and Technology, University Abd El Hamid Ibn Badis, Mostaganem 27000, Algeria

Published online: 15 June 2025

Solar Energy 300 (2025) 113860

Contents lists available at ScienceDirect

Solar Energy

journal homepage: www.elsevier.com/locate/solener

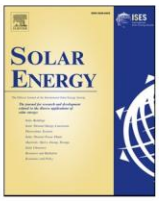

Theoretical insights into $Rb_2Pt_{1-x}Pd_xBr_6$ perovskite alloys for solar Cells: A combined DFT and SCAPS-1D study

Lakhdar Benahmedi [a,*], Anissa Besbes [a], Radouan Djelti [a], Samia Moulebhar [b,c], Ali Aissani [a], Sidahmed Bendehiba [a]

[a] Technology and Solids Properties Laboratory, Faculty of Science and Technology, Mostaganem University, 27000 Mostaganem, Algeria
[b] Analysis, Modeling, Advanced Materials for Renewable Energies Laboratory, Faculty of Science and Technology, University Abd El Hamid Ibn Badis, Mostaganem 27000, Algeria
[c] Laboratory of Electromagnetism and Guided Optics, Faculty of Science and Technology, University Abd El Hamid Ibn Badis, Mostaganem 27000 Algeria

ARTICLE INFO

Keywords:
Band gap engineering
DFT calculations
Photovoltaic performance
SCAPS-1D simulation
$Rb_2Pt_{1-x}Pd_xBr_6$double perovskites

ABSTRACT

In this work, we present a detailed theoretical investigation of the halide double perovskite alloy series $Rb_2Pt_{1-x}Pd_xBr_6$ (x = 0.0, 0.25, 0.5, 0.75, 1.0) using Density Functional Theory (DFT) and SCAPS-1D simulations to evaluate their potential as lead-free absorber materials for photovoltaic applications. Structural optimization confirms the stability of all compositions with calculated lattice parameters ranging from 11.46 Å for Rb_2PdBr_6 to 11.63 Å for Rb_2PtBr_6, decreasing consistently with increasing Pd content due to the smaller ionic radius of Pd compared to Pt. The electronic structure analysis reveals a crucial transition in the nature of the band gap: the parent compound Rb_2PtBr_6 exhibits an indirect band gap, while the alloys x = 0.25 and x = 0.75 transition to direct band gap semiconductors a beneficial feature for photovoltaic efficiency. The band gaps span a tunable range from 2.08 eV to 1.10 eV, becoming more favorable for solar absorption with increased Pd substitution. Mechanical and dynamical stability is confirmed via the elastic constants and phonon dispersion curves across the series. SCAPS-1D simulations reveal marked improvements in device performance, with power conversion efficiencies (PCEs) reaching up to 24.04 % for $Rb_2Pt_{0.25}Pd_{0.75}Br_6$, accompanied by a fill factor (FF) of 82.69 % and a short-circuit current density (J_{SC}) of 27.60 mA/cm^2. These findings demonstrate that controlled Pd incorporation in Rb_2PtBr_6 effectively tunes both the optoelectronic and mechanical properties, highlighting its promise as a lead-free perovskite absorber for next-generation photovoltaic devices.

1. Introduction

Alloying is a classical yet continually evolving technique in materials science, wherein two or more elements are combined to form a solid solution or intermetallic compound with improved or tailored physical, chemical, and electronic properties [1,2]. This approach has historically enabled breakthroughs in diverse fields ranging from structural materials to electronic devices [3]. By modifying the atomic composition, alloying alters the electronic band structure, defect chemistry, and structural stability of a material, offering a pathway to optimize performance for targeted applications [4]. Classic examples include brass (Cu-Zn) and bronze (Cu-Sn), where alloying improves workability and resistance to corrosion, or steel (Fe-C), where alloying drastically enhances mechanical strength [5]. In electronic materials, alloys such as $Si_{1-x}Ge_x$ are vital for high-speed transistors and thermoelectrics [6,7], while $Cd_{1-x}Zn_xTe$ is widely used in radiation detectors and photovoltaics [8,9]. $Ga_{1-x}In_xN$ and $Al_{1-x}Ga_xAs$ have revolutionized LED and laser technologies through band gap engineering [10,11]. Similarly, $Bi_{2-x}Sb_xTe_3$ and $Pb_{1-x}Sn_xTe$ alloys are benchmark thermoelectric materials exhibiting optimized transport properties and enhanced ZT values [12,13].

While alloying has been extensively exploited in conventional semiconductors, its application to halide perovskites and, more specifically, to double perovskites (A_2BX_6), is relatively recent but rapidly gaining attention [14]. The A_2BX_6 structure is a vacancy-ordered derivative of the ABX_3 perovskite, where only the B-site cation is present in octahedral coordination and one-half of the BX_6 octahedra are missing in an ordered fashion [15]. These halide double perovskites have shown promise as lead-free alternatives in optoelectronics and photovoltaics, owing to their non-toxic constituents, thermal and environmental

* Corresponding author.
E-mail address: lakhdarbenahmedi@gmail.com (L. Benahmedi).

https://doi.org/10.1016/j.solener.2025.113860
Received 6 May 2025; Received in revised form 28 July 2025; Accepted 3 August 2025
Available online 6 August 2025

Abstract: This thesis explores the potential of perovskite-based materials for renewable energy-powered embedded systems, with a focus on addressing the challenges posed by rising raw material costs and resource scarcity. By leveraging the unique properties of perovskites, including their structural flexibility, tunability, and promising optoelectronic characteristics, this research investigates alternative materials to conventional silicon, lithium, and III-V compounds used in energy-related components. The study employs theoretical and computational methods, including Density Functional Theory (DFT) and simulation tools such as SCAPS-1D, to analyze the structural, electronic, elastic, optical, and thermoelectric properties of various perovskite materials. The perovskites studied include $ASiCl_3$ (where A = Cs, Rb, Li), A_3SbAs (where A = Ba, Sr, Ca), A_3BiI_3 (where A = Ba, Sr, Ca), $Rb_2Pt_{1-x}Pd_xBr_6$ (a double perovskite alloy), Sr_2MnSbO_6, Ba_2InOsO_6, and $CsTaX_3$ (where X = S, Se). Key findings include the identification of perovskites with high photovoltaic efficiencies (up to 24%) and excellent potential for applications in solar cells, LEDs, and infrared sensors. The work also highlights the suitability of these materials for agricultural and off-grid embedded systems, paving the way for more cost-effective, sustainable, and energy-efficient technologies. This thesis contributes valuable insights into the development of advanced embedded systems with a focus on renewable energy solutions, offering a foundation for future research in the field.
Keywords: Perovskite materials, Renewable energy, Embedded systems, Photovoltaic efficiency, SCAPS-1D simulation.

الملخص: تستعرض هذه الأطروحة إمكانيات المواد القائمة على البيروفيسكايت لأنظمة المدمجة المعتمدة على الطاقة المتجددة، مع التركيز على معالجة التحديات الناجمة عن زيادة تكلفة المواد الخام ونقص الموارد. من خلال الاستفادة من الخصائص الفريدة للبيروفيسكايت، بما في ذلك مرونته الهيكلية، قابلية تعديله، وخصائصه البصرية والإلكترونية الواعدة، تبحث هذه الدراسة في البدائل للمواد التقليدية مثل السيليكون، والليثيوم، والمركبات من النوع III-V المستخدمة في المكونات المتعلقة بالطاقة. تعتمد الدراسة على أساليب نظرية وحسابية، بما في ذلك نظرية الوظائف الكثافة (DFT) وأدوات المحاكاة مثلSCAPS-1D ، لتحليل الخصائص الهيكلية والإلكترونية والمرنة والبصرية والحرارية للكهرباء للعديد من المواد البيروفيسكايت. تشمل المواد المدروسة $ASiCl_3$ (A = Cs, Rb, Li), A_3SbAs (A = Ba, Sr, Ca), A_3BiI_3 (A = Ba, Sr, Ca), $Rb_2Pt_{1-x}Pd_xBr_6$ Sr_2MnSbO_6, Ba_2InOsO_6, and $CsTaX_3$ (X = S, Se)تشمل النتائج الرئيسية تحديد مواد بيروفيسكايت تتمتع بكفاءات ضوئية عالية (تصل إلى 24%) وإمكانات ممتازة للاستخدام في خلايا شمسية، وأجهزةLED ، وأجهزة استشعار الأشعة تحت الحمراء. كما تسلط الدراسة الضوء على ملاءمة هذه المواد لأنظمة مدمجة في الزراعة والتطبيقات المستقلة عن الشبكة الكهربائية، مما يمهد الطريق لتقنيات أكثر فعالية من حيث التكلفة ومستدامة وموفرة للطاقة. تساهم هذه الأطروحة في تقديم رؤى قيمة حول تطوير الأنظمة المدمجة المتقدمة مع التركيز على حلول الطاقة المتجددة، مما يوفر أساسًا للبحوث المستقبلية في هذا المجال.
الكلمات الرئيسية :مواد البيروفيسكايت, الطاقة المتجددة, الأنظمة المدمجة, كفاءة الخلايا الشمسية, محاكاةSCAPS-1D

Résumé : Cette thèse explore le potentiel des matériaux à base de pérovskites pour les systèmes embarqués alimentés par des énergies renouvelables, en mettant l'accent sur les défis posés par la hausse des coûts des matières premières et la rareté des ressources. En exploitant les propriétés uniques des pérovskites, telles que leur flexibilité structurelle, leur modulabilité et leurs caractéristiques optoélectroniques prometteuses, cette recherche examine des matériaux alternatifs aux matériaux traditionnels comme le silicium, le lithium et les composés III-V utilisés dans les composants énergétiques. L'étude utilise des méthodes théoriques et computationnelles, telles que la théorie de la fonctionnelle de densité (DFT) et des outils de simulation comme SCAPS-1D, pour analyser les propriétés structurelles, électroniques, élastiques, optiques et thermoélectriques de divers matériaux pérovskites. Parmi les principaux résultats, on identifie des pérovskites ayant des rendements photovoltaïques élevés (jusqu'à 24 %) et un excellent potentiel pour des applications dans les cellules solaires, les LED et les capteurs infrarouges. Les matériaux étudiés incluent $ASiCl_3$ (où A = Cs, Rb, Li), A_3SbAs (où A = Ba, Sr, Ca), A_3BiI_3 (où A = Ba, Sr, Ca), $Rb_2Pt_{1-x}Pd_xBr_6$ (un alliage de pérovskite double), Sr_2MnSbO_6, Ba_2InOsO_6, et $CsTaX_3$ (où X = S, Se). Le travail met également en évidence la pertinence de ces matériaux pour des systèmes embarqués agricoles et hors réseau, ouvrant la voie à des technologies plus rentables, durables et efficaces en termes d'énergie. Cette thèse apporte des éclairages précieux sur le développement des systèmes embarqués avancés, en mettant l'accent sur les solutions d'énergie renouvelable, et offre une base pour les recherches futures dans ce domaine.
Mots-clés: Matériaux pérovskites, Énergie renouvelable, Systèmes embarqués, Efficacité photovoltaïque, Simulation SCAPS-1D.